Solidification Microstructure Selection In Aluminium-Based Alloys

by

Iain Todd

Thesis submitted for the degree of
Doctor of Philosophy in the Department of Engineering Materials
University of Sheffield.

May 1996.

William James describes a man who got the experience
from laughing-gas; whenever he was under its influence,
he knew the secrets of the universe, but when he came to,
he had forgotten it. At last, with immense effort,
he wrote down the secret before the vision had faded.
When he had completely recovered, he rushed to see
what he had written. It was 'A smell of petroleum
prevails throughout'.

Bertrand Russell

A History of Western Philosophy

SUMMARY

The Al-Fe and Al-Fe-Si intermetallics formed during solidification of commercial Al-alloys may have a considerable influence on subsequent fabrication and properties. A variety of stable and metastable phases may occur depending upon alloy composition and solidification rate. The factors influencing the relative stabilities of the phases are presently not well understood. The present work has determined the effect of solidification front velocity and alloy composition on second phase intermetallic formation for both the cumulative alloy series (Al-0.5%Fe[1], Al-0.5%Fe-0.1%Si, Al-0.5%Fe-0.1%Si-0.75%Mg and Al-0.5%Fe-0.1%Si-0.75%Mg-0.04%Cr) and the quaternary alloy series Al-X%Fe-0.1%Si-Z%Mg (X = 0.25 to 0.75 : Z = 0.5 or 0.75) and Al-0.5%Fe-Y%Si-0.75%Mg (Y = 0.05 to 0.15) by Bridgman directional solidification over the velocity range, V, 0.05 to 2.0mm/s in an imposed temperature gradient, G,of 8 to 12K/mm.

Intermetallic phase competition was observed to be between $Al_{13}Fe_4$, Al_6Fe, Al_xFe Al_mFe and α-AlFeSi for the alloys and conditions investigated. Identification of the second phase intermetallics was accomplished using a combination of x-ray diffraction and TEM techniques. TEM specimens were prepared both by electropolishing and by a technique where the α-Al matrix is dissolved in butanol to leave an intermetallic residue. Specimens for x-ray diffraction were prepared exclusively by this extraction method. The effect of alloy composition on the α-Al cell size and intermetallic phase distribution were investigated using optical microscopy.

The effect of cumulative additions of 0.1%Si, 0.75%Mg and 0.04%Cr to the base Al-0.5%Fe alloy composition was to increase sequentially the maximum solidification front velocity at which $Al_{13}Fe_4$ prevailed in competition with the metastable intermetallics. This change in the competitiveness of $Al_{13}Fe_4$ was associated with an increase in the incidence of (100) growth twins on the addition of Si and also to the tendency of Al_6Fe to grow in a faceted manner in the presence of Mg.

In the binary Al-0.5%Fe composition $Al_{13}Fe_4$ and Al_xFe which were found to co-exist at V=0.1mm/s were replaced by Al_6Fe at V > 0.5mm/s. Addition of 0.1%Si to Al-0.5%Fe resulted in Al_xFe instead of Al_6Fe displacing $Al_{13}Fe_4$ for V > 0.5mm/s, whilst the addition of 0.75%Mg resulted in Al_6Fe displacing $Al_{13}Fe_4$ at V > 0.5mm/s. In the quaternary Al-Fe-Si-Mg alloy series investigated the solidification front velocity at which $Al_{13}Fe_4$ was displaced was found to be dependent upon the Fe content of the alloy. In those alloys with Fe contents of 0.25 and 0.5%Fe the velocity at which $Al_{13}Fe_4$ was displaced was between 0.5 and 1.0mm/s, whilst in those compositions containing 0.75%Fe the velocity required for the displacement of $Al_{13}Fe_4$ was found to be between 1.0 and 2.0mm/s in the 0.75%Mg content alloy and in excess of 2.0mm/s in the alloy containing 0.5%Mg. Although the phase displacing $Al_{13}Fe_4$ in the quaternary alloys was found to be Al_6Fe in Al-0.5%Fe-0.05%Si-0.75%Mg the replacement phase at V>0.5mm/s was Al_mFe. This phase was found in only one other alloy condition, as a minor phase in Al-0.75%Fe-0.1%Si-0.5%Mg, at V=2.0mm/s. The effect of 0.04%Cr on phase selection in Al-0.5%Fe-0.1%Si-0.75%Mg was to increase the maximum V at which $Al_{13}Fe_4$ was observed as a major phase to 1.00mm/s, as compared with 0.5mm/s in the absence of Cr.

The primary α-Al cell spacings displayed the relationship $\lambda_1=K(G.V)^{-n}$ where n was approximately 0.5 and independent of alloy composition whilst the value of K was found to be 41.5 ± 3.4 $\mu m(K/s)^{1/2}$ for Al-0.5%Fe and approximately $80\mu m(K/s)^{1/2}$ for all 0.1%Si containing alloys, this value being largely unaltered by variation in Fe or Mg content or by the presence of Cr. The magnitude of this increase in the α-Al cell spacing in the presence of Si was consistent with a reduction in the activation energy for diffusion of Fe in liquid Al by 14% in the presence of Si.

---

[1] all compositions are in wt%.

PAGE MISSING IN ORIGINAL

ACKNOWLEDGEMENTS

I wish to express my thanks to my supervisor Prof. H.Jones for his advice throughout the duration of this project. I am also vey grateful to the University of Sheffield for funding my research via the Dr. Robert Styring scholarship over the period October 1991 to September 1994 and to Dr. D.A.Granger at ALCOA Technical Center, Pittsburgh for financial support and interest in this work.

I also wish to thank Dr.R.A.Buckley for his support, encouragement and interest in my work over the past 4 years, particularly for his advice on the interpretation of the "phoney lines" on the Guinier x-ray camera films, Dr. M.Al-Khafaji for his patient guidence in the use of the TEM and the interpretation of diffraction data and Dr.Ian Stone for helping me to sort out some of my ideas.

Thanks are also long overdue to my fellow inmates of the D-Floor "workroom" for the many interesting and eye-opening lunchtime converstations, and to Dave Hanlon, Dave Wilkes and Martin O'Reilly in particular. Their friendship and good humour made bearable what was, much of the time, a fruitless and frustrating task.

Finally I would like to thank my parents for their unending love and support and Suzanne for reminding me that there is so much more to life than small pieces of metal.

Contents

1. INTRODUCTION

Iron is the most common impurity found in aluminium. It has a high solubility in molten aluminium and is therefore readily dissolved at all molten stages in production. The solubility of iron in the solid state is, however, very low (0.04%)[1]. As a result most of the iron present above this level appears as an intermetallic second phase in combination with aluminium and other elements.

Numerous Al-Fe and Al-Fe-Si intermetallics have been identified in as-cast commercial purity aluminium and these have been the subject of extensive research because they can influence the material behaviour during subsequent fabrication steps and may have a critical influence on material quality. It is, therefore, of considerable technological interest to be able to exert control over the formation of these phases especially in dilute aluminium alloy compositions. This can be done most readily by controlling cooling rate during solidification or by modification of alloy chemistry to enhance the stability of a desired phase.

Several authors have dealt with the effects of further additions on phase stability in the binary Al-Fe alloy system. In particular the effect on phase stability of other transition metals which are known from studies of their equilibrium behaviour to be at least partially soluble in binary Al-Fe phases have shown that additions of these elements can cause significant changes in phase stability with respect to both the cooling rate during solidification and solidification front velocity. It has also been suggested on a number of occasions that the discrepancies often found when comparing the results of published work on both the binary Al-Fe and ternary Al-Fe-Si systems, are attributable even to trace levels of impurity in the compositions investigated. As a result the relative effects of each component present on phase incidence and stability remains uncertain. This is especially true of ternary compositions with low Si:Fe ratios and Al-rich quaternary Al-Fe-Si-Mg alloys where a clear picture of phase incidence versus solidification cooling rate has yet to emerge.

---

[1] All compositions in this document are given in wt.% unless otherwise indicated.

To date no systematic investigation has been conducted into the cumulative effect of common alloying additions and impurities on intermetallic phase stability in Al-base alloys. One objective of this thesis work was to determine the effect on phase stability and incidence of cumulative additions of 0.1%Si, 0.75%Mg and 0.04%Cr to a base composition of Al-0.5wt.%Fe over the range of solidification front velocity between 0.05 and 2.00mm/s during steady state growth at an imposed temperature gradient of 8 to 12 K/mm. The effect of minor changes in Fe, Si and Mg content on intermetallic phase selection in Al-Fe-Si-Mg alloys was also investigated under these imposed solidification conditions.

Chapter 2 provides a review of the phases reported to have been formed in dilute Al-Fe, Al-Fe-Si and Al-Fe-Si-Mg alloys and the local solidification conditions reported as being necessary for their formation. In addition, the effects reported in the available literature of low levels of impurities on the stability and morphology of the intermetallics will be surveyed. Chapter 3 describes the experimental procedures used including alloy preparation, directional solidification, and the techniques employed in the identification of the intermetallic phases formed. Chapter 4 presents the Results and Chapter 5 is the Discussion which attempts to interpret these results and to draw conclusions concerning their implications which are detailed in Chapter 6.

2. LITERATURE REVIEW

2.1 The equilibrium Al-Fe system

The equilibrium phase diagram at the Al-rich end of the Al-Fe system was established some time ago and is of the form shown in Fig.2.1 [Phillips 1976]. This indicates that α-Al forms a eutectic with $Al_{13}Fe_4$ at 655°C and 1.8%Fe.This $Al_{13}Fe_4$ is sometimes still referred to as Al_3Fe, though this older and simpler structural formula has fallen from favour in recent years. $Al_{13}Fe_4$ has a complicated structure, exhibits monoclinic symmetry [Black 1955a and b] and has a composition of ~39.4% Fe. The lattice parameters and crystallographic data for $Al_{13}Fe_4$ are presented in Table 2.1.

The growth behaviour of the αAl- $Al_{13}Fe_4$ eutectic during unidirectional solidification has been studied in some detail. Under these growth conditions the $Al_{13}Fe_4$ phase forms typically as ribbon-shaped plates in the [010] direction with (100) exposed at the longitudinal flat surfaces. At high growth velocities (V) under a low imposed thermal gradient (G) (i.e. $G/V \leq 1000$ Ks/mm^2 [Adam and Hogan 1972]) the $Al_{13}Fe_4$ tends to become branched [Adam and Hogan 1972, Adam and Hogan 1975, Hirai *et al.* 1977]. In addition, the (width/ thickness) aspect ratio of the plates is also observed to decrease as the growth velocity is increased.

This branching of $Al_{13}Fe_4$ disappears when freezing with a high thermal gradient to growth velocity ratio, determined as > 1000Ks/mm^2 [Adam and Hogan 1972] or >2800Ks/mm^2 [Hirai *et al.* 1977]. Under these imposed conditions the eutectic phases grow in a parallel manner such that :

$$[010]_{Al_{13}Fe_4} \parallel \langle 100 \rangle_{\alpha\text{-}Al} \parallel \text{growth direction}.$$

Liu and Dunlop [1988], claim to have observed further orientation relationships between the eutectic α-Al and $Al_{13}Fe_4$ observed in commercial purity D.C (direct chill) cast material. Three orientation relationships were reported:

OR-I

$$(200)_{Al_{13}Fe_4} \parallel (200)_{\alpha\text{-}Al}$$
$$(020)_{Al_{13}Fe_4} \parallel (020)_{\alpha\text{-}Al}$$
$$[001]_{Al_{13}Fe_4} \parallel [001]_{\alpha\text{-}Al}$$

$$[100]_{Al_{13}Fe_4} \parallel [100]_{\alpha\text{-}Al}$$

OR-II $$(020)_{Al_{13}Fe_4} \parallel (020)_{\alpha\text{-}Al}$$

$$(001)_{Al_{13}Fe_4} \parallel (002)_{\alpha\text{-}Al}$$

and

$$[100]_{Al_{13}Fe_4} \parallel [10\bar{1}]_{\alpha\text{-}Al}$$

OR-III $$(020)_{Al_{13}Fe_4} \parallel (020)_{\alpha\text{-}Al}$$

$$(001)_{Al_{13}Fe_4} \parallel (202)_{\alpha\text{-}Al}$$

although the evidence presented was slight and no statistics were stated to indicate the number of observations made of each orientation relationship. No preferential contact plane or orientation relationship has been reported for the eutectic structures grown by directional solidification other than for the coincidence of growth axes stated previously.

$Al_{13}Fe_4$ exhibits a number of crystallographic features including a marked tendency towards twin formation. Black [1955a and b] showed that two types of twinning could occur in $Al_{13}Fe_4$ crystals, the twin planes being (100) and (001). Both have been observed experimentally [Adam and Hogan 1975, Fung *et al.* 1987, Skjerpe 1987] although (001) appears to be the most common. Adam and Hogan [1975] reported that (001) twins were observed in $Al_{13}Fe_4$ crystals under all growth conditions whilst (100) twins were only to be found occasionally in crystals grown in high temperature gradients or with low solidification front velocities ($G/V > 1000 Ks/mm^2$).

The spacing of twins on (001) has been reported as ranging from 5 to 20 nm [Adam and Hogan 1975, Skjerpe 1987] a periodicity of approximately 4 to 16 times the (001) lattice spacing. This faulting gives rise to streaking of reciprocal lattice points in an electron diffraction pattern in the c* reciprocal lattice vector rows. This streaking is more pronounced for thin crystals with fine substructures and is phenomenologically related to

line broadening in x-ray diffraction. It has been proposed that the presence of these twins facilitates growth of the crystal via the twin plane re-entrant edge (TPRE) mechanism [Adam and Hogan 1975]. This growth mechanism removes the necessity for continual renucleation on an atomically smooth interface to allow propagation by two dimensional layer growth by forming re-entrant corners within which the atoms necessary for nucleation of consecutive planes are always in place. Adam and Hogan [1975] envisaged the crystallography of this growth mechanism to be that shown in Fig.2.2, where the self perpetuating re-entrant grooves exposed at the growing interface are formed by alternate (111) and $(1\,\bar{1}\,1)$ planes intersecting at emergent (001) twin planes.

The (100) twin mechanism has been proposed as that responsible for the formation of the ten pointed star morphology observed for sections of primary $Al_{13}Fe_4$ prisms in hypereutectic Al-Fe alloys [Louis *et al.* 1980, Fung *et al.* 1987]. In the primary $Al_{13}Fe_4$ dendrites this star morphology appears to become more common as growth velocity, V, (and, by inference, undercooling) increases. This observation of twinning behaviour in primary crystals appears to contrast with the behaviour of the intermetallic when a constituent of the αAl-$Al_{13}Fe_4$ eutectic where, as mentioned earlier, (100) twins are observed at high G/V (i.e. low growth velocities or high imposed temperature gradients).

Adam and Hogan [1975] initially considered that the longitudinal branching mechanism in eutectic $Al_{13}Fe_4$ would be directly and simply related to (001) or (100) twinning. Investigations of branched regions in the crystals, however, did not reveal any simple or consistent relationship between the parent crystal and branch. No further studies of longitudinal branching seem to have been published and as a result the mechanism by which this occurs remains undetermined.

2.2 Metastable phases in Al-Fe

The best known and characterised metastable intermetallic phase in Al-Fe is Al_6Fe. Besides Al_6Fe, however, a number of other metastable phases have been reported as forming during the solidification of hypoeutectic Al-Fe alloys. These include Al_xFe [Young and Clyne 1981, Westengen 1982, Skjerpe 1987], Al_9Fe_2 [Simensen and Vellasamy 1977] and Al_mFe [Miki *et al.* 1975, Skjerpe 1988, Chandresakeran *et al.*

1988]. The crystallographic data for these phases are presented in Table 2.1 and their reported characteristics will be discussed in the following sections .

2.2.1 Al_6Fe

As long ago as 1925 [Dix 1925] it was reported that casting an Al-1.7% Fe alloy into a cast iron mould could cause a modification to the structure of Al-Fe alloys, producing a structure consisting of primary α-Al dendrites and an unidentified fine fibrous, regular eutectic. Hollingworth, Frank and Willet [1962] reported that surface darkening during anodising of D.C. cast Al-2% Fe could be linked to the presence of a metastable phase with a similar morphology to that described by Dix and which gave rise to an x-ray pattern similar to Al_6Mn. Consequently they associated this phase with the stoichiometric formula Al_6Fe. A crystal of this metastable intermetallic was later isolated and investigated in detail by Walford [1965] who confirmed that the phase was isostructural with the corresponding Al-Mn phase. Later studies [Backerud 1968, Burden and Jones 1970, Adam and Hogan 1972, Hughes and Jones 1976] confirmed that sufficiently rapid cooling caused a transition in the intermetallic component of the eutectic from $Al_{13}Fe_4$ to Al_6Fe and that this phase typically displayed a rod-like morphology. The results of this previous work allowed the position of the metastable αAl-Al_6Fe eutectic point to be estimated as lying at approximately 650°C and 3.5%Fe, though more recent work has found the eutectic temperature to be 652.9°C [Liang and Jones 1993]. A phase diagram has been constructed [Murray 1983], after consideration of the experimentally generated data, which includes the metastable Al_6Fe phase boundaries. This is presented as Fig.2.3.

In contrast to the αAl-$Al_{13}Fe_4$ eutectic the constituents of the αAl-Al_6Fe system appear to grow in a coupled manner giving rise to a normal eutectic, with diffusion of Fe in the liquid at the growth front as the rate limiting process [Adam and Hogan 1972]. It was additionally proposed that the following orientation relationships existed between the intermetallic and α-Al [Adam and Hogan 1972]:

$$(\bar{1}\,1\,0)_{Al_6Fe} \parallel (\bar{1}\,1\,1)_{\alpha\text{-}Al}$$

$$(1\,3\,0)_{Al_6Fe} \parallel (\bar{1}\,1\,\bar{1})_{\alpha\text{-}Al}$$

$$(310)_{Al_6Fe} \parallel (00\bar{2})_{\alpha\text{-}Al}$$

$$[001]_{Al_6Fe} \parallel [110]_{\alpha\text{-}Al}$$

and that these presented a unique crystallographic relationship between the two phases. Again, as was the case for the proposed orientation relationships between α-Al and $Al_{13}Fe_4$ discussed in section 2.2.1, the evidence presented in support of these proposed relationships was limited. The authors also stated that the Al_6Fe rods were faceted, with (110), $(1\bar{1}0)$, (130) and (310) as the facet planes, although the published micrographs show little evidence of such behaviour.

Faceting behaviour in Al_6Fe has, however, been reported on two further occasions where supporting photographic evidence is more compelling [Burden and Jones 1970: Clyne 1981]. Although Clyne did not attempt to identify the facet planes, Burden and Jones reported that the prismatic plane orientations were close to {010}, {100} and {110} Al_6Fe and did not claim to have observed any preferential contact planes. With the exception of {110}, these differ significantly from those reported by Adam and Hogan [1972]. Burden and Jones also refer to the presence of a lath-lamella morphology of Al_6Fe observed at α-Al cell boundaries which would mean that identification of this phase based on microstructural observation alone should be regarded as insufficient.

2.2.2 Al_xFe

A phase which was morphologically and compositionally similar to Al_6Fe but structurally distinct was first reported in the early '80's from two independent sources [Young and Clyne 1981, Westengen 1982] although only Young and Clyne attempted to characterise the crystal structure . This phase, which was termed Al_xFe, was determined by them to exhibit monoclinic symmetry and to have the lattice parameters a = 2.160 nm, b = 0.930 nm, c = 0.905 nm and β = 94°. This, they stated, was to be regarded as a first approximation to the true crystal structure of the phase which was not determined fully as the crystals always contained many closely spaced faults. An x-ray pattern was also presented for the phase, although it emerges that this Al_xFe was identified during the course of their experimental work solely on the basis of electron diffraction methods. The x-ray and electron diffraction information gathered were not found to be entirely

consistent with each other and it has been suggested that these inconsistencies could be explained if the Al_xFe structure had a highly variable site occupancy, meaning that the lattice parameters could vary over an appreciable range [Skjerpe 1987].

Skjerpe [1987] also observed a phase which he termed Al_xFe. It was reported to give rise to complex electron diffraction patterns where the diffraction spots did not constitute a regular lattice. In spite of this, a set of lattice parameters were presented, these being the averages taken from a series of tilting experiments. It was claimed that the best fit was for a C-centred orthorhombic unit cell with approximate dimensions: a = 0.6 nm, b = 0.7 nm and c = 0.879 nm. These parameters are very similar to those for Al_6Fe (see Table 2.1) as was the Fe content of the phase and these observations led Skjerpe to conclude that the phases were structurally related, the differences between them simply reflecting the effect of the defects in the Al_xFe structure.

It would appear, then, that the phases reported by Skjerpe and Young and Clyne were not the same. To date, however, no results have been published to confirm either structure.

2.2.3 Al_mFe

Al_mFe was first identified by Japanese workers [Miki *et al.* 1975] investigating surface quality problems in D.C cast material and was also identified as the main constituent in strip cast Al-1.7% Fe by Morris [1979]. The structure of Al_mFe was determined to be body-centred tetragonal with a = 0.884 nm and c = 2.160 nm and a space group I4/mmm [Skjerpe 1988]. Chandresakeran *et al.* [1988] corroborated these observations with the exception of the space group which they determined to be I4mm. The phase is non-stoichiometric, the value of m having been determined by energy dispersive spectroscopy as 4 [Porter and Westengen 1981], 4.4 [Westengen 1982] and 4.2 [Skjerpe 1987]. Only a schematic x-ray diffraction pattern has been published to date [Asami *et al.* 1978] indicating a few low order reflections.

Electron microscopy of Al_mFe crystals extracted from the α-Al matrix revealed the morphology to be complex [Skjerpe 1988], the particles having a skeletal morphology with numerous protruding fingers. It was suggested that the phase was formed by a

metastable eutectic reaction although the position of the metastable eutectic point has not yet been determined. In addition Skjerpe[1987 and 1988] remarked that selected area diffraction patterns (SADP) contained many incommensurate reflections parallel to ⟨110⟩. These extra reflections were shown, by high resolution electron microscopy, to be associated with faults in the stacking sequence on the {110} planes. These stacking defects displayed a preferred periodicity of 5 times the spacing of {110}(d_{110} = 0.623nm) and produced reflections in the SADP of d-spacing approximately 3nm.

On the basis of close similarity between the appearance and angular relations between SADP's in $Al_{13}Fe_4$ and Al_mFe, a recent study [Kim and Cantor 1994] has suggested that these two phases are structurally related and that they are also very similar to the decagonal quasicrystalline phase observed in rapidly solidified hypereutectic Al-Fe alloys [Fung *et al.* 1986].

Clyne [1981] has also suggested that Al_mFe and Al_xFe could be related on the basis that they have an identical c-axis dimension (2.16nm). This, however, was stated as an aside and has not been investigated further.

2.2.4 Al_9Fe_2

Investigation of phase formation in strip cast Al-0.25%Fe-0.1%Si by transmission electron microscopy led Simensen and Vellasamy [1977] to conclude that the main intermetallic constituent was a phase with a composition corresponding to the structural formula Al_9Fe_2. The lattice parameters of the phase were determined as being very close to those of the isostructural Al_9Co_2 intermetallic [Douglas 1950] and superficial resemblances were noted between this phase and both $Al_{13}Fe_4$ (both exhibit a tendency to closely spaced faults) and Al_6Fe (SADP's of the phases show similarities between principal zone axes).

To date this phase has been reported only once, although a low-Si ternary phase termed α_v-AlFeSi (v for Vellasamy) has been reported by Dons [1985] which has lattice parameters remarkably similar to Al_9Fe_2. This phase is discussed further in section 2.6.1.

2.2.5 Other metastable binary phases

A number of other workers have reported metastable phases in binary Al-Fe which exhibit cubic symmetry. In several cases the evidence is inconclusive or incomplete [Jacobs *et al.* 1974, Chattopadhyay *et al.* 1978] whilst in others the phase is determined to be produced from solid solution on annealing [Fontaine and Guinier 1975].

Of greatest relevance to the present work, however, is a non-stoichiometric bcc phase termed Al_pFe (where p was determined as 4.5) which was observed to form as a major constituent in low Si-content Al-Fe-Si alloys [Liu and Dunlop 1986]. The observation and the structure of the phase has yet to be confirmed by independent study.

2.3 Phase selection in binary Al-Fe alloys

The critical cooling rates and growth velocities for $Al_{13}Fe_4$ to be replaced by metastable intermetallics in binary Al-Fe have been determined during the course of a number of previous investigations [Backerud 1968, Adam and Hogan 1972, Hughes and Jones 1974, Kosuge and Mizukami 1975, Tezuka and Kamio 1992 and Liang and Jones 1993]. The conditions required for a transition between αAl-$Al_{13}Fe_4$ and αAl-Al_6Fe eutectics has been studied most extensively, although approximate conditions for other phase transitions have also been reported.

The critical solidification conditions which have been reported in the literature will be reviewed and discussed in the following sections and are summarised in Fig.2.4.

2.3.1 $Al_{13}Fe_4$ to Al_6Fe transition

Results obtained during directional solidification under an imposed temperature gradient, G, of 15 to 20 K/mm [Adam and Hogan 1972, Hughes and Jones 1976, Liang and Jones 1993] suggest that $Al_{13}Fe_4$ is replaced by Al_6Fe at a growth velocity of between 0.05 [Adam and Hogan 1972] and 0.10 mm/s [Hughes and Jones 1976, Liang and Jones 1993], which corresponds to a critical cooling rate, $\dot{T}_c$, of approximately 1-2K/s (as $G_c.V_c = \dot{T}_c$). This value of critical solidification cooling rate for the $Al_{13}Fe_4$ to Al_6Fe eutectic transition was found to be largely independent of alloy Fe content and compares

favourably with that measured by Backerud [1968] during continuous cooling experiments on Al-1%Fe ($\dot{T}_c$= 3K/s), and also with that observed by Kosuge and Mizukami [1975] for D.C. cast Al-0.6%Fe ($\dot{T}_c$= 2K/s). In contrast, D.C. simulation work on Al-0.45%Fe performed by Granger [1990] showed the transition between $Al_{13}Fe_4$ and Al_6Fe to be a gradual one with both phases coexisting over the solidification cooling rate range 1 to 5K/s.

Interestingly, Tezuka and Kamio [1992] report that $Al_{13}Fe_4$ was not observed at all in Al-0.5%Fe solidified via a D.C. casting simulation technique in the course of their work. Instead, Al_6Fe was found to be the dominant intermetallic over the whole range of solidification cooling rates (1 to 10 K/s approximately).

This aside, there would appear to be a good degree of agreement that the critical solidification cooling rate for transition between the αAl-$Al_{13}Fe_4$ and αAl-Al_6Fe eutectics lies between 1 and 3K/s. Results obtained by unidirectional solidification with G of 15 to 20K/mm, however, show $\dot{T}_c$ to be between 1 and 2 K/s (i.e. the lower end of the range), whilst those obtained by continuous cooling and D.C. casting report $\dot{T}_c$ from 2 to 3K/s, suggesting that there are differences between the two experimental techniques.

Adam and Hogan [1972] observed the critical velocity at which $Al_{13}Fe_4$ was replaced by Al_6Fe during unidirectional solidification (V_{trans}) to be dependent upon the thermal gradient imposed on the system during growth experiments. Fig.2.5, taken from their work, shows that at low G, e.g. 2 K/mm, V_{trans} was approximately 0.15mm/s whilst under a higher imposed thermal gradient, e.g. 20K/mm, V_{trans} was reduced to about 0.05mm/s. These values suggest a range of $\dot{T}_c$ from approximately 1 to 0.3 K/s and demonstrate how such a dependence of V_{trans} on G could lead to variation in the reported values of $\dot{T}_c$.

Although Adam and Hogan [1972] noted this adverse effect of high imposed temperature gradient on the stability of eutectic $Al_{13}Fe_4$ with respect to growth velocity they presented only one interphase spacing-solidification front velocity (λ-V) relationship which they considered to be broadly applicable to all αAl-$Al_{13}Fe_4$ eutectic morphologies over the velocity range 5 to150 μm/s. This relationship was:

$$\lambda^{2.6}V = 3\ 180\ \mu m^{3.6}/s \qquad (2.1)$$

In contrast, Hirai *et al.* [1977] defined two relationships for eutectic $Al_{13}Fe_4$ growth over the range 1 to 10 μm/s, one for the parallel plate growth mode formed at high G/V (>2800Ks/mm^2) which they termed Type A growth, and a second which they found to be applicable to both the branched and branched-fibrous morphologies of eutectic $Al_{13}Fe_4$ which were designated Type B and C growth respectively. The relationships determined were:

$$\lambda^2V = 10\ 400\ \mu m^3/s \qquad \text{Type A growth} \qquad (2.2)$$

$$\lambda^2V = 4\ 020\ \mu m^3/s \qquad \text{Type B and C growth} \qquad (2.3)$$

To date, only one relationship has been presented for αAl-Al_6Fe eutectic [Adam and Hogan 1972]:

$$\lambda^2V = 10.2\ \mu m^3/s \qquad (2.4)$$

In their discussion of the relevance of the exponent in the $\lambda^n V$ = constant relationship for αAl-$Al_{13}Fe_4$, Adam and Hogan [1972] cite Tiller's proposal [1968] that, if n = 2, as is the case with αAl-Al_6Fe, then the growth of the eutectic should be controlled by the rate of solute diffusion at the growth front. At values of n > 2, however, the interfacial attachment kinetics of at least one of the phases becomes the rate determining factor, with the growth kinetics of that phase governing the overall rate of eutectic growth. This value for n observed for αAl-$Al_{13}Fe_4$, i.e.2.6, would suggest that the growth mechanism of $Al_{13}Fe_4$ is inflexible and imparts a "stiffness" to the spacing adjustment mechanism such that the intermetallic will eventually be replaced by a phase, such as Al_6Fe, which has no such difficulty in interphase spacing adjustment and which exhibits diffusion controlled growth. This stated value of n for αAl-$Al_{13}Fe_4$ eutectic growth could, however, have arisen from experimental scatter over the limited range of λ and V explored.

Eutectic growth of this type, i.e. where there is semi-cooperative growth of a faceted and non-faceted phase, is commonly referred to as anomalous. A number of anomalous

eutectics (i.e. Al-Si, borneol-succinonitrile and Fe-C) have been have been shown to exhibit functional relationships of the form [Fisher and Kurz 1980] :

$$\lambda = A\, V^{-1/2} G^{-1/3} \qquad (2.5)$$

where A is a constant.

Thus, in these systems, according to equation 2.5 as the applied thermal gradient increases the interphase spacings would be expected to decrease. The λ-V relationships given by Hirai *et al.*[1977], however, show the interphase spacing for the parallel plate morphology formed at high G/V to be 1.2 times that observed for the branched morphology of $Al_{13}Fe_4$.

The analytical model for growth of "anomalous eutectics" developed by Fisher and Kurz [1980] was found to predict correctly the observed dependence of interphase spacing on G in the Al-Si, borneol-succinonitrile and Fe-C systems and it was considered that the effect of increasing G was to cause an increase in the branching frequency of the faceted phase which, in turn, led to the observed decrease in interphase spacing. It was noted, however, that, although an increase in the thermal gradient caused a decrease in the interphase spacing in these systems, the effect was not common to all anomalous eutectics. In particular they stated that the αAl-$Al_{13}Fe_4$ eutectic did not behave in this way. Instead, as the effect of thermal gradient was to inhibit the lateral branching of $Al_{13}Fe_4$, the spacing in this system was found to increase with increasing G.

The overall effect of a high imposed thermal gradient in inhibiting branching is to effect a greater undercooling of the eutectic $Al_{13}Fe_4$ phase at a given growth velocity than would be experienced during growth in a low thermal gradient where lateral branching could occur. Under these conditions growth of Al_6Fe apparently becomes more favourable and the αAl-$Al_{13}Fe_4$ to αAl-Al_6Fe eutectic transition is observed at a lower solidification front velocity.

2.3.2 $Al_{13}Fe_4$ to Al_6Fe via Al_xFe

Young and Clyne [1981] reported that the transition in phase incidence, in the hypoeutectic and near-eutectic binary Al-Fe alloys investigated during the course of their

work (0.5 to 2.0% Fe), from $Al_{13}Fe_4$ to Al_6Fe was not as sharply defined as in that outlined in section 2.3.1. The transition was observed to be gradual, occurring over a solidification cooling rate range of approximately 0.5 to 2K/s, where $Al_{13}Fe_4$ was observed to co-exist with Al_xFe whilst, in material experiencing a solidification cooling rate of greater than 2K/s, Al_6Fe was the only phase observed. As the morphologies of branched-fibrous $Al_{13}Fe_4$, Al_xFe and Al_6Fe were observed to be very alike, it was considered that this gradual transition could have been overlooked in work prior to their discovery of Al_xFe.

The $\dot{T}_c$ for the $Al_{13}Fe_4$ to Al_xFe transition has been reported on only one other occasion [Fang and Granger 1991]. The critical solidification cooling rate given in this case (1K/s) is in good agreement with the range given by Young and Clyne. The $\dot{T}_c$ of 3K/s given for the transition from Al_xFe to Al_6Fe is also in good agreement with that reported by Clyne [1981].

2.3.3 Al_6Fe to Al_mFe

Whilst Al_mFe has been observed as coexisting with other intermetallic phases in commercial purity ingot material solidified with local cooling rates as low as 1 to 2 K/s [Skjerpe 1987] it is rarely found in high purity Al-Fe alloys. The only value of $\dot{T}_c$ published for this transition in binary Al-Fe is that given by Kosuge and Mizukami [1975] of 20 K/s in Al-0.6%Fe.

2.4 The effect of minor additions on phase selection in Al-Fe

2.4.1 Transition metals

The effect of Mn on phase selection in Al-Fe alloys was studied extensively by Backerud [1968] via continuous cooling experiments and Bridgman unidirectional solidification. Additions of Mn at low levels was observed to cause a change in stable intermetallic phase from $Al_{13}Fe_4$ to $Al_6(Fe,Mn)$ at all solidification cooling rates ($\dot{T}_s$). Al_6Fe and Al_6Mn seem to be mutually soluble in each other with the free energy of $Al_6(Fe,Mn)$ apparently lying below both Al_6Mn and $Al_{13}Fe_4$ when Mn occupies more than a certain

(very small) fraction of the Fe sites in the Al_6Fe lattice. The overall level of Mn required to maintain this occupation may however be quite high as a result of the sluggish diffusion of Mn in the liquid ahead of the growth front. If sufficient Mn is available, however, 50% site occupancy appears to be the most stable configuration. Neutron diffraction showed no sign of ordering and it was surmised that this was a simple enthalpy of mixing effect.

The effect of Co additions on phase stability was examined by Tezuka and Kamio [1992]. Using a D.C.casting simulation apparatus it was demonstrated that small additions of Co (0.067%) were sufficient to cause Al_mFe to become the preferred intermetallic over the whole range of $\dot{T}_s$ (1 to 10 K/s approximately) which compares to the base Al-0.5%Fe alloy composition where Al_6Fe was found to be dominant at all solidification cooling rates.

Further increasing the Co content to 0.13% caused $Al_9(Fe,Co)_2$, which is isostructural with Al_9Fe_2, to become the preferred phase. No explanation was offered for this effect although similarities with the situation described above for the effect of Mn are obvious.

2.4.2 Alkaline and Alkaline Earth Metals

Alkaline and alkaline earth elements have been considered as modifiers in Al-Fe alloys primarily because of their effect in modifying the eutectic growth morphology in Al-Si alloys. In view of the microstructural similarities between eutectic Si and $Al_{13}Fe_4$, it was proposed that elements which produced a modifying effect on Si (e.g. Ca, Li and Na) could also induce changes in the morphology of $Al_{13}Fe_4$.

Clyne [1981] noted that very low levels of Ca (0.01%) induced a change in the growth mode of $Al_{13}Fe_4$, apparently forcing repeated renucleation of the phase, causing a number of subgrains to form. Ca at this level also had the effect of completely suppressing the formation of Al_xFe, whilst higher levels of Ca (0.2%) effected a morphological change in $Al_{13}Fe_4$ from lath to "globular".

Tezuka and Kamio [1992] report a similar effect on phase selection in Al-0.5%Fe upon the addition of 0.04-0.11%Ca. Here, $Al_{13}Fe_4$ was found to be the preferred intermetallic

phase at all $\dot{T}_s$ in the range 1 to 10K/s. Both Clyne and Tezuka and Kamio note that the effect of Ca was enhanced in the presence of Si, and Clyne also noted that the presence of 0.01%Ti had the effect of increasing the range over which $Al_{13}Fe_4$ could grow. These effects were not discussed in any detail.

The addition of 0.012%Na to Al-2%Fe [Adam *et al.* 1981] produced an effect which was somewhat similar to that observed in Na-modified Al-Si alloys, causing the characteristic lath morphology of $Al_{13}Fe_4$ to be partially modified into a more fibrous intermetallic distribution. It was concluded, therefore, that structural modification of $Al_{13}Fe_4$ in this case was effected by a similar mechanism to that of Al-Si modification. This effect was not, however, studied further.

The effect of low level Li additions (0.03 and 0.1%) was extensively studied by Adam *et al.* [1981]. A gradual transition in growth morphology from lath to rod was observed which became more evident as the growth velocity was increased from 5 to 50μm/s. In addition a slight refinement of interphase spacing, as compared with that reported in earlier work on unmodified binary Al-Fe [Adam and Hogan 1972], was noted and the spacing of the (001) twins of $Al_{13}Fe_4$ in the modified alloy was found to have increased from 5 to 20nm, in the unmodified intermetallic, to 75 to 150nm in the presence of Li. These effects were linked to changes in the $Al_{13}Fe_4$ / liquid Al interfacial energy and a modification of the TPRE growth mechanism.

Notably, neither Na or Li were reported to affect the stability of $Al_{13}Fe_4$, with Al_6Fe replacing this phase as the dominant intermetallic at $V > 80$ μm/s, under an imposed thermal gradient of approximately 10K/mm, as in the unmodified alloy.

2.5 Ternary Al-Fe-Si intermetallics

Extensive reviews of the Al-Fe-Si system have been published by Rivlin and Raynor [1981]. Unfortunately the equilibrium Al-Fe-Si diagram is not particularly useful in predicting the phases formed at cooling rates experienced in modern casting practices or even those produced during subsequent homogenising heat treatments [Dons 1984]. The main reason for this would seem to be the propensity for, and persistence of, metastable

binary Al-Fe and ternary Al-Fe-Si formation in preference to the equilibrium intermetallic structures.

Silicon has a higher solid solubility in α-Al than does Fe and, as a result, the constituents found in dilute ternary Al-Fe-Si with low Si content at low $\dot{T}_s$ tend to be metastable binary Al-Fe based intermetallic phases. During solidification, Si partitions between the intermetallics and α-Al, the extent of this partitioning being dependent upon local solidification time and overall alloy composition, such that in low Si alloys, such as those under investigation here, approximately 15% of the total Si content is to be found in the intermetallics whilst the remainder will be in α-Al solid solution [Langsrud 1990]. Si is relatively soluble in both stable and metastable "binary" Al-Fe intermetallics, with the actual extent of this solubility being dependent upon the phase identity (Fig. 2.6). As the time for redistribution of Si decreases, i.e. as the local solidification cooling rate, $\dot{T}_s$, increases, the binary intermetallics may be replaced by ternary Al-Fe-Si phases. Therefore, under appropriate solidification conditions, ternary intermetallics may be observed in low-Si, Al-Fe-Si alloys.

The phase diagram, Fig.2.7, shows the Al-Fe-Si phases at the Al-rich end of the diagram to be α- and β-AlFeSi. These are, however, readily displaced by metastable ternary phases. To date ten Al-Fe-Si intermetallic structures have been reported as forming in commercial purity Al, of which eight are of the α-(low Si) type while the other two are forms of the higher Si content β-type. The relevant crystallographic and compositional data for these phases are listed in Table 2.2.

2.5.1 Intermetallic phases based on α-AlFeSi

Hexagonal or α'-AlFeSi is considered to be the equilibrium intermetallic in the α-phase field. However, difficulty of nucleation coupled with the very low cooling rates required to allow formation of this phase means that it is rarely observed in D.C.-cast commercial grade Al. A cubic phase is more commonly observed which is termed α-AlFeSi or cubic α. The thermal and thermodynamic stabilities of this phase appear to be greatly influenced by the presence of Mo, V, W and Mn [Skinner *et al.* 1986] in the commercial

Al-Fe-V-Si AA8009 high temperature alloy where cubic α-AlFeSi is employed as the strengthening dispersoid phase.

Many other metastable phases with compositions similar to α-AlFeSi have been reported. α'' or q_1-AlFeSi was first reported by Westengen [1982] and was considered to be a low-Si superstructure of cubic α-AlFeSi. The structure was determined as C-centred orthorhombic by Liu and Dunlop [1986] and this was later confirmed by Skjerpe [1987]. In addition Liu *et al.* [1986] also identified a further ternary phase termed q_2-AlFeSi which was determined as possessing monoclinic symmetry (Table2.2).

An interesting feature of cubic α-AlFeSi is that SADP's taken from certain principal zone axes can display extra reflections. The presence of the reflections has been explained previously in terms of an hexagonal superlattice [Turmezey 1984] or attributed to the existence of an altogether different phase with monoclinic symmetry, α_T-AlFeSi [Skjerpe 1987], though neither were considered to agree with systematically tilted SAD patterns [Liu and Dunlop 1986]. Intensive work by Liu and Dunlop [1988], however, revealed the spots to be the result of a rhombohedral superlattice of cubic α-AlFeSi, α_R, this superlattice arising from a vacancy ordering effect. In addition they predicted that this ordered superlattice should exhibit 4 variants and this was found to be borne out by experimental observation.

Dons [1985] reported that the closest fit to SADP's of an infrequently observed, phase in D.C.-cast commercial purity ingot material was by a monoclinic lattice with lattice parameters: a = 2.795 nm, b = 3.062 nm, c = 2.073 nm, β = 97.74°, proposed by Hoier [1985]. It is not clear from the description given, or the typical SADP published by Dons [1985], whether this phase, termed α_T-AlFeSi, was the same as that observed by Liu and Dunlop [1988] and Turmezey [1984]. Indeed, Dons also refers to the presence of diffuse scattering and extra spots in principal SADP's taken from cubic α-AlFeSi, a description which is much more akin to that for an SADP associated with the presence of a rhombohedral superlattice (α_R) though the description and discussion of this phase by Dons [1985] is both vague and confusing.

Unlike α_R, which transforms to a disordered structure after prolonged exposure to 100kV electrons [Liu 1990], q_1 and q_2 -AlFeSi are considered to be distinct phases. Neither phase transforms to cubic α during homogenisation heat treatment (600°C for 1 hr [Liu and Dunlop 1986]). Instead, q_1 was observed to transform to q_2 which was considered to be the most stable variant of the intermetallic. Westengen [1982] did not report such a change, indicating instead that q_1-AlFeSi was as common after 5 hours at 590°C as it was in the as cast condition.

Finally, Dons [1985] reported a ternary phase similar to Al_9Fe_2 but with the a-axis 2.6% shorter and the c-axis 3.6% shorter than in Al_9Fe_2 and which was termed α_v (v for Vellasamy). The composition of the phases was also found to be different, Al_9Fe_2 was observed by Simensen and Vellasamy [1977] to contain less than 2% Si whilst in α_v the Si content was found to range from 4.5 to 10.5%.

Of these eight variants then, seven are considered to be distinct phases whilst the remaining one, α_R is thought to arise from Fe vacancy ordering in the cubic α-AlFeSi lattice. Compositionally the phases are very similar with only the Si content exhibiting any significant variation. It should be noted that further papers to back up the first observations of α_v and α_T have not been published and some doubt must remain as to the actual identity of these phases.

2.5.2 Intermetallic phases based on β-AlFeSi

Phases of this type, which are relatively rich in Si, are unlikely to form in the low Si-content alloys under investigation in the present work. Two β-AlFeSi phases have, however, been observed in commercial purity D.C. cast material and the crystallographic data for these phases are included in Table 2.2.

Both the stable β and metastable β′ -AlFeSi exhibit monoclinic crystal structures and both have one axis of length 4.16nm. This, however, is where the similarity ends. The two structures were deemed to be distinct on the basis of observed differences in chemical composition(i.e. Fe:Si ratio for $\beta = 1$ for $\beta' > 2$) and in the other lattice parameters (Table 2.2). Therefore whilst the two may be related it was considered that one was not a defect structure of the other [Westengen 1982].

2.6 Phase selection in Al-rich ternary Al-Fe-Si alloys

Although the variation in intermetallic phase incidence with solidification cooling rate has been the subject of much research, phase selection in high purity Al-Fe-Si alloys (i.e. those alloys which have been prepared from high purity starting materials) is an area where there is little available literature. Much of the previous work has been concerned with change of phase incidence with local solidification cooling rate in commercially pure material and as such the effects observed can be classified in terms of phase selection in the presence of transition metal impurities [e.g. Asami *et al.* 1978] or more commonly in the presence of a grain refiner such as Al-5%Ti-1%B [Westengen 1982, Skjerpe 1987, Gjonnes *et al.* 1988], whilst other workers do not state alloy purity at all [e.g. Langsrud 1990] and, hence, defy classification.

This section is concerned with phase selection in Al-Fe-Si in the absence of such impurities and, as a result only the work of Liu and Dunlop [1986], Granger [1990] and Fang and Granger [1991], Tezuka and Kamio [1992] and Maggs *et al.* [1995] will be considered.

Liu and Dunlop [1986] considered the effect of two factors in the course of their work: the first was the effect of Fe and Si content on phase selection in commercial purity material, whilst the second was the effect on phase selection of removing incidental impurities.

The trend noted in the commercial purity material was for α-type AlFeSi intermetallics to be formed, replacing $Al_{13}Fe_4$ and Al_pFe in material experiencing high solidification cooling rates (approximately 10K/s) as the Si:Fe ratio was increased from 1:4 to 1:2, whilst at lower $\dot{T}_s$, given as approximately 1K/s, $Al_{13}Fe_4$ was found to be the only phase present.

When the high purity Al-0.2%Fe-0.1%Si alloy was examined, however, it was observed that, in addition to α-AlFeSi, $Al_{13}Fe_4$ and Al_pFe were also present in material solidified at high $\dot{T}_s$. There was no change in the dominant phase formed at 1K/s. This result would indicate a tendency for α-AlFeSi to be promoted in the presence of impurities.

It is also notable that Al_xFe was not observed in the course of their work and also that, where observed (in commercial purity Al-0.4%Fe-0.1%Si), Al_mFe and Al_6Fe were only present as minor constituents.

The trend for α-type phases to be formed at higher solidification cooling rates in alloys of higher Si:Fe ratio was also noted by Tezuka and Kamio [1992]. They conducted a series of experiments on Al-0.3%Fe-Y%Si and Al-0.5%Fe-Y%Si alloys, examining the effect on intermetallic phase incidence of varying Si content over the range Y=0.1 to 0.3%.

In the Al-0.3%Fe-Y%Si series (Fig.2.8) the major phase at all solidification cooling rates was observed to change from Al_mFe at 0.1%Si to α-AlFeSi at 0.25%Si. Increasing the Si content in the Al-0.5%Fe-Y%Si series (Fig.2.9) gave rise to a similar change in phase incidence. For the Al-0.5%Fe-0.1%Si composition the dominant phase at low $\dot{T}_s$ was found to be $Al_{13}Fe_4$ with Al_mFe dominant at high $\dot{T}_s$. The phase formed at high $\dot{T}_s$ on increasing the Si content of the alloy to 0.25% was observed as α-AlFeSi whilst $Al_{13}Fe_4$ remained stable at low $\dot{T}_s$. In the Al-0.5%Fe-0.3%Si composition, however, α-AlFeSi was the only phase observed at all $\dot{T}_s$.

Maggs *et al.* [1995] also demonstrated a similar change in phase distribution with respect to solidification cooling rate. In Al-0.2%Fe-0.1%Si (Si:Fe 1:2) the phases present were α-AlFeSi at high $\dot{T}_s$ (approximately 10K/s), an unknown phase termed U1 (the structure of which was not determined) at intermediate $\dot{T}_s$ (4-6K/s approximately) and $Al_{13}Fe_4$ at solidification cooling rate of about 1K/s. At the lower Si:Fe ratio of 1:4 in Al-0.4%Fe-0.1%Si, Al_6Fe was found in material which had experienced a high solidification cooling rate whilst at intermediate and low solidification cooling rates $Al_{13}Fe_4$ was found to be the only phase present. Increasing the Fe and Si content to Al-0.4%Fe-0.2%Si but maintaining the Si:Fe ratio as 1:2 resulted in a distribution similar to that observed in Al-0.2%Fe-0.1%Si, although in this case U1 had been replaced by Al_6Fe at intermediate $\dot{T}_s$.

Fig.2.10 reveals these results to exhibit a remarkably good level of agreement and the phase distribution reported by Granger [1990] in Al-0.5%Fe-0.1%Si (i.e. $Al_{13}Fe_4$ at cooling rates < 3K/s, $Al_{13}Fe_4$ (major constituent) plus Al_6Fe (minor constituent) between 3 and 10K/s, to Al_6Fe at cooling rates >10K/s) also ties in very well with these results. The phase distribution reported by Fang and Granger [1991], however, of $Al_{13}Fe_4$ as the sole constituent phase at solidification cooling rates < 1K/s, Al_xFe dominant between 2 and 10 K/s, β-AlFeSi ($Al_9Fe_2Si_2$) between 10 and 13K/s and Al_6Fe in material experiencing a solidification cooling rate in excess of 13K/s does not fit the general pattern of results (Fig.2.10) and must be regarded with some caution.

2.7 Effect of minor additions on phase stability in Al-Fe-Si alloys

2.7.1 Transition metal impurities

The effect of low level transition metal additions on intermetallic phase distribution were investigated by Maggs *et al.* [1995]. V, Ti and Mn were added to base alloys of composition Al-0.4%Fe-0.1%Si, Al-0.4%Fe-0.2%Si and Al-0.2%Fe-0.1%Si at levels of 0.02%, 0.04% and 0.02% respectively and their individual effects noted.

The range of phase incidence in the Al-0.2%Fe-0.1%Si alloy i.e. α-AlFeSi in material solidified with a high cooling rate, U1 in material experiencing intermediate cooling rates and $Al_{13}Fe_4$ in slowly cooled material , was affected by each of the additions to the same extent and in the same manner. The general effect was to suppress the formation of U1 and to extend the range of solidification cooling rates over which $Al_{13}Fe_4$ could form.

In Al-0.4%Fe-0.1%Si the additions did not result in any appreciable change in phase stability with Al_6Fe being observed in material experiencing a high $\dot{T}_s$ and $Al_{13}Fe_4$ observed as the dominant intermetallic at low solidification cooling rates in all alloys including the base composition.

The most notable effect, however, was on the phase stability in Al-0.4%Fe-0.2%Si. The phase distribution in the base alloy i.e. α-AlFeSi in material solidified with a high cooling rate, Al_6Fe at intermediate solidification cooling rates and $Al_{13}Fe_4$ in slowly cooled material, became $Al_{13}Fe_4$ at high solidification cooling rates with Al_6Fe at intermediate

and low solidification cooling rates in the presence of 0.02% V. The presence of Mn at 0.02% caused the distribution to become Al_6Fe at high $\dot{T}_s$, with $Al_{13}Fe_4$ at intermediate to low solidification cooling rates, whilst the distribution in the presence of 0.04%Ti was α-AlFeSi (major) plus Al_6Fe (minor) at high solidification cooling rates, Al_6Fe (major) and $Al_{13}Fe_4$ (minor) at intermediate rates and $Al_{13}Fe_4$(major) and Al_6Fe(minor) at low $\dot{T}_s$.

Why the effect should be greater in the Al-0.4%Fe-0.2%Si alloy than in the Al-0.2%Fe-0.1%Si with the same Si:Fe ratio (1:2) was not discussed but it does demonstrate that using Si:Fe ratio to classify solidification behaviour in Al-Fe-Si alloys is not as satisfactory a guide as it is widely held to be.

Asami, Tanaka and Hideno [1978] produced results for an alloy modelled on AA1100, to examine the fir tree zone defect in Al-Fe-Si-Mg alloys. The AA1100 composition was essentially a ternary Al-Fe-Si alloy (0.48%Fe-0.15%Si) with the addition of 0.11%Cu and 0.03%Ti. The phase formed at high solidification cooling rate was Al_6Fe whilst at intermediate and low cooling rates $Al_{13}Fe_4$ was produced. Comparison of this result with those of Maggs *et al.* above shows this distribution of intermetallics to be compatible with their observations on Al-0.4%Fe-0.1%Si in the presence of 0.04% Ti. It would appear then that the effect of Cu on phase selection is relatively weak though it is not possible to conclude this unequivocally.

2.7.2 Al-5%Ti-1%B grain refiner

TiB_2 is added to D.C. cast aluminium alloys, usually in the form of an Al-5%Ti-1%B master alloy to refine the grain structure. The alloy consists of TiB_2 particles and an excess of Ti in Al which, on addition to the melt, dissolves leaving the TiB_2 to act as a nucleant for primary Al. This combination of TiB_2 and dissolved Ti has a much greater grain refining effect than does Ti alone although the mechanism by which this refinement is achieved is still the subject of debate in the literature [see for example Sigworth 1996].

The effect of Ti on phase selection in Al-Fe-Si has been reviewed in the previous section (2.6.2) and in this section the effect of deliberate additions of Ti-B to the melt will be

examined and compared with the results of Westengen [1982] and Skjerpe [1987] for grain refined Al-0.25%Fe-0.13%Si.

Tezuka and Kamio [1992] reported that the addition of 0.03%Ti and 0.005%B to Al-0.3%Fe-0.1%Si caused Al_mFe to be stabilised over a wider range of solidification cooling rates as compared with the phase distribution in the base alloy, whilst the effect on Al-0.3%Fe-0.15%Si was to promote α-AlFeSi at all solidification cooling rates, replacing the distribution of, $Al_{13}Fe_4$ (major) plus Al_6Fe (minor) at low and intermediate $\dot{T}_s$ and Al_mFe at high solidification rates observed for the base alloy composition.

Similarly Maggs *et al.* [1995] reported cubic α-AlFeSi to be promoted as the major phase in both Al-0.2%Fe-0.1%Si and Al-0.4%Fe-0.2%Si alloys in the presence of Ti-B though in the absence of grain refiner their phase distributions were observed to be different as discussed in section 2.5. The effect of Ti-B on Al-0.4%Fe-0.1%Si was to cause Al_mFe to replace Al_6Fe as the major phase in material experiencing high solidification rates and Al_6Fe to replace the $Al_{13}Fe_4$, observed in the base alloy, at lower $\dot{T}_s$.

These results display an excellent level of agreement and also compare very well with those of Westengen [1982] who observed Al_mFe to form in regions experiencing high solidification cooling rates and Al_6Fe/Al_xFe in slowly cooled regions in grain refined D.C.-cast commercial purity Al, and also with Skjerpe [1987] who observed α-type phases (α / α_T /α'' (q_1)) to form in material experiencing a high cooling rate and Al_xFe and $Al_{13}Fe_4$ in slowly cooled material.

Maggs *et al.* [1995] suggested that this effect of Ti-B on phase selection could be explained if the hexagonal TiB_2 particles in the melt somehow promoted the nucleation of high symmetry intermetallic phases (i.e. cubic α and tetragonal Al_mFe) in preference to the low symmetry ones (e.g. $Al_{13}Fe_4$). This hypothesis, however, remains untested.

2.8 Phase stability in Al-rich quaternary Al-Fe-Si-Mg

There is little available literature on the effect of Mg on phase stability in Al-Fe-Si alloys. In the alloys under consideration in this work (0.5 to 0.75%Mg, Si from 0.05% to

0.15%) Mg_2Si would not normally be expected to form and the intermetallic phases observed should be similar to those observed in dilute Al-Fe-Si alloys.

Maggs *et al.* [1995] showed that there was little effect of low level (0.023%) additions of Mg on the intermetallic phase distribution in Al-0.4%Fe-0.1%Si and Al-0.2%Fe-0.1%Si. Several authors have reported, however, that Mg at higher concentrations exerts a greater influence. Granger [1990], for example, found that in Al-0.5%Fe-0.1%Si-0.75%Mg, Al_mFe was the major phase at all solidification cooling rates in excess of 2K/s whilst below this threshold $Al_{13}Fe_4$ was the stable intermetallic. This contrasts with the results of Fang and Granger [1991] for Al-0.5%Fe-0.1%Si-0.75%Mg who reported a phase distribution of $Al_{13}Fe_4$ in material solidified with a cooling rate of less than 3K/s, Al_xFe between 3 and 5K/s and Al_mFe tending toward Al_mFe plus Al_6Fe at solidification cooling rates of 5K/s and above. Tezuka and Kamio [1992] in contrast to the results of Granger [1990] and Fang and Granger [1991] did not observe Al_mFe to be promoted in the presence of Mg. Instead they reported that the addition of 0.5%Mg to Al-0.3%Fe-0.15%Si caused Al_mFe, which was dominant in Mg-free alloy which had been produced with a high solidification cooling rate to be replaced by Al_6Fe.

The available data in this area are clearly both sparse and confusing and fall into one of two camps, one of which shows Al_mFe to be promoted by the presence of Mg and while the other shows it to be destabilised. Such discrepancies highlight this as an area where further work is required.

2.9 Effect of minor additions on phase stability in Al-Fe-Si-Mg alloys

2.9.1 Transition metals

There is little available literature on the effects of minor alloy additions on intermetallic phase stability in Al-rich, quaternary Al-Fe-Si-Mg alloys. The most comprehensive study of low level additions available to the author is that of Granger [1990] which was concerned with the effect of low level additions on phase stability in quinternary Al-Fe-Si-Mg-Cu alloys based on an AA5005 alloy composition. It was stated that the addition of 0.1%Cu to Al-0.5%Fe-0.1%Si-0.7%Mg caused Al_6Fe, observed in the base

alloy at cooling rates in excess of 5K/s, to be suppressed and Al_mFe to be stabilised as the dominant intermetallic over the whole $\dot{T}_s$ range (0.3 to 16K/s).

Granger [1990] noted that the effects of low level transition metal additions on this quinternary Al-Fe-Si-Mg-Cu composition were greater if the elements were introduced as pairs. For example, in the presence of 0.04%Mn and 0.04%Cr $Al_{13}Fe_4$ was completely suppressed and Al_mFe was observed to be the major phase at all $\dot{T}_s$. Addition of 0.04%Cr and 0.04%Ni in combination had the effect of promoting $Al_{13}Fe_4$ formation as did the combination of 0.04%Cr and 0.04%Zr. The most notable effect of the Cr/Zr combination was, however, to suppress the formation of Al_mFe completely.

2.9.2 Al-5%Ti-1%B grain refiner

Tezuka and Kamio [1992] state that on the addition of 0.03%Ti and 0.005%B to an alloy of composition Al-0.3%Fe-0.15%Si-0.5%Mg, α-AlFeSi is formed at all $\dot{T}_s$ during D.C. simulated growth. This compares with the phase distribution observed in the base alloy where $Al_{13}Fe_4$ and Al_6Fe were observed to be the constituent phases at low and high $\dot{T}_s$ respectively and ties in well with the hypothesis of Maggs *et al.* [1995] concerning the effect of TiB_2 grain refiner on intermetallic phase selection (see section 2.7.2).

2.10 Factors affecting solidification microstructure selection

The results discussed so far in this review are for alloys based on hypoeutectic Al-Fe compositions. The observed microstructures in these Al-rich alloys result from the competition in nucleation and growth of the constituent intermetallic phases in an Al-matrix of cellular or dendritic morphology. In more concentrated alloys i.e. those with Fe content of greater than 2% Fe, the observed solidification microstructures are a result of competition between a number of monolithic (primary) crystal structures and morphologies and the metastable intermetallics.

Study of the competition between these various microstructural components has been the subject of both previous experimental work [Hughes and Jones 1976, Liang 1992] and of microstructural modelling analysis [Gilgien *et al.* 1995] with a view to constructing a solidification microstructure selection map (SMSM) for this complex system. These investigations and analyses have, to date, concentrated on hypereutectic Al-Fe over a much wider range of solidification front velocities than would usually be encountered during conventional D.C. casting processes (i.e. 0.04mm/s to 1m/s using a combination of Bridgman directional solidification, TIG weld traversing and laser resolidification under imposed positive thermal gradients, G, ranging from 10 to 2000K/mm, thus providing a total range of solidification cooling rate from 0.4 K/s to $2x10^6$K/s approximately, as compared with cooling rates of up to 20K/s in normal D.C. casting). These efforts will be reviewed briefly here and comparisons made between the modelled and experimental maps.

The ability to predict solidification microstructure is obviously of great technological interest as it can allow the selection of a desired set of material properties, e.g. grain size, phase distribution and type, by indicating the processing parameters required to produce them. The following information is required in order to make a reliable prediction of the outcome of the competitive processes involved in microstructure generation [Jones 1994]:

1) The identity of the competing constituents.

2) Their thermodynamic characteristics, such as formation temperature, as a function of alloy composition, including any non-equilibrium extensions beyond limiting compositions, e.g. liquidus, solidus and eutectic temperatures all embodying any effects of solute trapping at high V [Boettinger *et al.* 1988].

3) Constitutive equations characterising both nucleation and growth of the phases and the effects of any morphological changes on the stability of each competing phase with respect to a parameter such as solidification front velocity.

Whilst, for the map to be applicable to an actual solidification process a model relating the position and time dependencies of the temperature and/or solidification front velocity

in the transforming system to external variables such as an imposed cooling or heat dissipation rate must be available for the particular casting process under analysis.

The first of these requirements, i.e. that the identity of the competing phases be determined is perhaps the easiest met of these conditions. In addition to the three phases reported to be constituent intermetallics in the hypoeutectic Al-Fe system (i.e. $Al_{13}Fe_4$, Al_6Fe and Al_xFe) a number of phases have been identified as present in the hypereutectic alloys as primary phases (i.e. α-Al, $Al_{13}Fe_4$, and Al_mFe as well as a decagonal quasicrystalline phase) [Liang 1992, Kim and Cantor 1994] and at the highest growth velocities microcellular microstructures of α-Al with an intercellular micro-quasicrystalline phase have been reported [Kim and Cantor 1994].

The second item, measurement of formation and growth temperatures for the phases, has yet to be reported for any phases other than the equilibrium αAl-$Al_{13}Fe_4$ eutectic, primary α-Al and $Al_{13}Fe_4$ and the metastable αAl-Al_6Fe eutectic [Liang and Jones 1992] in the Al-Fe system. The formation temperatures of primary Al_mFe and the quasicrystalline phases, both as a primary phase and also as a microeutectic component, and the formation temperature of the αAl-Al_xFe combination are, as yet, unknown.

The third item on the list, the establishment of constitutive equations for nucleation and growth is an area where there has been significant activity in recent years, both in terms of their experimental determination and also in the development of analytical and numerical models to facilitate microstructure prediction. The first major success of such a technique was in the determination of the strong dependence of critical cooling rate for glass formation on alloy content in the (Pd,Ni)-Si-Cu system [Davies *et al.* 1974]. This approach has since been applied to the competitive formation or suppression of complex aluminides in undercooled aluminium alloys [e.g. Saunders and Tsakiropoulos 1988]. Fig.2.11, taken from Saunders and Tsakiropoulos [1988] shows the predicted minimum diameter at which Al-Cr alloy atomised droplets contain primary $Al_{13}Cr_2$ is in better agreement with observations if heterogeneous nucleation is assumed. If this is the case, however, it may be that a competitive growth model will explain resultant microstructure more readily than would a competitive nucleation model. Although such an analysis would tend to be applied to steady state solidification, such as laser remelting

or high velocity steady state Bridgman growth, Cochrane *et al.* [1991] employed this approach to explain the microstuctures of Al-8%Fe powders formed by drop-tube processing. Fig.2.12, taken from their work, shows for each size fraction the proportion of droplets in which a particular microstructural component initiated the solidification. In the largest of these droplets (1000 to 2000μm) it was found that there was an equal probability that solidification was initiated by primary $Al_{13}Fe_4$ (in one of its forms) or by the αAl-Al_6Fe eutectic structure. In spite of difficulties in applying such an analysis to drop-tube processing, where direct measurement of the undercooling is not possible, the predictions of their competitive growth model were found to display very good agreement with their experimental results.

The basis of a competitive growth analysis is that all of the possible phases are heterogeneously nucleated, either on potent nucleation sites or on whichever phase nucleates first. The important parameter governing phase selection in this case is the growth temperature dependence of each contending phase on solidification front velocity. This relationship, known as the interface response function, must be known or calculable for each competing phase if phase boundaries in SMSM's are to be predicted with accuracy. The interface response function of primary $Al_{13}Fe_4$ has been measured directly by Liang and Jones [1991 and 1993](Fig.2.13) as have those of the αAl-$Al_{13}Fe_4$ and αAl-Al_6Fe eutectics (Fig. 2.14 [Liang and Jones 1992]). Interestingly, however, these experimental results were not employed in the calculation of a recently published microstructure selection map for Al-Fe [Gilgien *et al.* 1995] which, rather than being a predictive model for this system was essentially an exercise in fitting calculated field boundaries to the experimental phase map produced by Hughes and Jones [1976] (Fig.2.15). Although the degree of "fit" to this data is now very high it remains to be seen how well this "predicted" diagram can be extended to encompass the more recent experimental results of Liang [1992](Fig.2.16) for more concentrated Al-Fe alloys.

It is clear, therefore, that it is not possible to predict very accurate solidification microstructure maps without complementary experimental observations because the required thermophysical parameters of the alloy constituents are often poorly defined. Moreover, some microstructural characteristics of the alloys are not clear: for example

the reasons for the change in the growth morphology of the stable αAl-$Al_{13}Fe_4$ eutectic from lath to rod-like as growth velocity is increased, the observation that the αAl-Al_6Fe eutectic appears sometimes as lamellar and sometimes rod like and the driving force behind the changes in primary $Al_{13}Fe_4$ growth morphology from lath to 10 pointed star via a series of intermediate morphologies is also poorly understood. A greater understanding of the system is, therefore, necessary before realistic predictive modelling of such complex competitive situations can be performed with confidence and also if systems exhibiting a greater degree of complexity such as ternary Al-rich Al-Fe-Si (Fig.2.17 [Liang 1992]) are to be modelled successfully.

2.11 Concluding remarks

It is clear from Sections 2.1 to 2.9 of the preceding review that the more complex the alloy is compositionally (i.e. the more elements there are present) the greater the difficulty in isolating the effects of individual elemental additions. It is clear from the literature concerning phase selection in the ternary and quaternary alloys in particular that few authors have adopted a systematic approach to the work. Much of the most frequently cited research has been conducted on commercially pure material and obviously such material will always contain impurities which, both individually and in combination, can significantly affect the outcome.

It is, therefore, evident that research is still required to elucidate the mechanisms governing phase formation in hypoeutectic Al-Fe and more particularly in Al-rich, Al-Fe-Si and Al-Fe-Si-Mg alloys both with and without additional alloying elements if the as-cast microstructure of commercial Al-alloys is to be effectively controlled.

3. EXPERIMENTAL PROCEDURE

3. 1 Alloy preparation and compositional analysis

Alloy preparation was a two stage process: the first was to produce master alloys in sufficient quantity to allow the experimental alloys to be prepared from the same basic stock and the second was to produce experimental alloys of the desired compositions by addition of these master alloys to super-pure (99.996 %) aluminium.

Master alloys of Al-6.2% Mg and Al-2.27% Fe were prepared as 5 kg ingots in air and Al-12.4% Si was prepared under a protective argon atmosphere in a small vacuum induction furnace. All alloys were produced from elements of the following purities:

super-pure aluminium	99.996 %
high purity magnesium ingot	99.9 %
electrolytic iron	$C \leq 0.05$ %
high purity silicon	99.9 %

whilst a high purity Al-27%Cr. master alloy was obtained from London and Scandinavian metallurgical Co. Ltd. All master alloy compositions were analysed by the ion coupled plasma spectroscopy (ICP) technique and the impurity contents are given in Table 3.1.

The required dilute alloy compositions were obtained by adding these master alloys to super-pure aluminium in the correct proportions and melting in a small vacuum induction furnace. The melting procedure was as follows: the furnace chamber was evacuated to 10^{-2} torr and back filled with N_2 to a pressure of 400 mm Hg and an R.F. coil employed to melt the charge which was contained in a magnesia or alumina crucible. The alloy mixture was allowed to homogenise for 10 minutes at a medium R.F. coil current which produced active stirring of the melt. The coil current was dropped to a lower level for the final 5 minutes prior to casting, which was into a cast iron chill mould of internal dimensions 15 x 50 mm in section by 150 mm in height, to give an ingot of approximately 300g in weight. The ingot was then left to cool under N_2 for at least 1 hour.

Samples for chemical analysis, in the departmental analytical facility, were taken from both bottom and top of the resulting ingot, after removing the piped section in the upper part of the ingot. Chemical analyses were again produced by the ICP method which has a precision of ±0.02% for all elements found in the present experimental alloys. No

significant difference in composition was detected between the samples taken from the top and bottom of the ingots and, so, they were considered to be compositionally homogeneous. A comparison of target and actual compositions is given in Table 3.2.

3.2 Solidification

3.2.1 Specimen preparation

The as-cast alloys were cold rolled to 60 % reduction, cut into strips 10mm wide parallel to the rolling direction and then mechanically swaged to 5mm rod. The rod was then cold drawn to 2.9mm diameter wire, straightened and cut into 150mm lengths. These were then inserted into recrystallised alumina tubes 160mm long, with 4mm external diameter and 3mm bore, and one end sealed off with Autostik refractory cement.

If the sample was to be used for thermal analysis experiments a further stage of specimen preparation was required. A semi-circumferential nick was cut in the filled alumina tube 75mm from the closed end, using a diamond wafering blade, and a 1mm hole drilled in the exposed alloy wire perpendicular to and towards the long axis. A 316 stainless steel sheathed K-type thermocouple was positioned in this hole such that the bead was at the centre of the specimen and cemented in place using Autostik. The thermocouple was then secured to the alumina tube using refractory metal wire and the cement allowed to dry for at least 24 hours prior to directional solidification in the Bridgman apparatus. This arrangement is shown in Fig. 3.1.

3.2.2 Bridgman unidirectional solidification apparatus

The directional solidification apparatus used in this work consists mainly of three parts: heating unit, coolant and traction mechanism.

As a result of electrical noise caused by the generator, the induction coil previously used as a heating source by Liang [1992] was replaced by an MTF 10/15 Carbolite electrical resistance tube furnace with a Eurotherm temperature controller. The furnace was 150mm long of which 130mm was the heated length and the bore of the ceramic work tube was 15mm in diameter.

A bath of circulating water immediately below the electrical resistance furnace ensured that a positive temperature gradient was maintained during the withdrawal of the crucible from the furnace. Control of the temperature gradient was achieved by controlling melt

super-heat. For the liquidus temperature of the Al-0.5% Fe alloys investigated, 660 ± 10°C, a furnace winding temperature of 890 °C was found to produce consistently a melt super-heat of 100 ± 10 K and this, in turn, provided a reproducible temperature gradient over the whole range of withdrawal velocities employed.

The temperature gradient was determined from the temperature-time curves of a random sample of ten Bridgman specimens, one for each of the basic alloy compositions: each at two of the withdrawal velocities employed. As can be seen from Table 3.3 no significant variation in temperature gradient was observed from composition to composition or with change in withdrawal speed. The G/V ratios employed in this work were always less than, or equal to, 1000Ks/mm^2 and, therefore, in the intermediate to low G/V range defined by Adam and Hogan [1972].

Crucible withdrawal speed was controlled by employing a ten speed synchronous motor with a drive shaft acting as a winch. Previous experimental work [Liang 1992] on α-Al-Al_2Cu eutectic alloys at G = 10-15 K/mm contained in 3 mm bore x 0.5 mm wall thickness alumina tubes had shown that nominal withdrawal speed and solidification front velocity did not differ significantly over the range 0.001 to 3.00 mm/s. The withdrawal speeds employed in this study of 0.01 to 2.0 mm/s were, therefore assumed to reflect the actual solidification front velocities. A sectional view of this Bridgman-type apparatus is shown in Fig.3.2.

3.2.3 Solidification procedure

One of the Bridgman samples was clamped, by means of a pin-chuck, to the top of a vertical brass withdrawal rod which, in turn, was attached to the winch by a length of steel cord. The furnace bore was arranged so that it and the specimen were concentric and a pad of rock-wool insulating material was placed over the open end of the furnace work tube to reduce furnace air convection during operation. The furnace was then heated to the required temperature and the alloy allowed to melt and then equilibrate for fifteen minutes. The specimen was then solidified unidirectionally by being drawn downwards into the circulating water bath at a pre-selected rate using the stepped drive shaft of the traction unit as a winch.

If thermal analysis was being performed, readings from the embedded thermocouple were recorded throughout by use of a Viglen 386 PC computer equipped with an analogue to digital (A/D) converter, which made it possible to automate the recording and analysis of the cooling curves.

3.3 Optical metallography

High purity hypoeutectic alloys are commonly composed of hard intermetallic particles in a soft matrix and can thus be difficult to polish. Because of the inconsistency of the polish obtained by hand a Struers Abramin automated grinding and polishing unit was employed in the preparation of metallographic specimens. The polishing schedule used is given in Table 3.3.

Each polished specimen was then etched by immersion in 10% NaOH solution at 70°C for between 10 and 15 seconds to give good phase contrast and the surface de-smutted by swabbing with 50 % HNO_3 in distilled water.

Quantification of the microstructure was accomplished using the method of mean linear intercepts. Ten lines of length 100 mm were drawn onto the enlarged transverse section micrographs, at random, and the number of intercepts of these lines with the cell boundaries was determined. Cell size was then calculated using the formula :

$$\overline{\lambda} = l / n \qquad (3.1)$$

where n = the total number of intercepts and l = total measure line length/magnification.

Magnification was calculated from a photograph of a standard graduated slide which was taken at the same magnification and printed with the same enlargement ratio as the structure micrographs. The 95% confidence limits of this mean cell size were obtained by taking two standard deviations from the mean, i.e.:

$$\pm 2\sigma_{\overline{\lambda}} = 2 \times 0.65\overline{\lambda} / n^{0.5} \qquad (3.2)$$

These results were then plotted against calculated cooling rate $\dot{T}$ to allow any systematic changes in microstructural scale with alloy composition to be identified and also to facilitate easy comparison with the results of previous experimental work.

3.4 X-ray diffraction and associated techniques

3.4.1 Guinier focusing camera technique

A quadrupole Guinier-de Wolff focusing camera was employed in the x-ray analysis of the phases present in the directionally solidified alloy material in the early stages of the experimental work. The principle of this method is illustrated in Fig.3.3, whilst a fuller explanation of the principles underlying the technique can be found in standard reference texts [e.g. Cullity, 1978].

To evaluate the applicability of this technique to the present experimental work both powder and solid x-ray specimens were produced from the directionally solidified alloy rods. The camera configuration employed meant that all specimens had to be transparent to the incident x-ray beam.

Solid specimens for investigation were cut from both transverse and longitudinal sections of the alloy rods and also at 45 degrees to the growth axis. These sections were ground on SiC papers to x-ray transparency (approximately 100 to 125μm) before securing into position in the specimen holder with a commercial adhesive. Powder samples for examination in the camera were prepared by filing rods and sieving the resultant powders to -73μm to remove large particles. The sieved powder was then mixed with a weak solution of a commercial adhesive (UHU) in acetone before being fixed into the specimen holder.

Specimens so prepared were then positioned in the camera and exposed to Cu-Kα radiation produced by a Philips x-ray tube operating at 35 kV and 20 mA. After an exposure time of 15 hours the resultant x-ray films were developed and indexed.

For a number of reasons, which are documented fully in Appendix 1, this method of x-ray investigation proved to be unsuitable for the present work and an alternative procedure was sought.

3.4.2 Extraction of second phase intermetallics

The low volume fraction of second phase material present in the alloys under investigation meant that the usual methods of x-ray specimen preparation, e.g. filing and sieving, did not provide samples of sufficiently high second phase content for conventional x-ray diffraction experiments.

Extraction and, hence, concentration of the constituent phases seemed to offer a solution to this problem and an extensive survey of the available literature was undertaken to identify a suitable extraction procedure. Details of this full survey can be found in Appendix 2 along with an evaluation of the relative efficacy of the various techniques attempted experimentally.

Of all the methods tried only the HCl electrolysis and butanol reflux methods were found to be suitable for the extraction of constituent phases in the present work. Closer examination of the resultant powders produced by the HCl extraction process, however, showed that extensive dissolution of the intermetallics, particularly those grown at higher velocities, could occur. Chemical analysis of the acid used in the extraction cell also showed that considerable levels of Fe were present after the extraction process was completed, compared with the Fe content of the HCl solution prior to use (Table 3.5).

The results of these analyses also showed that the extent of dissolution was erratic and unpredictable, presumably a function of intermetallic corrosion resistance. Use of the technique was, therefore, discontinued.

The butanol reflux method was considered too time consuming and technically demanding to be performed in-house and, so, the constituent phases were extracted from the matrix at SINTEF in Oslo. Samples of Bridgman solidified alloy 5g in weight were sent to Norway and the intermetallic residues returned on 5 μm pore Teflon filters for preparation as x-ray and TEM specimens

3.4.3 X-ray diffractometry

a) Specimen preparation

Teflon filters used in the collection of intermetallics after dissolution of the matrix were individually placed, face down, on a clean sheet of plate glass. The filtrate was then removed by wetting the back of the filter with a small amount of acetone and gently scraping the back of the filter with the side of a clean glass microscope slide. This scraping action left the filtrate in suspension in the acetone on the surface of the plate glass and the filter was lifted free of the suspension and discarded.

When the acetone had completely evaporated (after approximately 3 to 5 minutes) the powder was collected together using the edge of a clean glass slide and transferred to a silica x-ray slide using a clean spatula. The powder was then secured to the surface of the slide by a weak solution of UHU in acetone

.b) Diffraction procedure

X-ray diffraction of the extracted second phase crystals was performed using a Philips 1710 diffractometer utilising Co-Kα radiation (weighted average wavelength λ = 0.17902nm). The apparatus was controlled via a BBC micro-computer in the early stages of the experimental work and in the later stages by a PC running Seimens Seitronics software. The Philips x-ray tube was operated at a voltage of 40 kV and an anode current of 25 mA and scan parameters were selected to give a total trace data capture time of approximately 5 hours.

Scanning from 10 to 100 degrees 2θ was considered to be a good range over which to collect data to afford unambiguous phase identification. The patterns obtained were solved with reference to standards given in the JCPDS files, in the case of well verified equilibrium intermetallic phases, and with those found in the literature or calculated patterns in the case of non-equilibrium and less well defined structures. The relevant

reference files used in the solution of the patterns obtained in the present work are presented as Tables 3.6 to 3.12.

3.5 Transmission electron microscopy

3.5.1 Specimen preparation

Two types of specimen were prepared for examination in the TEM: standard electropolished foils and, for more detailed investigation of crystal morphology, powder samples produced from the material returned by SINTEF.

Those for the investigation of intermetallic crystals *in-situ* in the aluminium matrix were taken from the transverse section of the directionally solidified alloy rods. To produce a foil discs cut from the rods using a LECO Vari-Cut precision cutting tool were ground on both sides to a thickness of 100-150μm on SiC papers and thoroughly cleaned in acetone. Electron transparency was achieved by electropolishing with a Struers Tenupol unit. Optimal foil thinning results were obtained using a solution of moisture free 25% HNO_3 in high purity CH_3OH at a temperature between -30 and -20°C. Specimens of all alloys were successfully thinned using a voltage of 10-15V, which produced a current of approximately 0.1A, and a unit electrolyte flow rate of 5 in the initial stages increased to 9 after about 30s of polishing. The foils were then washed in high purity CH_3OH prior to investigation in the TEM.

Specimens of extracted powder were collected on 300 mesh copper grids and the grids tapped gently to remove any loose particles. The intermetallic crystals were found to be sufficiently transparent to 100 kV electrons to give good electron diffraction information but were too thick to allow further investigation of their internal structure.

3.5.2 Use of the instrument

The bulk of the TEM work was carried out on a Philips EM-420T instrument operating at 100 kV, using a double tilt specimen stage (±45 and ±30 degrees about the X and Y axes respectively) to record consistent series of electron diffraction patterns for each of the intermetallic crystals investigated. In the later stages of experimental work a JOEL 200-CX instrument operating at 200 kV was also employed.

In order to identify the phases present, the intermetallic crystals were tilted about their principal axes using experimental methods outlined in many of the standard reference texts [e.g. Loretto,1994] and a series of selected area diffraction patterns (SADP) were taken. These patterns were then solved with the aid of a computer program, written by Dr. M.Al-Khafaji of the Sorby Centre staff, paying close attention to the forbidden

reflection rules for the specific crystal structures under investigation as given in the International Tables of Crystallography [1959]. The diffraction information and micrographs were correctly oriented with respect to one another by implementing the rotation correction appropriate to the combination of diffraction camera length and microscope magnification employed. The rotation corrections relevant to the present experimental work are given in Appendix 3. Performing this particular correction allowed the nature of certain crystallographic features of the intermetallics to be elucidated.

At least two SADP were taken for each intermetallic investigated and for each specimen condition examined in the microscope information was obtained from at least two foils and diffraction information recorded for a minimum of 10 individual particles. Although this number of particles does not constitute a large enough population on which to perform a meaningful statistical analysis, it does give an indication of the relative proportion of each intermetallic found in any given alloy condition investigated.

4. RESULTS

4.1 Metallography and cell size analysis

Optical micrographs of directionally solidified material sectioned in the plane transverse to the growth direction show that, in all of the alloys investigated, the intermetallics outline a cellular α-Al structure. In the ternary and multi-component alloys intermetallics were also found within the α-Al cells. The SEM micrograph, Fig.4.1, shows a typical example of this form of intermetallic growth. This particular example was observed in a sample of Al-0.5%Fe-0.05%Si-0.75%Mg which had been solidified with V= 1.00 mm/s. The morphology of the α-Al cell surrounding the intracellular intermetallic is typical. These intracellular phases were not observed in the binary Al-0.5%Fe alloy.

The micrographs, Fig.4.2a and b, of the α-Al cell structures found in the quaternary Al-0.5%Fe-0.05%Si-0.75%Mg alloy after unidirectional solidification at 0.05 mm/s and 2.00 mm/s respectively, show that as growth velocity was increased, and as the delineating intermetallic morphology changed from a lamellar to rod-like morphology, the cellular structure of the alloy became better defined. Similar micrographs were produced for all of the alloys under investigation and measurements of cell spacing, λ_1, taken at each growth velocity employed were plotted against solidification cooling rate $\dot{T}_s$, defined as the product of solidification front velocity V and temperature gradient G (with G assumed to be the average value of 10 K/mm), to determine whether any systematic or significant changes were observed with changes in alloy chemistry.

Fig.4.3 shows this plot of λ_1 against $\dot{T}_s$ for the binary Al-0.5%Fe, ternary Al-0.5%Fe-0.1%Si, Al-0.5%Fe-0.1%Si-0.5%Mg, Al-0.5%Fe-0.1%Si-0.75%Mg and Al-0.5%Fe-0.1%Si-0.75%Mg-0.04%Cr alloys. Regression analysis of the curves revealed the following relationship to be obeyed :

$$\lambda_1 = K\,(G.V)^{-n} \qquad (4.1)$$

where G.V is equivalent to the solidification cooling rate $\dot{T}_s$, λ_1 the primary cell spacing and K and n are constants. Equation 4.1 is of the form expected [Flemings, 1974] and

was found to be broadly appropriate for all alloys under investigation. Secondary arm spacings tend to be affected by coarsening phenomena and the exponent is, in this case, close to 1/3, however, primary spacings tend to display an exponent near to 1/2 [Tiller 1991]. The values of K and n for these alloys are given in Table 4.1. The observed values of n are very close to 1/2.

The presence of 0.1% Si caused a coarsening of the solidification cell structure, as compared with the binary alloy, but no alteration of the value of the exponent which remained close to 1/2. This value also remained unaltered in the presence of Mg, and the addition of Cr to the list of alloy constituents caused no significant coarsening or refinement of the cell structure from that of the Si containing alloy was observed.

Fig 4.4 shows the effect of changes in composition within the quaternary Al-Fe-Si-Mg alloys on primary cell spacing. The values of K and n for this alloy series are given in Table 4.2. The results show that for a given Si:Fe ratio changing the Mg content of the alloy did not effect a significant alteration of the observed primary cell spacing. Any changes in the Si or Fe content of the alloys, however, is seen to cause a change in cell spacing. The value of the exponent n was not altered by changes in Si:Fe ratio and was found to be close to 1/2 in all cases.

4.2 Effect of alloy composition and solidification velocity on second phase formation and stability

4.2.1 Al-0.5%Fe

The x-ray diffraction trace given as Fig.4.5a was taken from intermetallic powders extracted from a sample of this alloy that had been unidirectionally solidified at 0.05mm/s. The trace indicates that $Al_{13}Fe_4$ is present as the major second phase constituent. In addition, the presence of Al_xFe is suggested by the appearance of the $Al_{13}Fe_4$ (4 0 2), (0 2 5) and (8 0 2) peaks, which display uncharacteristically high intensities as compared with the standard $Al_{13}Fe_4$ pattern (Table 3.6), and also by the presence of weak reflections corresponding with (9 5 0) and (12 5 0) in the pattern given by Young and Clyne [1981]. The appearance of these weak reflections does not, however, constitute conclusive proof of the presence of the Al_xFe phase.

(indicated by the letters D and E in Fig 4.5a). The appearance of these weak reflections does not, however, constitute conclusive proof of the presence of the Al_xFe phase.

The phases found in this alloy after unidirectional solidification at 0.10mm/s have been identified by analysis of SAD patterns produced during investigation in the TEM as $Al_{13}Fe_4$ and Al_xFe. The results of these observations are summarised in Table 4.3, and show that the phases are co-dominant in this alloy condition.

$Al_{13}Fe_4$ is found to display a decreased tendency to faceting when formed under these conditions. Fig. 4.6a shows an example of the fibrous morphology commonly found at cell triple points, these tight groups of non-faceted rod-like intermetallics bear a stronger resemblance to normal eutectics, such as Al-Al_6Fe, than to the faceted lath morphology usually associated with this phase. The growth mode of the particles is not without some degree of directionality, however, and the crystals have aspect ratios of between 2 and 6:1 with the long axis corresponding to the ⟨001⟩ crystallographic direction. The particles are also found to contain stacking faults or twins on (001) planes, the presence of which is indicated both by the light and dark contrast bands in the crystals in ⟨001⟩ and faint streaking of the c* reciprocal lattice vector rows in the [010] diffraction pattern, Fig.4.7a. The boundaries of these faults are, in this case, quite diffuse, perhaps a function of foil thickness, but their spacing can be measured as ranging from 50 to 100nm. At cell boundaries the non-faceting rods tend to group together to form large laths such as that indicated in Fig.4.7a.

Also present in Fig.4.7a is a large fibrous particle typical of that of the Al_xFe crystallites found in this alloy condition. There was no evidence of any internal defect structure in the Al_xFe crystallites observed or of any tendency toward the exposure of preferential external facet planes.

In specimens solidified at 0.5 and 1.00 mm/s x-ray diffraction of extracted crystals showed Al_6Fe to be the dominant intermetallic, the x-ray traces Figs.4.5b and c clearly arising from this phase, though, in common with the trace given in Fig.4.5a the presence of Al_xFe is suggested by the appearance of several weak principal reflections in both traces.

In contrast TEM examination of two foils prepared from a specimen of this alloy which had been unidirectionally solidified at 2.00mm/s showed that Al_6Fe was the sole intermetallic present. The phase identification results are summarised in Table 4.4. This phase was observed to form as both a divorced eutectic delineating the α-Al cell boundaries (Fig.4.8) and as more developed eutectic groups at cell triple points (Fig.4.9). No evidence of facetting was observed in any of the individual Al_6Fe crystals examined.

4.2.2 Al-0.5%Fe-0.1%Si

$Al_{13}Fe_4$ was the only phase that could be positively identified from the x-ray trace, given as Fig.4.10a, as forming in this alloy after unidirectional solidification at 0.05mm/s. The enhanced intensities of certain $Al_{13}Fe_4$ peaks and the presence of two defining peaks from the x-ray pattern cited by Young and Clyne [1981] was considered insufficient evidence on which to base a positive identification of Al_xFe in this alloy condition. The position of possible Al_xFe peaks are, however, indicated on the diffractogram.

The results of TEM investigation of three foils prepared from an alloy rod that had been unidirectionally solidified at 0.10mm/s are summarised in Table 4.5.

The $Al_{13}Fe_4$ phase, which was found to be the dominant intermetallic formed under these solidification conditions, was observed to form as high aspect ratio plates or laths. Fig.4.11a shows one such $Al_{13}Fe_4$ platelet viewed with the electron beam almost parallel with [010] $Al_{13}Fe_4$. Crystallographic defects are evident on both (001) and (100) and these defects were determined as having average spacings of 12nm and 100nm respectively. Closer examination of the path of a (100) fault, Fig 4.11b reveals that this type of defect changes direction by approximately 35 degrees each time it crosses a (001) defect boundary whilst the (001) defects are seemingly unaffected by the (100) faults.

The fan-shaped $Al_{13}Fe_4$ crystal shown in Fig 4.12a also contains many crystallographic defects on both (001) and (100) of spacing 8-12nm and 15-25nm respectively. The fan is actually composed of two $Al_{13}Fe_4$ crystals which displayed a very small mis-orientation with respect to each other. The SADP (Figs.4.12c to e) were taken from the larger of these crystals. It is interesting to note that the region of this crystal marked A was imaged in this case with **B=Z=** [010] whilst that marked B was simultaneously oriented

direction across this (100) twin plane by approximately 35 degrees. Close examination of the region where both (001) and (100) defects are present, Fig.4.12b, reveals that (100) defects tend to deviate from their path by 35 degrees when crossing an (001) fault, whilst, apart from the exception of crossing the (100) twin plane, (001) faults appear to be unaffected by (100) defects.

The x-ray trace, Fig.4.10b, taken from intermetallics extracted by the butanol reflux method from an alloy sample that had been unidirectionally solidified at 0.50mm/s revealed that both $Al_{13}Fe_4$ and Al_6Fe co-existed in this alloy condition. The strongest signal was obtained from Al_6Fe and this was, therefore, considered to be the dominant intermetallic in this case.

Extensive TEM work on crystals extracted from an alloy specimen which had been solidified at 1.00 mm/s revealed the dominant intermetallic in this alloy condition to be Al_xFe as defined by the lattice parameters given by Young and Clyne (Table 2.1) whilst $Al_{13}Fe_4$ was found as a minor constituent. The results of this investigation are summarised in Table 4.6. The x-ray trace taken from this same residue (Fig.4.13) could not, however, be indexed using the x-ray pattern given by Young and Clyne (Table 3.9) nor does the pattern fit any of the other standards found in the literature. A comparison of the peak data taken from this x-ray trace, Table 4.7, shows The closest fit in terms of peak grouping was with the Al_xFe pattern in use by ALCOA, Table 3.10, although this did not show a good match with respect to reflection intensity. That the electron diffraction work should show that the dominant phase was Al_xFe, as defined by the lattice parameters of Young and Clyne, whilst x-ray diffraction produces a pattern which bears little resemblance to the pattern cited by them as belonging to this phase, casts some doubt on the validity of their standard pattern. Direct observation of the Al_xFe phase was, therefore, considered the only reliable method of identification. X-ray peaks corresponding to those given in the Young and Clyne pattern are, however, indicated on all diffractograms in which they are present.

Figs.4.14a and b show the skeletal morphology of two of these extracted Al_xFe crystals. The particles were single crystals, no differences in orientation between the protruding

Figs.4.14a and b show the skeletal morphology of two of these extracted Al_xFe crystals. The particles were single crystals, no differences in orientation between the protruding fingers and the main body of the crystal was evident from the diffraction information obtained, save for a small deviation which was attributed to crystal curvature.

It was a simple matter to obtain good diffraction data from extracted Al_xFe intermetallics. The five most commonly obtained zone axes are given in Fig.4.15 a to e. These patterns were solved using the lattice parameters proposed by Clyne (i.e. a = 2.16nm, b = 0.930nm, c = 0.905nm and $\beta = 94°$) as shown in Table 4.8-4.11. In all but one case the patterns were found to be consistent with the monoclinic structure proposed, corresponding indices are given for these patterns. The one zone axis which appeared to be an exception was, however, found to match one given by Clyne which was found to be incommensurate with the structure he proposed. The interplanar angles and ratios of the diffraction spots in reciprocal space for this incommensurate zone are presented in Table 4.12.

Results of a TEM investigation of three foils taken from an alloy sample which had been solidified at 2.00mm/s are summarised in Table 4.13. These data show that the dominant intermetallic structure in this case was Al_xFe with $Al_{13}Fe_4$ present as a minor constituent (again less than 30% of the total observed intermetallic population).

Fig.4.16 shows a group of Al_xFe intermetallics typical of those observed in this alloy condition. Both low and high aspect ratio fibrous morphologies of the phase are present in this particular group. There was no evidence of crystallographic facetting in any of the Al_xFe crystals observed in this case.

The $Al_{13}Fe_4$ phase was typically of the morphology shown in Fig.4.17a. The crystals show a high density of (100) crystallographic faults, of spacing 8-12nm, and no evidence of any (001) type defects. The particular example shown here also contains a single (100) twin plane at the position indicated on the micrograph from which the selected area diffraction pattern Fig.4.17b was taken. The facets could be indexed as (100), (001) or $(\bar{2}01)$.

Al_mFe was observed as a very minor constituent in this alloy condition. This phase where observed was found within the α-Al cells themselves. The morphology of this intercellular Al_mFe was typically as shown in Fig.4.18.

4.2.3 Al- 0.25%Fe-0.1%Si-0.5%Mg

The results of the TEM investigation of the phases found in this alloy after unidirectional solidification at 0.05mm/s are summarised in Table 4.14. The sole intermetallic found in this alloy condition was $Al_{13}Fe_4$. A typical platelet of this phase is shown in Fig.4.19a. The electron diffraction pattern Fig.4.19b confirms that this particular crystal contains a (100) twin plane, the position of which is indicated on the micrograph. There is also evidence of (100) and (001) crystallographic faults although only the (100) faults have sharply defined boundaries. This (100) fault spacing was measured in this case as 13 nm and the (001) faults were measured to a lesser accuracy, because of the diffuse nature of their boundaries, as 35 nm.

Occasionally clusters of $Al_{13}Fe_4$ crystals were observed in the interior of the α-Al cells. These groups consisted of several grains or sub-grains. Fig.4.20a shows one such intracellular group. Numerous (001) and (100) faults are evident in these crystallites with average spacings of 20nm and 13 nm respectively. The diffraction pattern given as Fig.4.20b shows that the orientation relationship $[010]_{Al_{13}Fe_4} \| [110]_{\alpha\text{-}Al}$ existed in the case of at least one particle in this group although no evidence of a common contact plane was found. Several other crystallites in this group were found to lie within a few degrees of this particular orientation.

The remainder of the alloy conditions were investigated by x-ray diffraction methods and the traces are given in Figs.4.21 a to c.

Fig.4.21a shows that $Al_{13}Fe_4$ was the main intermetallic constituent present in specimens of this alloy solidified at 0.10mm/s. The trace in this instance was taken from intermetallic powders extracted by the HCl electrolysis technique and is of relatively poor quality. It does, however, contain enough information to give a positive identification of this phase.

The trace taken from powders extracted by the butanol method from an alloy specimen unidirectionally solidified at 0.50mm/s, Fig.4.21b, shows that both $Al_{13}Fe_4$ and Al_6Fe are to be found in this alloy condition. It is difficult to tell which is the dominant phase as the strengths of the principal reflections were similar. In this case it was, therefore, assumed that the phases coexisted in similar proportions.

Specimens unidirectionally solidified at 2.00mm/s were found to contain only Al_6Fe. The x-ray trace, taken from HCl extracted intermetallic powder is given as Fig.4.21c.

4.2.4 Al-0.5%Fe-0.1%Si-0.5%Mg

Analysis of x-ray traces taken from HCl extracted intermetallics and a limited TEM investigation of the phases found in samples of this alloy, unidirectionally solidified at velocities of less than 0.50mm/s, revealed $Al_{13}Fe_4$ to be the major intermetallic constituent. Fig.4.22a shows the trace obtained from the intermetallic residue extracted from the sample solidified at 0.10mm/s.

The results of TEM investigations of three foils produced from a sample of this alloy solidified at 0.50mm/s are summarised in Table 4.15. $Al_{13}Fe_4$ was identified as the only second phase intermetallic present in this alloy condition.

Fig.4.23a shows a typical group of ribbon-like $Al_{13}Fe_4$ crystallites found on the α-Al cell boundaries. Light and dark striations in [001] reveal the crystallites to contain many (001) defects the average spacing of which is 10nm. The accompanying SAD pattern, Fig.4.23b, shows the orientation relationship:

$$[010]_{Al_{13}Fe_4} \,||\, [100]_{\alpha\text{-Al}}$$

$$(001)_{Al_{13}Fe_4} \,||\, (100)_{\alpha\text{-Al}}$$

This exact relationship, it should be stressed, was not one which was commonly observed although many of the crystallites in this group lie within a few degrees of this OR. No evidence was found to suggest the presence of any low energy interfacial plane of contact between α-Al and $Al_{13}Fe_4$.

In specimens solidified at 1.00mm/s and 2.00mm/s x-ray diffraction of HCl extracted crystals, Fig.4.23b and c, showed Al_6Fe to be the only phase present..

4.2.5 Al-0.75%Fe-0.1%Si-0.5%Mg

Analysis of x-ray data taken from intermetallics extracted by the HCl method from alloy specimens solidified at V < 0.05mm/s (Fig.4.24a and b) showed $Al_{13}Fe_4$ to be the dominant intermetallic in both cases.

The results of a TEM investigation of intermetallics found in three foils produced from a specimen of this alloy solidified at 0.50mm/s are summarised in Table 4.16. The two phases found in this alloy condition were $Al_{13}Fe_4$, which was the dominant structure, and Al_6Fe which was found as a minor constituent (less than 20% of the total intermetallic population).

The morphology of $Al_{13}Fe_4$ crystals found in this alloy condition was quite complex. Fig.4.25a shows the sub-structure of one such $Al_{13}Fe_4$ crystal, which was seen to be composed of several grains or sub-grains. It is not a simple task to locate the crystallite boundaries or to discern which are grains and which are sub-grains. It is thought, however that this group consists of perhaps two to four crystallites. The largest of the crystals contains one (100) twin boundary at the position indicated and is observed to contain numerous fine contrast bands indicating the presence of (001) defects. The average spacing of these defects is 7nm. The smaller crystallite which appears to form as a branch coming off the main crystal is also found to contain a (100) twin boundary the presence of which is shown by (001) faults displaying this 35 degree deviation when crossing the twin plane.

Another morphology of $Al_{13}Fe_4$ found in this alloy condition is shown in Fig.4.26. This low aspect ratio (≈2:1) crystal can be seen to contain many fine contrast bands corresponding to (001) and (100) crystallographic faults. These defects have average spacings of 7 and 16nm respectively. The (001), (100) and $(\bar{2}01)$ external boundary planes are indicated on the micrograph.

The morphology of the facetted Al_6Fe particle shown in Fig.4.27a is typical of that found in this alloy condition. The prismatic planes were found, by orientation of the image with respect to the diffraction pattern Fig.4.27b, to be of the {110} type, based on the assumption that the axis of the rod was parallel to the [001] electron beam direction. No

evidence of any specific orientation relationship with respect to α-Al was observed in this case.

Analysis of the x-ray trace taken from intermetallics, extracted by the butanol reflux method from an alloy specimen which had been solidified at 1.00mm/s (Fig.4.24c) showed that $Al_{13}Fe_4$ was still the dominant intermetallic in this alloy condition and that Al_6Fe was found as the minor second phase component.

The results of a TEM investigation of intermetallics extracted from an alloy specimen solidified at 2.00mm/s by the butanol reflux method are summarised in Table 4.17. In this case the major second phase component was again found to be $Al_{13}Fe_4$ whilst the minor constituent was observed as Al_mFe.

Fig.4.28 shows one such extracted Al_mFe crystal. The morphology of this phase was almost exclusively dendritic. No orientation difference between protruding fingers and the main part of the particle save for a small deviation caused by crystal curvature was apparent from the diffraction patterns.

4.2.6 Al-0.25%Fe-0.1%Si-0.75%Mg

Figs.4.29a and b show the x-ray traces obtained from second phase intermetallics extracted, by the HCl method, from specimens of this alloy which had been unidirectionally solidified at 0.05mm/s and 0.50 mm/s respectively. The major constituent phase was determined in both cases to be $Al_{13}Fe_4$.

In specimens solidified at 1.00mm/s, however, the x-ray trace taken from the butanol extracted second phase material (Fig.4.29c) revealed that the main constituent was Al_6Fe, with $Al_{13}Fe_4$ present as only a very minor component.

The results of an investigation of three TEM foils, prepared from a specimen of this alloy which had been unidirectionally solidified at 2.00mm/s, are summarised in Table 4.18. These data show that Al_6Fe is the main intermetallic phase present and also that two other intermetallic phases were found as minor constituents in this alloy condition.

Fig. 4.29a shows a faceted Al_6Fe crystal typical of those observed in this alloy condition. Relating the [001] selected area diffraction pattern to the image revealed the interfacial

bounding planes of the crystal to be (110) and (100) as indicated on the micrograph. This observation was not isolated. Of the six Al_6Fe intermetallics examined five displayed this type of facetting behaviour whilst the sixth showed evidence of both the exposure of preferential bounding planes and of faulting on (110) planes.

A transverse section electron micrograph showing detail of these (110) faults in Al_6Fe is given as Fig.4.31a. The average spacing of these defects was measured directly from the TEM negative as 1.97 ± 0.23nm. The [001] diffraction pattern, Fig.4.31b, taken at the position indicated displays many incommensurate reflections on [110]*. These maxima have a periodicity, in real space, of 1.95 ± 0.10nm, a value remarkably similar to that of the measured (110) fault spacing. This preferred periodicity corresponds to a spacing four times that of the interplanar spacing of {110} Al_6Fe. It is also interesting to note that the interface of the featureless and faulted regions in this particular crystal forms a series of steps.

The minor phases found in these foils were of two types. The first, a superstructure of α-AlFeSi which, on the basis of experimental observation, was found to account for less than 5 % of the total intermetallic population and the second $Al_{13}Fe_4$ which was present as approximately 10% of the total.

Fig.4.32a shows a group of intermetallic particles which were identified as possessing a superstructure of bcc α-AlFeSi. The selected area diffraction pattern given as Fig.4.32b could be solved with marginally better success for the monoclinic (α_T) crystal than for the rhombohedral (α_R) superstructures, as shown in Table 4.19. This improvement of fit for the monoclinic lattice parameters over those of the rhombohedral structure does not, however, provide sufficient evidence to support this as being the correct structure, and so, does not provide sufficient information to allow a positive identification of this phase. Regrettably a fuller investigation of this phase was not possible as the condensed electron beam caused a transformation to the bcc α-AlFeSi after about 10 minutes of continuous exposure.

The $Al_{13}Fe_4$ crystallites shown in Fig.4.33a and b are typical of those observed in this alloy condition. Both crystallites contain faults on (100) of spacing between 4 and 10nm. No evidence of any (001)defects was observed.

4.2.7 Al-0.5%Fe-0.1%Si-0.75%Mg

The x-ray diffraction trace taken from intermetallics extracted by the HCl method from a specimen of this alloy unidirectionally solidified at 0.05mm/s is given as Fig.4.34a. This trace indicates that $Al_{13}Fe_4$ was the major second phase in this alloy condition.

TEM investigation of intermetallics extracted, by the butanol method, from an alloy sample which had been solidified at 0.10mm/s showed that $Al_{13}Fe_4$ was the sole intermetallic found in this alloy condition. The results of this TEM work are summarised in Table 4.20.

Fig.4.35a shows a typical extracted $Al_{13}Fe_4$ crystallite. The morphology of the phase is exclusively lath-like. A typical tilt series for $Al_{13}Fe_4$ is shown in Fig.4.35b. Faint streaking of the (001) reciprocal lattice vector rows in the [110] pattern is indicative of the presence of (001) faults in the crystal. It was not, however, possible to investigate the internal structure of the extracted crystallites in this case as they were opaque to 100kV electrons.

Three foils taken from specimens of the alloy which had been unidirectionally solidified at 0.50mm/s were examined in the TEM. The results of this work are summarised in Table 4.21. The two constituent phases observed, $Al_{13}Fe_4$ and Al_xFe, were found to be co-dominant.

Fig.4.36 shows cell boundary $Al_{13}Fe_4$ crystallites typical of those found in this alloy condition. Al_xFe was typically to be found as strings of crystallites delineating the α-Al cell boundaries. Fig.4.37 shows one such group displaying both low and high aspect ratio fibrous morphologies characteristic of Al_xFe are present in this case.

In specimens solidified at 1.00mm/s the major phase, as indicated in Fig.4.34b, was found to be Al_6Fe with $Al_{13}Fe_4$ present, in this case, as a minor constituent. This x-ray trace was taken from intermetallics extracted by the butanol reflux method.

The results of a TEM investigation of three foils taken from a specimen of this alloy which had been solidified at 2.00mm/s are summarised in Table 4.22. Al_6Fe was identified as the major phase with $Al_{13}Fe_4$ present as a minor component.

Al_6Fe is observed, in this case, both as laths delineating α-Al cell boundaries and as a more developed eutectic at cell triple points. Fig.4.38a shows a typical ellipsoidal Al_6Fe particle which formed part of one such triple point group. It was apparent that there was some tendency toward the formation of preferential bounding planes although the crystals could not be regarded a displaying a truly faceted morphology. The diffraction pattern, Fig.4.38b, corresponding to this image revealed the interfacial bounding planes to be {110} and {100} as indicated on the micrograph. Five of the seven Al_6Fe crystals observed displayed this neo-facetting behaviour; the remaining two showed no tendency to facet and possessed morphologies more reminiscent of the $Al_{13}Fe_4$ lath morphology. An example of this lath morphology is shown in Fig.4.39.

$Al_{13}Fe_4$, where observed, formed as small crystallites, usually isolated from the Al_6Fe intermetallics, and, was most commonly observed as lying on the α-Al cell boundaries. The example given as Fig.4.40 is typical of the morphology of Al_6Fe found in this alloy condition.

4.2.8 Al-0.75%Fe-0.1%Si-0.75%Mg

The x-ray traces in Fig.4.41a and b, show that $Al_{13}Fe_4$ was the dominant intermetallic found in specimens of this alloy at growth velocities of 0.05mm/s and 1.00mm/s.

The trace taken from intermetallics extracted from the an alloy specimen solidified at 2.00mm/s by the butanol method, Fig.4.41c, shows the major constituent to be Al_6Fe. A number of low intensity $Al_{13}Fe_4$ reflections are still present in this trace.

4.2.9 Al-0.5% Fe-0.05% Si-0.75% Mg

The x-ray trace taken from the second phase intermetallics extracted, by the HCl method, from a specimen of this alloy which had been unidirectionally solidified at 0.05mm/s, Fig.4.42a, shows that $Al_{13}Fe_4$ is the main constituent phase in this alloy condition.

TEM work on three foils taken from a specimen of this alloy which had been unidirectionally solidified at 0.10mm/s showed $Al_{13}Fe_4$ to be the only phase present. The SAD phase identifications are summarised in Table 4.23. Fig.4.43a shows a group of $Al_{13}Fe_4$ crystallites typical of those observed in this alloy condition. Many of the crystallites contain (001) faults of average spacing 10nm. Several particles also contain (100) defects. Many of the crystallites in this group lie within four degrees of the orientation relationship $[010]_{Al_{13}Fe_4} || [100]_{\alpha\text{-}Al}$ shown in Fig.4.43b.

X-ray investigation of the intermetallic crystals extracted, by the HCl method, from a specimen of this alloy solidified at 0.50mm/s showed that $Al_{13}Fe_4$ was the dominant phase in this case also, (Fig 4.42b).

The x-ray trace, Fig.4.43c, was taken from intermetallics extracted from a specimen of this alloy which had been unidirectionally solidified at 1.00mm/s, The trace indicates that both Al_6Fe and Al_mFe are present in this particular alloy condition. To give an indication of the relative proportion of each phase an investigation of the extracted intermetallics was undertaken in the TEM. The results of this work are summarised in Table 4.24. Al_6Fe was found to constitute approximately 70% of the total intermetallic population with Al_mFe present as about 30%.

The morphology of Al_6Fe was observed to be as shown in Fig.4.44a. The intermetallics seem to have grown in a ribbon-like manner under these imposed growth conditions with branches forming in the growth direction which are fibrous in cross section.

The results of TEM work on three foils taken from a specimen of this alloy which had been unidirectionally solidified at 2.00mm/s are summarised in Table 4.25. These results indicate that the Al_mFe had become the dominant phase in this case occurring as 70% of the observed intermetallic population. $Al_{13}Fe_4$ was found to be the other phase present in this alloy condition.

Fig.4.45a shows the typical morphology of the Al_mFe phase as observed in these transverse section foils. Its morphology is similar to that of the Al_6Fe crystal shown in Fig.4.39.

The group of crystals, Fig.4.46a, shows the typical morphology of $Al_{13}Fe_4$ as found in this alloy condition. Many of the crystals contain defects on either or both of (001) and (100) the spacings of which are between 5 and 10nm in the case of both types of fault. The crystal marked A contains a (100) twin plane from which the selected area diffraction pattern Fig.4.46b was taken.

4.2.10 Al-0.5%Fe-0.15%Si-0.75%Mg

The x-ray trace given as Fig.4.47a was taken from intermetallics extracted, by the HCl method, from an alloy specimen which had been solidified at 0.05mm/s. The trace indicates that $Al_{13}Fe_4$ was the major constituent phase.

X-ray diffraction of the butanol extracted intermetallics taken from an alloy specimen after it had been unidirectionally solidified at 0.50mm/s (Fig.4.47b) showed that $Al_{13}Fe_4$ was still present as a constituent phase, although it was the minor component in this case. The major second phase intermetallic phase found in this alloy condition was Al_6Fe.

The trace obtained from the intermetallics extracted from a specimen of this alloy which had been solidified at 2.00 mm/s is given as Fig.4.47c. The major phase is again seen to be Al_6Fe with $Al_{13}Fe_4$ found once more as the minor intermetallic constituent.

4.3 The effect of 0.04% Cr on intermetallic phase stability in Al-0.5%Fe-0.1% Si-0.75% Mg

Intermetallics extracted, by the butanol method, from a specimen of this alloy solidified at 0.05mm/s give rise to the x-ray trace given as Fig.4.48a. This trace indicates that $Al_{13}Fe_4$ was the only phase which could be positively identified as being present in this alloy condition.

TEM investigation of three foils prepared from a specimen of this alloy which had been solidified at 0.10mm/s yielded the results which are summarised in Table 4.26. These results show that $Al_{13}Fe_4$ was the only intermetallic phase encountered in these foils. All of the $Al_{13}Fe_4$ crystallites observed in this alloy condition were found to contain at least one (100) twin plane. The example show in Fig.4.49a contains three or possibly four

such twin planes, the electron diffraction pattern Fig.4.49b being taken from the most obvious of these. The presence of these (100) twins has caused the crystal to become branched, the angle between these branches being approximately 35 degrees. This particular crystallite also contains many defects on (001) of spacing 20nm and a region containing a high density of (100) faults of spacing 25nm. The external planes of the crystallite are, as would be expected, (100), (001) and (201).

Many of the $Al_{13}Fe_4$ crystals observed in this alloy condition have feathery internal features. An example of a crystal of type is shown in Fig.4.50a. The feathery markings seem to join at a central spine which defines the position of the (100) twin plane. The markings themselves appear to lie on low packing density (401) planes and to be strongly affected by crossing (001) defect boundaries in much the same way that (100) defects are. The selected area diffraction pattern given as Fig.4.50b shows that, as well as containing a (100) twin, this crystal particular crystal displays the orientation relationship $[010]_{Al_{13}Fe_4} \parallel [100]_{\alpha\text{-}Al}$. Indeed all of the $Al_{13}Fe_4$ crystallites investigated in this alloy condition lay within four degrees of this orientation. No evidence was obtained to suggest a common set of contact planes between the two crystal structures.

The x-ray trace given as Fig.4.48b shows the intermetallics formed after solidification at 0.50mm/s to be a mixture of Al_6Fe and $Al_{13}Fe_4$, with $Al_{13}Fe_4$ appearing to be the major phase. This was also found to be the result of x-ray investigation of the intermetallics extracted from a specimen of this alloy solidified at 1.00mm/s, although in this case, the Al_6Fe phase was considered to be co-dominant with $Al_{13}Fe_4$. The sole intermetallic found after solidification at 2.00mm/s was Al_6Fe as indicated in Fig.4.48c.

5. DISCUSSION

5.1 Effect of composition and cooling rate on primary α-Al spacing

The primary α-Al spacings in the alloys under investigation were observed to obey the general relationship:

$$\lambda_1 = K(G.V)^{-n} \qquad (5.1)$$

where K and n are constants, the units of K being $\mu m(K/s)^n$. The value of the exponent n was found to be approximately 0.5 for all alloys investigated in the course of the present work,typical of primary cells [Flemings 1974, Tiller 1991], and to be largely unaffected by changes in alloy composition, whilst the value of K was observed to be strongly affected by changes in alloy chemistry.

The relationship determined for the binary Al-0.5% Fe alloy composition i.e.:

$$\lambda_1 = (41.5 \pm 3.4).\ (G.V)^{-0.48 \pm 0.03} \qquad (5.2)$$

was found to be in excellent agreement with that reported by Clyne [1981] as being broadly applicable to all hypoeutectic binary Al-Fe alloys i.e.:

$$\lambda_1 = 42\ \dot{T}_s^{-0.5} \qquad (5.3)$$

The addition of 0.1% Si led to a significant increase in microstructural scale indicated by an increase in the value of K to $76.7 \pm 4.0\ \mu m(K/s)^{1/2}$. Within the bounds of experimental error, this value is largely unaltered by the presence of Mg at both 0.5% and 0.75% or by the addition of 0.04% Cr. It would seem, therefore, that Si is solely responsible for this coarsening of the microstructure.

The magnitude of this increase in the microstructural scale in the presence of Si is predicted by the cellular array growth model of Shu-Zu Lu and Hunt [1995] and can be attributed to a significant decrease in the activation energy for Fe in Al in the presence of Si [Miki and Warlimont 1968]. The cellular array model and the results of the analysis based upon it are presented in Appendix 4.

This effect is further confirmed by examination of the effect of variation in Si content on α-Al cell size in the quaternary alloy series Al-0.5%Fe-0.05%Si-0.75%Mg, Al-0.5%Fe-0.1%Si-0.75%Mg and Al-0.5%Fe-0.15%Si-0.75%Mg. The data presented in Tables 4.1 and 4.2 show that lowering the Si content resulted in a slight refinement of the microstructure, whilst the converse was true for the 0.15%Si containing alloy.

Changing the Fe content of the Al-Fe-Si-Mg alloys had little effect on the α-Al cell size. The trend was for a slight refinement of cell spacing with increasing Fe content irrespective of the Mg content of the alloys but again within the limits of experimental error this effect was considered to be insignificant.

5.2 Intracellular phase formation

Intermetallic phases forming within the α- Al cells have been reported previously by Furrer [1979] and Westengen [1982]. Westengen commented that, where observed, these intracellular intermetallic particles were more or less spherical with distinct internal subgrain / grain boundary networks. This was also observed to be the case in the present work (e.g.Fig 4.20). No attempt was made by either author to explain this phenomenon.

Explanations for the occurrence of intracellular phases in other alloy systems have been based upon i) upquenching, i.e. super-solidus re-heating leading to localised remelting followed by resolidification of solute enriched regions and hence to the formation of intermetallic crystals [Reiso *et al* 1994], ii) a peritectic reaction giving rise to a spontaneous precipitation of intermetallics within the parent crystal [Ogilvy 1981] and iii) the effects of dendrite arm coarsening [Genda *et al.* 1987].

Mechanism i) is unlikely to have been responsible for the formation of intermetallics in the present case because of the low equilibrium solid solubility and diffusivity of Fe in α-Al . The local concentration of Fe required to give rise to intracellular phase formation by this mechanism is in excess of 26%. Therefore, whilst this mechanism is relevant to systems such as Al-Zn, Al-Cu and Al-Mg [see, for example, Reiso *et al.* 1994] with higher equilibrium solubilities and diffusivities, it is not considered relevant to phase formation in the present alloys.

The second approach, i.e. peritectic reaction leading to the formation of intermetallics in the solid state, has been applied to the analysis of tool steel microstructures by Ogilvy [1981]. However, as the peritectic reactions in the Al-Fe-Si system rarely, if ever, occur under normal solidification conditions it is unlikely that this mechanism was responsible for the formation of these intermetallic phases in the present work.

The most likely candidate would appear to be dendrite arm coarsening. An examination of the available literature revealed the coarsening mechanism proposed by Genda *et al.* [1987] to be the most useful in accounting for the results of the present work. Fig.5.1 is a schematic representation of their proposed coarsening mechanism. It was postulated that during the coarsening process adjacent dendrite arms first swell and join at the mid point (Fig5.1a). Coalescence then proceeds from the mid-point to both the roots and the tips. The effect of solidification from the mid-point would be to cause terminal reactions at both the root and the tip because of the low mobility of Fe in α-Al and, so, intermetallics would be expected to form at both the cell walls (tip) and within the α-Al (root).

Interestingly this could lead to the formation of intermetallics within the dendrites that were of a different type to those formed under different solidification conditions at the dendrite walls. Whilst this is not always the case it was certainly observed, in the present work, on a number of occasions where phases such as Al_mFe and α_T/α_R-AlFeSi were to be found within the α-Al as very minor constituents whilst Al_6Fe was observed to be the major constituent phase at the cell boundaries.

As the phenomenon was not observed in the binary alloy composition it could be that it is somehow linked to a change in the primary α-Al growth morphology, the reported retarding effect of Fe on the growth of dendrite arms [Trung *et al.* 1973] perhaps being partly negated by the presence of the additional solute elements. It is, however, uncertain whether any such changes in the primary growth morphology had occurred and this is an area for possible further investigation.

5.3 The effect of cumulative alloying additions on phase morphology and stability

The results of studies of this type are typically interpreted in one of two ways. The first is by means of a competitive growth model, which has been used to describe growth behaviour in binary systems exhibiting multiple eutectics including Al-Fe [Kurz and Trivedi 1990, Cochrane *et al.* 1991, Liang and Jones 1992] and cast irons [Hillert and Subba Rao 1967].

This model assumes that all possible phases may nucleate with equal ease and also that the phase which has the highest growth temperature at a given solidification front velocity will be the one observed. The transition between phases is assumed to occur at well defined local solidification front velocities and a plot of growth velocity (V) against growth temperature (T) can be used to explain the observed phenomena. If the effect of an additional solute element was to alter the form of the V-T curve for a given phase then this could be related back to the thermodynamic properties of that phase and this in turn used to explain experimental phase stability observations. This type of analysis is of most use where the V-T curves for the phase, both with and without the additional solute element, have been obtained experimentally. A reverse analysis (i.e. one where phase transitions have been observed but without the V-T relationship having been established experimentally), which would employ hypothetical V-T curves to explain the observations, can yield little in the way of useful insight.

An alternative approach was adopted by Backerud [1968] and by Adam and Hogan [1972,1975]. The discussion of their results was based on a kinetic approach. The concepts employed were outlined by Backerud [1968] following the ideas of Jackson [1957] regarding the classification of eutectics.

Jackson [1957] defined a growth factor α which consisted of the entropy of melting , ΔS, and a crystallographic factor ξ. The value of this factor, ξ , usually varies between 0.5 and 1.0 depending upon the crystallographic direction in which growth is taking

place and is essentially a measure of the number of available interfacial attachment sites. The definition of α is :

$$\alpha = \xi \frac{\Delta S}{R} \qquad (5.4)$$

where R is the universal gas constant.

α factors of less than two govern the growth of atomically rough surfaces which grow without requiring surface nucleation. The growth rate of these surfaces is often diffusion controlled and crystals of this type readily develop a dendritic growth pattern.

When the value of α is greater than two the growth rate is restricted by the rate of surface nucleation. In this type of crystal some planes will have α factors of less than two and consequently, embryonic growth of the crystal will occur preferentially in these directions. However, the growth of these planes will, inevitably, lead to the formation of high density, slow growing planes with α factors of greater than two. After a relatively short time the crystal will be bounded by high density planes which will thereafter determine the growth rate.

The calculated thermodynamic data cited by Backerud [1968] (Table 5.1) indicate that Al_6Fe and Al could grow in a non-faceted manner. However, the values of $\Delta S/R$ for the intermetallic phases show that if ξ is assumed to be 1.0, Al_6Fe is only marginally non-faceting ($\Delta S/R = 1.8$) and likewise that $Al_{13}Fe_4$, with $\Delta S/R = 2.3$, is only just within the faceted classification. Thus, anything affecting a change in ΔS or ξ will have an effect on the growth mode and, potentially, the ranges of phase stability.

Interpretation of the results of the present work will be based on this kinetic approach and this will be applied as far as is possible to explain the observed phenomena.

Fig 5.2 presents the results of cumulative alloying additions on phase stability as a function of both alloy composition and solidification front velocity. These results suggest that the alloy additions operate synergistically to provide an environment in which the

$Al_{13}Fe_4$ phase becomes the most thermodynamically and kinetically favoured intermetallic. However, whilst the $Al_{13}Fe_4$ phase is stabilised to a very significant extent by these additions there is no reason to assume that they affect the growth of only this phase. Changes in the range of stability of the metastable intermetallics formed at the higher solidification front velocities show that a change in the relative stability of these phases is also effected by the presence of these additional elements.

The changes in morphology of the phases and their ranges of incidence with respect to alloy composition and solidification front velocity (and, by calculation, solidification cooling rate) will be discussed in the following sections.

5.3.1 Binary Al-0.5% Fe

The observed ranges of stability of the phases in Al-0.5%Fe are in good agreement with those previously reported in the literature [Granger 1990, Fang and Granger 1991, Tezuka and Kamio 1992]. Fig 5.3 compares the results of the present work with those for Al-0.4%-0.5%Fe taken from the literature. Most results are given in terms of solidification cooling rate and, so, to allow an easy comparison to be made, the solidification front velocities were converted to solidification cooling rate using the standard relationship:

$$G.V = \dot{T}_s \qquad (5.5)$$

where G is the imposed temperature gradient, here taken to be 10 K/mm (the average of the measured values of G) and V is the solidification front velocity in mm/s. In general, the transition from $Al_{13}Fe_4$ as dominant intermetallic is observed to occur at a cooling rate of between 1 and 5 K/s. There is, however, some disagreement as to the phase which immediately replaces $Al_{13}Fe_4$ and also as to whether a transition region is observed where two intermetallic phases coexist. There is also little indication given by these authors as to whether any morphological transitions occur prior to the actual phase transition.

The morphological transition observed for $Al_{13}Fe_4$ in the binary alloy in the present work prior to the phase transition was from faceted, lath-like, growth at low growth velocities

(solidification cooling rates) to a rod morphology. This transition has been reported in more concentrated alloys on a number of occasions [Burden and Jones 1970, Adam and Hogan 1972,Hirai *et al.* 1977, Clyne 1981]. Although the Jackson and Hunt [1966] analysis predicts that the rod morphology of a phase will grow with less undercooling than a lath, this morphology of $Al_{13}Fe_4$ would appear to be kinetically unstable. The rod form of $Al_{13}Fe_4$ was observed in the present work to coexist with Al_xFe at 0.1mm/s (~1.0 K/s) and to be replaced by Al_6Fe at 0.50mm/s (~5 K/s). These observations are in close agreement with those of previous workers [Burden and Jones 1970, Adam and Hogan 1972] who reported that, where observed, the rod morphology of $Al_{13}Fe_4$ in the αAl-$Al_{13}Fe_4$ eutectic always coexisted with the αAl-Al_6Fe eutectic and then only over a short transitional range of growth velocities (60 to 100μm/s) in 2.00 wt.%Fe [Adam and Hogan] or of cooling rates in Al-4.2 wt.% Fe [Burden and Jones].

It is worth examining how this type of faceted to non-faceted growth transition occurs in a eutectic system exhibiting semi-cooperative growth of a faceted (e.g.$Al_{13}Fe_4$) and non-faceted (e.g.α-Al) component and also to speculate as to why the growth mode is, apparently, unstable.

At low growth velocities the sides of the growing $Al_{13}Fe_4$ plates can be regarded as inert, i.e. at low undercooling when the TPRE (twin plane re-entrant edge, see section 2.1) mechanism is operating at the leading edges of the plates, the sides of the plates are atomically smooth and two dimensional nucleation and growth are negligible. However, isolation of these plates can give rise to increased undercooling of the plate walls. When this undercooling exceeds some critical value, atoms can attach themselves at any point on the interface leading to uniform advance of the growing interface. This interfacial region may now be several atoms thick and diffuse and growth of the interface can be regarded as normal. Thus, the transition from lath to rod growth morphology could be regarded as a transition from a semi-cooperative to a cooperative growth mode. Concomitant with this change will be transverse coupling of the diffusion fields of the two eutectic components. If the interfacial attachment kinetics of the rod form of $Al_{13}Fe_4$ are insufficiently flexible to allow continued coupled growth of the eutectic then it will be replaced by one which is both more readily nucleated by the α-Al eutectic component

and which exhibits more flexible attachment kinetics. Adam and Hogan [1972] proposed that Al_6Fe was such a phase.

The observation of Al_xFe as an intermediate phase is in good agreement with the results of earlier work [Clyne 1981, Fang and Granger 1991] although the coexistence of this phase with $Al_{13}Fe_4$ has only been reported once in the open literature [Young and Clyne 1981]. In cross section the morphology appears to be very similar to that of Al_6Fe found in these dilute alloys, so much so that Clyne [1981] suggested that the phase could have been mis-identified as Al_6Fe in earlier work. This concern would appear to be unfounded, however, as the results of the work in question [Burden and Jones 1970, Adam and Hogan 1972, Hughes and Jones 1976] were obtained using a combination of x-ray and TEM investigation techniques although it was noted that some SADP remained unsolved in the work of Hughes and Jones [1976].

5.3.2 Al-0.5%Fe-0.1%Si

A comparison of the results of the present work with those for Al-0.5%Fe-0.1%Si alloys taken from the available literature [Granger 1990, Fang and Granger 1991, Tezuka and Kamio 1992] is given as Fig.5.4. In contrast to the results of the binary Al-0.5%Fe alloy there is little overall agreement between the results of the present work and those of previous investigations. Indeed, it is fair to say that no two sets of results produced for this alloy composition show a reasonable degree of correlation. Even those originating from the same source (e.g. the work of Granger [1990] and of Fang and Granger [1991]) exhibit significant disagreement. These discrepancies are likely to be a function of the alloy cleanliness and impurity content, degree of melt superheat and the experimental technique employed though these details are not available in all cases.

Fig.5.3 reveals there to be a slight increase in the stability of $Al_{13}Fe_4$ with respect to solidification front velocity as compared with the binary alloy. At V=0.1 mm/s $Al_{13}Fe_4$ is the only intermetallic constituent present. At 0.5 mm/s, however, the phase constitutes only approximately 30% of the total intermetallic population the remainder of which is made up of Al_6Fe. This increase in stability of $Al_{13}Fe_4$ in the presence of Si is coincident with an increase in the frequency of observation of (100) twin planes and stacking faults

within the intermetallic. According to Black [1955a and b] two possible twin systems may operate in $Al_{13}Fe_4$, the relevant twin planes being (001) and (100) respectively. Twins on (001) are present in all $Al_{13}Fe_4$ crystals and it has been proposed that these twins allow growth of the phase by providing re-entrant sites for the TPRE (twin plane re-entrant edge) growth mechanism [Adam and Hogan 1975]. Adam and Hogan [1975] also reported that (100) twinning was more prevalent in the binary system in $Al_{13}Fe_4$ plates grown at low velocity in high temperature gradients. In contrast, it is the observation of this work that (100) twin planes are rarely observed in $Al_{13}Fe_4$ in the binary alloy but are present in almost all $Al_{13}Fe_4$ crystals observed in the Si-containing alloys.

These (100) twins are readily identified by the spectacular SADP which can be obtained from the region of the intermetallic crystal containing the 100 twin plane when the intermetallic crystal is imaged with B=Z=[010] or B=Z=[$0\bar{1}0$]. As exemplified by Fig.4.12a-e, the SADP taken from the twinned region when the intermetallic crystal is in this orientation is actually a composite $\langle 010 \rangle$ SADP formed by combination of [010] and [$0\bar{1}0$] $Al_{13}Fe_4$. Fig.5.5a shows a typical composite pattern whilst Fig.5.5b illustrates the indexing of the $\langle 010 \rangle$ SADP. The two differently oriented c* axes are indicated both on the SADP and the schematic diagram and the two different unit cells are outlined. The presence of (100) twins can be very easily confirmed by obtaining this composite pattern and this also proves useful in differentiating between grain / subgrain boundaries in $Al_{13}Fe_4$ and (100) twin planes.

It is relevant to consider how such growth twins originate. The driving force for nucleation of twinned monolayers on the crystal-liquid interface is $\Delta S \Delta T_k$ (ΔS = entropy of fusion per atom, ΔT_k = kinetic undercooling), and if the two dimensional embryo is twinned with respect to the substrate crystal, this is reduced by the twin boundary energy, σ_T, $atom^{-1}$. There will be no driving force for such events to occur until $\Delta S \Delta T_k > \sigma_T$. This energetic criterion is clearly met for growth twinning on (001) as this type of defect is observed in all $Al_{13}Fe_4$ crystals, even those grown with very low velocities [Adam and Hogan 1975] and which are, by inference, subject to low ΔT_k. The low

incidence of (100) twin planes in $Al_{13}Fe_4$ in the binary system would seem to imply that their twin boundary energy is significantly higher than that of (001) type twin planes.

Si has also been shown, by Liang [1995], to alter the growth mode of primary $Al_{13}Fe_4$ during directional solidification of hyper-eutectic Al-Fe and Al-Fe-Si. The morphology of the primary $Al_{13}Fe_4$ prisms was observed to change from the normal lath-form to a 10 pointed star morphology at a lower growth velocity in the presence of Si (2.00mm/s c.f. >3.00mm/s). This 10 pointed star morphology has been attributed to the presence of multiple (100) twin planes within the intermetallic crystal [Louis *et al.* 1980, Fung *et al.* 1987]. It would seem, therefore, that the presence of Si also leads to a change in the growth behaviour of primary $Al_{13}Fe_4$.

Groups of faceted $Al_{13}Fe_4$ crystals were also observed to form in the presence of Si. Many of the members of these groups appeared to be connected because they shared a common [010] crystallographic growth direction and appeared to contain (100) twin planes. In fact some of these 'twin planes' were common contact planes where neighbouring crystals coincided such that they displayed characteristics common to (100) twins (e.g. the change in direction of striae on (001) by approximately 35 degrees when crossing from one crystal to another) but showed a small divergence of [010] growth direction. These groups of crystals could arise from a repeated renucleation mechanism with the presence of Si causing the activation of emergent dislocations and jogs on (100) as preferential nucleation sites for new crystals growing in [010].

It is interesting to note that the transition from faceted to non-faceted growth mode observed in the binary alloy is not observed in the presence of Si. Clearly for the growth of $Al_{13}Fe_4$ to continue at higher growth velocities some mechanism must operate to enhance the interfacial attachment kinetics. It has already been suggested that Si acts to reduce the energy of the liquid / (100) facet plane interface and this could in turn lead to a reduction in the undercooling required to facilitate formation of two dimensional nuclei on exposed (100) planes. As the interfacial undercooling increases the number of these two dimensional nuclei will also increase such that the interface becomes roughened and a very high number of potential sites will be available for atomic attachment or autonucleation.

If this were the mechanism in operation, it might be expected that the aspect ratio of the growing crystals would change, with the dimensions in [100] and [001] crystallographic directions becoming more alike. The observations made in the course of this work, though limited, would appear to support this hypothesis although a much more intensive study of $Al_{13}Fe_4$ in this alloy would be required to provide confirmation.

It is proposed that all of the changes in growth mode are induced by the presence of Si and that they lead to the enhanced stability of the phase with respect to growth velocity although the mechanism by which this is achieved has yet to be clarified.

Al_xFe has been previously reported as a dominant intermetallic structure in Al-0.5Fe-0.1Si [Fang and Granger 1991] at solidification cooling rates between approximately 4 and 10 K/s. The results presented here, however, show the phase to be dominant in material solidified with velocities between 1.00 and 2.00 mm/s equating to solidification cooling rates of between 10 and 20 K/s. Fang and Granger reported two further phase transitions, firstly to the, high Si, β-AlFeSi phase at a solidification cooling rate of 10.8K/s and then to Al_6Fe at approximately 12 K/s. These phase transitions were not observed in the present work. Indeed, it is difficult to envisage how such a sequence could occur as β-AlFeSi would have had to crystallise well outside of the β phase field in this case.

The observation of Al_xFe as a dominant constituent contradicts the idea of it being a transient phase with an unstable crystal structure as proposed by Young and Clyne [1981] and Skjerpe [1987] and shows that the phase must gain some form of stability in the presence of 0.1%Si as this is the only system alteration from the binary alloy composition. The reported higher solubility of Si in Al_xFe than in Al_6Fe [Langsrud 1990] may be a contributing factor to the enhanced stability of the phase in the presence of Si. However, as no quantitative compositional information was obtained during the course of this investigation this possibility remains unproven.

5.3.3 Al-0.5%Fe-0.1%Si-0.75%Mg

There is little agreement between the phase stability results of this work and those taken from the available literature [Granger 1990, Fang and Granger 1991]. Fig.5.6 shows that,

in contrast to the results in the literature which show that Al_mFe to be the dominant intermetallic at higher solidification cooling rates, only $Al_{13}Fe_4$ and Al_6Fe and Al_xFe were observed in samples of this alloy composition during the course of the present work. A transition in phase dominance from $Al_{13}Fe_4$ to Al_6Fe occurred at a growth velocity between 0.50 and 1.00 mm/s, although the exact transition velocity was not determined experimentally.

The addition of 0.75%Mg causes the $Al_{13}Fe_4$ phase to be stabilised as a major constituent to a growth velocity of between 0.50 and 1.00 mm/s at which point it was observed to have been completely replaced by Al_6Fe. After solidification at 0.10 mm/s the $Al_{13}Fe_4$ intermetallic crystals observed by TEM displayed very similar characteristics to those found after solidification under similar conditions in the ternary Al-0.5%Fe-0.1%Si alloy.

The increase in phase stability above that in the Si-containing composition would seem to arise as a direct result of the presence of Mg. The absence of any obvious change in morphology or twinning behaviour, however, means that it is more difficult to identify the role of Mg in causing this stabilisation, particularly in the absence of compositional data, as it is not known where the Mg resides in the microstructure after solidification is complete.

Whilst this is the case, the result of the present work was found to be in good agreement with recent findings of Maggs *et al.* [1995] who noted that the range of incidence of $Al_{13}Fe_4$ was increased on the addition of a low level of Mg (0.023%) to dilute Al-Fe-Si alloys during simulated DC casting. The magnitude of this effect was observed to be greater in alloys with a low Si:Fe ratio.

The presence of Mg has the effect of restoring Al_6Fe as the dominant intermetallic at higher growth velocities. The change in dominance of $Al_{13}Fe_4$ from major to minor second phase component occurs in a similar way to that observed in the binary alloy, i.e. that $Al_{13}Fe_4$ first becomes co-dominant with Al_xFe and is then replaced by Al_6Fe. The critical transition velocity is, however, now an order of magnitude greater than in the binary alloy. These results are in good general agreement with the observations of Tezuka and Kamio [1992]. They reported that the addition of 0.5% Mg to an Al-0.3%Fe-0.15%Si alloy caused the stabilisation of $Al_{13}Fe_4$ and Al_6Fe at low and high

solidification cooling rates respectively compared with $Al_{13}Fe_4$ and Al_mFe at low and high solidification cooling rates in the comparable Mg-free alloy composition.

In the presence of Mg, Al_6Fe displayed a marked tendency toward faceted behaviour with many of the crystals observed revealing {110} and {100} bounding planes. This type of faceting behaviour in Al_6Fe has been reported on a number of occasions [Burden and Jones 1970, Adam and Hogan 1972, Clyne 1981]. Burden and Jones [1970] reported that the prismatic plane orientations observed during the course of their investigation were close to {010}, {100} and {110}, which is in agreement with the results of this work, whilst Adam and Hogan observed the facet planes to be (110), $(1\bar{1}0)$, (130) and (310). Adam and Hogan also claimed that there was evidence of lattice matching of the intermetallic and α-Al components of the Al_6Fe eutectic and that a consistent orientation relationship between the eutectic components was evident. No evidence of any form of lattice matching was observed here nor was there evidence of the existence of any form of orientation relationship between Al_6Fe and α-Al.

The thermodynamic data presented by Backerud [1968] (Table 5.1) would suggest that Al_6Fe is only marginally non-faceting and, so, any changes is the local growth environment of the phase such as the presence of Si or Mg in the interdendritic liquid could cause changes in the interfacial surface tension or surface roughness. Such changes could influence the growth mode.

It was observed that Al_6Fe could also exhibit a plate-like growth form. Similar platelet growth morphologies of Al_6Fe have been reported as occurring at eutectic cell boundaries in both Al-4.2 % Fe by Burden and Jones [1970] and also in ternary Al-Fe-Mg alloys by Keong *et al.*[1977]. In contrast to the statement of the previous paragraph both groups of authors attributed the occurrence of the plate morphology of Al_6Fe to local instabilities as a result of interfacial curvature effects rather than modification of the interfacial energy anisotropy. The effect of additional solute elements on the growth behaviour of Al_6Fe is, therefore, clearly an area requiring further work.

5.3.4 Al-0.5%Fe-0.1%Si-0.75%Mg-0.04%Cr

There is little published work on effects of minor alloying additions on the stability of intermetallic Al-Fe and Al-Fe-Si phases and that which has been published has tended to concentrate on the binary Al-Fe [Tezuka and Kamio 1992] and ternary Al-Fe-Si [Maggs *et al.* 1995] systems. Granger [1990] has reported on the effects of low level additions of a number of transition metal elements both individually and in combination on intermetallic phase stability in quaternary Al-Fe-Si-Mg alloys. The effect of Cr, however, was investigated only in combination with Cu and Mn. There are, then, no published data with which to compare the results of the present work.

Fig.5.2 shows that $Al_{13}Fe_4$ is stabilised as a major second phase constituent to a solidification front velocity of 1.00mm/s, in the presence of Si, Mg and Cr, where it was observed to be co-dominant with Al_6Fe. No other phases were observed in this alloy composition over the range of solidification front velocities employed.

That Cr has any effect at all is rather surprising as in the binary Al-Cr alloy system Cr segregates to the solidifying Al leaving the interdendritic liquid depleted of solute at the end of solidification. However, it is known, from studies of the equilibrium ternary Al-Fe-Cr system [Mondolfo 1976] that Cr can replace up to 10% of the Fe atoms in $Al_{13}Fe_4$ and it may be that some substitution of Cr for Fe imparts a greater stability to the phase.

In the absence of compositional data, however, the role of Cr in stabilising the $Al_{13}Fe_4$ phase remains unclear. TEM observations of the phase in samples of this alloy solidified at 0.1 mm/s reveal growth morphologies typical of those observed in Si containing alloys. It is possible that the 100 twin density is higher in the Cr-containing alloy as many intermetallics contain two or more 100 twin planes. The number of $Al_{13}Fe_4$ intermetallics observed (9 in total), however, does not constitute a statistically significant population on which to base such a hypothesis.

Whilst it is possible to speculate on the role of Cr in stabilising $Al_{13}Fe_4$, this would be unwise until a more detailed analysis of chromium-containing alloys has been performed and some idea of the extent of chromium dissolution and the distribution within the intermetallic has been gained.

5.4 Observations on the phase Al_xFe

In the transverse section TEM conducted in the present work the morphology of the Al_xFe phase was always the same, irrespective of whether it was observed as a major or minor constituent and independent of alloy composition and solidification growth velocity. The phase was non-faceted and displayed both rod-like and lath growth forms. The morphology of Al_xFe clusters was very similar to that observed for αAl-Al_6Fe eutectic in these dilute alloys. These observations are in good agreement with those of Westengen [1981] and of Clyne [1981] in particular.

The crystal structure of Al_xFe has been proposed as both monoclinic with lattice parameters, a=2.16 nm, b= 0.93 nm, c= 0.905 nm and β= 94.0° [Young and Clyne 1981] and orthorhombic with the raher more approximate lattice parameters, a = 0.6nm, b = 0.7nm and c = 0.47 nm [Skjerpe 1987].

Analysis of the SAD patterns taken from this type of intermetallic showed the majority to be consistent with the lattice parameters proposed by Young and Clyne [1981]. However, one of the most commonly observed principal zones for the phase was found to be incompatible with the proposed structure.This, combined with the relatively large error between the "ideal" computer generated zone patterns and those observed in practice (Tables 4.8-4.12), would suggest that the proposed monoclinic lattice is in need of some refinement. Also, when two or more of these patterns were obtained from the same particle the tilt angles between the corresponding specimen orientations were not compatible with the calculated inter-zonal angles based on the monoclinic structure.

These observations are in close agreement with those of Clyne [1981] particularly in respect of the existence of a principal zone axis which is incompatible with the proposed scheme. A comparison of the characteristics of the incommensurate zone observed in the course of this work with those reported by Clyne (Table 4.12) revealed the two to be identical.

It would appear that the parameters given by Young and Clyne, though not absolutely correct, are a useful first approximation to the actual structure of the intermetallic observed in the present work. Those parameters given by Skjerpe do not give consistent

solutions of the SADP's obtained in the present study and some doubt must arise as to whether the Al_xFe of Clyne is indeed the same phase as that observed by Skjerpe.

Al_xFe crystals extracted, by the butanol reflux method, from Al-0.5%Fe-0.1%Si which had been solidified with V=1.00 mm/s, were examined both by TEM and x-ray methods. The results of this combined approach were surprising in that, whilst the TEM analysis of the extracted crystals revealed them to be predominantly Al_xFe as defined by the Young and Clyne lattice parameters, the x-ray trace taken from this extracted residue could not be indexed using the x-ray pattern for Al_xFe given in the open literature. Indeed, the results were so different that it is difficult to envisage how such a major discrepancy could arise.

The specimen for production of this "standard" was obtained by rolling a unidirectionally solidified rod of an alloy known to contain Al_xFe to x-ray transparency (100-150μm approximately). The x-ray pattern given by Young and Clyne was not, therefore, obtained under ideal conditions and could contain some degree of error arising from the extreme directionality of the x-ray specimen. However, such a large difference between the results of the present work and those published previously by Young and Clyne [1981] would suggest that a major error has occurred.

The closest match for the x-ray pattern taken from the extracted Al_xFe intermetallics, in terms of interplanar spacing, was found to be the Al_xFe pattern supplied by ALCOA [Granger 1993] as shown in Table 4.7 of the results. The match for reflected intensity was, however, very poor. No further attempt was made to index the pattern obtained from the extracted Al_xFe crystals during the course of this investigation.

It is apparent then that identification of Al_xFe by x-ray methods alone should be regarded as insecure and that positive identification of the phase should be made only after direct observation in the TEM. It is worth noting that, although Young and Clyne reported the standard x-ray pattern and discussed it in relation to their proposed crystal structure for Al_xFe, they used TEM methods exclusively in their analysis of the intermetallics in these dilute alloys.

5.5 Effects of compositional variation on phase stability in the quaternary system

5.5.1 The effect of compositional variation on phase stability

The results of investigations into intermetallic phase stability with respect to solidification cooling rate in Al-Fe-Si alloys are often interpreted using Si:Fe ratio[Liu and Dunlop 1986, Tezuka and Kamio 1992, Maggs *et al.* 1995]. This treatment of results has proved very useful in revealing trends in phase incidence, but it is evident that the absolute Si and Fe content of the alloys are more important in phase selection. Indeed high and low alloy content materials with the same Si:Fe ratio may exhibit different phase stability ranges under similar solidification conditions. This method of interpretation of results is discussed more fully in section 2.6.

In the quaternary system, however, no data are available in the open literature and as a result no trend in phase incidence with variation in alloy composition and solidification front velocity has yet been identified. In order that trends in phase incidence could be identified, the results for the quaternary alloys were arranged according to Si:Fe ratio with constant 0.75%Mg (Fig.5.7), Si:Mg ratio at a constant 0.5%Fe (Fig.5.8) and Fe:Mg ratio with constant 0.1%Si (Fig.5.9). No obvious trend in phase stability was highlighted in performing these analyses and, although it was possible that the compositions investigated were not sufficiently different to effect major changes in phase incidence, it was considered that taking the ratio of two elements in a quaternary system such as this would not necessarily show the underlying effects of composition on phase stability .

Changes in phase stability with composition in this series of alloys is largely a function of the actual Fe and Si content. The magnesium content of the alloy exerted a minor influence on phase stability which was evident only in the 0.75%Fe content alloys (Figs.5.10 and 5.11). In the low (0.5%) Mg alloy (Fig.5.10) $Al_{13}Fe_4$ is stabilised to 2.00 mm/s whilst $Al_{13}Fe_4$ is replaced by Al_6Fe at 2.00 mm/s in the 0.75%Mg alloy (Fig.5.11). Decreasing the Si content to 0.05% in the 0.75% Mg alloy (Fig.5.12) leads to the stabilisation of Al_mFe as the main constituent in this alloy destabilising Al_6Fe. In general,

however, the change in phase dominance from $Al_{13}Fe_4$ to Al_6Fe occurs at some undetermined velocity between 0.5 and 1.00 mm/s.

These changes in composition linked, as they are, to changes in the equilibrium solidification pathway might be expected to yield results of this type. It is interesting that the high Fe and low Si content alloys show changes in phase stability when compared with the main sequence of alloy compositions. These changes in phase stability are not, however, linked to a decrease in Si:Fe ratio. Instead some form of ternary interaction would appear to be influencing the overall phase stability. This would seem to be particularly true of the Al_mFe intermetallic phase which is stabilised at both low Si (0.05%) in the Al-0.5%Fe-Y%Si-0.75%Mg (Y= wt.% Si) alloys and at high Fe in the Al-X%Fe-0.1%Si-0.5%Mg (X = wt.% Fe) alloy series. The form of this interaction, which may define ranges of phase stability dependent upon absolute Fe, Si and Mg content is not yet well understood and would require extensive work to be determined fully. This is a possible area for further investigation.

5.5.2 Effect of compositional variation on intermetallic morphology

The morphology of $Al_{13}Fe_4$ in these quaternary alloys is very similar to that described in sections 5.3.2 and 5.3.3. Insufficient observations of this phase were made at each of the alloy compositions to facilitate an analysis of the effect of Fe, Si and Mg content on morphology and twinning behaviour. This is a possible area for further investigation as there is a distinct effect of alloy Fe and Si content on the range of stability of this phase.

The faulted morphology of Al_6Fe observed in the Al-0.25%Fe-0.1%Si-0.75%Mg alloy would also appear to warrant further investigation. A faulted form of this phase does not appear to have been reported previously. If another such crystal could be found a full crystallographic investigation would allow the nature of the incommensurate diffraction maxima on [110]* and the periodic {110} faults to be investigated more fully. However, only one such crystal was observed in the course of this work.

The presence of the α-AlFeSi phase in this same alloy composition was, again, considered to be relatively unimportant because of the low incidence of observation. It should also be noted that, whilst the SAD pattern measurements appear to fit the

monoclinic structure proposed by Hoier [1985] to a higher degree of accuracy than the rhombohedral superstructure of Liu and Dunlop [1988]. The observation that the extra spots became diffuse after prolonged exposure of the crystal to the incident electron beam, coupled with comments made in section 2.5.1 would, however, suggest that the phase observed in the present work was in fact α_R.

5.6 Summary

5.6.1 Cumulative Addition of Si, Mg and Cr to Al-0.5%Fe

Phase competition in this alloy series appears to be between only three constituents $Al_{13}Fe_4$, Al_xFe and Al_6Fe. The results of this investigation are notably simpler than those reported elsewhere. They also show a clear progression in phase incidence and exhibit a degree of consistency which is lacking in the available literature. It emerged that there was very little agreement between the results of previous experimental work and those obtained in the present program. This was particularly true of the ternary and quaternary alloy compositions where it was found that no two sets of experimental results, even those originating from the same source, showed significant levels of agreement.

As the alloy composition becomes more complex and the number of possible interactions increase it becomes more difficult to speculate on the role of an individual addition in altering phase stability. This proved to be particularly true of Cr, where although the low level addition caused a substantial change with respect to solidification front velocity it was not possible to isolate any specific effect or identify the mechanism by which this alteration in phase stability was attained. It is not known whether Cr would have this effect in isolation i.e. in Al-0.5%Fe-0.04%Cr or whether the effect of Cr is synergistic with the Si, Mg or both. This is an area where further investigation would be of great benefit.

5.6.2 Quaternary alloy composition

As discussed in section 5.5 the phase stability in the quaternary system appears to be governed by the Fe and Si contents of the alloys. In practice, however, it is likely that

tramp transition metal elements such as Cr, V , Mn and Ti which are present at trace levels in all commercial purity Al melts, will exert a significant influence on intermetallic phase selection.

Recent work [Maggs *et al.* 1995] presents evidence which questions whether macrosegregation of intermetallics is the most important factor in the formation of anodising defects such as the fir tree zone (FTZ) in commercial alloys. They showed that transition metal additions which did not lead to a change in relative phase stability could lead to a change in the oxidation response of the phases such that different regions containing different phases displayed similar etching responses.

The problem would, then, appear to be more complex than was previously thought and future investigations into the effect of tramp elements on intermetallic phase selection and FTZ formation should be conducted in the light of both their results and those of the present work..

6. CONCLUSIONS

1. Microstructure maps have been constructed showing the influence of solidification front velocity and alloy composition on second phase intermetallic formation and stability for both the cumulative alloy series (Al-0.5%Fe, Al-0.5%Fe-0.1%Si, Al-0.5%Fe-0.1%Si-0.75%Mg and Al-0.5%Fe-0.1%Si-0.75%Mg-0.04%Cr) and the quaternary alloy series Al-X%Fe-0.1%Si-Z%Mg (X = 0.25 to 0.75% : Z = 0.5% or 0.75%) and Al-0.5%Fe-Y%Si-0.75%Mg (Y = 0.05 to 0.15%) by Bridgman directional solidification over the velocity range 0.05 to 2.00mm/s in an imposed temperature gradient of 8 to 12K/mm.

2. Identification of the intermetallic constituents by x-ray diffractometry was achieved by extracting the second phase material from the α-Al matrix. Two methods were employed: HCl electrolytic extraction and the Butanol reflux method. The Butanol method was found to be the better of the two techniques, providing extracted material suitable for both x-ray and TEM analysis. These techniques were complemented by optical microscopy of the α-Al morphology and thin film TEM of *in-situ* second phase intermetallics.

3. Intermetallic phase competition was observed to be between $Al_{13}Fe_4$, Al_6Fe, Al_xFe and Al_mFe in all of the alloys investigated, although Al_mFe was observed infrequently.

4. The effect of cumulative additions of 0.1%Si, 0.75%Mg and 0.04%Cr to a base Al-0.5%Fe alloy composition was to increase sequentially the stability of $Al_{13}Fe_4$ with respect to solidification front velocity.

5. In the binary Al-0.5%Fe alloy composition. the $Al_{13}Fe_4$ phase was found to undergo a transition from faceted to non-faceted growth mode prior to displacement by Al_6Fe at a growth velocity between 0.1 and 0.5mm/s. This non-faceted growth morphology was observed to co-exist with the metastable Al_xFe phase. No such transition in growth mode was observed for $Al_{13}Fe_4$ in the presence of Si.

6. (100) twins and faults which were rarely found in $Al_{13}Fe_4$ crystals observed in the binary Al-0.5%Fe alloy were frequently observed in alloys containing Si. This increased (100) fault frequency in the presence of Si could have resulted from a decrease in the solid / liquid interfacial energy of (100). It was considered that these faults and twins on (100) increase the nucleation or growth temperature of the phase at increased solidification front velocity.

7. In the Al-0.5%Fe-0.1%Si alloy the phase which displaces $Al_{13}Fe_4$ as the dominant intermetallic at growth velocities in excess of 0.5mm/s was found to be Al_xFe. Upon incorporation of 0.75%Mg into the alloy composition Al_6Fe was found to be the dominant phase at growth velocities in excess of 0.5mm/s in the quaternary alloy composition and 1.00mm/s in the presence of 0.04%Cr.

8. In the presence of Mg, Al_6Fe shows a marked tendency toward faceted behaviour. Many of the Al_6Fe crystals observed in Mg-containing alloys exhibited {110} and {100} bounding planes, and could also exhibit a lath-like growth form. It was considered that these changes in growth morphology of Al_6Fe could account for the slight increase in the incidence of $Al_{13}Fe_4$ as a major phase with solidification front velocity in the presence of Mg by making the growth of Al_6Fe more difficult.

9. The change in the incidence of the $Al_{13}Fe_4$ phase, with respect to solidification front velocity, with Fe content in the alloy series Al-X%Fe-0.1%Si-Z%Mg (X = 0.25 to 0.75% : Z = 0.5 or 0.75%Mg) could be attributed to changes in the equilibrium solidification path. In general the transition in second phase dominance from $Al_{13}Fe_4$ to metastable intermetallic was found to occur between 0.5 and 1.0mm/s.

10. There was no readily discernible trend in the intermetallic phase type replacing $Al_{13}Fe_4$ in the quaternary alloys investigated. While, in general $Al_{13}Fe_4$ was displaced by Al_6Fe, Al_mFe was found to replace $Al_{13}Fe_4$ at a growth velocity in excess of 1.0mm/s in Al-0.5%Fe-0.05%Si-0.75%Mg and to be observed on only one further occasion as a minor phase in Al-0.75%Fe-0.1%Si-0.5%Mg at V=2.0mm/s, suggesting that some form of ternary interaction between Fe, Si and Mg was influencing the overall phase selection with respect to solidification front velocity.

11. The effect on the stability of $Al_{13}Fe_4$ with respect to solidification front velocity on the addition of 0.04%Cr to a base Al-0.5%Fe-0.1%Si-0.75%Mg alloy is in marked contrast to the subtle variations in phase selection effected by changes in Fe, Si and Mg content of these alloys. In the presence of Cr the maximum solidification growth velocity at which $Al_{13}Fe_4$ was observed as a major constituent was 1.0mm/s as compared with 0.5mm/s in the absence of Cr. This would suggest that impurities such as Cr are very influential in intermetallic phase selection in commercial alloy compositions. The mechanism by which Cr affects phase selection was not, however, elucidated.

12. Faulted Al_6Fe of the type observed as a minor phase in Al-0.25%Fe-0.1%Si-0.75%Mg after unidirectional solidification at 2.00mm/s has not been previously described in the open literature. This morphology displayed regular faults at intervals of ~2.0nm on {110} which is equivalent to a periodicity of 4 times that of the {110} interplanar spacing.

13. A minor phase was observed in Al-0.25%Fe-0.1%Si-0.75%Mg after unidirectional solidification at 2.00mm/s which gave SADP's that could be interpreted as arising from either α_T and α_R-AlFeSi. Although the lattice parameters given in the literature for α_T-AlFeSi appear to give a better fit with the SADP data, the morphology of the crystal and the observed disappearance of the super-lattice spots after prolonged exposure to the 100kV electron beam are associated in the literature with α_R-AlFeSi. This, coupled with the uncertainty surrounding the identification of α_T-AlFeSi, leads to the conclusion that the phase is more likely to be α_R-AlFeSi.

14. A phase was frequently observed which provided electron diffraction information consistent with the lattice parameters given by Young and Clyne [1981] for Al_xFe. The x-ray diffraction trace taken from extracted crystals of this phase, however, was found to be markedly different from that given by Young and Clyne for Al_xFe. The closest fit to the obtained x-ray pattern was found to be the Al_xFe pattern in use by ALCOA, although the match of reflected intensities between the pattern obtained in the present work and that of ALCOA was found to be poor.

15. The primary α-Al cell spacings of all of the alloys investigated displayed the relationship $\lambda_1 = K(G.V)^{-n}$ where n was approximately 0.5 and independent of alloy composition whilst the value of K showed some dependence on alloy composition. K was found to be 41.5 ± 3.4 $\mu m(K/s)^{1/2}$ for Al-0.5%Fe and approximately $80\mu m(K/s)^{1/2}$ for all 0.1%Si containing alloys, this value being largely unaltered by variation in Fe or Mg content or the presence of Cr. Increasing the Si content was not found to alter the spacing appreciably, however, a reduction of Si content from 0.1% to 0.05% was found to reduce the value of K to $55.6 \pm 4.2\mu m(K/s)^{1/2}$.

16. The magnitude of this increase in the α-Al cell spacing in the presence of 0.1%Si was predicted correctly, by use of an analytical model [Lu and Hunt 1995], if the activation energy for diffusion of Fe in Al was assumed to decrease by 14% in the presence of Si in accordance with the experimental data of Miki and Warlimont [1968].

7 FURTHER WORK

1. Investigate the effects of low level transition metal (TM) additions (e.g. Cr, Mn, Ni, V, Zr) on intermetallic phase selection in Al-0.5%Fe, Al-0.5%Fe-0.1%Si and Al-0.5%Fe-0.75%Mg grown by Bridgman unidirectional solidification under the same imposed growth conditions employed in the present work. This programme would need to employ compositional analysis in the TEM as well as the techniques employed in the present work.

2. This type of investigation could also be extended to encompass the effects of TM additions on intermetallic phase selection in more concentrated , eutectic or near eutectic alloys. This work could provide important information such as the λ-V and ΔT-V relationships for different morphologies of the αAl-$Al_{13}Fe_4$ and αAl-Al_6Fe eutectics (i.e. fibrous αAl-$Al_{13}Fe_4$, lath αAl-Al_6Fe) and also for the αAl-Al_xFe and αAl-Al_mFe eutectic structures. Such data would prove particularly useful in the modelling of competitive growth in this alloy system.

3. Because D.C.casting is the standard commercial route for processing compositions of this type, it is proposed that the compatability of phase selection results obtained by steady-state Bridgman unidirectional solidification with those obtained by suitable non steady-state simulation of D.C.casting should be investigated.

Appendix 1:

Origin of extra lines on exposed Guinier camera films

A1.1 Introduction

In the course of the x-ray investigation of alloy specimens by the Guinier focussing camera method, as described in section 3.4.1, a number of extra reflections were recorded on the resultant x-ray films. These extra reflections correspond to inter-planar spacings which are exactly twice those of the fundamental aluminium interplanar spacings. These were considered to arise from some form of second order diffraction effect in the camera itself. A series of experiments were therefore undertaken in order that the precise nature of the phenomenon could be determined.

A1.2 Background

When a quartz monochromator is set such that the $(10\bar{1}0)$ plane diffracts radiation of wavelength λ (in this case Cu-Kα λ = 0.15418 nm) there will also be diffraction by second order $(20\bar{2}0)$ and third order $(30\bar{3}0)$ planes etc. in the quartz crystal because of the non-zero structure factors of these planes. For monochromatic radiation these diffractions occur at higher angles than the first order and are not transmitted to the sample.

However, for a polychromatic beam the second and third order diffraction for half and third order etc. wavelengths occur at exactly the same angle as the first order since:

$$2\sin\theta = \frac{\lambda n}{d} \qquad \text{(A1.1)}$$

where n is an integer value corresponding to the order of diffraction, d is the interplanar spacing of the diffracting plane, θ the angle of incidence and λ the wavelength of incident radiation.

Thus the monochromator will transmit not only the characteristic Kα wavelength but fractions of this wavelength $\lambda/2$, $\lambda/3$ etc. provided, as is the case for quartz, the structure factor of these diffractions is significant.The intensity of the various components of the poly-chromatic radiationis governed by the structure factor of the diffracting plane in the quartz crystal. According to the JCPDS file No.5-0490, the relative intensities of the reflections from $(10\bar{1}0)$, $(20\bar{2}0)$ and $(30\bar{3}0)$ are 100, 7 and <1 respectively. Reflections from $(30\bar{3}0)$ are, therefore considered to be too weak to be of importance.

The resulting effect is that essentially two or three powder diffraction patterns are superimposed on the film in the Guinier camera. The main Kα pattern and subsidiary

patterns at lower angles for the half and third etc. wavelengths. This can cuase great difficulty in interpretation of weak diffractions from minor second phases. The effect may be exacerbated if the absorption coefficients of the specimen (Al) is significantly lower for the fractional wavelength beam components than for the full wavelength. The following experiment was carried out to verify that this is in fact the case.

A1.3 Experimental

Two continuous spectra or bremsstrahlung were taken for Cu-Kα in the following way: a Philips 1710 diffractometer was stripped back to the essential components i.e.source, divergence slits, convergence slits and detector, and the detector positioned so that the unmonochromated beam was directly incident upon it. The tube voltage was selected as 35kV to mimic that employed in the focussing camera work, whilst a minimum tube current was employed to cut down on the flux of x-rays incident upon the detector and hence minimise risk of damage. This low current does not affect any change in behaviour of the x-rays produced save for limiting the total flux.

A pulse height energy distribution was then taken for this wavelength of radiation. A number of sheets of aluminium foil, of total thickness 94μm, were then placed in the path of the beam in front of the detector and a further pulse height distribution trace taken. Comparison of the two traces allowed quantification of the beam attenuation by this thickness of aluminium for all wavelengths including the characteristic wavelength 0.15418nm and the half wavelength radiation, 0.07709 nm.

A1.4 Results

The relative intensities of the x-ray radiation at the characteristic Kα peak and also at Kα/2, with and without the aluminum shielding are given in Table A1.

Wavelength	I without Al foil (cps)	I with 94μm of Al foil (cps)	μ / ρ (cm^2/gm)
λ (0.15418nm)	10.32×10^4	2.94×10^4	49.5
λ/2 (0.07709nm)	6.4×10^3	4.00×10^3	18.5

Table A1: Intensity of x-rays incident on the detector with and without Al sheilding and the values of μ/ρ for Cu-Kα and Cu-Kα/2 in Al calculated from the attenuation of the x-ray beam.

A1.5 Discussion

The information taken from the continuous x-ray spectra was used to calculate mass absorbtion coefficients from λ and λ/2 radiation in aluminium. These were calculated using the equation:

$$I_x = I_o \exp\left[{}^{-\mu}/_{\rho}.(\rho x)\right] \qquad \text{(A1.2)}$$

Where I_x and I_o are the intensity of the beam after and before attenuation respectively and x ins the thickness of the material being penetrated.The value of the mass absorbtion coefficient, μ/ ρ, for pure Al found in Cullity [1978] irradiated by Cu-Kα is 50.23cm^2/gm which is in excellent agreement with the value of 49.5cm^2/gm found in this work, whilst that for λ/2 is much lower , the value of this being calculated as 18.5cm^2/gm.

To illustrate the significance of these results, consider the effect of these differences in μ/ρ on the attenuation of the λ and λ/2 components by 130 μm of aluminium, the average thickness of transmission x-ray specimens employed in the present work: only 17.6% of the incident full wavelength beam will be transmitted by this thickness of Al as compared with 52.2% of the half wavelength radiation.

The relative intensities of the incident full and half wavelength radiation is dramatically reduced from 100:7 to 4.8:1 when passing through this thickness of Al,meaning that the Al reflections in the second order are now only 5 times weaker than the first order reflections.The first and second order reflections will, therefore, display comparable intensities.

The real problem, however, is that the second order lines posess intensities easily comparable with those produced by the second phase particles found in Al-0.5%Fe and related alloys. This is made more important again by the fact that many of the d-spacings of these second phases are coincident with these second order lines (Table A2).

The Al lines obtained by the camera technique, in both the first and second order, are also quite diffuse because of the long exposure times employed. Significant film darkening caused by low angle white radiation is also apparent (short wavelength, high energy radiation is poorly attenuated by Al) and this darkening obscures much of the low angle diffraction information.

These factors, when considered together, indicate that the focussing camera technique is unsuited to long exposure x-ray analysis of Al-alloys and dilute alloys based on Al-Fe especially.

(hkl)	$N = h^2+k^2+l^2$	α-Al interplanar spacings (nm)	Half wavelength α-Al interplanar spacings (nm)	also corresponds to lines in these phases
(111)	3	0.2337	0.4674	α
(200)	4	0.2025	0.4040	α
(220)	8	0.1432	0.2863	Al_mFe/Al_6Fe
(311)	11	0.1221	0.2442	Al_6Fe/Al_mFe
(222)	12	0.1167	0.2337	Al_6Fe/Al_mFe
(400)	16	0.1012	0.2025	$Al_{13}Fe_4/\alpha/\beta$
(331)	19	0.0929	0.1858	Al_xFe
(420)	20	0.0905	0.1806	Al_mFe

Table A1.2: Examples of possible "clashes" between the extra Al lines and principal x-ray lines produced by interaction with second phase intermetallics. This list is by no means intended to be exhaustive.

CONCLUSIONS

1) Quartz is a poor choice of monochromating crystal because of the non-zero structure factor of the (2 0 $\bar{2}$ 0) and (3 0 $\bar{3}$ 0) crystallographic planes which leads to the production of poly-chromatic radiation.

2) Diffraction of Al by the incident poly-chromatic radiation produces extra lines which are stronger in comparison to the fundamental reflection than would be expected as a result of poor attenuation of the second order beam component by Al in comparison with the full wavelength component.

3) This technique, employing quartz as monochromating crystal, is unsuited to the long exposure x-ray investigation of Al-alloys.

Appendix 2:

Extraction of intermetallic particles from α-Al

A2.1 Introduction

For reasons outlined in Appendix 1, the Guinier focusing camera technique was found to be unsuitable for the analysis of the second phase intermetallics found in alloys of the type under investigation in the present work. It was noted that a number of techniques for the extraction of intermetallics and hence concentration of the constituents had been previously employed by researchers in this field. Concentration of the intermetallic phases was considered necessary to allow conventional x-ray analysis to be performed. After an extensive literature review the following techniques were identified as the most promising and the relative efficacy of these methods assessed experimentally.

A2.2 Oxine

This method was pioneered by Honda and Hirokawa [1972] in the NaOH containing, non-electrolytic form and later developed for use as an electrolyte by Skladniekiewitz and Tenzler [1988]. The solution of 20 wt.% methanolic benzoic acid, 5wt,% oxine (8-hydroxyquinoline, C_9H_7NO), 20 vol.% chloroform and 0.02wt% NaOH is not recommended for general laboratory use because of the carcinogenic and highly volatile nature of chloroform and uncertainty as to the nature of the by-product of the dissolution reaction. Thus, in spite of the apparent success of this technique in previous investigations it was not attempted in the present work.

A2.3 Caustic etch NaOH

Systematic investigation of the effects of immersion time on the dissolution of the α-Al matrix in these dilute alloys in aqueous 0.1M NaOH proved disappointing with most of the corrosive attack being in the early stages (< 15 mins) with the corrosion rate slowing considerably after this initial attack had occurred. The intermetallics also seemed to be dissolved in the weak alkali solution.

These observations are in accord with the results of Nisancioglu [1991] for 1xxx and 3xxx series alloys. Indeed it was suggested that caustic etching of the surface of these alloys could dramatically improve their corrosion resistance. This technique was therefore found to be unsuitable for use in second phase extraction in this case.

A2.4 Extraction using HCl as an electrolyte

This technique has proved particularly successful in the dissolution of eutectic matrices to leave primary intermetallic crystals in hyper-eutectic Al-alloys. It was first documented by Wakeman and Raynor [1947] who employed a solution of 7.5 vol.% conc. HCl in distilled water as an electrolyte to remove primary crystals from hyper-eutectic Al-Mn-Si alloys.

This procedure, with a 2.5 % HCl solution in place of the 7.5 % solution has proved to be a fairly successful method of extracting the second phase material in terms of yield. The 2.5 % solution was found to be the optimum with respect to yield and required dissolution time.

The extraction procedure employed was as follows:

i) The surface of the directionally solidified solidified rods was cleaned in conc.HCl and thoroughly washed in running water.

ii) The rod was then used as the anode in an electrolytic cell with a solution of 0.25 M HCl as the electrolyte and pure Ni as the cathode. The cell was operated at a potential difference of 3V (giving rise to a current of 0.1 A) until full dissolution of the matrix had occurred. This procedure took approximately 8 hours in total.

iii) The resultant solution was then filtered through a 0.5μm millipore teflon filter using a vacuum filtration unit. The residue was then rinsed through with 200ml of pure ethanol to remove unwanted by-products and allowed to dry on the filter.

This technique was, however, found to be erratic and inconsistent in respect of second phase yields and the use of this particular technique was discontinued.

A2.5 Butanol reflux method

This technique, first described by Simensen et al [1984], is currently the best method available for the extraction of second phase intermetallics from their matrices as pure butanol, in contrast to other extraction media, apparently does not attack the intermetallic phases. Chemical analysis of the reaction by products also allows the composition of the matrix to be determined accurately. The extraction procedure is long and involved and requires the use of specialised, dedicated, equipment. The procedure is currently performed commercially by two research agencies SINTEF in Norway who pioneered this extraction procedure and ALCAN, Banbury who license this technique from SINTEF. Because of the sensitive nature of this work the extraction of the second phase material was carried out at SINTEF in Oslo.

A2.6 Analysis of extracted residues

The residues obtained by both the HCl extraction procedure and the butanol reflux method were examined using a JEOL-6400 instrument operating with an accelerating voltage of 15kV at working distance of 15mm.

Fig.A2.1 shows the residue of the HCl extraction technique. Intermetallics are clearly present although only large crystals were observed in the samples analysed. These appear to be surrounded by a reaction by-product which exhibits a blocky morphology. It was considered, on the basis of both this evidence and that presented in Table 3.5, that the smaller intermetallic crystals had been dissolved either during the extraction process or subsequent to extraction when they were exposed to HCl for a period of several hours. It was considered that dissolution of the intermetallics by HCl was responsible for the relatively poor quality of the x-ray traces produced from samples of this residue.

In contrast Fig.A2.2, of the residue produced by the butanol reflux method, shows that this extraction procedure does not lead to the dissolution of smaller intermetallic crystals. Indeed, the crystal specimens produced by this extraction technique were of excellent quality and the material yielded was suitable for both x-ray investigation and examination in the TEM as the intermetallics were found to be transparent to 100 kV electrons.

A2.7 Conclusions

The results of the present work indicate that the butanol extraction procedure developed at SINTEF in Oslo is the best method available for second phase intermetallic extractions. Of the others reviewed many were considered potentially hazardous to health, only the HCl electrolytic method was considered safe enough to use on a daily basis.

This extraction procedure was, however, found to cause significant and unpredictable dissolution of the smaller intermetallics and use of this procedure was discontinued. In contrast the butanol extraction procedure was found to provide excellent intermetallic crystal specimens which were suitable for examination by both x-ray and TEM techniques.

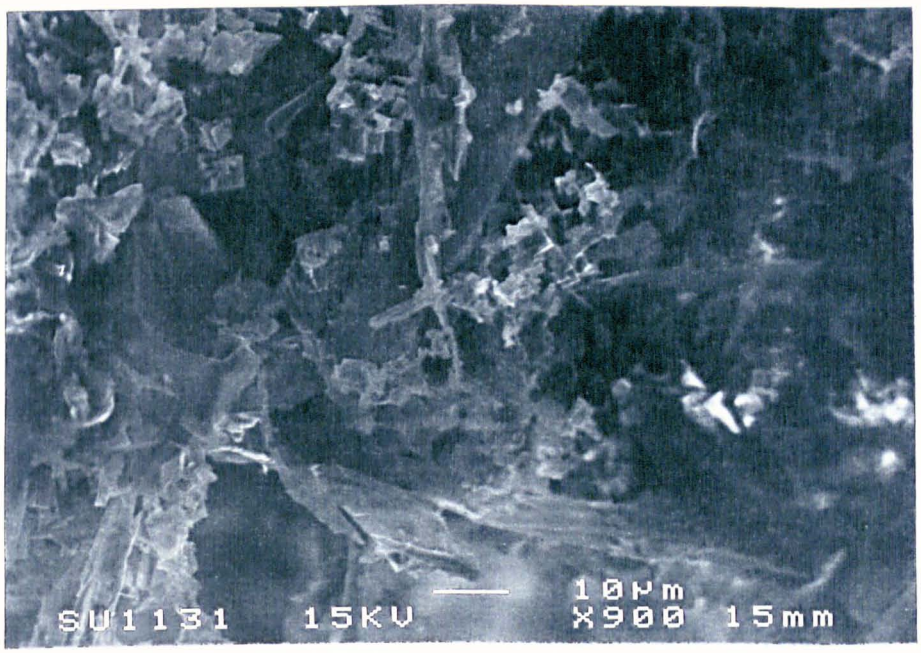

Fig.A2.1: Intermetallic crystals extracted from a sample of Al-0.5%Fe-0.1%Si-0.75%Mg which had been unidirectionally solidified at 0.5mm/s. Note that only large intermetallic crystals are present in in this case.

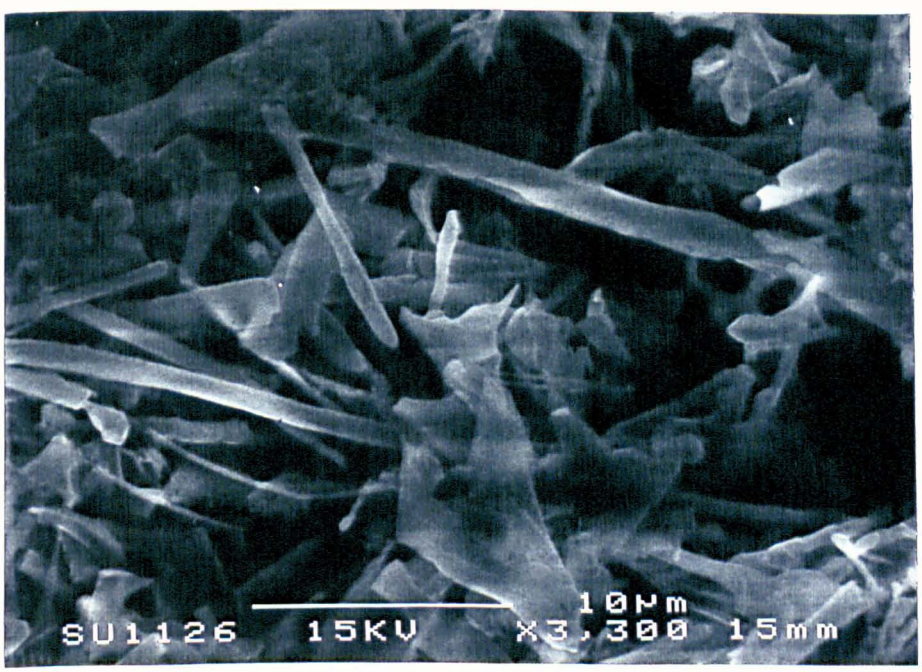

Fig.A2.2: Intermetallic crystals extracted from a sample of Al-0.5%Fe-0.1%Si-0.75%Mg which had been unidirectionally solidified at 0.5mm/s by the butanol reflux technique at SINTEF in Oslo. Both large and small intermetallic crystals are present in this sample.

Appendix 3:

Rotation corrections for the Philips 420-T

All SADP and TEM images in the present work were indexed with the negative emulsion side up, that is as is it is in the microscope, to preserve geometrical continuity in relating the specimen, its image and its diffraction pattern. This series of specimen rotation corrections is applicable only to SADP analysed in this way and is specific also to a camera length setting of 660mm on the Philips EM420-T operating at 100kV.

The sense of rotation is defined thus:

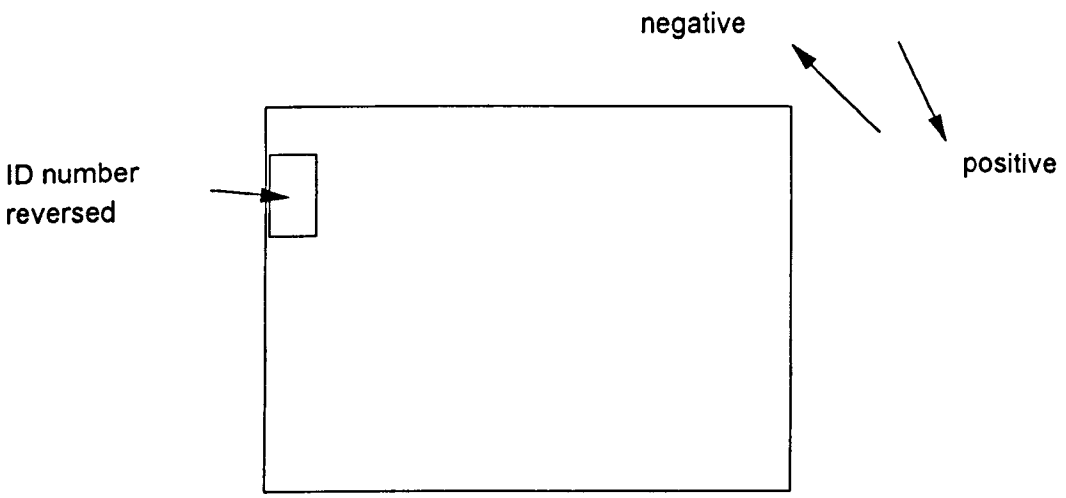

The rotation corrections appropriate to the range of magnifications employed in this work are given in the table below.

Magnification (x 10^{-3})	Angular rotation (degrees)
13.5	0
18.5	+4
24	+9
31	+25
37.5	-138
51	-135.5

APPENDIX 4:

Modelling of primary α-Al cell spacing

A 4.1 Introduction

Regression analysis of the primary α-Al spacing results in the present work showed the following relationship to hold in all cases:

$$\lambda_1 = K(G.V)^{-n} \qquad \text{(A4.1)}$$

where λ_1 is the primary spacing, G is the thermal gradient (taken to be 10K/mm), V is the growth velocity in mm/s., and K and n are constants. The value of n in the present work was found to be close to 0.5 in all cases, a value typical of primary cell spacings [Tiller 1991] and, therefore, to be independent of alloy composition. K, on the other hand, was found to be strongly dependent upon alloy composition. In particular, the presence of Si as an alloy constituent was observed to cause a marked coarsening of the α-Al spacings.

Si has been reported to cause a decrease in the activation energy required for Fe solute diffusion in Al [Miki and Warlimont 1968]. The effect of such a change in the activation energy required for Fe diffusion on primary spacing has been investigated by the use of an analytical microstructure model. The results of this analysis are presented here.

A 4.2 The Model

The expressions employed in the prediction of primary α-Al cell spacings in this analysis were taken from Lu and Hunt [1995]. These expressions were derived from an earlier numerical model [Lu and Hunt 1992], which has been shown to predict correctly the trends in primary spacing in a number of alloy and organic systems, by a series of curve fitting analyses and were intended to be used to gain an insight into the primary growth processes and to allow gauge the sensitivity of the predictions to physical properties of the system. These analytical expressions are given in the following sections.

A 4.2.1 Analytic expressions

In the original numerical model the undercooling was calculated as a function of dimensionless spacing, velocity and distribution coefficient. The numerical model also contains a term which accounts for the surface energy anisotropy of the growing cellular array, termed E_4. To derive a series of analytical expressions based on this model the value of E_4 was considered to be zero and the array spacing was calculated as a function of the dimensionless velocity, dimensionless gradient and equilibrium distribution coefficient. The dimensionless undercooling, $\Delta T' = \Delta T / \Delta T_o$ and spacing $\lambda' = \lambda \Delta T_o / (\Gamma k)$ are calculated as a function of these three parameters $G' = G\Gamma k / \Delta T_o^2$, $V' = V\Gamma k / (D\Delta T_o)$ and $k = C_s / C_L$ where $\Delta T_o = mC_o(k-1)/k$. The terms employed in these equations are defined in Table A4.1.

A 4.2.2 Cell undercoolings

The total growth undercooling is the sum of both the solutal and curvature under cooling terms. The curvature undercooling is much smaller than the solutal under cooling at low velocity and as such is not employed in the present calculation.

The following expression was found to fit the result of numerical model for cell undercooling:

$$\Delta T_s' = \frac{G'}{V'} + a + (1-a)V'^{0.45} - \frac{G'}{V'}(a(1-a)V'^{0.45}) \qquad \text{(A4.2)}$$

where a = 5.273E-3 + 0.5519k + 0.1865 k^2. In a more recent paper [Lu and Hunt 1996] this expression has be made dimensional by taking $a = k/2$ and changing the power of V' from 0.45 to 0.5. This gave:

$$\Delta T_s = \frac{GD}{V} + \left(1 - \frac{k}{2}\right)\left(\frac{V\Gamma mC_0(k-1)}{D}\right)^{0.5} + \left(\frac{mC_o(k-1)}{2}\right) \qquad \text{(A4.3)}$$

which is a result comparable to that given in an earlier intuitive model [Burden and Hunt 1974] for the total undercooling:

$$\Delta T_s = \frac{GD}{V} + 2^{1.5}\left(\frac{V\Gamma mC_0(k-1)}{D}\right)^{0.5} \qquad \text{(A4.4)}$$

A 4.2.3 Cell spacings

The analytical expression found to fit best the results of the numerical model was:

$$\lambda' = 4.09k^{-0.485}V'^{-0.29}(V' - G')^{-0.3}\Delta T_s'^{0.3}(1 - V')^{-1.4} \qquad \text{(A4.5)}$$

Away from the extreme limits i.e. the constitutional undercooling and absolute stability limits the expression may be reduced to :

$$\lambda' = 4.09k^{-0.485}V'^{-0.59} \qquad \text{(A4.6)}$$

When made dimensional [Lu and Hunt 1996] this expression becomes:

$$\lambda = 4.09k^{-0.335}\left(\frac{\Gamma}{mC_o(k-1)}\right)^{0.41}\left(\frac{D}{V}\right)^{0.59} \qquad \text{(A4.7)}$$

When it is considered that k, m, C_o, Γ and D are taken to be constants at low V may be represented as :

$$\lambda = K'.V^{-0.59} \qquad \text{(A4.8)}$$

which is remarkably similar in form to the experimentally determined relationship for primary cell spacing (equation A4.1).

A 4.3 Choice of thermophysical parameters

The thermophysical parameters employed in the modelling of the primary cell spacings in the present work are, in the main, the same as those employed by Lu *et al.*[1994] and these are presented in Table A4.2. The only exception is the value of the activation energy for Fe diffusion used in the determination of the primary α-Al spacing in the presence of Si. Miki and Warlimont [1968] determined that, in the presence of very low concentrations of Si (approximately 0.05%) the activation energy for Fe diffusion in the presence of Si was 14% lower than in Si-free alloys. In accordance with this observation the value of the activation energy for Fe diffusion employed in the calculation of primary spacing in the Al-0.5%Fe-0.1%Si alloy composition was taken to be 34,000J/mol. Following the recommendation of Kurz *et al.*[1992], the liquidus curves for the two

alloys were considered to be approximately equal. The terminal reaction temperature was assumed to be approximately 925K, giving a value of ΔT_o of 4.0K for both alloys.

A 4.4 Results and Discussion

The results of this analysis are shown in Fig.A4.1. It is clear that a change in the activation energy for diffusion of Fe in Al can give rise to a significant coarsening of the primary cell spacings. The predicted spacings for Al-0.5%Fe-0.1%Si are 1.8 times those calculated for the Al-0.5%Fe alloy which is exactly the magnitude observed experimentally. The measured values of the α-Al primary cell spacings were, however, found to be consistently three times larger than the spacings predicted by the model.

Lu and Hunt [1995]presented comparisons between the results of their numerical model and experimental results for primary cell and dendritic spacings in Al-0.34%Si-0.14%Mg [McCartney and Hunt 1981] (FigA4.2). The trend revealed was for experimentally determined cell spacings to lie at the upper extreme of the calculated array stability limit, in good agreement with the present results,whilst the experimental dendritic spacings were found to lie at the lower limit of the numerically modelled dendritic spacing range.

Power law regression analysis of the calculated λ_1 - V curves for Al-0.5%Fe and Al-0.5%Fe-0.1%Si reveals the following relationship between λ_1 and V:

$$\lambda_1 = K'.V^{-n} \qquad \text{(A4.9)}$$

where K′ is a constant and n is close to 0.5 in both cases (0.54 for Al-0.5%Fe and 0.56 for Al-0.5%Fe-0.1%Si). The power law regression of this calculated data is, therefore, very similar in form to equation A4.1.

In view of the many assumptions made in modelling the growth of the primary cell spacings for these alloys the agreement between the predicted and modelled results are remarkable and show that coarsening of the microstructural scale in the presence of Si can be attributed solely to a decrease in the activation energy for Fe diffusion in Al in the presence of Si of the scale reported by Miki and Warlimont[1968], although this cannot be considered the only contributing factor.

A4.5 Conclusions

1. The analytical expressions, given in section A4.2, allow both the effects of changes in thermophysical constants on hypothetical systems to be determined and, also to gain an insight into the possible mechanisms affecting microstructural development.
2. Although the Hunt and Lu analytical model predicts correctly the variation of primary cell spacings with respect to solidification front velocity, the cell spacings predicted by the model were smaller than those observed experimentally by a factor of three.
3. In the present case it is concluded that a decrease of 14% in the activation energy for Fe diffusion (from 40,000 to 34,000J/mol) was sufficient to induce a significant change in the scale of the primary cell spacings in α-Al.

Symbol	Definition
C_o	bulk alloy composition (wt.%)
C_S	equilibrium solid growth composition at growth temperature (wt.%)
C_L	equilibrium liquid growth composition at growth temperature (wt.%)
D	liquid solute diffusion coefficient (m^2/s)
D_o	Proportionality constant in $D = D_o \, exp \, [-Q/(RgT)]$ (m^2/s)
E_4	anisotropic surface energy parameter [Lu and Hunt 1992]
G	temperature gradient (K/m)
G'	$G\Gamma k / \Delta T_o^2$, dimensionless temperature gradient
Q	activation energy for diffusion
Rg	the gas constant (8.314 J/mol K)
T	temperature (K)
V	local growth velocity (m/s)
V'	$V\Gamma k / (D\Delta T_o)$, dimensionless velocity
k	C_s / C_L , equilibrium solute distribution coefficient
m	equilibrium liquidus slope (K/wt.%)
ΔT	interface undercooling (K)
$\Delta T'$	$\Delta T / \Delta T_o$, dimensionless undercooling
ΔT_o	$mC_o(k-1)/k$, the equilibrium alloy freezing range (K)
Γ	$\gamma / \Delta S$, the Gibbs-Thompson coefficient (Km)
λ	primary cell spacing (m)
λ'	$\lambda \Delta T_o / (\Gamma k)$, dimensionless cell spacing

Table A4.1: Nomenclature.

Alloy	D_o (m^2/s)	Q (J/mol)	Γ (Km)	ΔT_o (K)
Al-0.5%Fe	$2.95x10^{-7}$	40,000	$1x10^{-7}$	4[Φ]
Al-0.5%Fe-0.1%Si	$2.95x10^{-7}$	34,000	$1x10^{-7}$	4[Φ]

[Φ] Calculated based on : T_L = 933.6 - 7.29117C + $0.3067477C^2$ - $0.07033261C^3$ (C in at.%) = 929K ; and T_{Eu} ~ 925K.

k = 0.16792 - 1.5244x10-4 T = 0.02630 at 929K.

Table A4.2: Thermophysical parameters employed in the modelling of primary α-Al cell spacings.

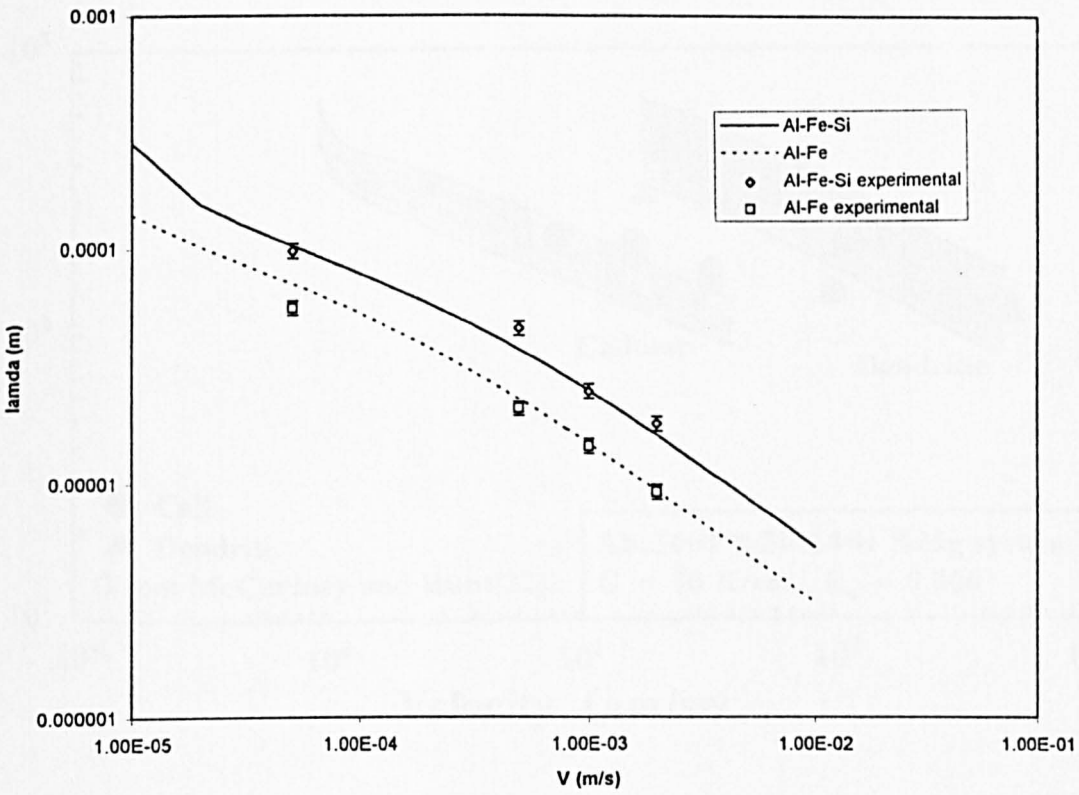

Fig.A4.1: Analytical predictions (lines) fitted to experimentally measured primary cell spacings for Al-0.5%Fe and Al-0.5%Fe-0.1%Si alloys. The actual spacings are 3 times greater than those predicted by the Analytical model, the magnitude of the effect of the presence of Si on cell spacing is, however, correctly predicted by use of the analytical expressions given by Lu and Hunt [1995].

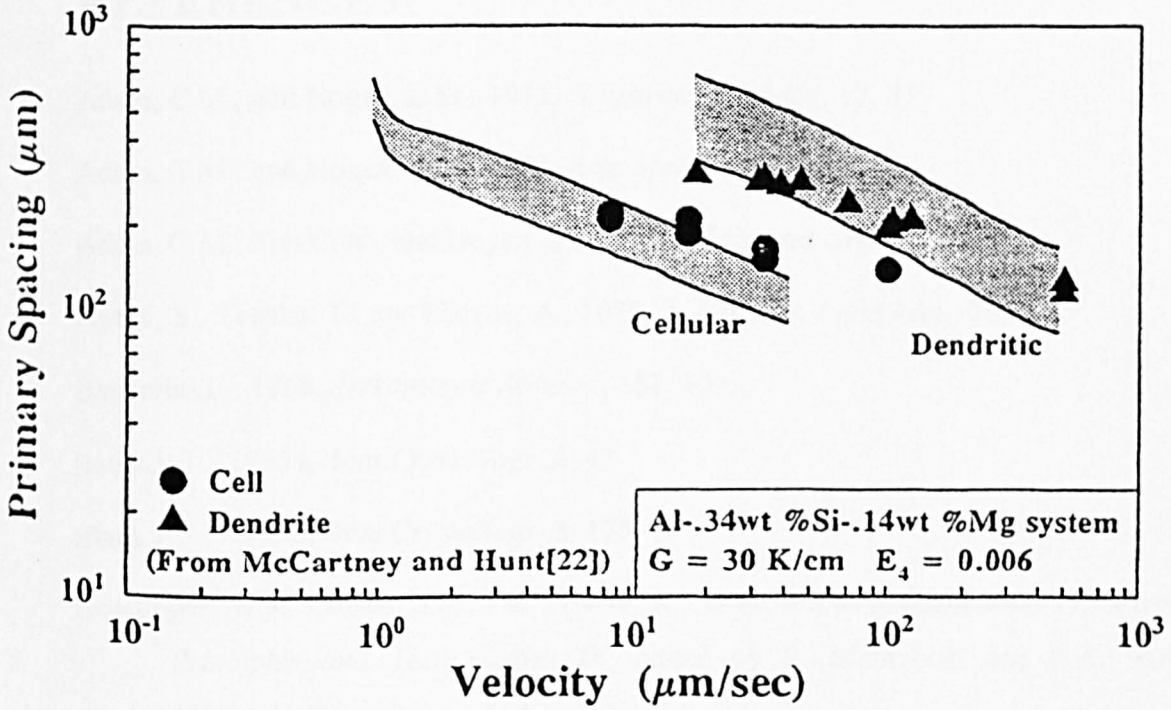

Fig.A4.2: Comparison of numerically modelled and experimentally determined λ_1 - V relationships for low velocity cells and dendrites. Note that the predicted cell spacings are generally lower than those determined experimentally. (from Lu and Hunt [1992], experimental data from McCartney and Hunt [1981])

REFERENCES

Adam, C.M., and Hogan, L.M., 1972, *J.Austral. Inst. Met.*, **17**, 81.

Adam, C.M., and Hogan, L.M., 1975, *Acta Metall.*, **23**, 345.

Adam, C.M., Tan,C.W., and Hogan, L.M.,1981, *J.Crystal Growth*, **51**, 525.

Asami, S., Tanaka, T., and Hideno, A., 1978, *J. Jap. Inst. Light Met.*, **28**, 321.

Backerud,L., 1968, *Jerkontorets Annaler*, **152**, 109.

Black,P.J., 1955a, *Acta Crystallogr.*,**8**, 43.

Black,P.J., 1955b, *Acta Crystallogr.*,**8**, 175.

Boettinger, W.J., Coriell, S.R., and Trivedi, R., 1988, *Rapid Solidification Processing: Principles and Technologies IV*, edited by R. Mehrabian and P.A. Parish (Claitor's: Baton Rouge,L.A), p.13.

Burden,M.H., and Hunt, J.D., 1974, *J.Crystal Growth*, **22**, 99.

Burden, M.H., and Jones, H., 1970, *Metallography*, **3**, 307.

Chattopadhyay, S., Lele, S., and Ramachandrarao, J., 1978, *J. Mater. Sci.*, **13**, 2730.

Clyne, T.W., 1981,Final Technical Report on Aluminium on Fonds', Project No.185, EPF-Lausanne.

Cochrane, R.F., Evans, P.V., and Greer, A., 1991, *Mater. Sci. Engg.*, **A133**, 803.

Cooper, M., 1967, *Acta Crrstallogr.*, **23**, 1106.

Cooper, M., and Robinson, K., 1966, *Acta Crystallogr.*, **20**, 614.

Cullity, B.D., 1978, Elements of X-Ray Diffraction (Addison Wesley).

Chandrasekeran, M., Lin, Y.P., Vincent, R., and Staniek, G., 1988, *Scripta Metall.*, **22**, 797.

Davies, H.A., Aucote, J., and Hull, J.B., 1974, *Scripta Metall.*, **8**, 1179.

Dix, E.H., 1925, *Proc. ASTM*, **25**,120.

Dons, A.L., 1984, *Z. Metallk.*, **75**, 170.

Dons, A.L., 1985, *Z. Metallk.*, **76**, 151.

Douglas, A.M.B., 1950, *Acta Crystallogr.*, **3**, 19.

Fang, Q., and Granger, D.A., 1991, Private communication.

Fisher, D.J., and Kurz, W., 1980, *Acta Metall.*, **28**, 777.

Flemings, M.C., 1974, Solidification Processing (McGraw-Hill).

Fontaine, A., and Guinier, A., 1975, *Phil.Mag.*, **31**, 839.

Fung, K.K., Yang, C.Y., Zhou, J.G., Zhan, W.S., and Shen, B.C., 1986, *Phys. Rev. Lett.*, **56**, 2060.

Fung, K.K., Zou, X.D., and Yang, C.Y., 1987, *Phil. Mag. Lett.*, **55**, 27.

Furrer, P., 1979, *Aluminium*, **70**, 699.

Genda, G., Yuyon, C., and Geing, A., 1987, *Proceedings of the Third International Conference on Solidification Processing*, Sheffield, England, September 1987, edited by J.Beech and H.Jones (London: The Institute of Metals), p.511.

Gilgien, P., Zryd, A., and Kurz, W., 1995, *Acta Metall.Mater.*, **43**, 3477.

Granger, D.A., 1990, Ph.D. Thesis, Brunel University.

Granger, D.A., 1992, Private communication.

Hillert, M., and Subba Rao, V., 1968, in *"The Solidification of Metals"*, Iron and Steel Institute Publication No. 110, 204.

Hirai, M., Sato, T., and Ohira, G., 1977, *J. Crystal Growth*, **38**, 340.

Hoier, R., cited by Dons, A.L., 1985, *Z. Metallk.*, **76**, 151.

Hollingsworth, E.H., Frank, G.R., Jr., and Willet, R.E., 1962, *Trans. TMS-AIME*, **224**, 188.

Honda, F., and Hirokawa, K., 1972, *Z. Anal. Chem.*, **262**, 170.

Hudd, R.C., and Calvert, L.D., 1953, *Acta Crystallogr.*, **15**, 441.

Hughes, I.R., and Jones, H., 1976, *J.Mater. Sci.*, **11**, 1781.

International Tables of Crystallography, Vol.II, 1959 (Birmingham: The Kynoch Press).

Jackson, K.A., 1957, Mechanism of growth. Liquid metals and solidification, *Am. Soc. Metals*, Cleveland, Ohio, 174.

Jackson, K.A., and Hunt, J.D., 1966, *Trans. TMS-AIME*, **236**, 1129.

Jacobs, M.H., Doggett,A.G., and Stowell, M.J., 1974, *J.Mater. Sci.*, **9**, 1631.

Jones, H., 1994, *Mater. Sci. Engg.*, **A179/A180**, 1.

Kim,D.H., and Cantor, B., 1994, *Phil. Mag. A*, **69**, 45.

Keong, P.G., Sames, J.A., Adam, C.M., and Sharp, R.M., 1977, in *"Solidification and Casting of Metals"* (London: The Metals Society), 110.

Kosuge, H., and Mizukami, I., 1975, *J.Jap. Inst.Light Met.*, **25**,48.

Kurz, W., and Trivedi, R., 1990, *Acta Metall. Mater.*, **38**, 1.

Kurz.W,1992, Brite Euram Project No. BREU-0065 C, Lausanne, September, 1992.

Langsrud,Y., 1990, *Key Engg. Mater.*, **44** and **45**, 95.

Liang, D., 1992, Ph.D. Thesis, University of Sheffield.

Liang, D., 1995, Private communication.

Liang, D., and Jones, H., 1992, *Z. Metallk.*, **83**, 4.

Liang, D., and Jones, H., 1993, *Scripta Metall. Mater.*, **28**, 7.

Liu, P, 1990, *Key Engg. Mater.*, **44** and **45**, 69.

Liu, P., and Dunlop, G.L., 1986, *Proceedings of the First International Conference on Aluminium Alloys: Their Physical and Mechanical Properties*, editors E.A.Starke Jr. and T.H. Sanders Jr., Charlottesville,Virginia, 1.

Liu, P., and Dunlop, G.L., 1988, *J. Mater. Sci.*, **23**, 1419.

Liu, P., Thorvaldsson, T., and Dunlop, G.L., 1986, *Matls. Sci. and Tech.*, **2**, 1009.

Louis, E., Mora, R., and Pastor, J., 1980, *Met. Sci.*, **14**, 591.

Lu, S.Z. and Hunt, J.D., 1992, *J. Crystal Growth*, **123**, 17.

Lu, S.Z., and Hunt, J.D., 1995, *Modelling of Casting, Welding and Solidification Processes VII*, edited by M.Cross and J.Campbell, (The Metals, Minerals and Materials Society).

Lu, S.Z., and Hunt, J.D., 1996, *Mater. Trans. A*, **27A**, 611.

Lu, S.Z., Hunt, J.D, Gilgien, P., and Kurz, W., 1994, *Acta Metall. Mater.*, **42**, 1653.

M°Cartney, D.G., and Hunt, J.D., 1981, *Acta Metall.*, **29**, 1851.

Miki, I., Kosuge, H., and Nagahama, K., 1975, *J. Jap. Inst. Light Met.*, **25**, 1.

Miki, I., and Warlimont, H., 1968, *Z. Metallk.*, **56**, 254.

Mondolfo, L.F., 1976, Aluminium Alloys: Structure and Properties (London: Butterworths).

Morris, L.R., 1979, in *" Solidification and Casting of Metals"* (London: The Metals Society) 218.

Murray, J.L., 1983, *Alloy Phase Diagrams*, Materials Research Symposium on Proceedings, Vol.19 (Boston, Massachusetts: Materials Research Society), 249.

Maggs, S.J., Cochrane, R.F., Flood, S.C., and Evans, P.V.,1995, TMS Annual Meeting, Las Vegas, Nevada, February 1995.

Nisancioglu, K., 1991, *Proceedings of International Conference on Recent Advances in the Science and Engineering of Light Metals*, edited by K. Hirano, H.Oikawa and K.Ikeda, Tokyo, Japan, p.359.

Ogilvy, J.W., 1981, Ph.D. Thesis, University of Sheffield.

Philips, H.W.L., 1976, Annoted Equilibrium Phase Diagrams of some Aluminium Alloy Systems (London: The Institute of Metals).

Phragmen, G., 1958, *J.Inst.Met.*, **77**, 498.

Porter, D.A., and Westengen, H., 1981, in *"Quantitative Micro-Analysis with High Spacial Resolution"* (London: The Metals Society), 94.

Raynor, G.V., and Wakeman, D.W., 1947, *Proceedings of the Royal Society of London*, **190A**, 82.

Rivlin, V.G., and Raynor, G.V., 1981, *Int. Met. Rev.*, **3**, 133.

Robinson, K., and Black, P.J., 1953, *Phil. Mag.*,**44**, 1392.

Reiso, O., Ryum, N., and Strid, J., 1994, *Met. Trans. A*, **24A**, 2629.

Saunders, N., and Tsakiropoulos, P., 1988, *Mater. Sci. Technol.*, **5**, 609.

Sigworth, G.K., 1996, *Scripta. Mater.*, **34**, 919.

Simensen, C.J., Fartum, P., and Andersen, A., 1984, *Freznius Z. Anal. Chem.*, **319**, 286.

Simensen, C.J., and Vellasamy, R., 1977, *Z. Metallk.*, **68**, 428.

Skinner, D.J., Bye, R.L., Raybould, D., and Brown, A.M., 1986, *Scripta Met.*, **20**, 867.

Skjerpe, P., 1987, *Met. Trans. A*, **18A**, 189.

Skjerpe, P., 1988, *Acta Crystallogr. B*, **44B**, 486.

Skjerpe, P., Gjonnes, J., and Langsrud, Y., 1987, *Ultramicroscopy*, **22**, 239.

Skladniekewitz, S., and Tenzler, U., 1988, *Neue Hutte*, **3**, 178.

Tezuka, H., and Kamio, A., 1992, in *Proceedings of the Third International Conference on Aluminium Alloys*, edited by L.Arnberg, O.Lohne, E.Nes and N.Ryum, Trondheim, Norway, (Aedermansdorf: Transtech) 117.

Tiller, W.A., 1968, Recent Research on Cast Iron , (New York: Gordon and Breach).

Tiller, W.A., 1991, The Science of Crystallisation: Macroscopic Phenomena and Defect Generation (Cambridge: Cambridge University Press).

Turmezey, T., 1984, in *Proceedings 8th European Congress on Electron Microscopy*, edited by A.Csanady, P.Rohlicch and D.Szabo, Budapest, Hungary, 741.

Trung, N.A., Takehashi,.T., Kamio, A., and Kojima, Y., 1973, *J.Jap. Inst. Light Met.*, **23**, 501.

Walford, L.K., 1965, *Acta Crystallogr.*, **18**, 287.

Westengen, H., 1982, *Z. Metallk.*, **73**, 360.

Young, R.M.K., and Clyne, T.W., 1981, *Scr. Metall.*, **15**, 1211.

Phase	Bravais Lattice	Lattice parameters (nm)	Density (g/cm^3)	References
Al_3Fe $Al_{13}Fe_4$	C-centred monoclinic C2/m	a = 1.549 b = 0.808 c = 1.245 β = 107.75°	3.8	Black [1955] Hudd and Calvert [1953]
Al_mFe m=4-4.4	body centred tetragonal I4mm or I4/mmm	a = 0.884 c = 2.160		Miki *et al.*[1975] Skjerpe [1987]
Al_xFe (1) x = 5-5.8	Monoclinic (?)	a = 2.160 b = 0.930 c = 0.905 β = 94°		Young and Clyne [1981]
Al_xFe (2) x = 5-5.8	C-centred orthorhombic	a = 0.6 b = 0.7 c = 0.47		Skjerpe [1987]
Al_6Fe	C-centred orthorhombic Ccmm or Ccm2	a = 0.649 b = 0.744 c = 0.879	3.45	Hollingworth *et.al* [1962] Walford [1965]
Al_9Fe_2	monoclinic $P2_1/a$	a = 0.890 b = 0.635 c = 0.632 β = 93.4°		Simensen and Vellasamy [1977]
Al_pFe	cubic bcc	a = 1.03		Liu and Dunlop [1986]
Al_7Fe	cubic fcc	a = 0.77		Fontaine and Guinier [1975]
Al_2Fe	diamond cubic/ CaF_2 prototype	a = 0.585		Jacobs et al. [1974]

Table 2.1: Crystallographic data for phases reported as forming in binary Al-Fe alloys.

Phase	stoichiometric formula	Bravais lattice	Lattice parameters (nm)	References
α-AlFeSi	$Al_{12}Fe_3Si$ $Al_{15}Fe_3Si$	primitive cubic Pm3 bcc Im3	a = 1.252 a = 1.256	Robinson and Black[1953] Cooper and Robinson [1966] Cooper [1967]
α'-AlFeSi	$Al_{11.8}Fe_3Si_{1.7}$- $Al_{12}Fe_3Si_2$	hexagonal $P6_3/mmc$	a = 1.23 c = 2.62	Rivlin and Raynor [1981] Robinson and Black [1953]
α_v-AlFeSi	$Al_9Fe_2Si_2$	monoclinic $P2_1/a$	a = 0.869 b = 0.635 c = 0.632 β = 93.4°	Dons [1985]] Skjerpe *et al.* [1988]
α''-AlFeSi q_1-AlFeSi		c-centred orthorhombic Cmmm	a = 1.27 b = 3.62 c = 1.27	Westengen [1982] Liu and Dunlop [1986] Liu [1990]
α_T-AlFeSi		c-centred monoclinic	a = 2.795 b = 3.062 c = 2.073 β = 97.74°	Hoier [1985] Skjerpe [1987]
α_R-AlFeSi		rhombohedral superlattice $R\bar{3}$	a_{sup} = 3.076 c_{sup} = 3.623	Liu and Dunlop [1988]
q_2-AlFeSi		monoclinic Pm	a = 1.250 b = 1.230 c = 1.970 β = 109°	Liu and Dunlop [1986] Liu [1990]
β-AlFeSi	$Al_9Fe_2Si_2$	monoclinic	a = 0.612 b = 0.612 c = 4.16 β = 91.0°	Phragmen [1958] Rivlin and Raynor [1981]
β'-AlFeSi		monoclinic	a = 0.890 b = 0.490 c = 4.16 β = 92.0°	Westengen [1982]

Table 2.2: Crystallographic data for ternary intermetallic phases reported as forming in Al-rich, Al-Fe-Si alloys.

	Composition wt% (± 0.02)				
Alloy	Fe	Si	Mg	Cr	Impurities
Al-Fe	2.27	0.05	-	-	≤0.02
Al-Si	-	12.4	-	-	≤0.02
Al-Mg	-	0.05	6.23	-	≤0.02
Al-Cr	-	0.10	-	27.20	≤0.02

Table 3.1: Results of ICP analysis of master alloys used

Nominal Alloy Composition (wt.%)				Actual Composition (±0.02%wt.%)			
Fe	Si	Mg	Cr	Fe	Si	Mg	Cr
0.5	0.1	-	-	0.50	0.10	-	-
0.5	0.10	0.75	-	0.47	0.11	0.77	-
0.25	0.10	0.75	-	0.25	0.11	0.78	-
0.75	0.10	0.75	-	0.73	0.11	0.77	-
0.50	0.05	0.75	-	0.47	0.05	0.74	-
0.50	0.15	0.75	-	0.49	0.16	0.75	-
0.25	0.10	0.50	-	0.52	0.10	0.53	-
0.50	0.10	0.50	-	0.26	0.11	0.50	-
0.75	0.10	0.50	-	0.75	0.11	0.48	-
0.50	-	-	-	0.50	-	-	-
0.50	0.10	0.75	0.04	0.50	0.09	0.72	0.04

Table 3.2: Comparison of nominal and actual dilute experimental alloy compositions.

Alloy composition	Growth velocity ,V (mm/s)	Measured temperature gradient, G (K/mm) ± 1
Al-0.5%Fe-0.1%Si-0.75%Mg	0.05	8
Al-0.5%Fe	0.05	11
Al-0.5%Fe-0.05%Si-0.75%Mg	0.10	12
Al-0.25%Fe-0.1%Si-0.75%Mg	0.10	9
Al-0.25%Fe-0.1%Si-0.5%Mg	0.50	11
Al-0.75%Fe-0.1%Si-0.75%Mg	0.50	10
A1-0.5%Fe-0.1%Si	1.00	8
Al-0.25%Fe-0.1%Si-0.5%Mg	1.00	11
Al-0.5%Fe-0.15%Si-0.75%Mg	2.00	12
Al-0.75%Mg-0.1%Si-0.5%Mg	2.00	10

Table 3.3: Experimentally measured temperature gradients at the solid-liquid interface during Bridgman unidirectional solidification.

Step		Media	Force (N)	Lubrcant	Time
Grinding	i)	#500 SiC	150	water	until plane
	ii)	#1200 SiC	200	water	30 secs
Polishing	i)	9 μm diamond	200	DP-blue	6 minutes
	ii)	6 μm diamond	15	DP-blue	6 minutes
	iii)	3 μm diamond	10	DP-red	4 minutes
Finishing		0.05 colloidal SiO_2	hand ,light pressure	water	4 minutes

Table 3.4 : Struers Abramin polishing schedule used in the preparation of specimens for optical metallography.

Alloy dissolved in electrolyte	Growth velocity of sample (mm/s)	initial weight of sample (g)	final undissolved weight of sample (g)	Weight of dissolved material (mg)	Fe content in 50 ml of electrolyte (mg)	Proportion of Fe in original sample lost to electrolyte
Al-0.5%Fe-0.1%Si-0.75%Mg	0.05	0.91	0.54	1.55	1.55	0.88
	1.00	0.91	0.43	3.11	2.59	0.84
Al-0.25%Fe-0.1%Si-0.75%Mg	0.05	0.84	0.51	1.26	0.63	0.50
	0.10	0.95	0.59	0.90	0.66	0.73
Al-0.5%Fe-0.05%Si-0.75%Mg	0.10	1.10	0.65	2.12	0.22	0.10
	0.50	0.88	0.37	2.40	0.23	0.09
Al-0.75%Fe-0.1%Si-0.5%Fe	0.10	0.93	0.52	3.08	1.03	0.34
	2.00	1.15	0.52	4.73	0.95	0.27

Table 3.5: Fe content of 50ml of HCl solutions after use in the electrolytic extraction of second phase intermetallics from the α-Al matrix over a period of typically 8 hours . The erratic nature of the procedure is immediately obvious from these results.

d (nm)	I	hkl	d (nm)	I	hkl
0.4064	29	2 0 2	0.2101	75	6 2 0
0.4040	35	$\bar{2}$ 0 3,0 2 0	0.2095	100	$\bar{6}$ 2 3,2 0 5
0.3962	40	0 0 3	0.2078	38	$\bar{2}$ 0 6,$\bar{7}$ 1 3
0.3689	28	4 0 0	0.2062	26	6 0 2
0.3674	32	$\bar{4}$ 0 2	0.2049	85	0 2 5,$\bar{6}$ 0 5
0.3545	53	2 2 0,$\bar{2}$ 2 1	0.2041	83	4 2 3,7 1 0
0.3342	28	0 2 2	0.2031	62	$\bar{4}$ 2 5
0.3268	30	2 2 1,$\bar{2}$ 2 2	0.2021	62	0 4 0
0.2261	17	$\bar{1}$ 3 3	0.2015	46	$\bar{5}$ 3 2,5 1 3
0.2161	10	1 1 5, $\bar{6}$ 2 2	0.19898	16	5 3 0
0.2130	10	$\bar{5}$ 1 5,$\bar{7}$ 1 2	0.1936	13	$\bar{8}$ 0 2

Table 3.6: Strong x-ray lines of monoclinic $Al_{13}Fe_4$ as given in JCPDS file 29-42.

d_{calc} (nm)	$I_{experimental}$	hkl	d_{calc} (nm)	$I_{experimental}$	hkl
0.4880	50	1 1 0	0.2239	70	1 3 1
0.4390	20	0 0 2	0.2195	35	0 0 4
0.4625	20	1 1 1	0.2133	100	2 2 2
0.3425	10	0 2 1	0.2070	50	3 1 0
0.3263	20	1 1 2	0.2048	95	1 3 2
0.3231	15	2 0 0	0.2014	*	3 1 1
0.2838	10	0 2 2	0.2002	20	1 1 4
0.2603	20	2 0 2	0.1890	10	0 2 4
0.2351	*	2 2 1	0.1872	10	3 1 2
0.2315	*	1 3 0	0.1820	10	0 4 1
0.2300	*	0 2 3			

Table 3.7: Major x-ray peaks for orthorhombic Al_6Fe, calculated by Jones [private communication] from the lattice parameters given by Walford [1965] and indexed according to the indices given in JCPDS file 6-0665 for the isomorphous phase Al_6Mn. The intensities given are those which were observed experimentally by Jones.
(* indicates that this line was masked experimentally by an α-Al peak).

d (nm)	I	h k l	d (nm)	I	h k l
0.624		1 1 0	0.221	20	4 0 0
0.440	75	2 0 0	0.215	20	?
0.406		1 1 4	0.214	100	3 0 7
0.346	75	2 1 3	0.208	90	3 3 0
0.242		2 1 7	0.205	100	4 1 3

Table 3.8: Strong x-ray lines from tetragonal Al_mFe. This list was compiled by indexing the x-ray pattern given by Asami, Tanaka and Hideno [1978].

d (nm)	I	h k l	d (nm)	I	h k l
0.4037	weak	4 1 1	0.1936	v.strong	$\overline{1}\overline{1}$ 1 0
0.3864	strong	3 2 0	0.1913	medium	1 1 1 0
0.3682	v.strong	$\overline{5}$ 1 1	0.1849	v.weak	1 1 1 1
0.3252	medium	6 0 1	0.1589	weak	1 3 1 1
0.2569	medium	7 2 0	0.1474	strong	9 5 0
0.2450	medium	8 1 1	0.1292	strong	12 5 0
0.2058	strong	1 0 0 1			

Table 3.9: Al_xFe x-ray diffraction pattern determined by Furrer and indexed by Clyne [1981] in accordance with the monoclinic crystal structure proposed for this phase.

d (nm)	I / I_o	d (nm)	I / I_o
6.30	2	1.86	5
5.40	2	1.70	5
3.99	40	1.60	2
3.80	5	1.52	2
3.72	5	1.485	5
3.13	40	1.415	5
3.07	10	1.395	40
2.435	20	1.36	5
2.425	50	1.305	2
2.255	25	1.30	25
2.23	15	1.26	5
2.11	20	1.24	2
2.085	5	1.223	15
1.99	5	1.195	40
1.965	100	1.125	15
1.885	2		

Table 3.10: X-ray pattern for Al_xFe supplied by ALCOA [Granger 1992].

d (nm)	I	h k l	d (nm)	I	h k l
0.528	10	0 2 1	0.233	30	1 4 1
0.497	10	0 2 2	0.2176	50	0 4 7
0.457	10	0 2 3	0.2142	40	1 4 5
0.400	30	1 2 1	0.2110	50	0 5 2
0.355	20	0 3 1	0.2058	100	1 4 6
0.344	20	1 2 4	0.2032	20	2 4 0
0.330	10	0 3 3	0.1981	30	2 4 3
0.321	20	1 2 5	0.1881	30	?

Table 3.11: Strong x-ray lines of the ternary equilibrium hexagonal phase α′-AlFeSi as given in JCPDS file 20-30.

d (nm)	$I_{experimental}$	h k l	d (nm)	$I_{experimental}$	h k l
0.4462	15	2 2 0	0.2302	20	5 2 1
0.3985	43	3 1 0	0.2163	74	4 3 3
0.3639	13	2 2 2	0.2099	43	4 4 2
0.3372	13	3 2 1	0.2046	100	5 3 2
0.2474	20	5 1 0	0.1995	17	6 2 0

Table 3.12: Major x-ray reflections of the bcc α-AlFeSi phase. This trace was obtained experimentally during the course of this work by indexing x-ray data taken from a sample of AA8009 sheet known to contain a distribution of randomly oriented α-phase particles which contained substituted V [Courtesy of D.Wilkes].

Alloy	K ($\mu m(K/s)^n$)	| error |	n	| error |
Al-0.5%Fe	41.49	3.4	0.479	0.030
Al-0.5%Fe-0.1%Si	76.74	4.0	0.462	0.015
Al-0.5%Fe-0.1%Si-0.5%Mg	74.35	3.6	0.457	0.020
Al-0.5%Fe-0.1%Si-0.75%Mg	81.2	4.6	0.510	0.025
Al-0.5%Fe-0.1%Si-0.75%Mg-0.04%Cr	76.2	3.7	0.540	0.016

Table 4.1: Experimentally obtained values of the parameters K and n in the equation $\lambda_1 = K.\dot{T}_s^{-n}$ for the series of alloys Al-0.5%Fe, Al-0.5%Fe-0.1%Si, Al-0.5%Fe-0.1%Si-0.5%Mg, Al-0.5%Fe-0.1%Si-0.75%Mg and Al-0.5%Fe-0.1%Si-0.75%Mg-0.04%Cr.

Alloy	$K(\mu m(K/s)^n)$	| error |	n	| error |
Al-0.25 Fe-0.1 Si-0.5 Mg	83.77	2.5	0.53	0.030
Al-0.5 Fe-0.1 Si-0.5 Mg	74.35	3.6	0.46	0.020
Al-0.75 Fe-0.1 Si-0.5 Mg	72.09	3.2	0.45	0.020
Al-0.25 Fe-0.1 Si-0.75 Mg	82.72	3.6	0.51	0.020
Al-0.5 Fe-0.1 Si-0.75 Mg	81.19	4.6	0.51	0.025
Al-0.75 Fe-0.1 Si-0.75 Mg	80.55	1.5	0.61	0.040
Al-0.5 Fe-0.05 Si-0.75 Mg	55.61	4.2	0.47	0.020
Al-0.5 Fe-0.15 Si-0.75 Mg	90.5	2.3	0.47	0.030

Table 4.2: Experimentally obtained values of the parameters K and n in the equation $\lambda_1 = K.\dot{T}_s^{-n}$ for the quaternary Al-Fe-Si-Mg alloy compositions.

Foil number	$Al_{13}Fe_4$	Al_xFe	Al_6Fe	Al_mFe	α-AlFeSi
1	3	2	-	-	-
2	2	3	-	-	-
3	2	2	-	-	-

Table 4.3: Results of selected area diffraction analysis of intermetallic crystals found in three thin foils taken from an Al-0.5%Fe alloy specimen which had been unidirectionally solidified at 0.10mm/s.

Foil number	$Al_{13}Fe_4$	Al_xFe	Al_6Fe	Al_mFe	α-AlFeSi
1	-	-	4	-	-
2	-	-	5	-	-

Table 4.4: Results of selected area diffraction analysis of intermetallic crystals found in two thin foils taken from an Al-0.5%Fe alloy specimen which had been unidirectionally solidified at 2.00mm/s.

Foil number	$Al_{13}Fe_4$	Al_xFe	Al_6Fe	Al_mFe	α-AlFeSi
1	5	-	-	-	-
2	4	-	-	-	-

Table 4.5: Results of selected area diffraction analysis of intermetallic crystals found in two thin foils taken from an Al-0.5%Fe-0.1%Si alloy specimen which had been unidirectionally solidified at 0.10mm/s.

Grid number	$Al_{13}Fe_4$	Al_xFe	Al_6Fe	Al_mFe	α-AlFeSi
1	2	8	-	-	-

Table 4.6: Results of selected area diffraction analysis of intermetallic crystals extracted, by the butanol method, from an Al-0.5%Fe-0.1%Si alloy specimen which had been unidirectionally solidified at 1.00mm/s.

ALCOA Al_xFe Pattern		Pattern obtained for "Al_xFe" residue	
d (nm)	I	d (nm)	I
6.30	2	6.246	3
5.40	2		
3.99	40	3.966	33
3.80	5		
3.72	5	3.71	30
3.13	40	3.14	4
3.07	10		
2.435	20	2.441	20
2.425	50	2.416	17
2.255	25	2.273	9
2.23	15	2.231	13
2.11	20	2.116	91
2.085	5	2.085	7
1.99	5	1.992	8
1.965	100	1.972	28
1.885	2	1.884	13
1.52	2	1.526	5
1.395	40	1.396	5
1.305	2	1.306	36
1.30	25		

Table 4.7 : Comparison of the pattern obtained by x-ray analysis of butanol extracted residue which had been determined by TEM analysis to be Al_xFe as defined by Clyne [1981] with the standard Al_xFe pattern supplied by ALCOA. This provided the closest match to the obtained pattern in terms of the number of coincident groups and interplanar spacings,however, the level of matching in the reflected intensity distribution was relatively poor.

Selected area diffraction spot ratio r_1/r_n				Angle between spots θ (1,n)			
Ratio	Experimental	Calculated	$\|\Delta\|$	Angle	Experimental	Calculated	$\|\Delta\|$
r_1/r_2	0.7175	0.700	0.0175	θ(1,2)	135	134.15	0.85
r_1/r_3	1.00	1.023	0.023	θ(1,3)	90	90.5	0.5
r_1/r_4	0.7175	0.7130	0.0135	θ(1,4)	46	45.85	0.15

a)

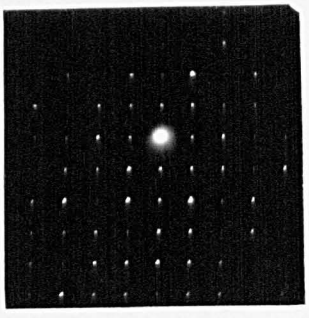

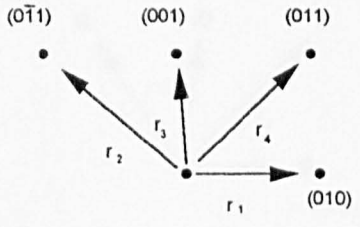

b)

Table 4.8 : a) Comparison of experimentally obtained values of selected area diffraction spot ratio and interplanar angles with those calculated for principal spots in [$\bar{1}$00] Al_xFe. The calculations are based on the monoclinic lattice parameters proposed by Clyne [1981].

b) Schematic representation of [$\bar{1}$00] Al_xFe giving the miller indices of the planes represented as r_1 to r_4 and the corresponding [$\bar{1}$00] SADP.

Selected area diffraction spot ratio r_1/r_n				Angle between spots θ (1,n)			
Ratio	Experimental	Calculated	$\|\Delta\|$	Angle	Experimental	Calculated	$\|\Delta\|$
r_1/r_2	0.7369	0.7586	0.0217	θ(1,2)	130	129.76	0.241
r_1/r_3	0.6552	0.6650	0.0098	θ(1,3)	82.0	79.48	2.52
r_1/r_4	0.9560	1.003	0.0470	θ(1,4)	40.0	38.28	1.72

a)

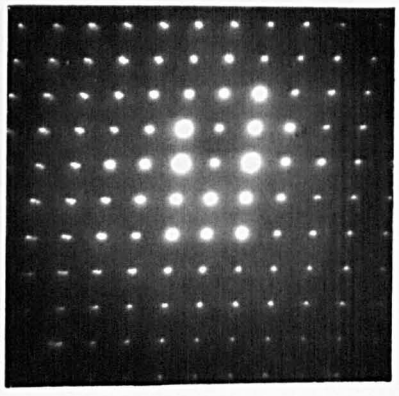

b)

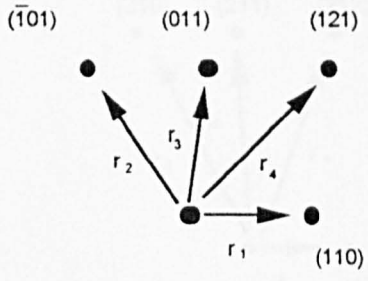

Table 4.9: a) Comparison of experimentally obtained values of selected area diffraction spot ratio and interplanar angles with those calculated for principal spots in $[\bar{1}1\bar{1}]$ Al_xFe. The calculations are based on the monoclinic lattice parameters proposed by Clyne [1981].

b) Schematic representation of $[\bar{1}1\bar{1}]$ Al_xFe giving the miller indices of the planes represented as r_1 to r_4 and the corresponding $[\bar{1}1\bar{1}]$ SADP.

Selected area diffraction spot ratio r_1/r_n				Angle between spots θ (1,n)			
Ratio	Experimental	Calculated	$\|\Delta\|$	Angle	Experimental	Calculated	$\|\Delta\|$
r_1/r_2	0.6188	0.6289	0.0101	θ(1,2)	126	131.74	5.74
r_1/r_3	0.7615	0.7800	0.0185	θ(1,3)	88	87.39	0.61
r_1/r_4	0.6100	0.6289	0.0189	θ(1,4)	52	53.69	1.69

a)

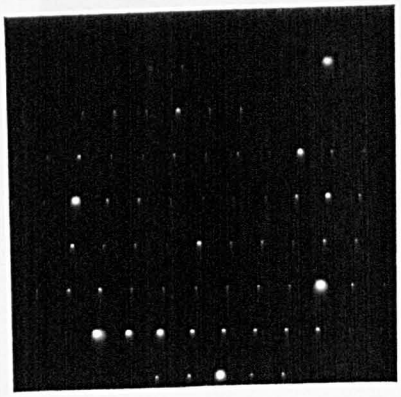

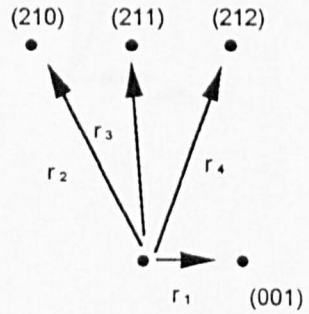

b)

Table 4.10 : a) Comparison of experimentally obtained values of selected area diffraction spot ratio and interplanar angles with those calculated for principal spots in $[1\bar{2}0]$ Al_xFe. The calculations are based on the monoclinic lattice parameters proposed by Clyne [1981].

b) Schematic representation of $[1\bar{2}0]$ Al_xFe giving the miller indices of the planes represented as r_1 to r_4 and the corresponding $[1\bar{2}0]$ SADP.

Selected area diffraction spot ratio r_1/r_n				Angle between spots θ (1,n)			
Ratio	Experimental	Calculated	$\|\Delta\|$	Angle	Experimental	Calculated	$\|\Delta\|$
r_1/r_2	0.4640	0.4324	0.0316	θ(1,2)	87.0	87.83	0.83
r_1/r_3	0.4228	0.3915	0.0313	θ(1,3)	62.5	64.82	2.32

a)

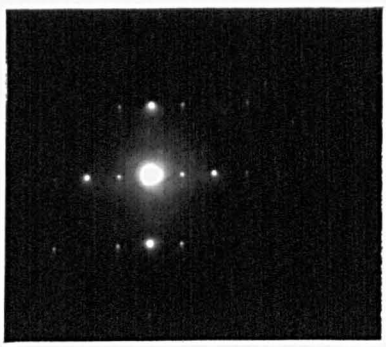

b)

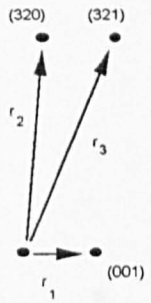

Table 4.11 a) Comparison of experimentally obtained values of selected area diffraction spot ratio and interplanar angles with those calculated for principal spots in $[2\bar{3}0]$ Al_xFe. The calculations are based on the monoclinic lattice parameters proposed by Clyne [1981].

b) Schematic representation of $[2\bar{3}0]$ Al_xFe giving the miller indices of the planes represented as r_1 to r_3 and the corresponding $[2\bar{3}0]$ SADP.

Selected area diffraction spot ratio r_1/r_n				Angle between spots θ (1,n)			
Ratio	Experimental	Clyne [1981]	$\|\Delta\|$	Angle	Experimental	Clyne [1981]	$\|\Delta\|$
r_1/r_2	0.710	0.704	0.060	θ(1,2)	97	96	1.00
r_1/r_3	0.561	0.595	0.034	θ(1,3)	58	57.5	0.50

a)

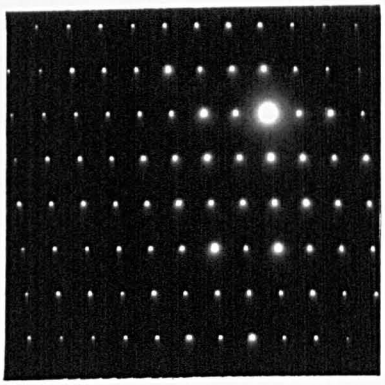

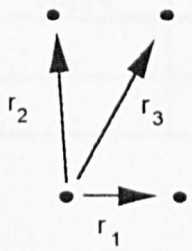

b)

Table 4.12: a) Comparison of experimentally obtained values of selected area diffraction spot ratio and interplanar angles with those taken from Clyne [1981] for principal spots in the so-called incommensurate zone [IZ] in Al_xFe.

b) Schematic representation of [IZ] Al_xFe showing the identity of the planes represented as r_1 to r_3 and the corresponding [IZ] SADP.

Foil number	$Al_{13}Fe_4$	Al_xFe	Al_6Fe	Al_mFe	α-AlFeSi
1	2	3	-	-	-
2	1	3	-	-	-
3	1	4	-	-	-

Table 4.13: Results of selected area diffraction analysis of intermetallic crystals found in three thin foils taken from an Al-0.5%Fe-0.1%Si alloy specimen which had been unidirectionally solidified at 2.00mm/s.

Foil number	$Al_{13}Fe_4$	Al_xFe	Al_6Fe	Al_mFe	α-AlFeSi
1	5	-	-	-	-
2	4	-	-	-	-

Table 4.14: Results of selected area diffraction analysis of intermetallic crystals found in two thin foils taken from an Al-0.25%Fe-0.1%Si-0.5%Mg alloy specimen which had been unidirectionally solidified at 0.05mm/s.

Foil number	$Al_{13}Fe_4$	Al_xFe	Al_6Fe	Al_mFe	α-AlFeSi
1	4	-	-	-	-
2	5	-	-	-	-

Table 4.15: Results of selected area diffraction analysis of intermetallic crystals found in two thin foils taken from an Al-0.5%Fe-0.1%Si-0.5%Mg alloy specimen which had been unidirectionally solidified at 0.50mm/s.

Foil number	$Al_{13}Fe_4$	Al_xFe	Al_6Fe	Al_mFe	α-AlFeSi
1	3	-	4	-	-
2	2	-	2	-	-

Table 4.16 : Results of selected area diffraction analysis of intermetallic crystals found in two thin foils taken from an Al-0.75%Fe-0.1%Si-0.5%Mg alloy specimen which had been unidirectionally solidified at 0.50mm/s.

Foil number	$Al_{13}Fe_4$	Al_xFe	Al_6Fe	Al_mFe	α-AlFeSi
1	4	-	-	2	-
2	3	-	-	2	-

Table 4.17: Results of selected area diffraction analysis of intermetallic crystals found in two thin foils taken from an Al-0.75%Fe-0.1%Si-0.5%Mg alloy specimen which had been unidirectionally solidified at 2.00mm/s.

Foil number	$Al_{13}Fe_4$	Al_xFe	Al_6Fe	Al_mFe	α-AlFeSi
1	2	-	4	-	1
2	-	-	4	-	-

Table 4.18: Results of selected area diffraction analysis of intermetallic crystals found in three thin foils taken from an Al-0.25%Fe-0.1%Si-0.75%Mg alloy specimen which had been unidirectionally solidified at 2.00mm/s.

Ratio of spot spacing, r, and angle between spots, θ	Rhombohedral [111] zone axis (calculated)	Monoclinic [101] zone axis (calculated)	Experimental results (Fig.4.32b)
r_1/r_2	1.000	1.006	1.025
r_1/r_3	0.557	0.583	0.619
r_1/r_4	0.468	0.378	0.420
$\theta(r_1, r_2)$	60.00	60.00	60.00
$\theta(r_1, r_3)$	30.00	30.00	30.00
$\theta(r_1, r_4)$	19.11	19.00	19.00

Table 4.19 : Comparison of calculated and experimental values for the ratios of selected area diffraction spot spacing and angle between spots for the α_R and α_T superstructures of the bcc α-AlFeSi phase.

Grid number	$Al_{13}Fe_4$	Al_xFe	Al_6Fe	Al_mFe	α-AlFeSi
1	4	-	-	-	-
2	3	-	-	-	-

Table 4.20: Results of selected area diffraction analysis of intermetallic crystals extracted, by the butanol method, from an Al-0.5%Fe-0.1%Si-0.75%Mg alloy specimen which had been unidirectionally solidified at 0.10mm/s.

Foil number	$Al_{13}Fe_4$	Al_xFe	Al_6Fe	Al_mFe	α-AlFeSi
1	2	5	-	-	-
2	2	3	-	-	-

Table 4.21 : Results of selected area diffraction analysis of intermetallic crystals found in two thin foils taken from an Al-0.5%Fe-0.1%Si-0.75%Mg alloy specimen which had been unidirectionally solidified at 0.50mm/s.

Foil number	$Al_{13}Fe_4$	Al_xFe	Al_6Fe	Al_mFe	α-AlFeSi
1	2	-	4	-	-
2	1	-	3	-	-
3	2	-	4	-	-

Table 4.22 : Results of selected area diffraction analysis of intermetallic crystals found in three thin foils taken from an Al-0.5%Fe-0.1%Si-0.75%Mg alloy specimen which had been unidirectionally solidified at 2.00mm/s.

Foil number	$Al_{13}Fe_4$	Al_xFe	Al_6Fe	Al_mFe	α-AlFeSi
1	2	-	4	-	-
2	3	-	2	-	
3	2	-	3	-	-

Table 4.23 : Results of selected area diffraction analysis of intermetallic crystals found in three thin foils taken from an Al-0.5%Fe-0.05%Si-0.75%Mg alloy specimen which had been unidirectionally solidified at 0.10mm/s.

Grid number	$Al_{13}Fe_4$	Al_xFe	Al_6Fe	Al_mFe	α-AlFeSi
1	-	-	4	2	-
2	1	-	3	1	-

Table 4.24 : Results of selected area diffraction analysis of intermetallic crystals extracted, by the butanol method, from an Al-0.5%Fe-0.05%Si-0.75%Mg alloy specimen which had been unidirectionally solidified at 1.00mm/s.

Foil number	$Al_{13}Fe_4$	Al_xFe	Al_6Fe	Al_mFe	α-AlFeSi
1	2	-	-	5	-
2	2	-	-	3	-

Table 4.25 : Results of selected area diffraction analysis of intermetallic crystals found in three thin foils taken from an Al-0.5%Fe-0.05%Si-0.75%Mg alloy specimen which had been unidirectionally solidified at 2.00mm/s.

Foil number	$Al_{13}Fe_4$	Al_xFe	Al_6Fe	Al_mFe	α-AlFeSi
1	3	-	-	-	-
2	4	-	-	-	-
3	2	-	-	-	-

Table 4.26 : Results of selected area diffraction analysis of intermetallic crystals found in three thin foils taken from an Al-0.5%Fe-0.1%Si-0.75%Mg-0.04%Cr alloy specimen which had been unidirectionally solidified at 0.10mm/s.

Phase	$\alpha/\xi = \Delta S/R$
Al	1.35
$Al_{13}Fe_4$	2.3
Al_6Mn	1.8
Al_6Fe	1.8

Table 5.1: $\alpha/\xi = \Delta S/R$ for Al, $Al_{13}Fe_4$, Al_6Mn and Al_6Fe from Backerud [1968].

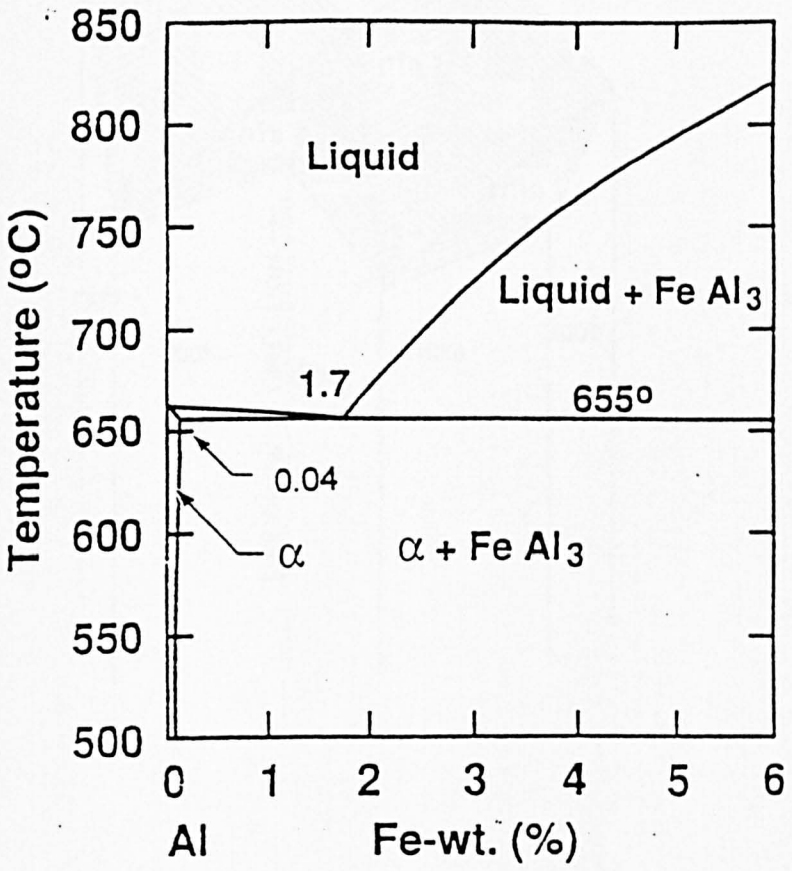

Fig.2.1: The aluminium rich end of the Al-Fe phase diagram [Phillips 1976].

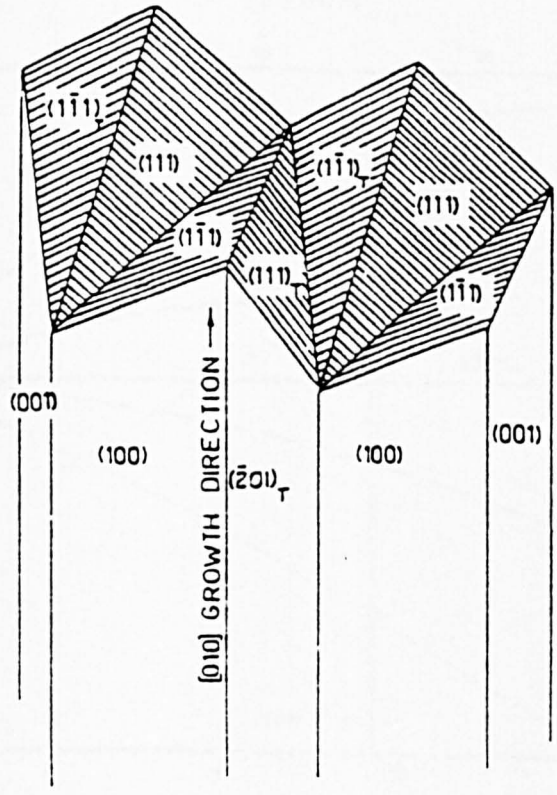

Fig.2.2: Growth crystallography of $Al_{13}Fe_4$ eutectic plates based on the TPRE mechanism [Adam and Hogan 1975].

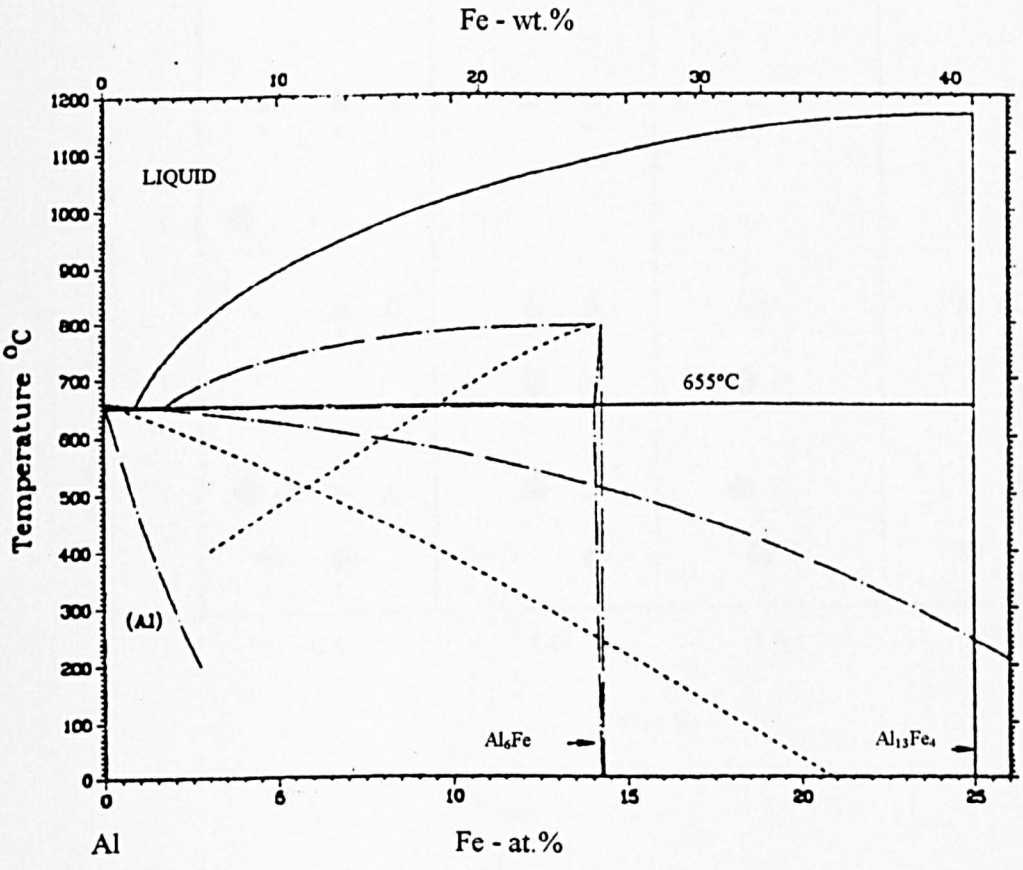

Fig.2.3: Aluminium rich portion of the Al-Fe phase diagram showing the position of both the stable αAl-$Al_{13}Fe_4$ and metastable αAl-Al_6Fe eutectic points [Murray 1983].

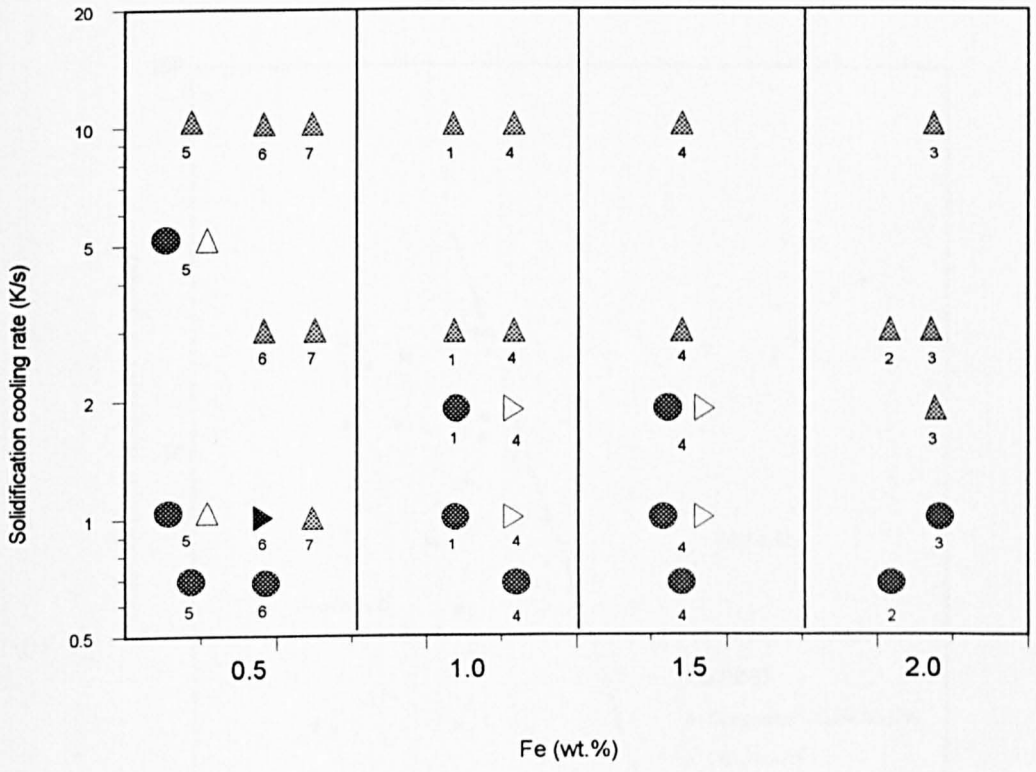

Fig.2.4: Solidification cooling rate versus alloy composition phase map for hypoeutectic binary Al-Fe alloys constructed from data presented in the literature. The numbers indicate the source of the data: 1) Backerud [1968], 2) Adam and Hogan [1972], 3) Hughes and Jones [1976], 4) Young and Clyne [1981], 5) Granger [1990], 6) Fang and Granger [1991] and 7) Tezuka and Kamio [1992]. Phase dominance is denoted by use of a shaded symbol.

Key:-

$Al_{13}Fe_4$ Al_6Fe Al_xFe Al_mFe β-AlFeSi

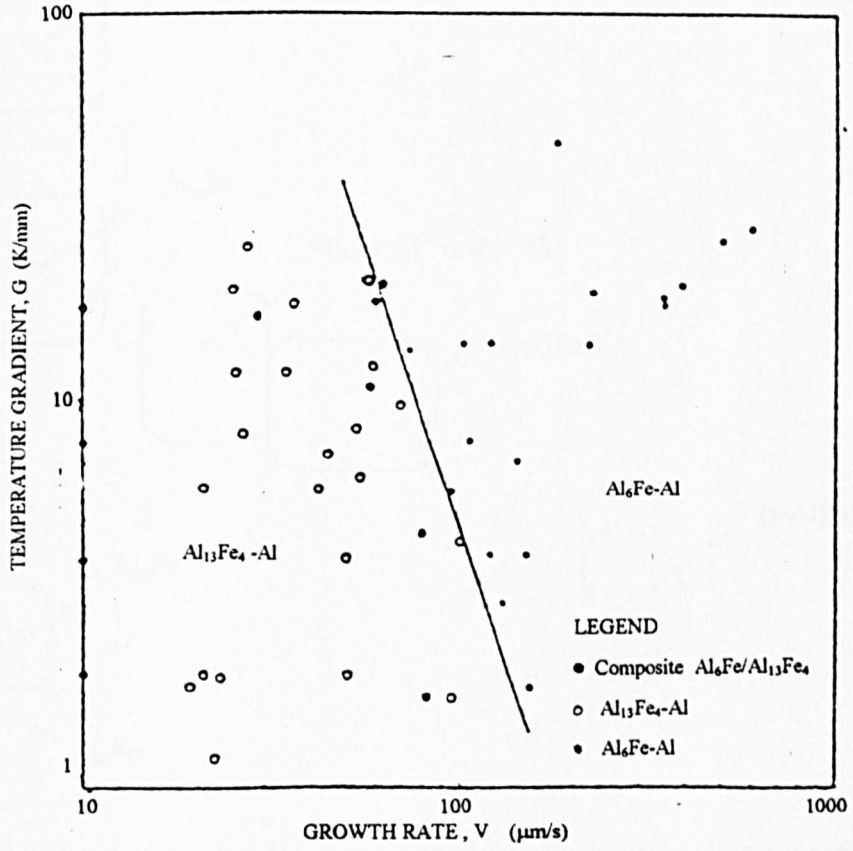

Fig.2.5: The effect of imposed thermal gradient conditions on the αAl-$Al_{13}Fe_4$ to αAl-Al_6Fe eutectic transition velocity [Adam and Hogan 1972].

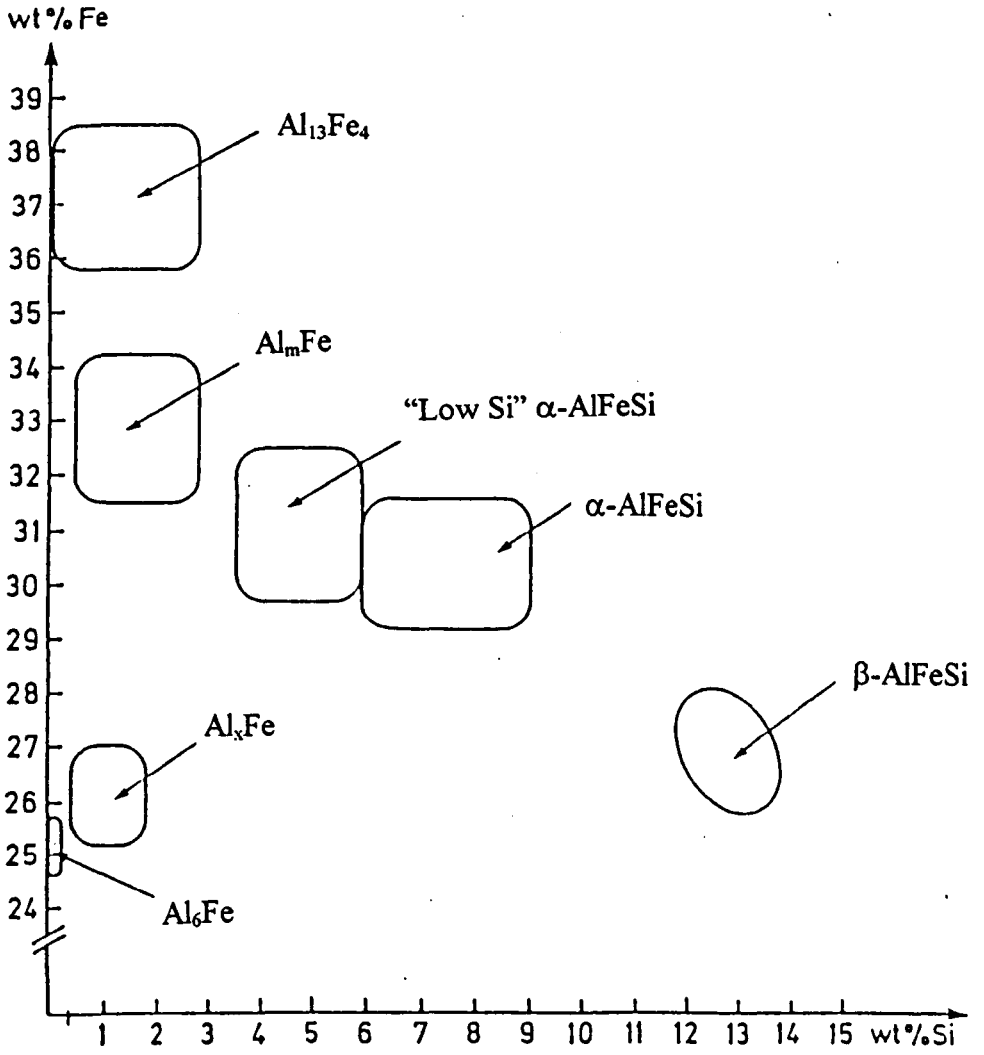

Fig. 2.6: Representation of the composition ranges of intermetallic particles found in commercial purity, D.C.-cast Al alloys, showing the extent of Si dissolution in the "binary" phases [Langsrud 1989].

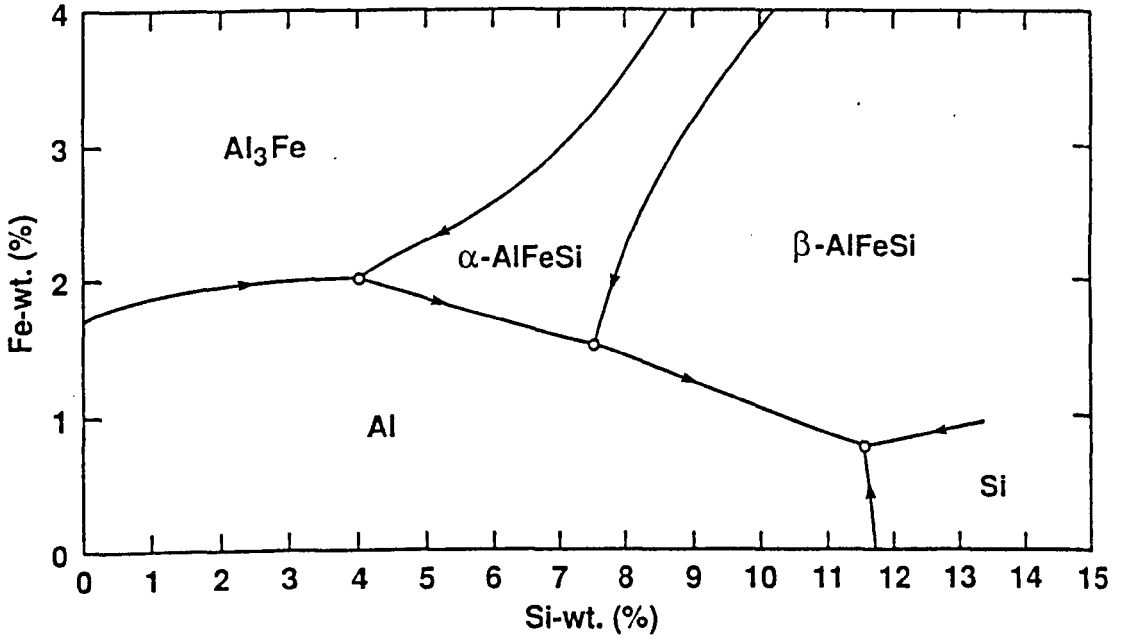

Fig.2.7: Al-rich corner of the Al-Fe-Si phase diagram showing the liquidus surface. Arrows indicate solidification paths. [Rivlin and Raynor 1981]

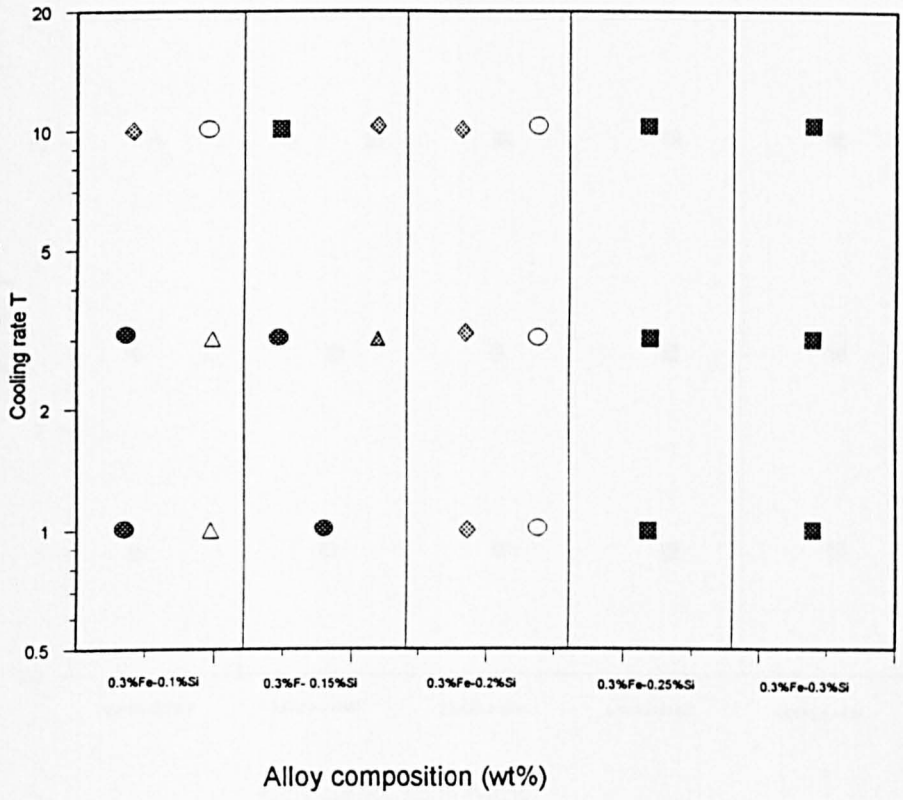

Fig.2.8: Effect of Si content on intermetallic phase formation and stability in the alloy series Al-0.3%Fe-Y%Si (Y = 0.1 to 0.3%). All data from Tezuka and Kamio [1992]. Phase dominance is indicated by use of a shaded symbol.

Key:-

● ○ $Al_{13}Fe_4$ ◈ ◇ Al_mFe ◭ △ Al_6Fe ■ □ α-AlFeSi

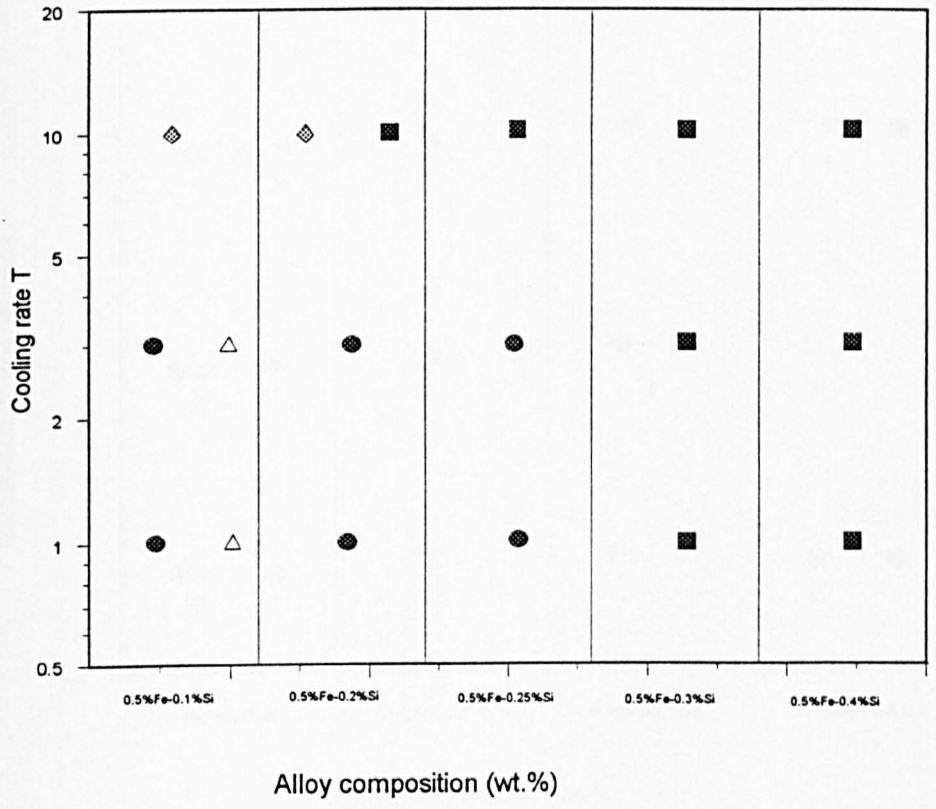

Fig.2.9: Effect of Si content on intermetallic phase formation and stability in the alloy series Al-0.5%Fe-Y%Si (Y = 0.1 to 0.3%). All data from Tezuka and Kamio [1992]. Phase dominance is indicated by use of a shaded symbol.

Key:-

● ○ $Al_{13}Fe_4$ ◈ ◇ Al_mFe ▲ △ Al_6Fe ■ □ α-AlFeSi

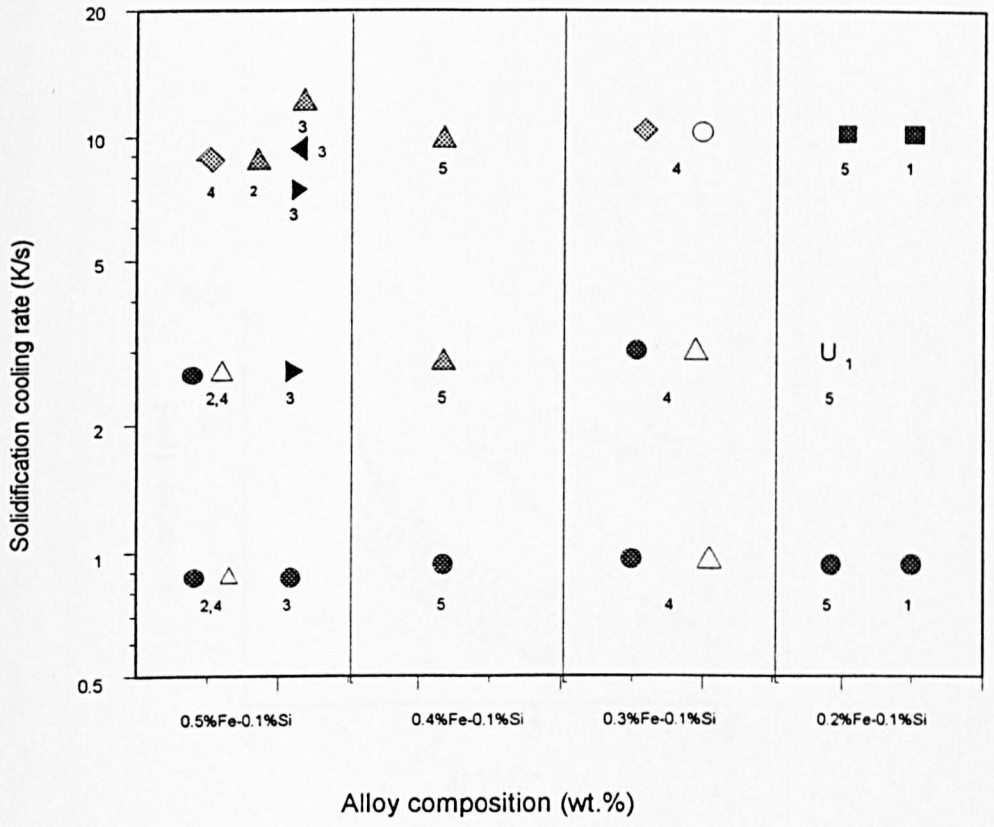

Fig.2.10: Solidification cooling rate versus alloy composition phase map constructed from data found in the literature for the series Al-X%Fe-0.1%Si (X = 0.2 to 0.5%). The numbers indicate the source of the data: 1)Liu and Dunlop [1986], 2) Granger [1990], 3) Fang and Granger [1991], 4) Tezuka and Kamio [1992], 5)Maggs *et al.* [1995]. Phase dominance is denoted by use of a shaded symbol.

Key:-

$Al_{13}Fe_4$ Al_mFe Al_6Fe α-AlFeSi β-AlFeSi

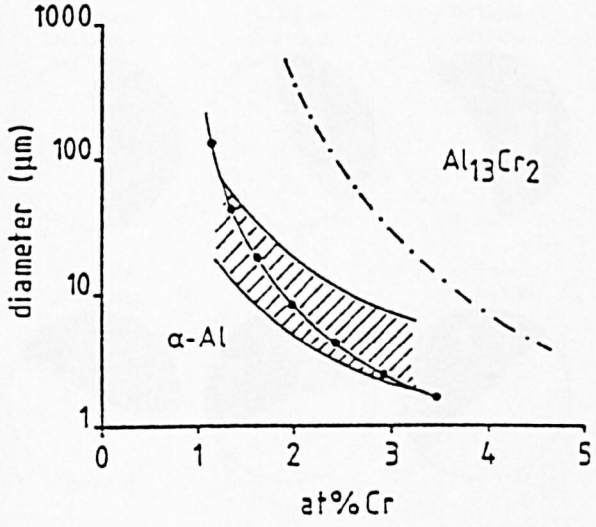

Fig.2.11: Critical diameter above which atomised droplets contain primary $Al_{13}Cr_2$ as a function of Cr content in Al-Cr alloys. The hatched area represents results of experimental observation. The dash-dot line is the prediction for homogeneous nucleation while the full line is for heterogeneous nucleation with contact angle 85° for both phases.[Saunders and Tsakiropoulos 1988].

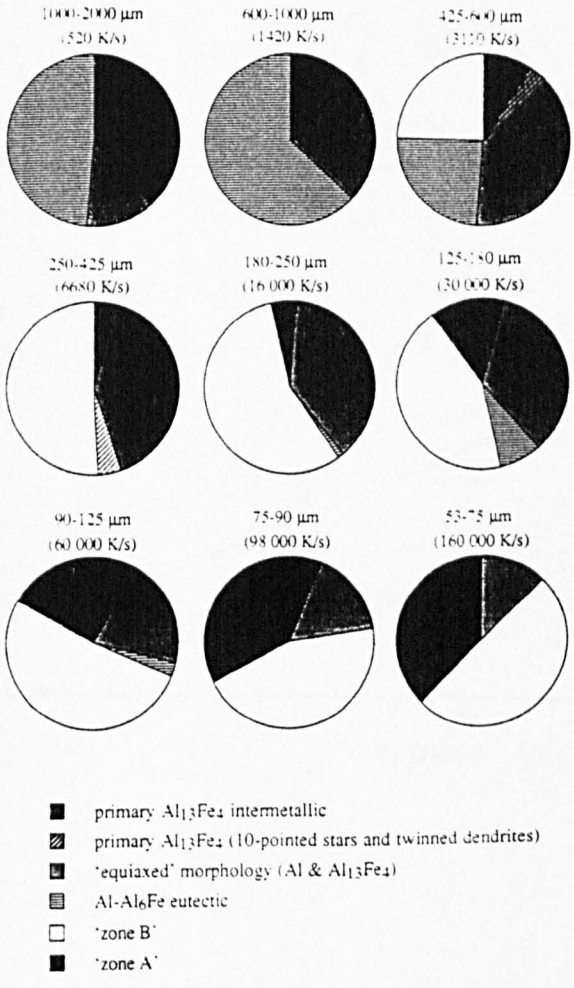

Fig.2.12: Fractions of droplet population in each size range which commenced solidification with a particular structure. Also shown is the mean calculated cooling rate. [Cochrane *et al.* 1991].

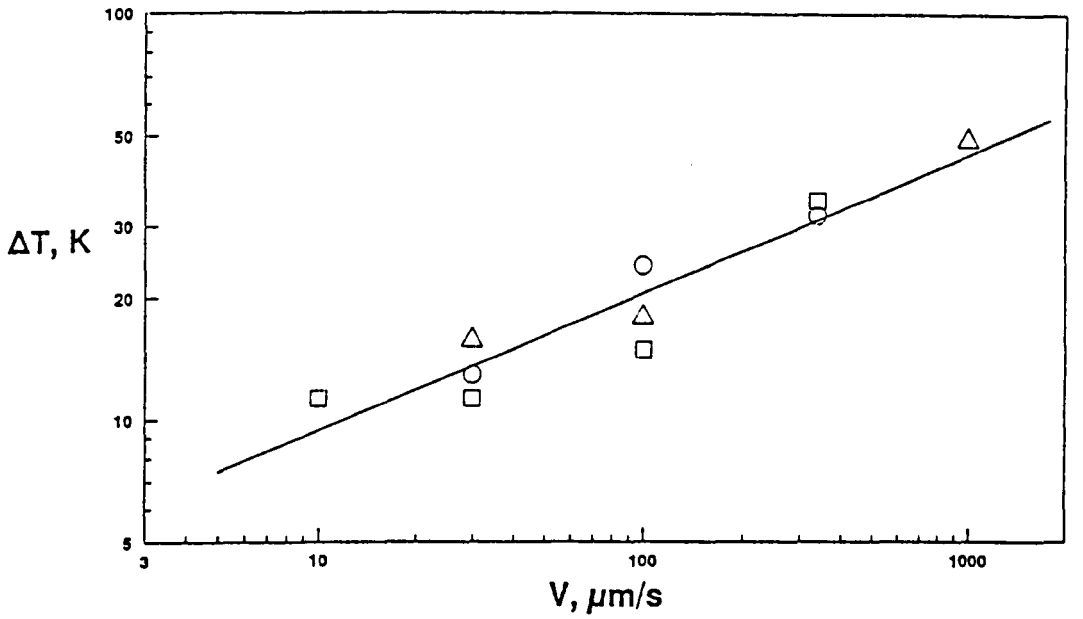

Fig.2.13: Growth undercooling ΔT for primary $Al_{13}Fe_4$ in Al-4.7 to 6.1 wt.%Fe alloys as a function of growth velocity V at a temperature gradient of 8 to 15K/mm. [Liang and Jones 1991].

Key: ○ 4.7 □ 5.3 △ 6.1wt%.

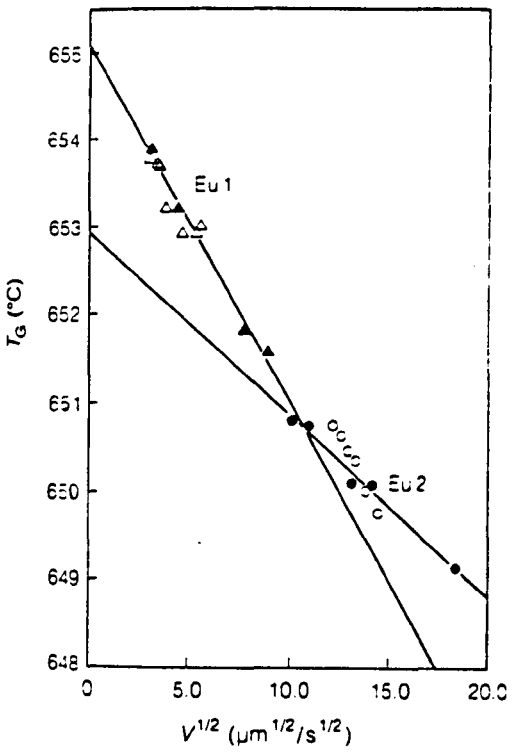

Fig.2.14: Experimental determination of eutectic formation temperatures (V→0) for the equilibrium αAl-$Al_{13}Fe_4$ (Eu1) and metastable αAl-Al_6Fe (Eu2) eutectics in Al alloys containing Al-3wt.%Fe. T_G is measure growth temperature at growth velocity V imposed by steady state Bridgman growth [Liang and Jones 1992].

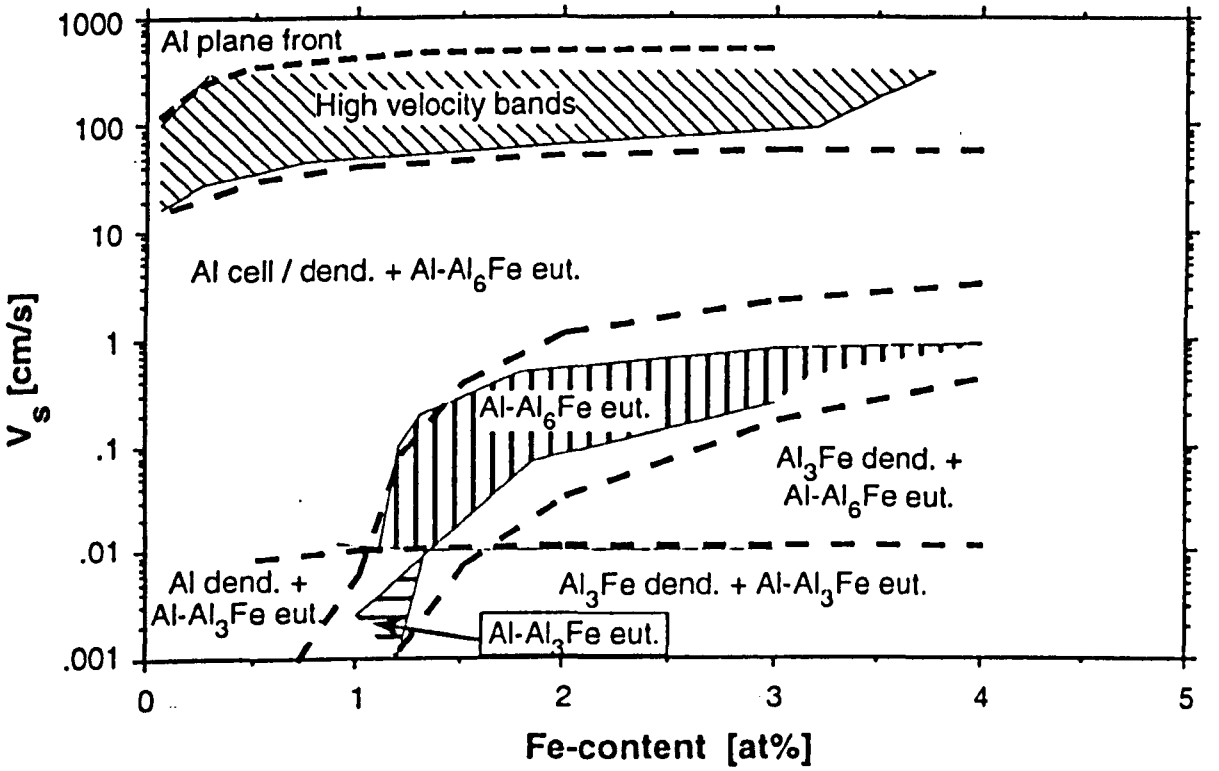

Fig.2.15: Constituent selection diagram for Al-rich Al-Fe alloys grown under steady state conditions at temperature gradient between 10 and 2000K/mm and growth velocity V between 0.04mm/s and 1m/s. Those calculated by competetive growth modelling [Gilgien *et al.* 1995] (broken lines) are superimposed on the experimental results (full lines) of Hughes and Jones [1976].

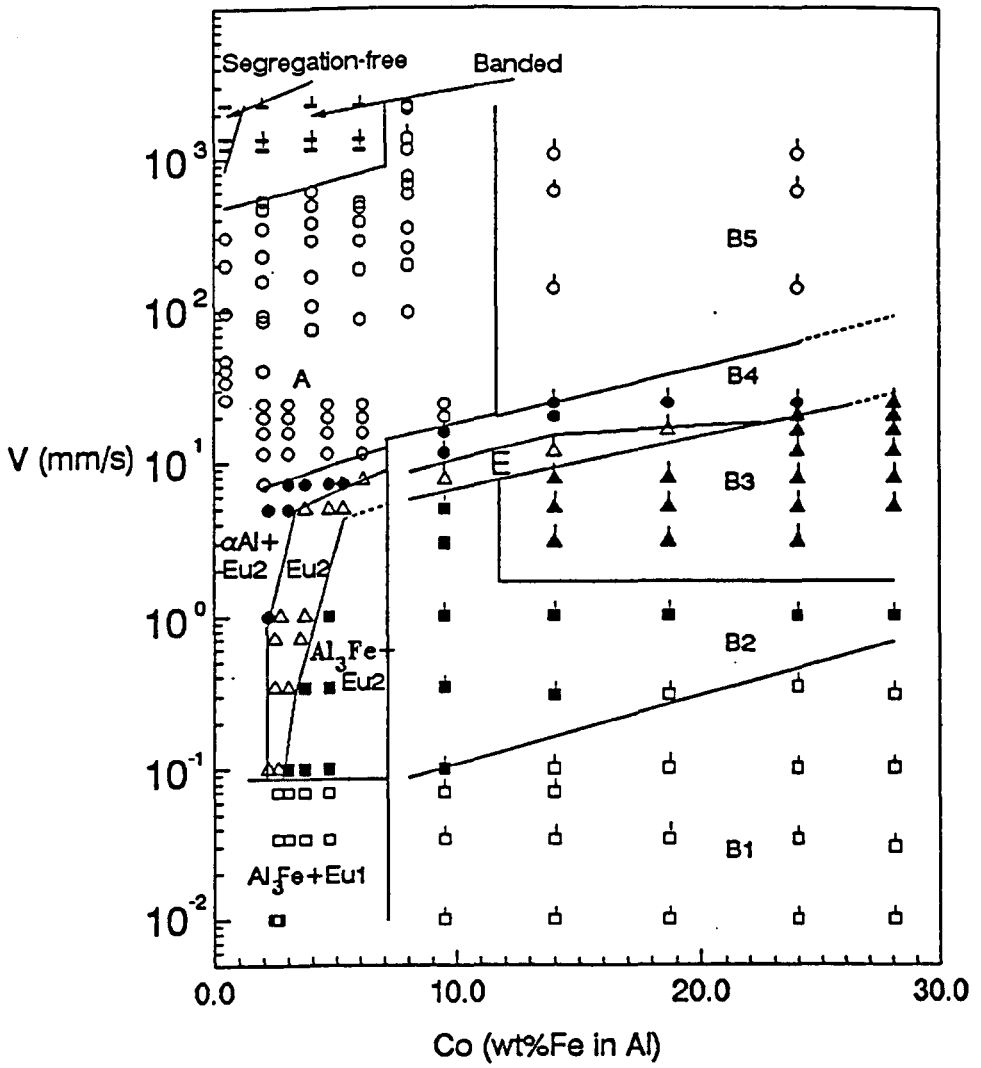

Fig.2.16: Solidification microstructure selection map constructed by Liang [1992] for Al-Fe alloys over the compsition range 2 to 30 wt.%Fe by Bridgman solidification (V = 0.01 to 5.0mm/s: G = 8 to 15K/mm), TIG weld traversing (V = 7.3 to 24.3 mm/s: G ~ 100K/mm) and Laser resolidification (V ~ 1 cm/s to 1 m/s: G ~ 2000K/mm).

Key is as follows: B1= irregular primary $Al_{13}Fe_4$ plus αAl-$Al_{13}Fe_4$ eutectic, B2 = irregular primary $Al_{13}Fe_4$ plus αAl-Al_xFe eutectic, B3= regular primary $Al_{13}Fe_4$ plus αAl-Al_xFe eutectic, B4= primary Al_mFe plus microcellular αAl-intermetallic network, B5= globular primary plus microcellular αAl-intermetallic network. Eu1 = αAl- $Al_{13}Fe_4$, Eu2 = αAl-Al_6Fe, E = αAl-Al_xFe and A = microcellular αAl-intermetallic network structure.

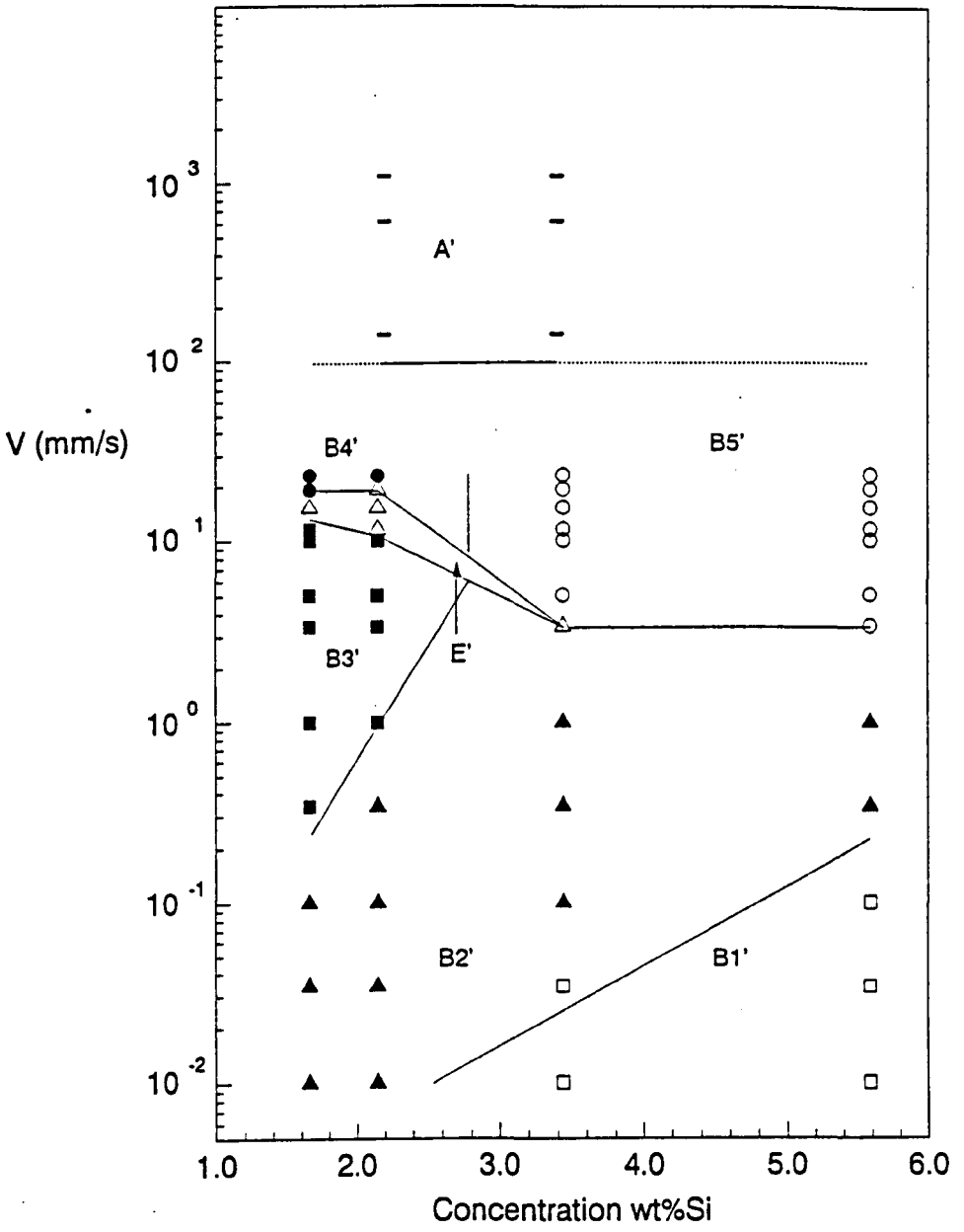

Fig.2.17: Solidification microstructure selection map constructed by Liang [1992] for Al-8.5%Fe-Y%Si alloys over the composition range Y = 0 to 6 wt.%Si by Bridgman solidification (V = 0.01 to 5.0mm/s: G = 8 to 15K/mm), TIG weld traversing (V = 7.3 to 24.3 mm/s: G ~ 100K/mm) and Laser resolidification (V ~ 1 cm/s to 1 m/s: G ~ 2000K/mm).

Key is as follows: B1′= irregular primary $Al_{13}Fe_4$ plus αAl-α′AlFeSi/βAlFeSi eutectic, B2′ = irregular primary $Al_{13}Fe_4$ plus αAl--α′AlFeSi eutectic, B3′= regular primary $Al_{13}Fe_4$ plus αAl-Al_9Fe_2 eutectic, B4′= primary Al_mFe plus αAl-Al_9Fe_2, B5′= primary Al_9Fe_2 plus αAl-Al_9Fe_2 eutectic. E′ = αAl-Al_9Fe_2 and A=microcellular αAl-intermetallic network structure.

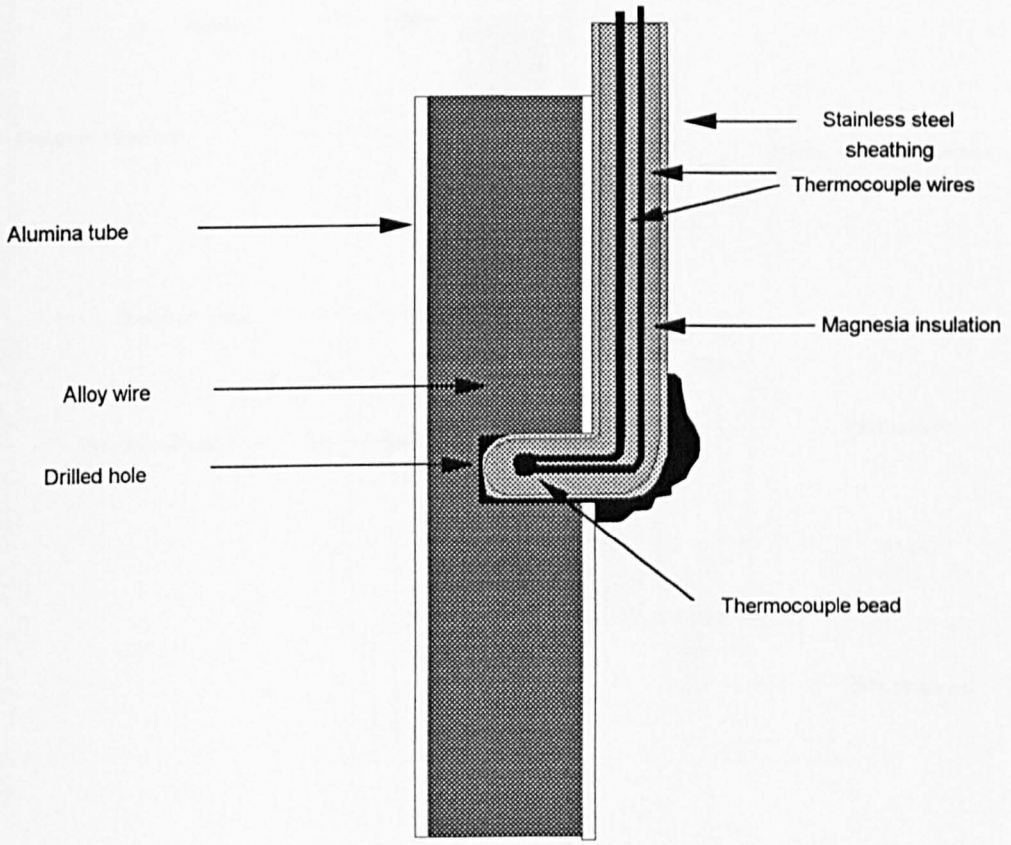

Fig.3.1: Schematic longitudinal section of Bridgman specimen prepared for thermal analysis during unidirectional solidification.

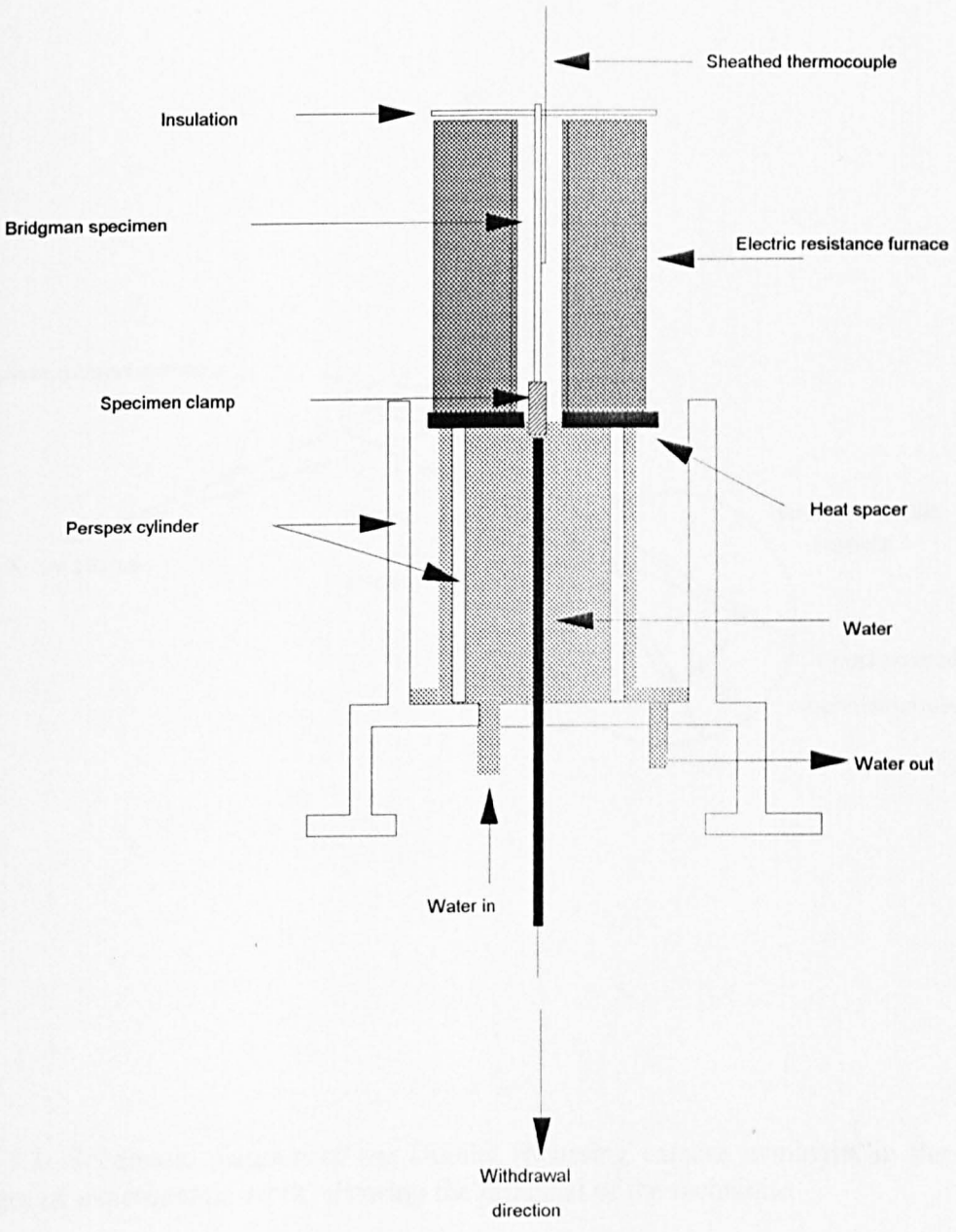

Fig.3.2: Schematic diagram of the Bridgman unidirectional solidification apparatus employed in the present work.

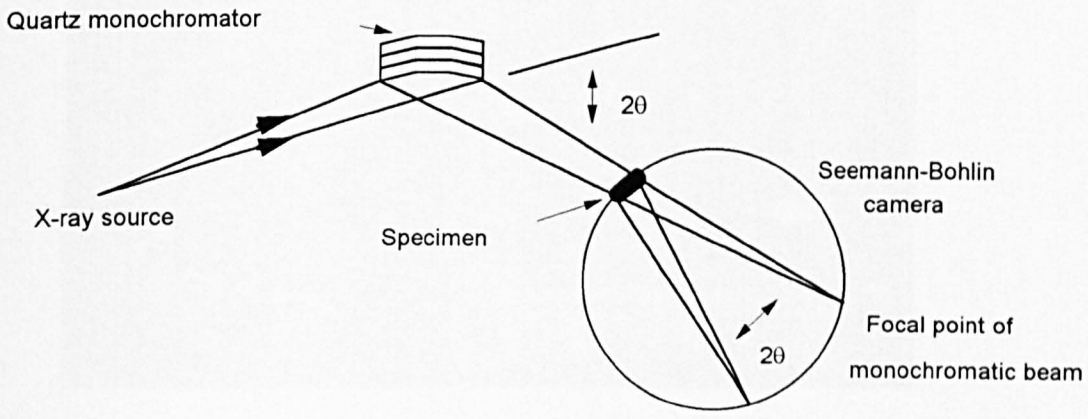

Fig.3.3: Schematic diagram of the Guinier focussing camera employed in the early stages of experimental work, showing the principal of the technique.

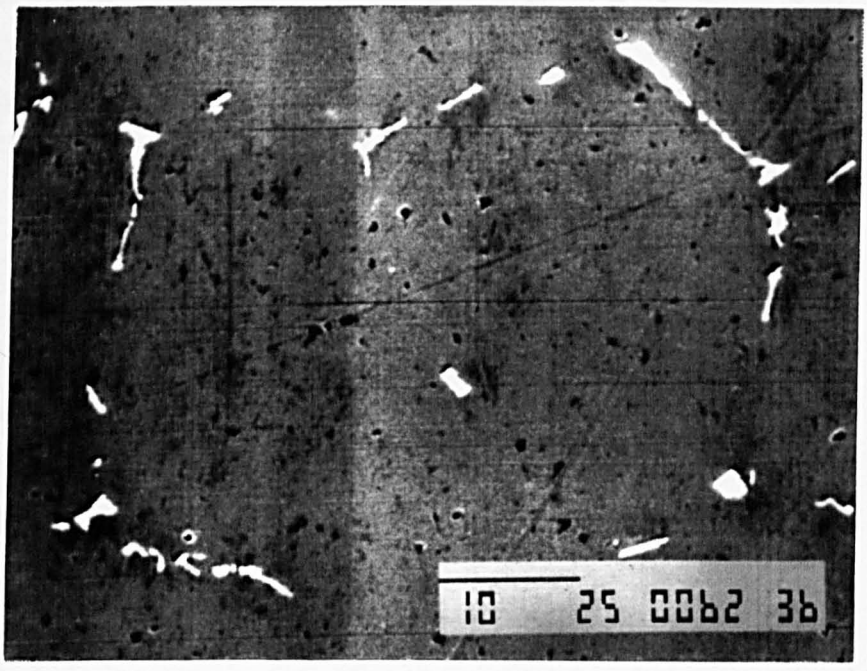

Fig.4.1: Scanning electron micrograph of an intermetallic particle found within an α-Al cell in an Al-0.5%Fe-0.05%Si-0.75%Mg alloy sample which had been unidirectionally solidified at 1.00mm/s.

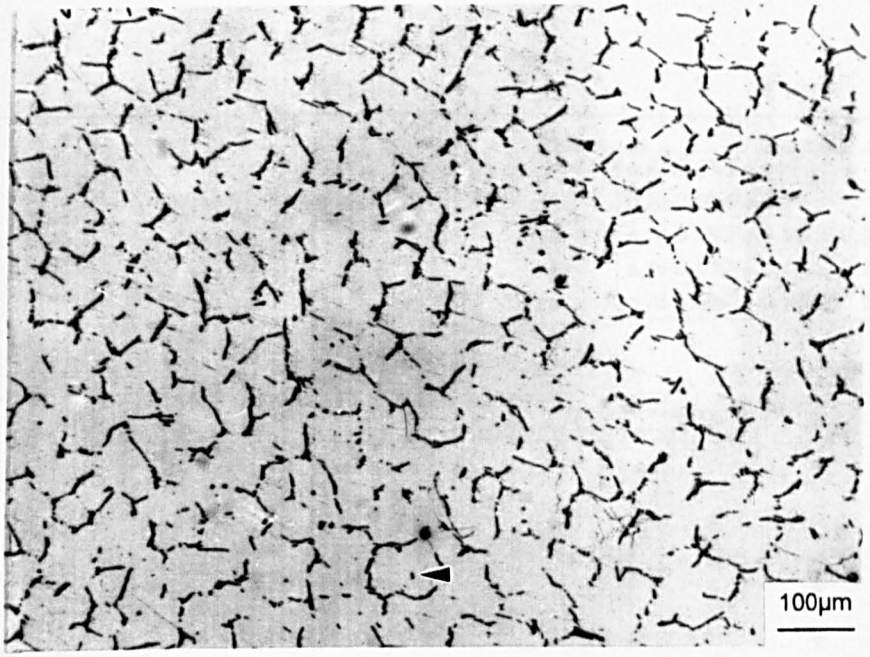

a)

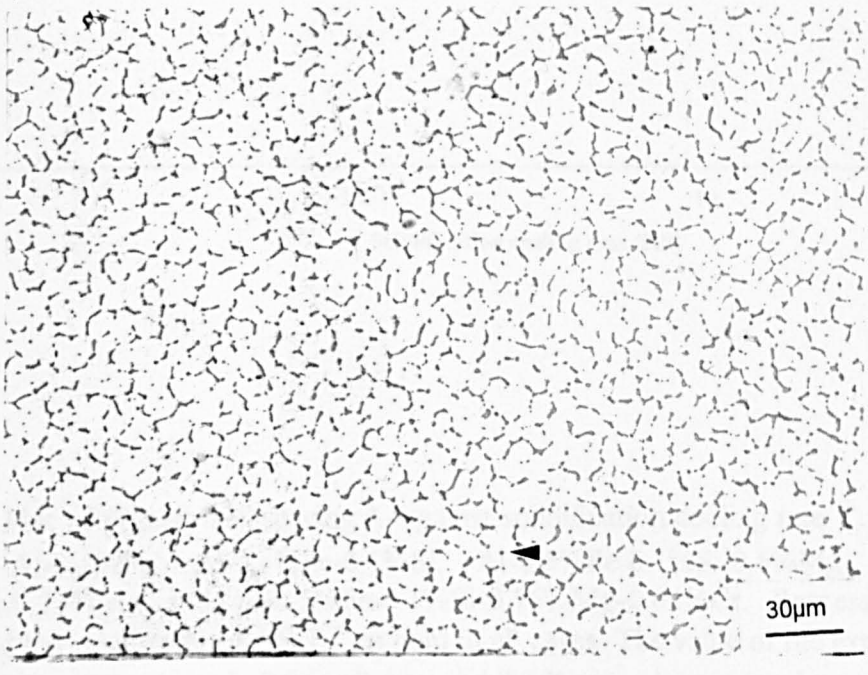

b)

Fig.4.2: Optical micrographs showing cellular structures typical of those found in Al-0.5%Fe-0.1%Si-0.75%Mg after unidirectional solidification at, a) V=0.05 mm/s and b) V = 2.00 mm/s. Note that the cell structure becomes better defined with the transition in intermetallic morphology from lath to rod. Also note that the incidence of intracellular phases increases with growth velocity. Examples of intracellular intermetallics are arrowed in both micrographs.

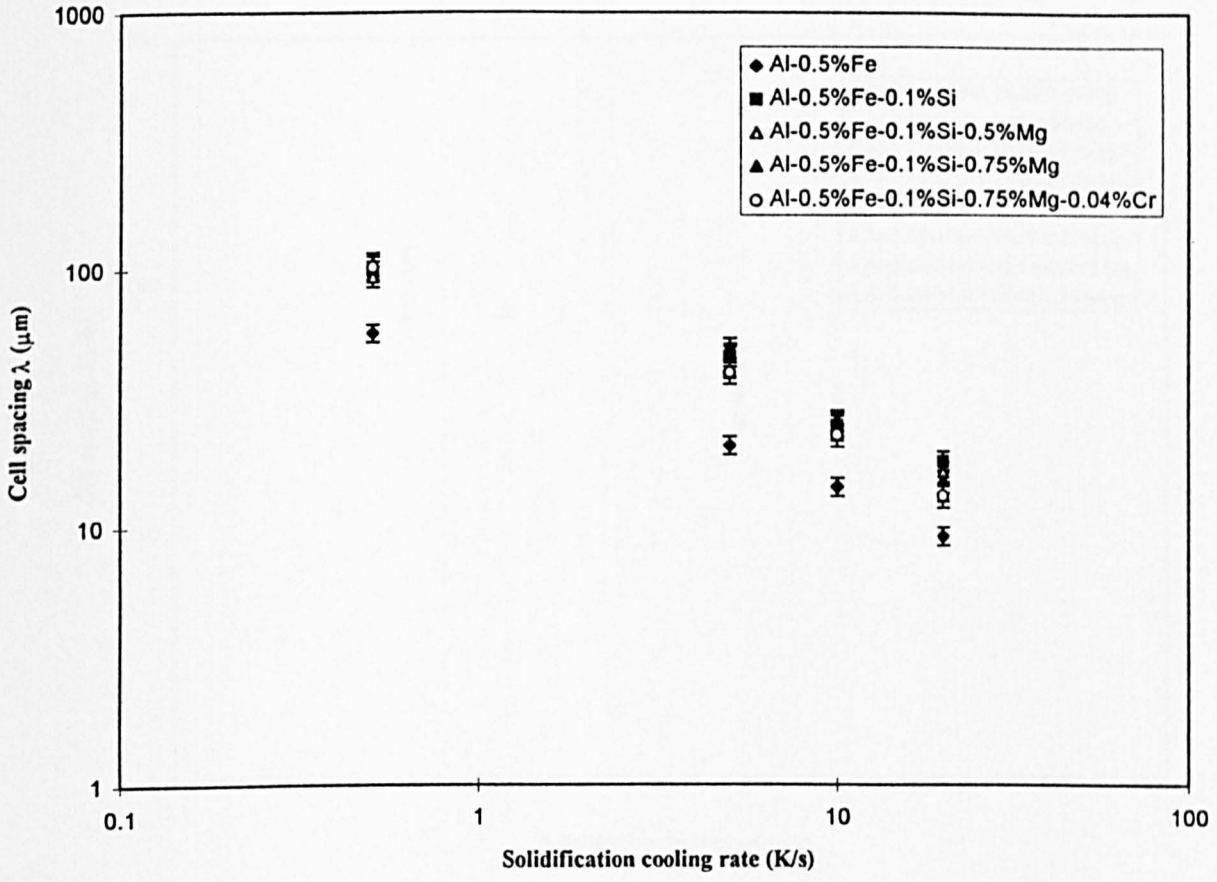

Fig.4.3: Plot of primary cell spacing λ_1 against solidification cooling rate $\dot{T}_s$ for the alloy series Al-0.5%Fe, Al-0.5%Fe-0.1%Si, Al-0.5%Fe-0.1%Si-0.5%Mg, Al-0.5%Fe-0.1%Si-0.75%Mg and Al-0.5%Fe-0.1%Si-0.75%Mg-0.04%Cr. Regression analysis revealed the relationship $\lambda_1 = K \dot{T}_s^{-n}$ to hold in all cases. The value of the exponent n was found to be approximately 0.5 in all cases whilst K was observed to be sensitive to the presence of Si.

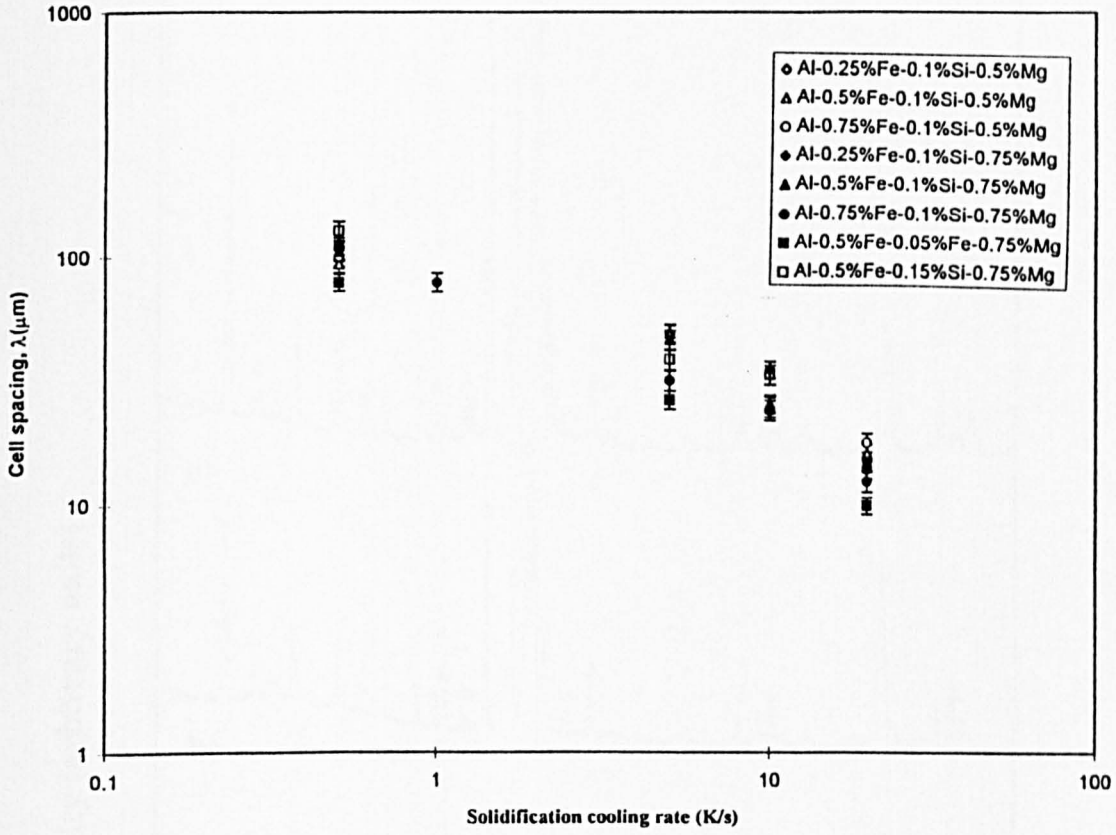

Fig.4.4: Plot of primary cell spacing λ_1 against solidification cooling rate $\dot{T}_s$ for the alloy series Al-X%Fe-0.1%Si-Z%Mg (X = 0.25 to 0.75%: Z=0.5 or 0.75%) and Al-0.5%Fe-Y%Si-0.75%Mg (Y = 0.05 to 0.15%). Regression analysis revealed the relationship $\lambda_1 = K \dot{T}_s^{-n}$ to hold in all cases where n was found to be approximately 0.5 and K was found to be largely insensitive to alloy composition.

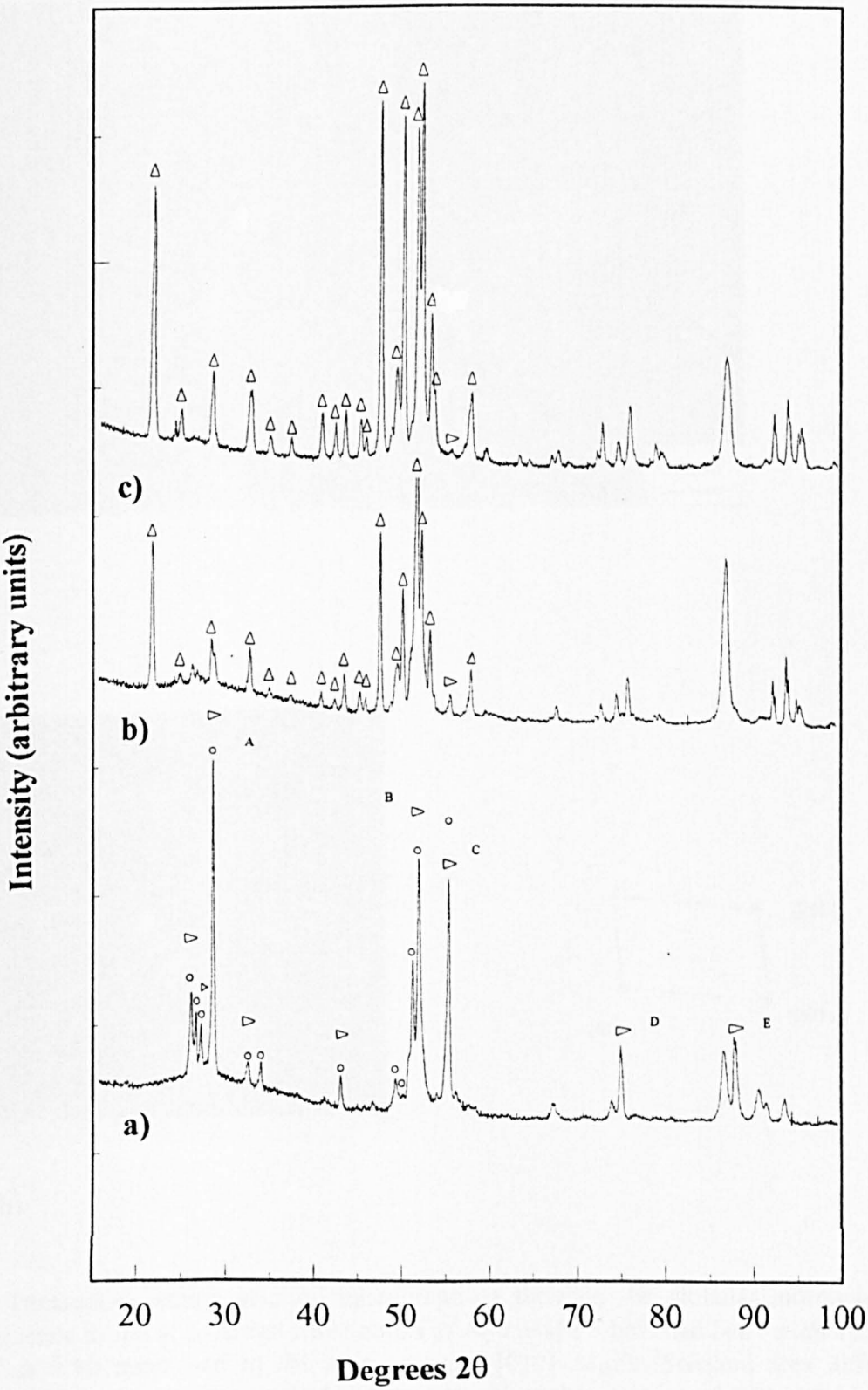

Fig.4.5: X-ray diffraction patterns of second phase intermetallics extracted, by the butanol reflux method, from Al-0.5%Fe alloy specimens which had been unidirectionally solidified at a) 0.05mm/s, b) 0.50mm/s and c) 1.00mm/s.

Key: ○ - $Al_{13}Fe_4$, △ -Al_6Fe, ▷ -Al_xFe.

a)

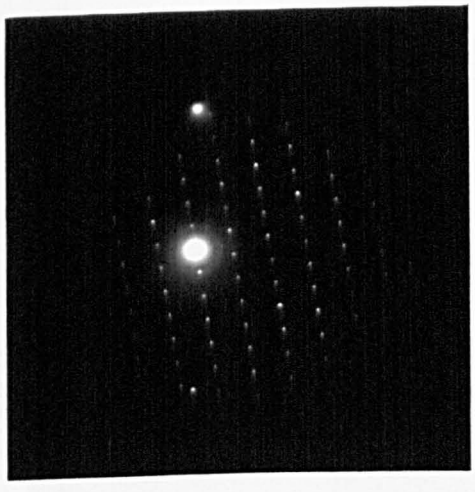

b)

Fig 4.6: Transverse section electron micrograph a) showing the globular morphology of $Al_{13}Fe_4$ crystals found at α-Al cell triple points in Al-0.5%Fe which had been unidirectionally solidified at 0.10 mm/s and b) the accompanying [010] $Al_{13}Fe_4$ Selected area diffraction pattern taken from the particle marked by the arrow. Note the presence of (001) stacking fault contrast and evidence of faint streaking in the c* reciprocal lattice vector rows in the SADP.

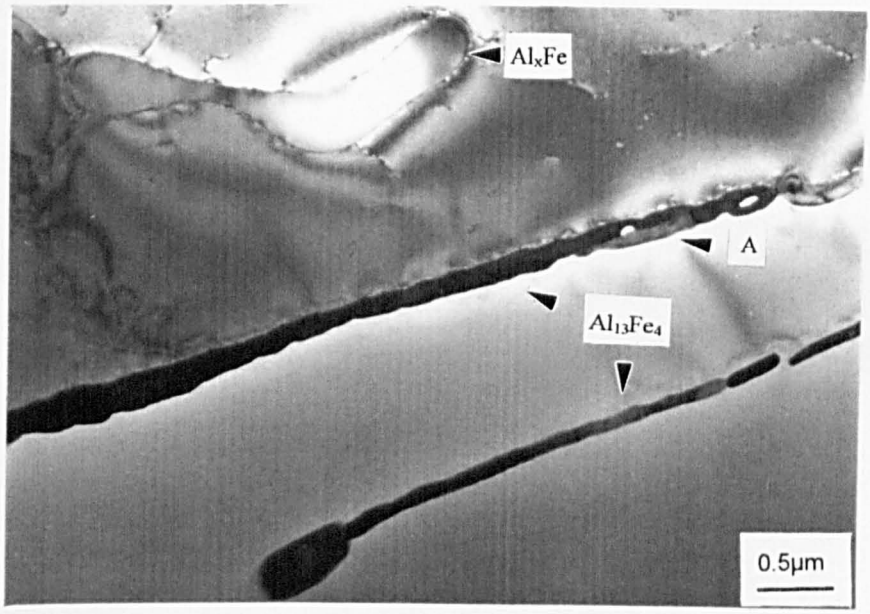

a)

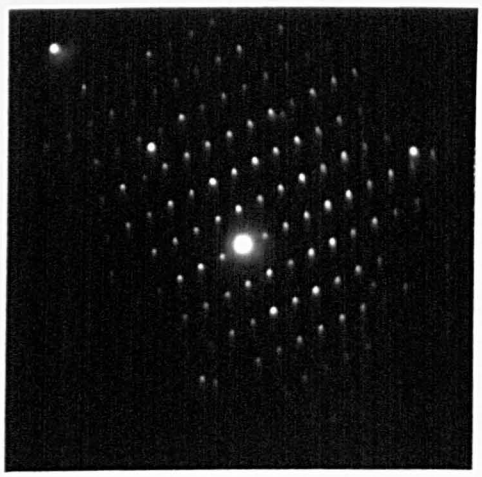

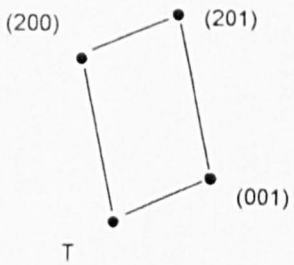

b)

Fig. 4.7: Transverse section electron micrograph a) showing lath-like clusters of $Al_{13}Fe_4$ crystals found on α-Al cell boundaries (A) and a large dog-bone morphology particle of Al_xFe (indicated) found in Al-0.5%Fe unidirectionally solidified at 0.10mm/s and b) the corresponding SADP taken from particle A showing that the electron beam direction was near to $[010]_{Al_{13}Fe_4}$.

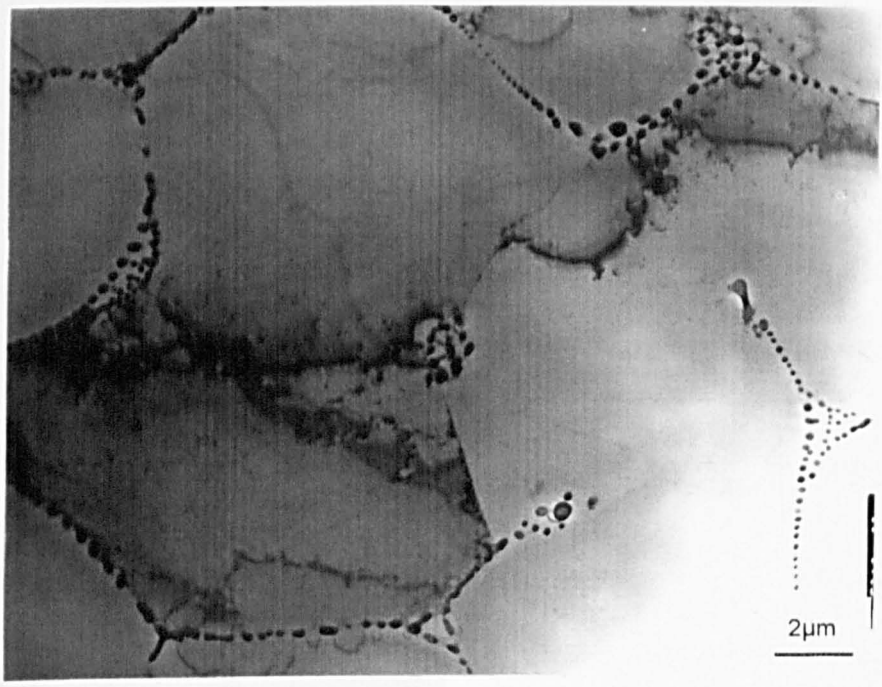

Fig.4.8: Transverse section electron micrograph showing Al_6Fe delineating the α-Al cell boundaries in an Al-0.5%Fe alloy specimen unidirectionally solidified at 2.00mm/s.

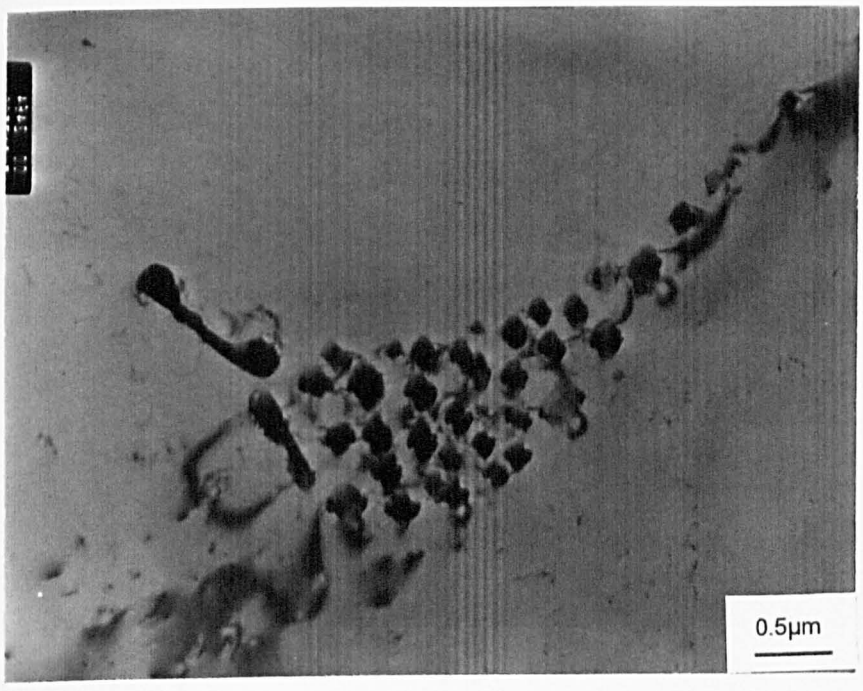

a)

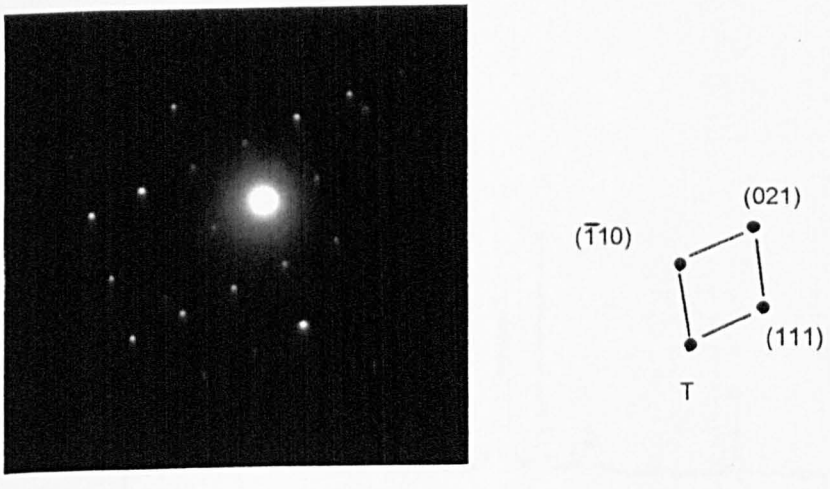

b)

Fig.4.9: Transverse section electron micrograph showing an Al_6Fe eutectic group typical of those formed at α-Al cell triple points in Al-0.5%Fe unidirectionally solidified at 2.00mm/s. b) accompanying $[1\,\bar{1}\,\bar{2}]_{Al_6Fe}$ SADP.

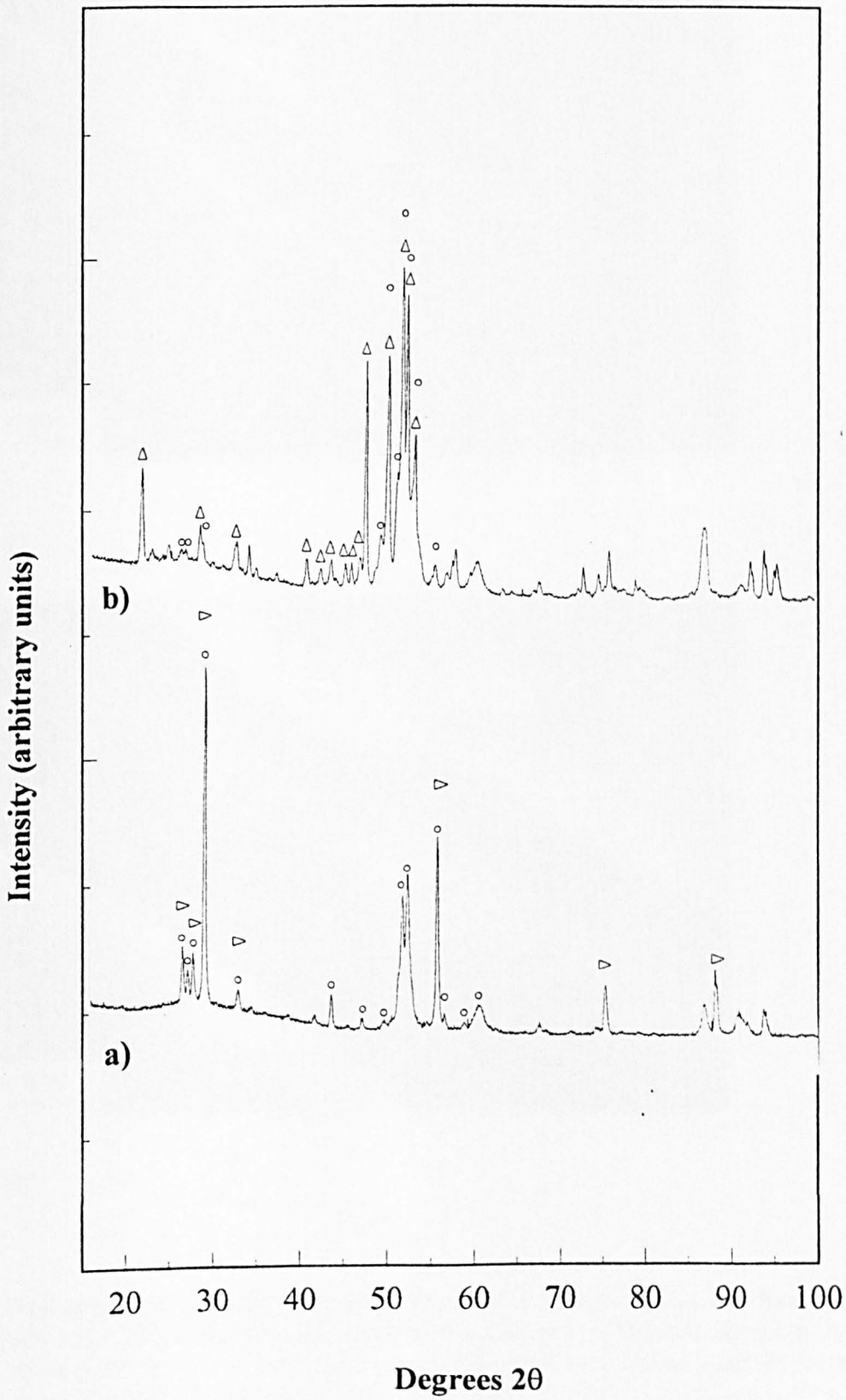

Fig.4.10: X-ray diffraction patterns of second phase intermetallics extracted, by the butanol reflux method, from Al-0.5%Fe-0.1%Si alloy specimens which had been unidirectionally solidified at a) 0.05mm/s and b) 0.50mm/s.

Key: ○ - $Al_{13}Fe_4$, △ -Al_6Fe, ▷ -Al_xFe.

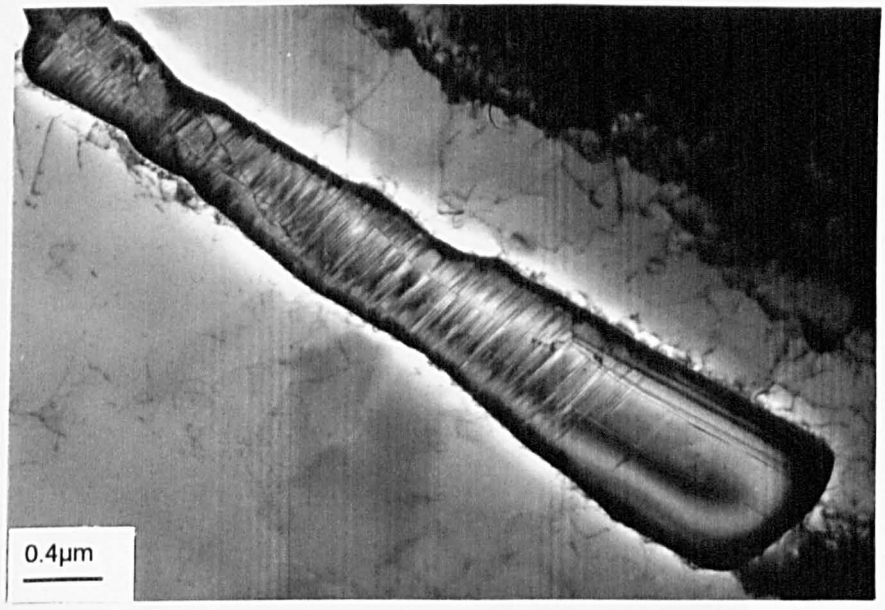

a)

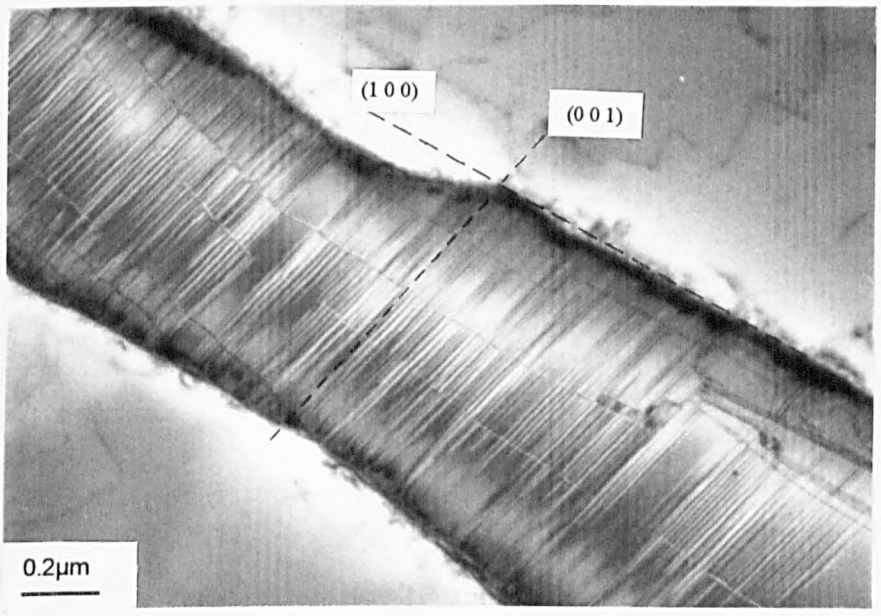

b)

Fig.4.11: Transverse section electron micrograph a) of a typical $Al_{13}Fe_4$ lath found in Al-0.5%Fe-0.1%Si after unidirectional solidification with V = 0.10mm/s, showing the presence of contrast bands on both (001) and (100): and b) a higher magnification micrograph showing details of these faults. The SADP c) shows $[010]_{Al_{13}Fe_4}$ to be almost coincident with $[100]_{\alpha\text{-Al}}$, the two being separated by a very small angle determined experimentally as approximately 2 degrees.

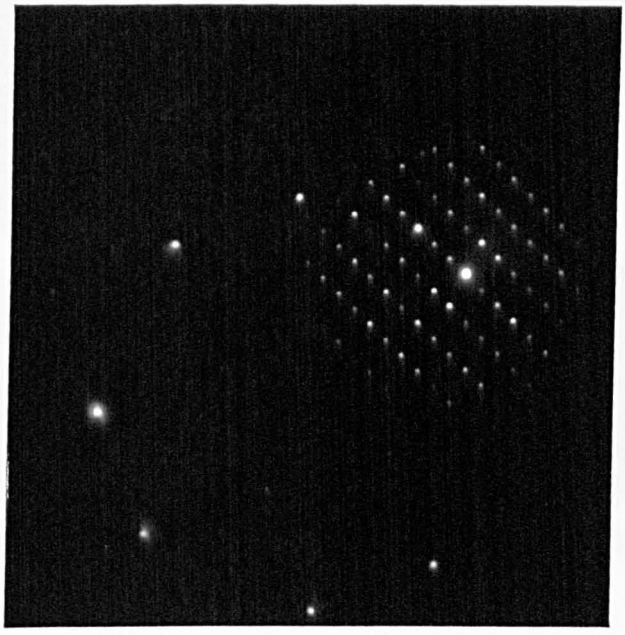

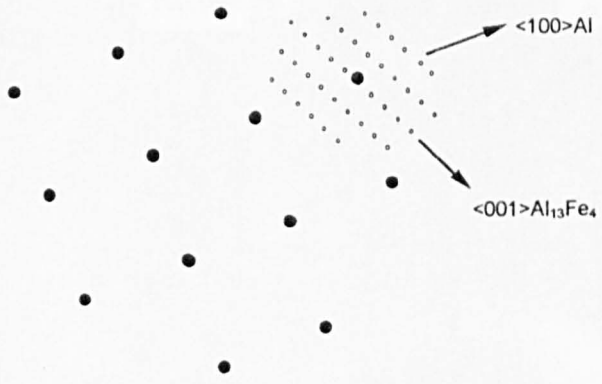

c)

Fig.4.11: continued.

a)

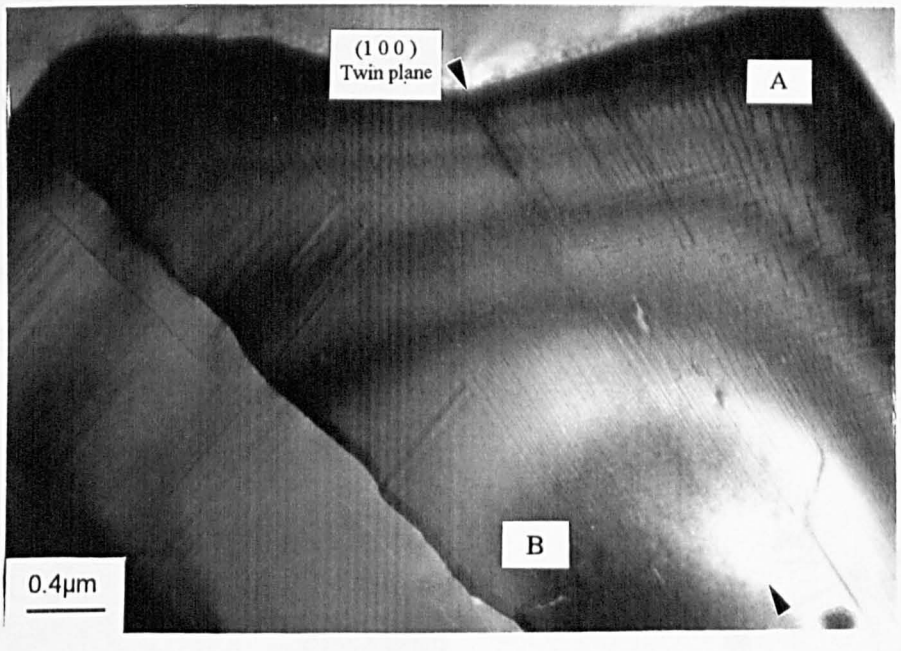

b)

Fig.4.12: Transverse section electron micrograph a) of a fan-shaped $Al_{13}Fe_4$ crystal group found in a specimen taken from an Al-0.5%Fe-0.1%Si alloy rod which had been unidirectionally solidified at 0.10mm/s, showing the presence of contrast bands on both (001) and (100): and b) a higher magnification micrograph showing details of these faults. The presence of these defects gives rise to streaking in both a* and c* in the corresponding $\langle 010 \rangle_{Al_{13}Fe_4}$ SADP (c and d). The larger of these crystals was observed to contain a single 100 twin plane at the position indicated, from which the diffraction pattern, e, was taken. The crystal on either side of this twin plane was observed to be in different orientations the region marked A being imaged with the electron beam near to $[010]_{Al_{13}Fe_4}$ (c), whilst B is imaged with $\mathbf{B}=\mathbf{Z}=[0\,\bar{1}\,0]$ (d).

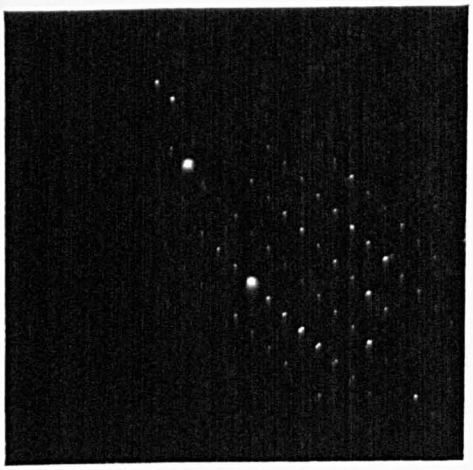

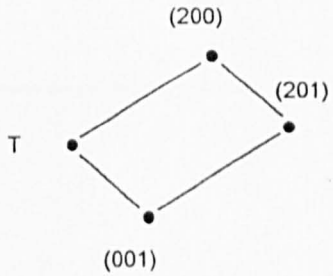

c)

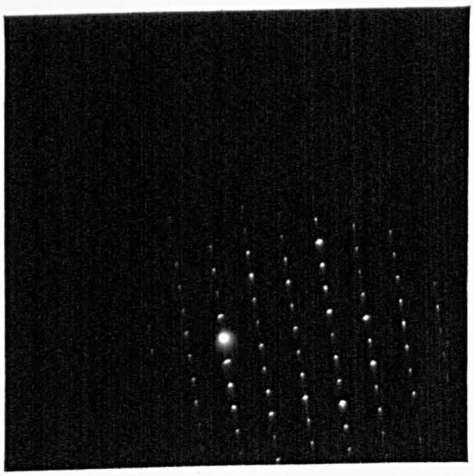

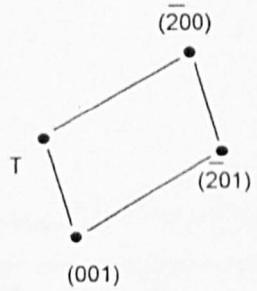

d)

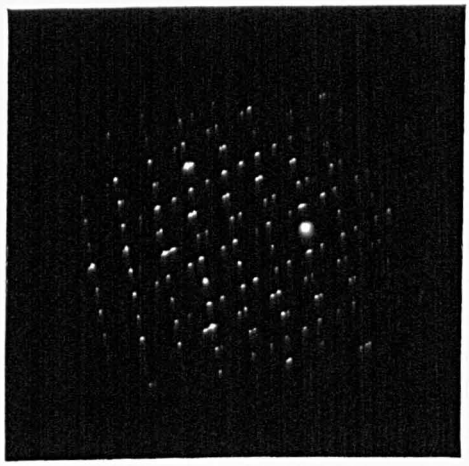

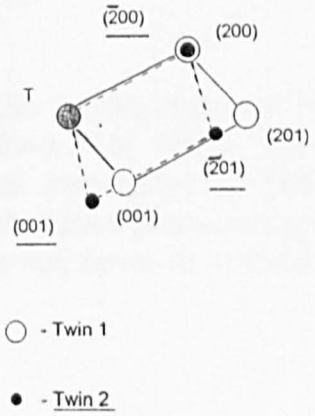

e)

Fig.4.12: continued.

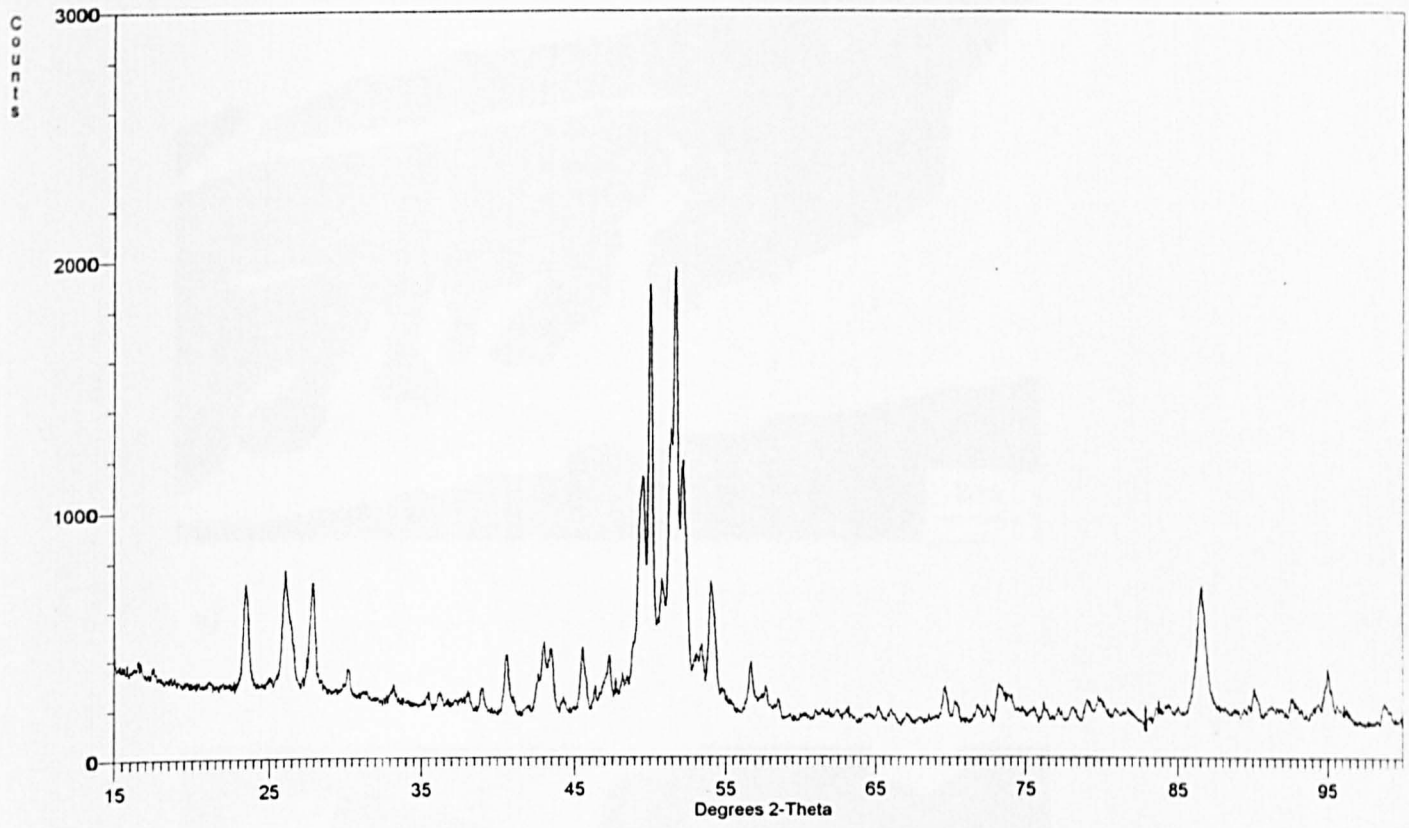

Fig.4.13: X-ray diffraction trace taken from intermetallic residue extracted by the butanol reflux method from a sample of Al-0.5%Fe-0.1%Si which had been unidirectionally solidified at 1.00mm/s. This residue was investigated by TEM and found to give rise to SADP which could be solved using the lattice parameters given by Young and Clyne [1981] for Al_xFe. The x-ray trace does not, however, correlate well with that given for Al_xFe by Young and Clyne (Table3.9).

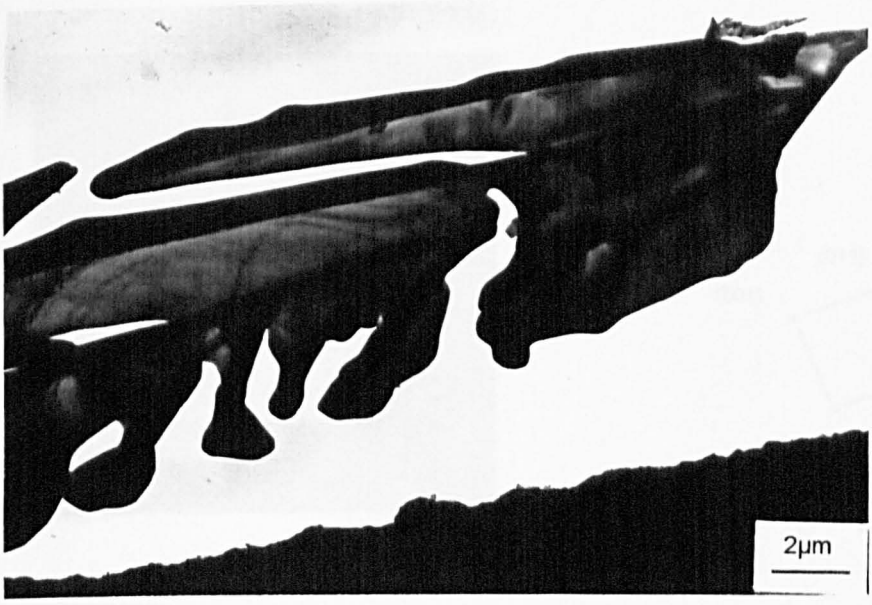

a)

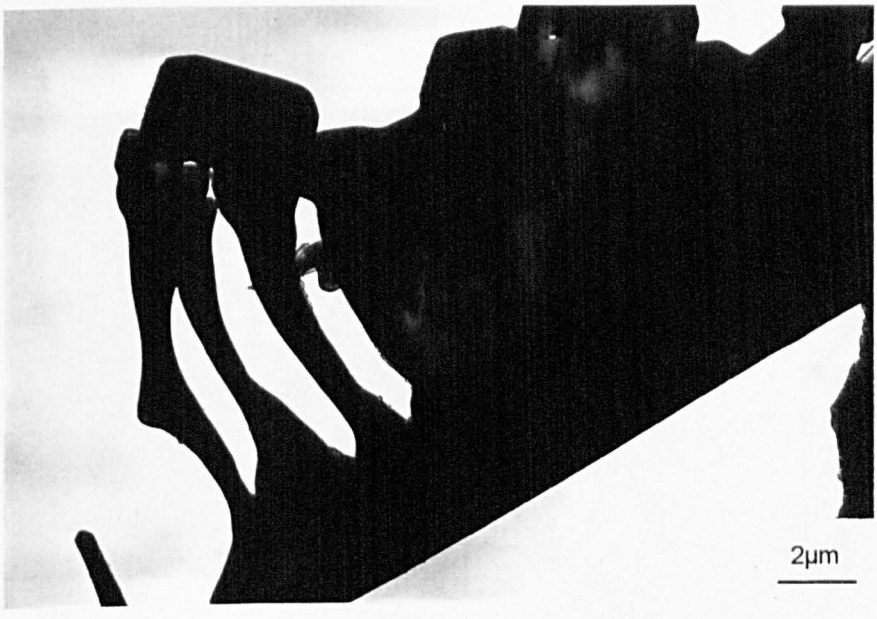

b)

Fig.4.14: a and b Typical morphology of Al_xFe crystals extracted from an Al-0.5%Fe-0.1%Si specimen which had been unidirectionally solidified at 0.10mm/s.

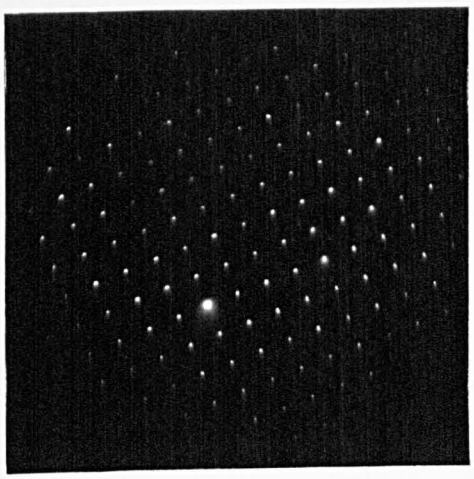

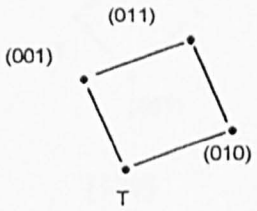

$[\bar{1}00]$

a)

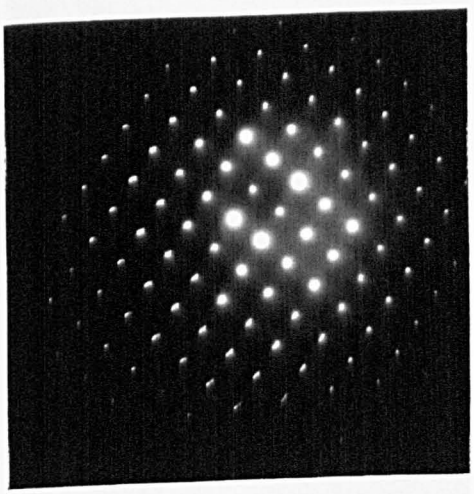

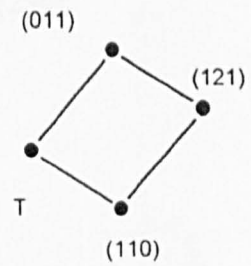

$[\bar{1}1\bar{1}]$

b)

Fig.4.15: a to e) Principal electron diffraction patterns taken from the Al_xFe phase together with indexations based upon the monoclinic crystal structure proposed Clyne [1981]. The measurements of interplanar angles and the ratios of spacings in reciprocal space are presented in Tables 4.8 to 4.12 where they are compared with those calculated based on the lattice parameters determined by Young and Clyne [1981].

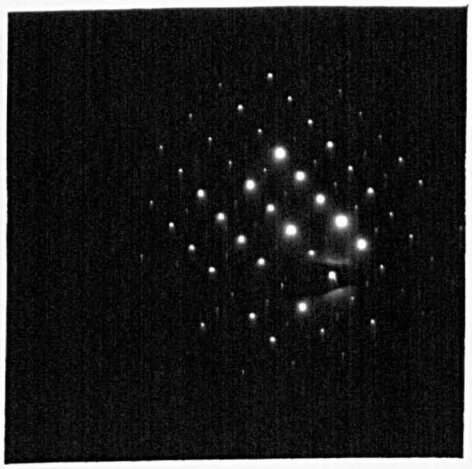

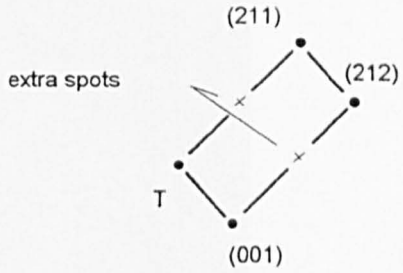

$[1\bar{2}0]$

c)

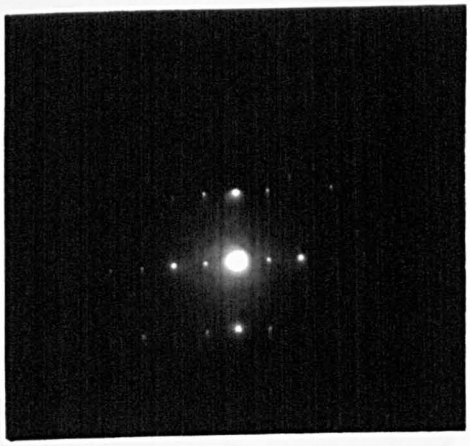

$[2\bar{3}0]$

d)

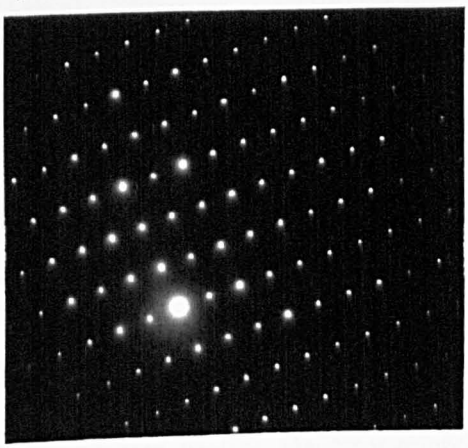

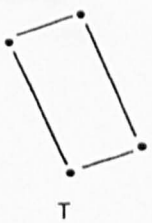

Incommensurate zone

e)

Fig.4.15: continued.

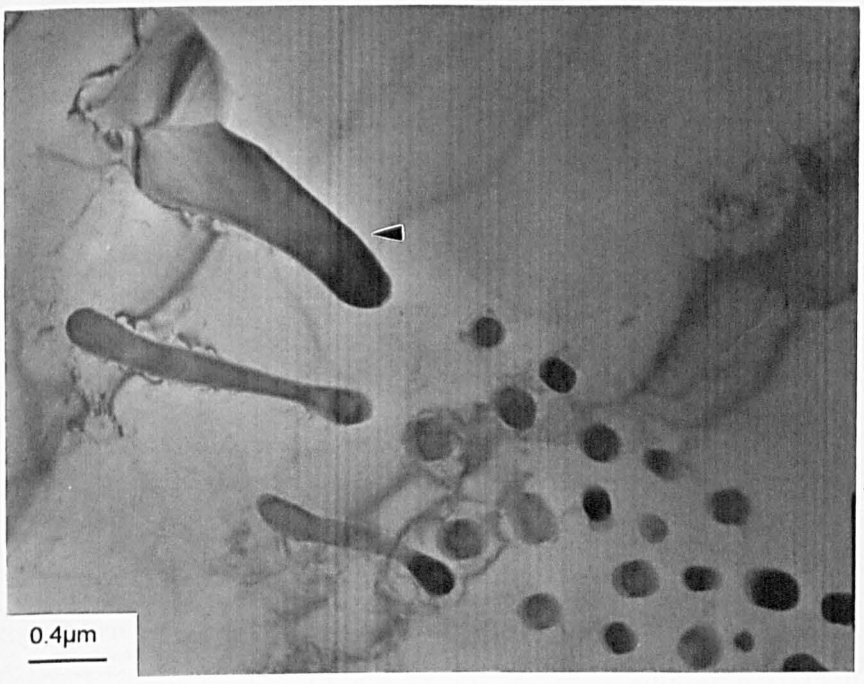

a)

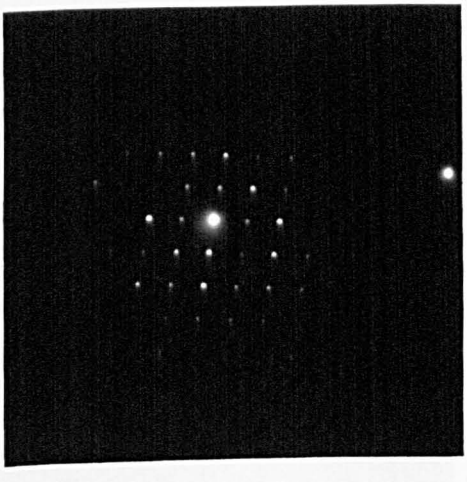

b)

Fig.4.16: Transverse section electron micrograph a) of a cluster of Al_xFe crystals and b) the corresponding SADP, taken from the crystal indicated by the arrow, showing the beam direction to be near to $[\bar{1}1\bar{1}]_{Al_xFe}$. This grouping was observed in Al-0.5%Fe-0.1%Si solidified at 2.00 mm/s. Note that the morphology of this group of Al_xFe crystals is very similar to that of the Al_6Fe eutectic grouping shown in Fig.4.9.

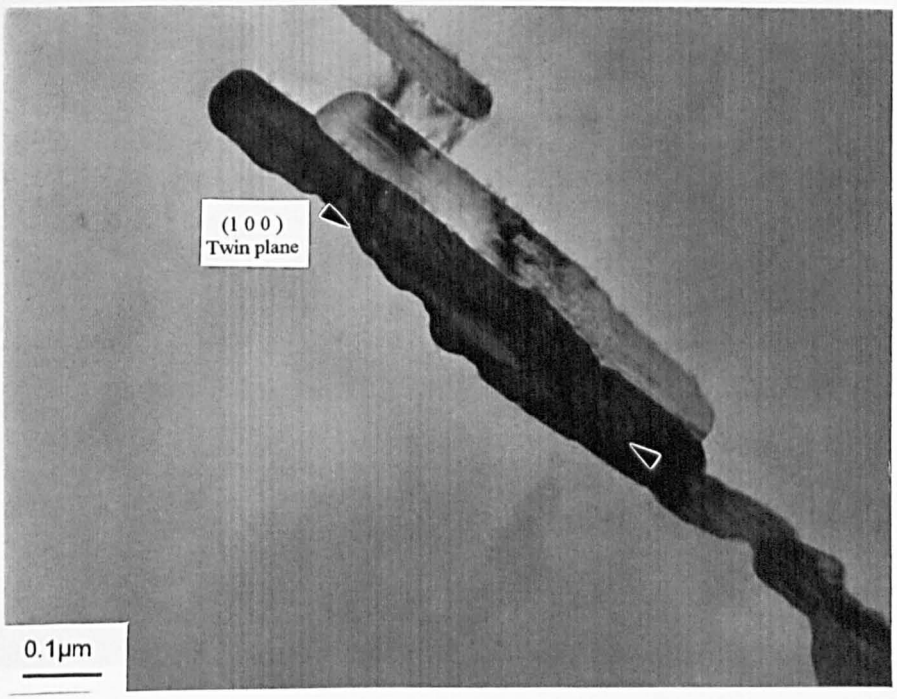

a)

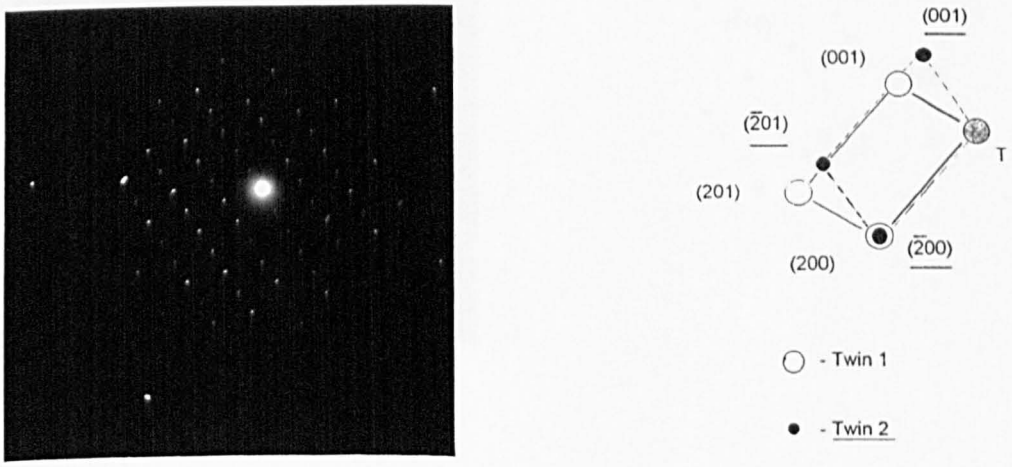

b)

Fig.4.17: Transverse section electron micrograph a) showing the morphology of $Al_{13}Fe_4$ intermetallics observed in Al-0.5%Fe-0.1%Si unidirectionally solidified at 2.00mm/s. These crystals show a high density of (100) faults but no evidence of any (001) type defects. One of the crystals also contains a single (100) twin plane at the position indicated from which the $[010]_{Al_{13}Fe_4}$ SADP b) was taken.

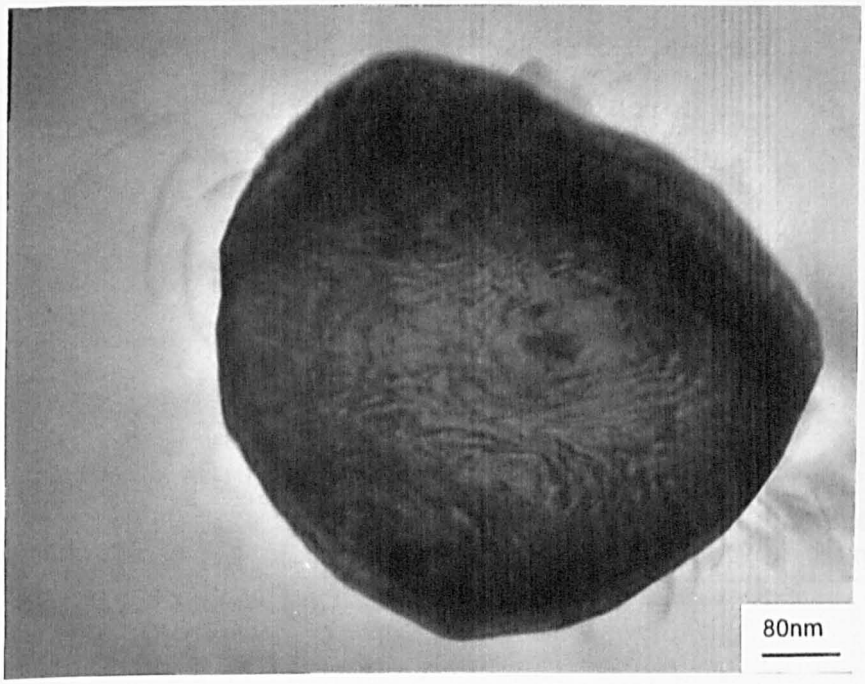

a)

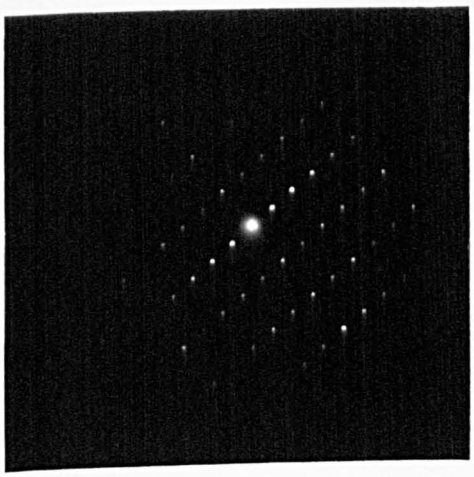

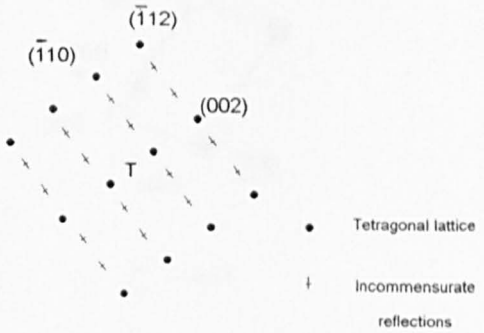

b)

Fig.4.18: a) Typical example of an Al_mFe particle observed in an Al-0.5%Fe-0.1%Si alloy unidirectionally solidified with V= 2.00mm/s taken with **B**=**Z**=[110]$_{Al_mFe}$ b). Note the presence of extra relections in [110]* in the SADP.

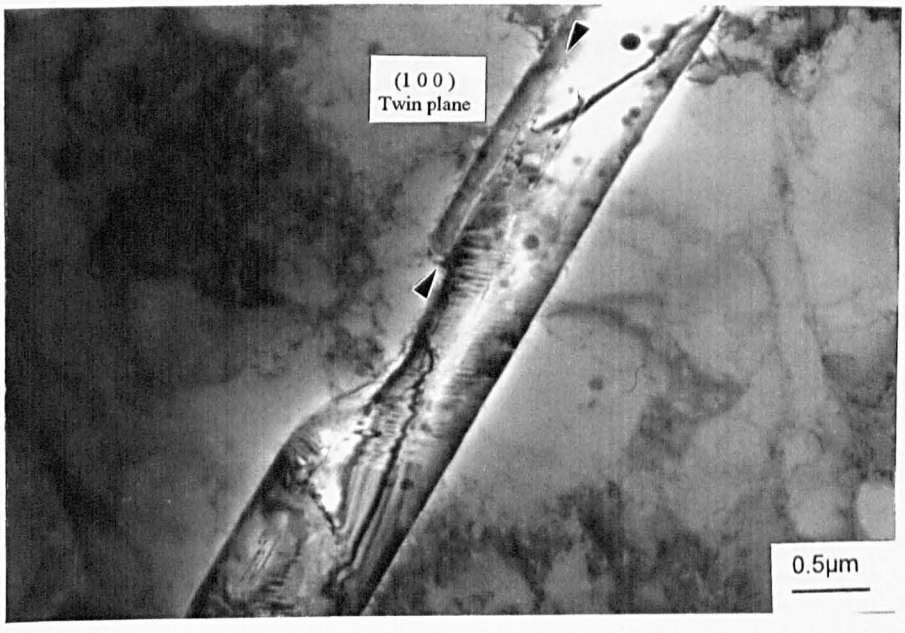

a)

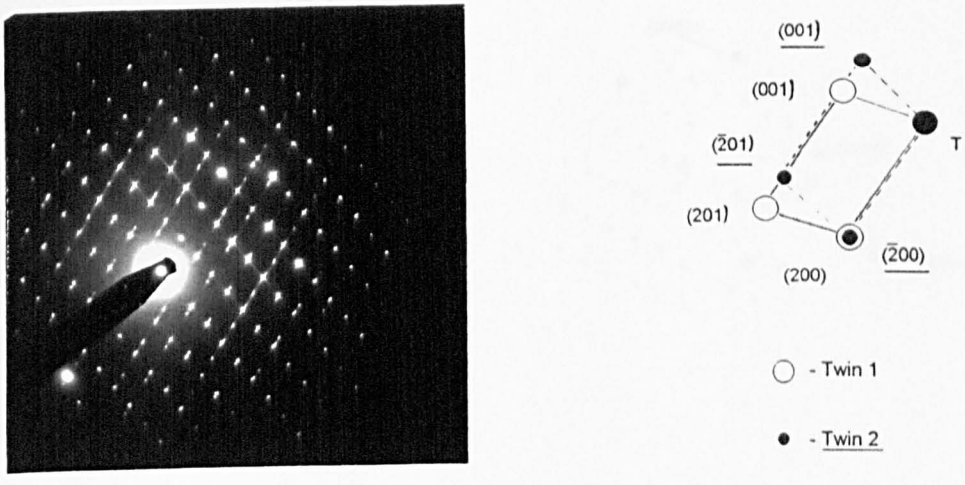

b)

Fig.4.19: Transverse section electron micrograph a) of an $Al_{13}Fe_4$ crystal observed in an Al-0.25%Fe-0.1%Si-0.5%Mg alloy specimen which had been unidirectionally solidified at 0.05 mm/s. The electron diffraction pattern b) confirms that this crystal contains a single (100) twin plane, the position of which is indicated. There is also evidence of streaking in both the (100) and (001) reciprocal lattice vector rows in this $[010]_{Al_{13}Fe_4}$ SADP indicating the presence of fine (001) and (100) faults although it is clear that only the (100) faults have sharply defined boundaries in this micrograph.

a)

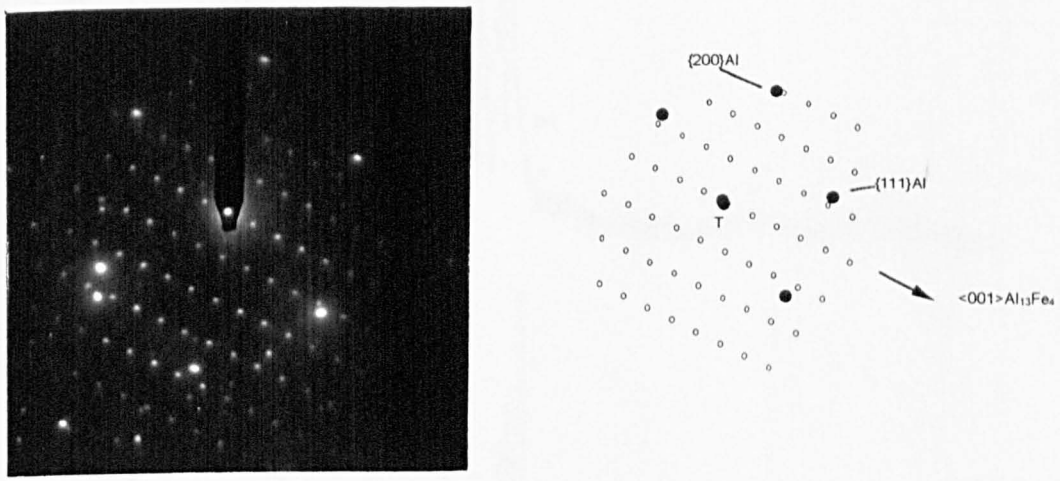

b)

Fig.4.20: Transverse section a) through a cluster of $Al_{13}Fe_4$ crystals found within an α-Al cell in an Al-0.25%Fe-0.1%Si-0.5%Mg alloy specimen which had been unidirectionally solidified at 0.05 mm/s Numerous (001) and (100) faults are evident. (100) twin planes are also present in a number of the crystals. The position of one such defect is indicated by means of an arrow. The diffraction pattern, b), shows $[010]_{Al_{13}Fe_4}$ to be near-coincidental with $\langle 110 \rangle_{\alpha\text{-Al}}$.

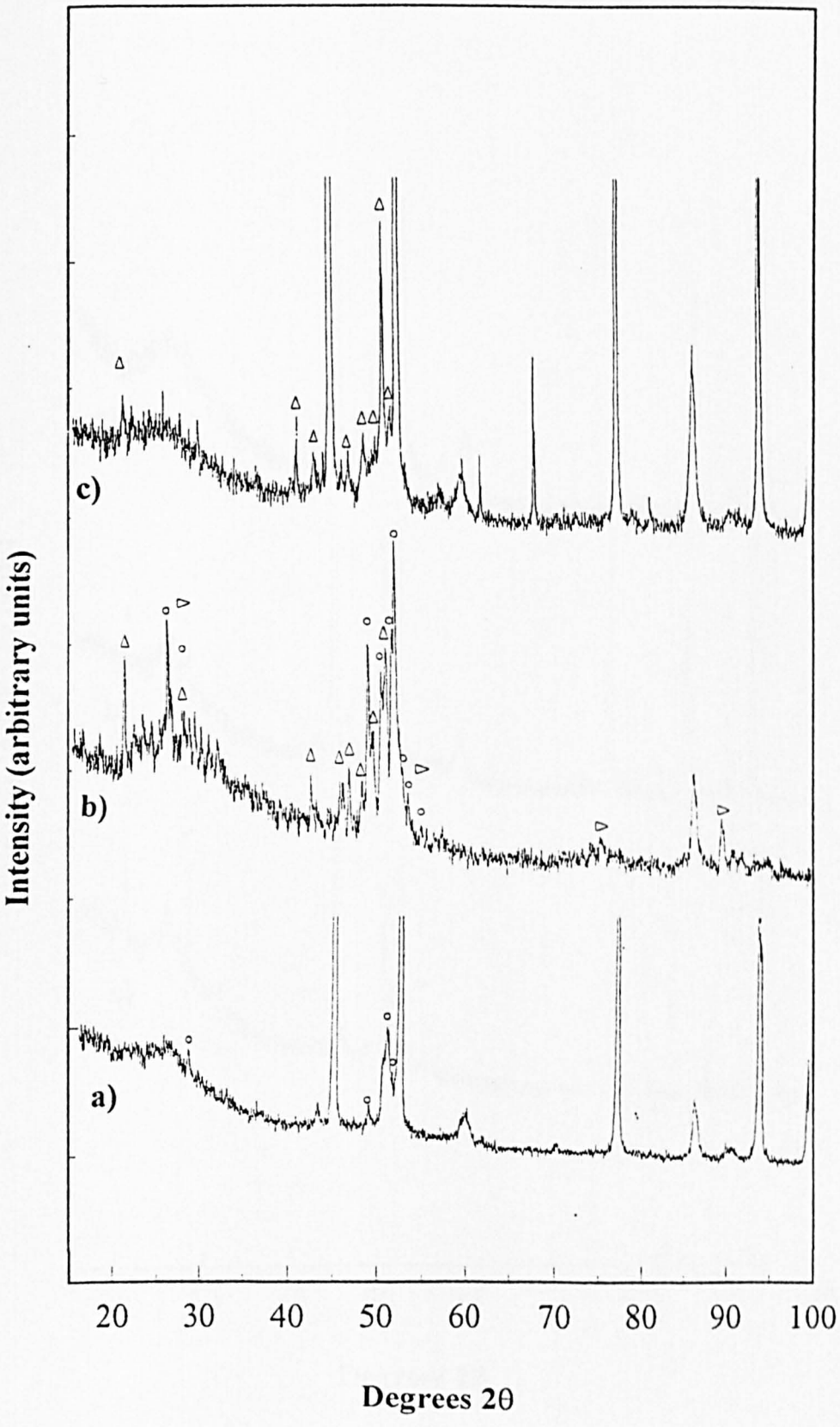

Fig.4.21: X-ray diffraction trace taken from intermetallics extracted from Al-0.25%Fe-0.1%Si-0.5%Mg solidified at a) 0.10mm/s, b) 0.50mm/s and c) 2.00mm/s respectively. The traces a and c were taken from HCl extracted material whilst b was produced from butanol extracted intermetallics.

Key: ○ - $Al_{13}Fe_4$, Δ -Al_6Fe, ▷ -Al_xFe.

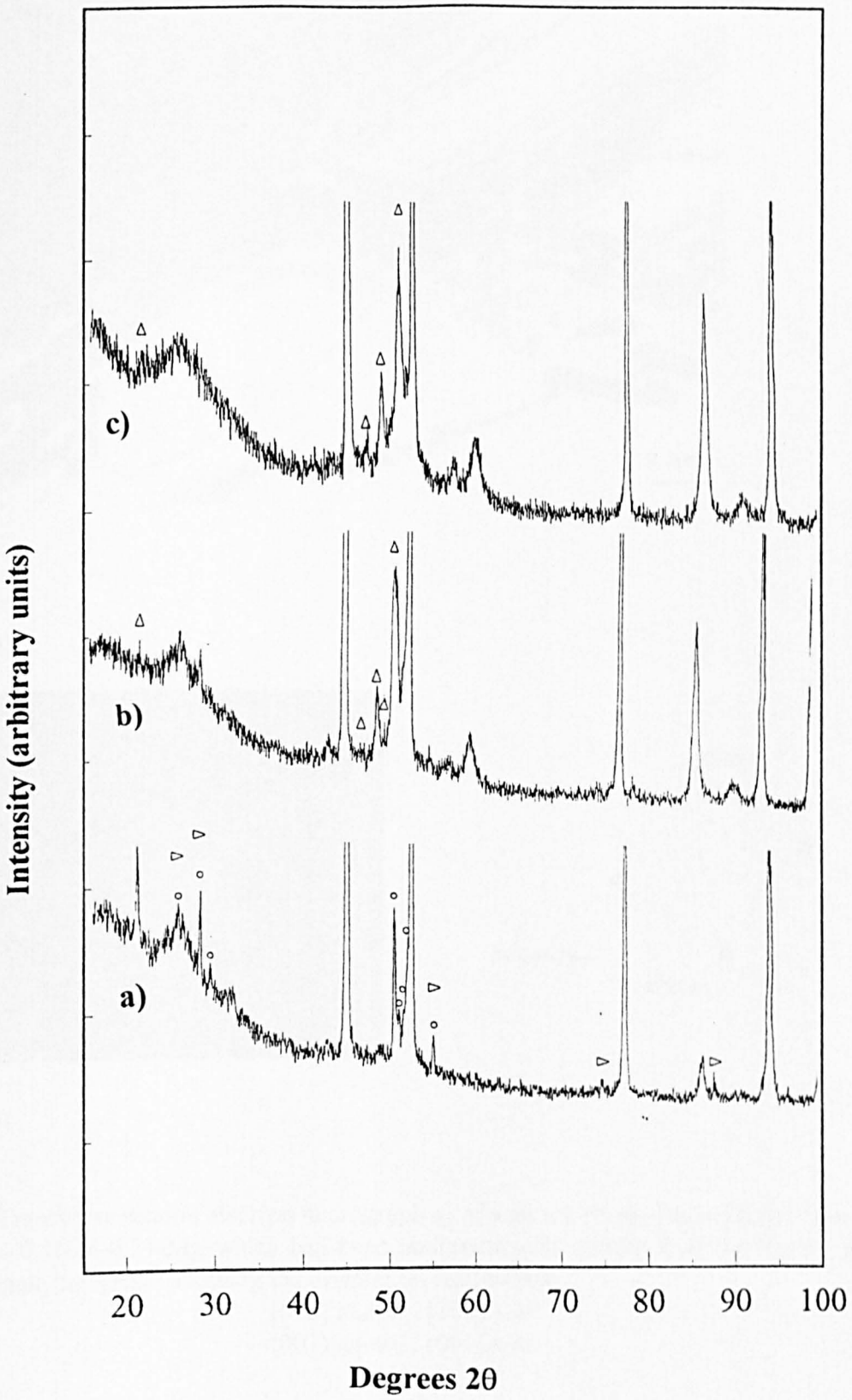

Fig.4.22: X-ray diffraction trace taken from intermetallics extracted, by the HCl method, from Al-0.5%Fe-0.1%Si-0.5%Mg alloy specimens which had been unidirectionally solidified at a) 0.10mm/s, b) 1.00mm/s and c) 2.00mm/s.

Key: ○ - $Al_{13}Fe_4$, △ -Al_6Fe, ▷ -Al_xFe.

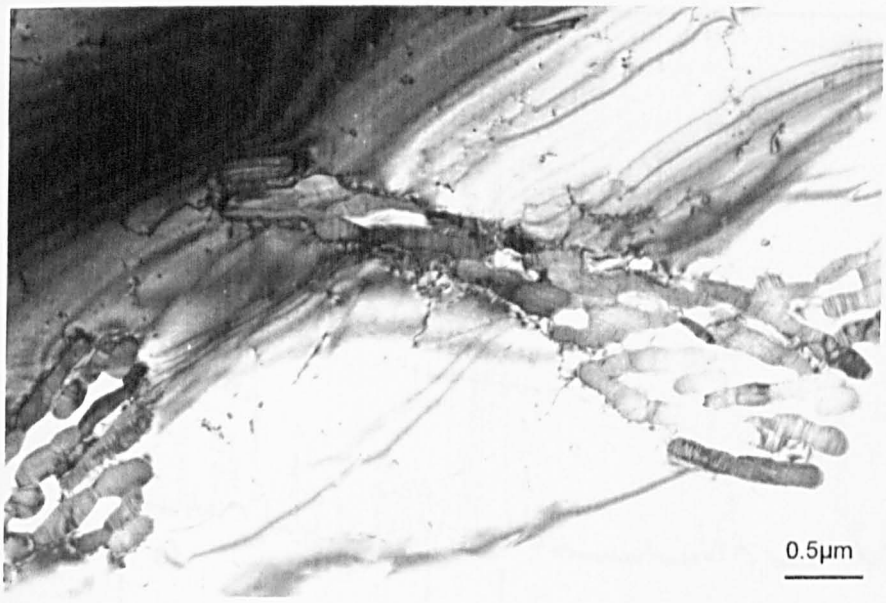

a)

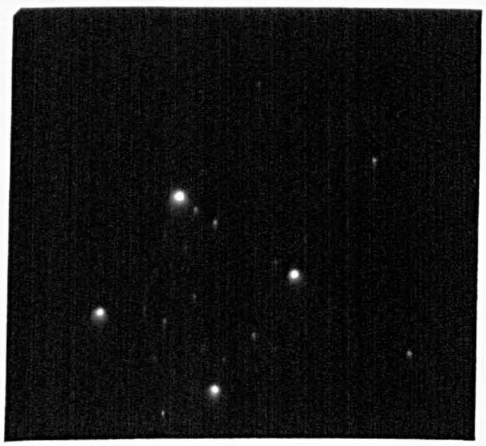

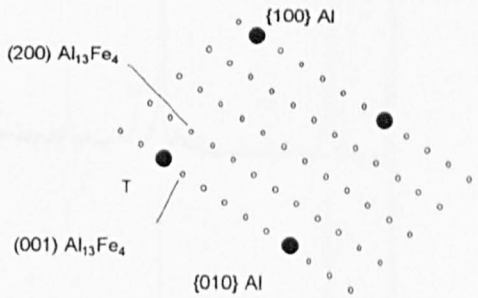

b)

Fig.4.23: Transverse section electron micrograph a) of a group of $Al_{13}Fe_4$ crystals observed in Al-0.5%Fe-0.1%Si-0.5%Mg which had been unidirectionally solidified at 0.50mm/s; and b) the accompanying SADP showing the orientation relationship:

$[010]\ Al_{13}Fe_4 \,||\, [100]\ \alpha\text{-Al}$

$(001)\ Al_{13}Fe_4 \,||\, (001)\ \alpha\text{-Al}$

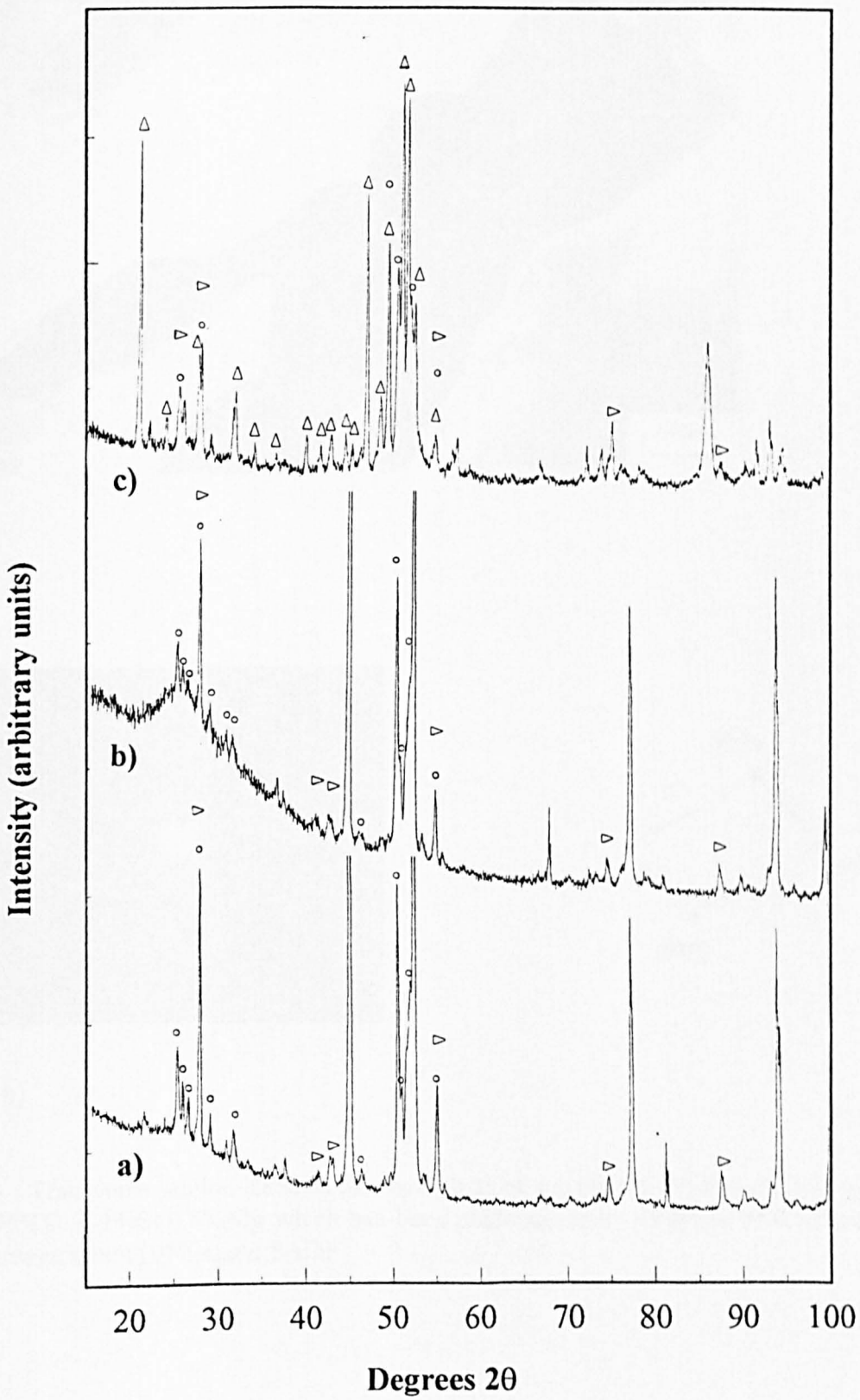

Fig.4.24: X-ray diffraction traces taken from intermetallics extracted from Al-0.75%Fe-0.1%Si-0.5%Mg which had been unidirectionally solidified at a) 0.05mm/s, b) 0.10mm/s and c) 1.00mm/s respectively. Traces a and b were taken from material extracted by the HCl method whilst c was taken from butanol extracted residue.

Key: ○ - $Al_{13}Fe_4$, △ -Al_6Fe, ▷ -Al_xFe.

a)

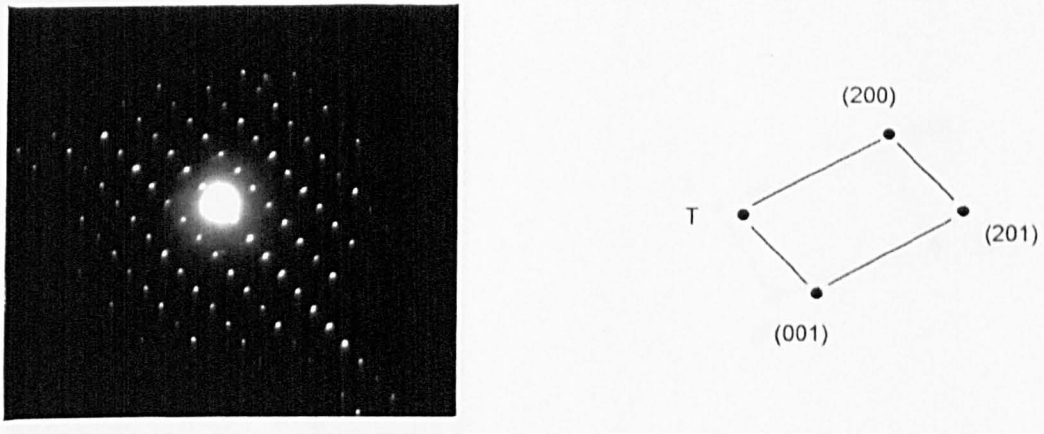

b)

Fig. 4.25 : Transverse section electron micrograph a) of a group of $Al_{13}Fe_4$ crystals observed in Al-0.75%Fe-0.1%Si-0.5%Mg which had been unidirectionally solidified at 0.50 mm/s:and b) the corresponding $[010]_{Al_{13}Fe_4}$ SADP.

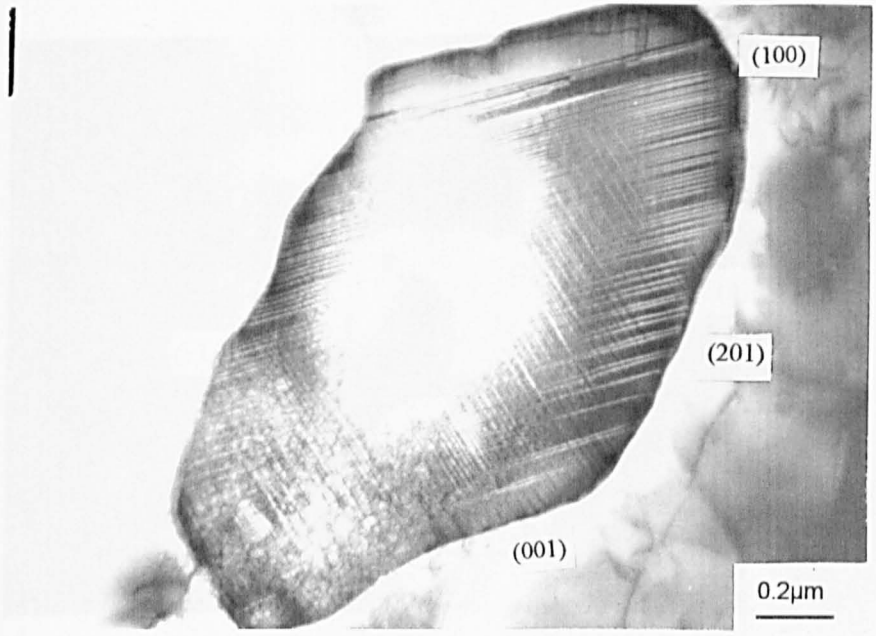

a)

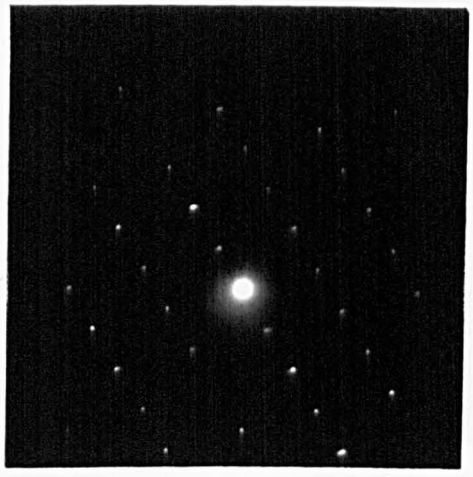

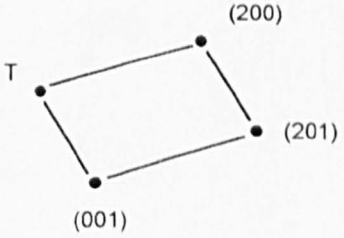

b)

Fig.4.26: Transverse section a) of an $Al_{13}Fe_4$ crystal found in a sample of Al-0.75%Fe-0.1%Si-0.5%Mg alloy which had been unidirectionally solidified at 0.50mm/s; and b) the corresponding [010] $Al_{13}Fe_4$ SADP. The fine contrast bands arise from both (001) and (100) type crystallographic faults. The prismatic planes of the intermetallic are indexed based on the assumption that the axis of the crystal was perpendicular to the [010] electron beam direction.

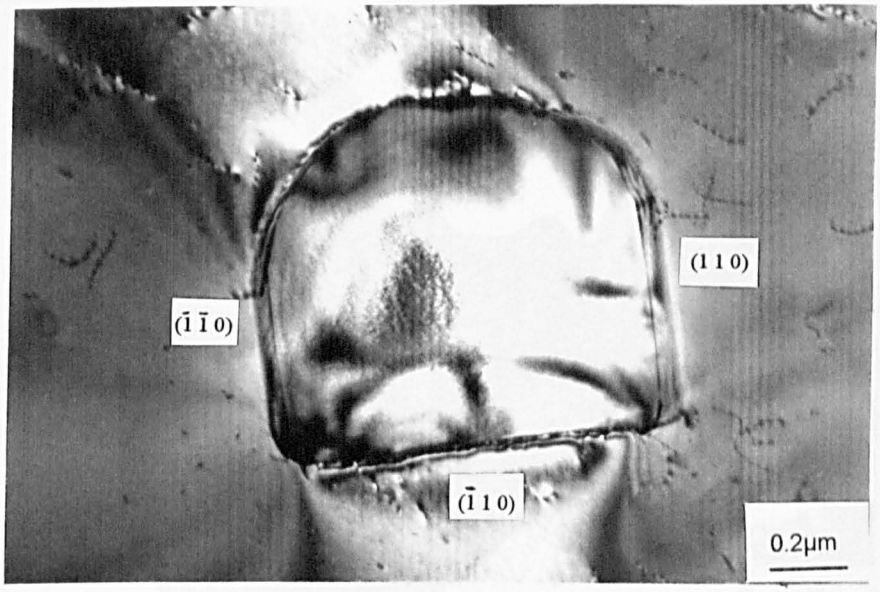

a)

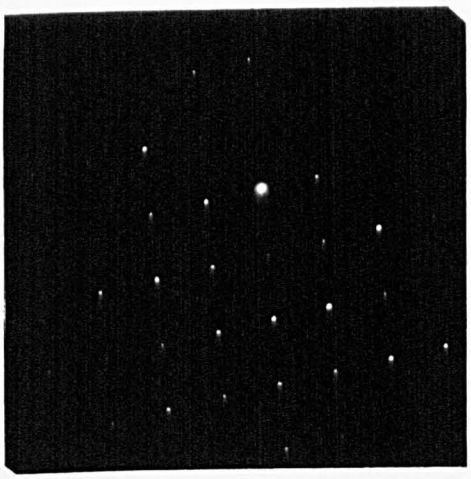

b)

Fig.4.27: Transverse section electron micrograph a) showing a typical, faceted, Al_6Fe crystal found in Al-0.75%Fe-0.1%Si-0.5%Mg which had been unidirectionally solidified at 0.50 mm/s. If the assumption is made that the axis of the intermetallic crystal is parallel to the electron beam direction then the primatic face orientations are found to be close to {110} as indicated.

a)

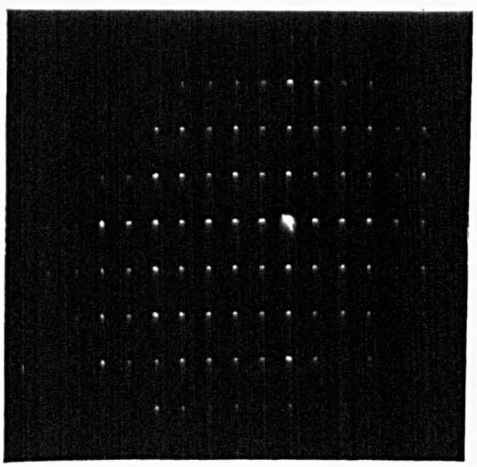

b)

Fig.4.28: TEM micrograph showing the morphology of a typical Al_mFe crystal, extracted from a specimen of Al-0.75%Fe-0.1%Si-0.5%Mg alloy which had been unidirectionally solidified at 2.00mm/s: and b) Corresponding SADP showing the [110] zone of Al_mFe. Note the presence of diffuse scattering between the diffraction maxima.

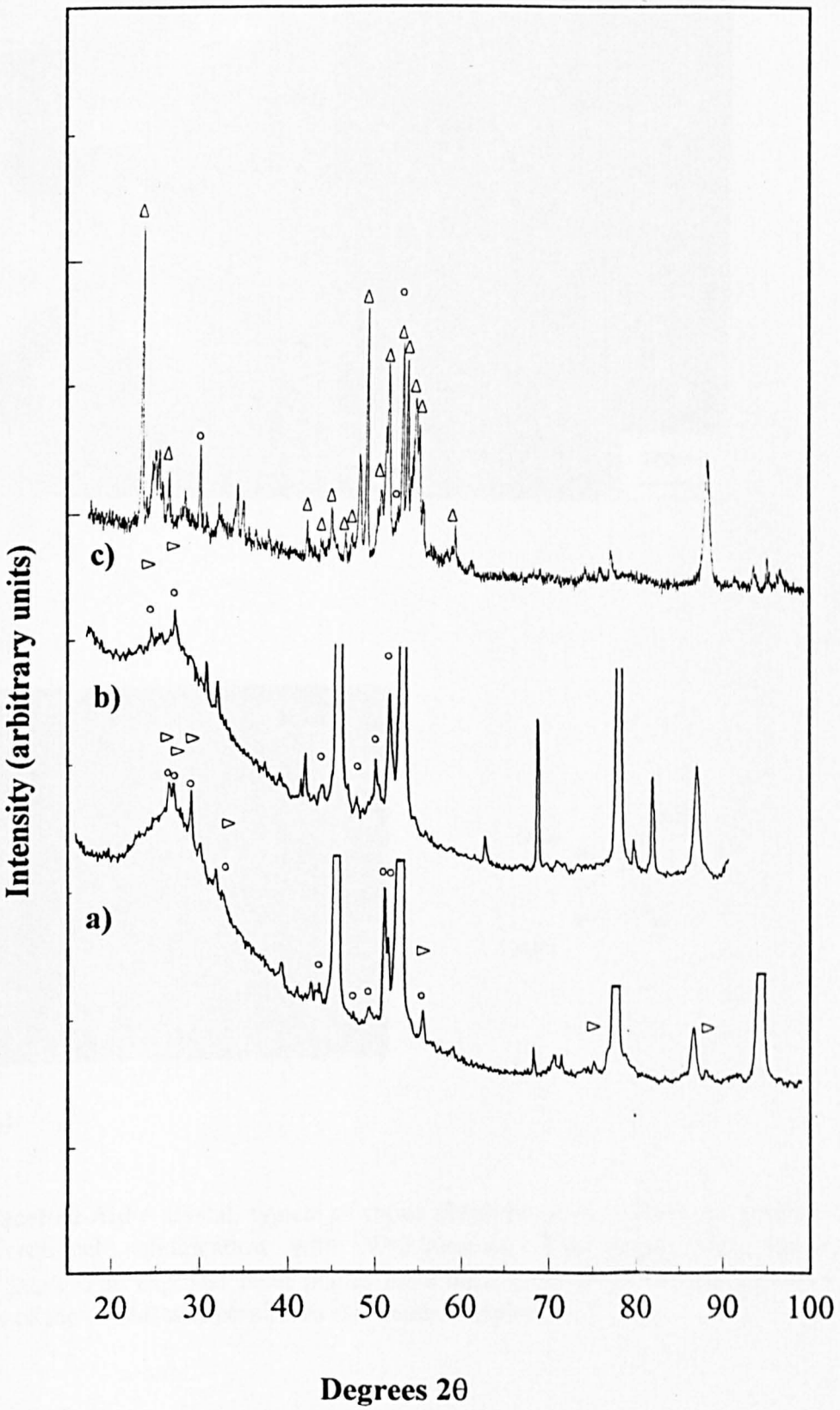

Fig.4.29: X-ray diffraction traces of second phase intermetallics extracted from Al-0.25%Fe-0.1%Si-0.75%Mg specimens which had been unidirectionally solidified at a) 0.10mm/s, b) 0.50mm/s and c) 1.00mm/s. Traces a and b are taken from HCl extracted intermetallics whilst c is taken from butanol extracted material.

Key: ○ - $Al_{13}Fe_4$, △ -Al_6Fe, ▷ -Al_xFe.

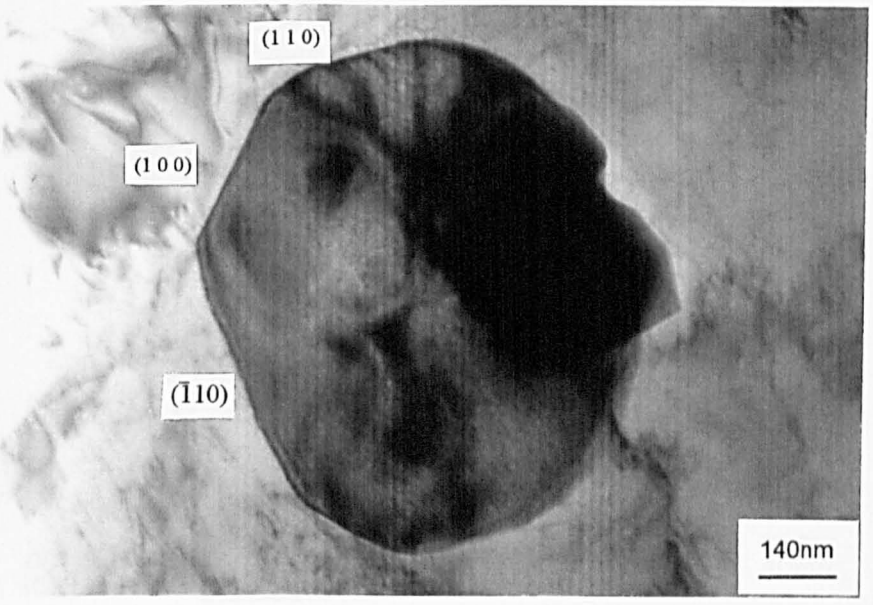

a)

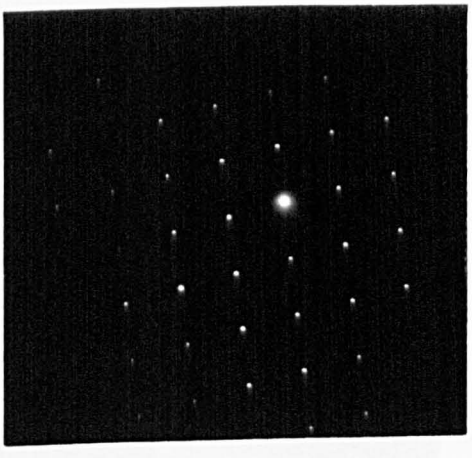

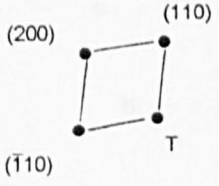

b)

Fig.4.30: Facetted Al_6Fe crystal, typical of those observed in Al-0.25%Fe-0.1%Si-0.75%Mg after unidirectional solidification with V=2.00mm/s. This image was formed with $\mathbf{B}=\mathbf{Z}=[00\bar{1}]_{Al_6Fe}$. The exposed facet planes have been indexed on the assumption that the growth axis of the crystal was parallel to this beam direction.

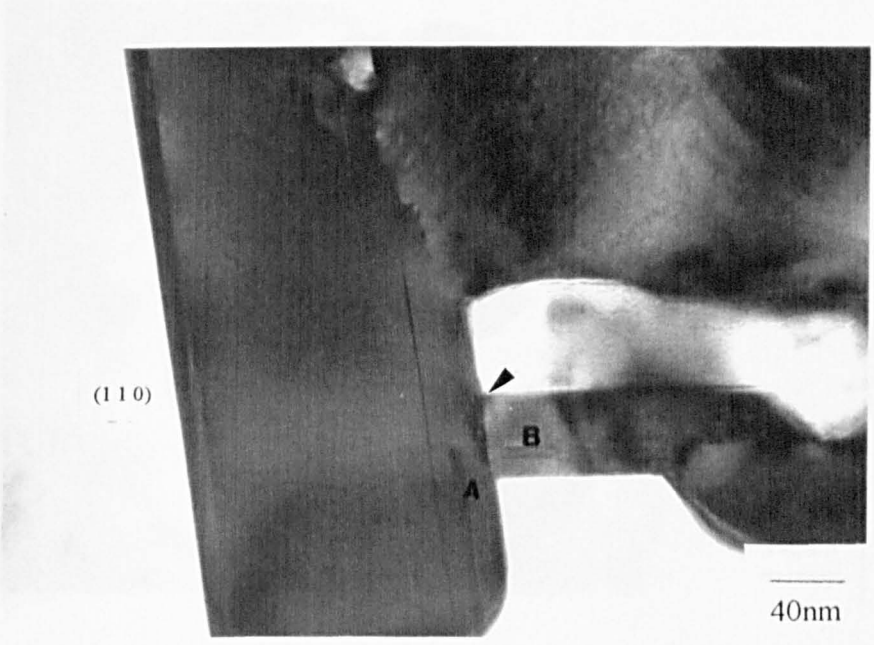

a)

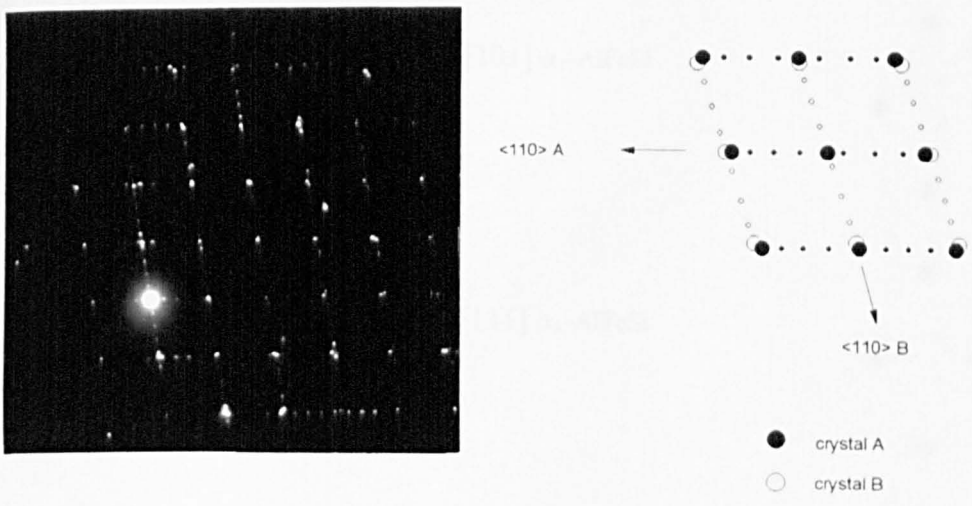

b)

Fig.4.31: Transverse section electron micrograph showing detail of {110} faulting in an Al_6Fe crystal group observed in an Al-0.25%Fe-0.1%Si-0.75%Mg alloy specimen which had been unidirectionally solidified at 2.00mm/s. The average spacing of these defects has been measured as approximately 2nm which correlates well with the spacing of the incommensurate [110]* reflections in the accompanying $[001]_{Al_6Fe}$ SADP, b, which was taken at the position arrowed on the micrograph. It is also interesting to note that the interface between the faulted and unfaulted Al_6Fe crystals forms as a series of steps.

a)

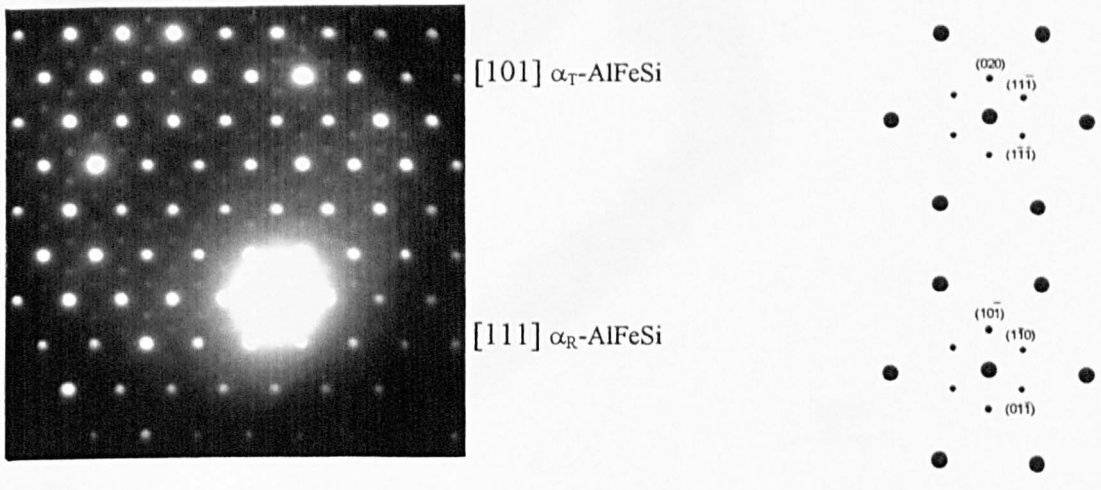

b)

Fig.4.32: Transverse section electron micrograph of a group of α-AlFeSi type intermetallics observed in Al-0.25%Fe-0.1%Si-0.75%Mg which had been unidirectionally solidified at 2.00mm/s. The accompanying SADP, b, can be indexed successfully using either, the lattice parameters of Hoier [1985] for the monoclinic α_T-AlFeSi phase or those proposed by Liu and Dunlop [1988] for the rhombohedral superlattice of α-AlFeSi termed α_R , as shown.

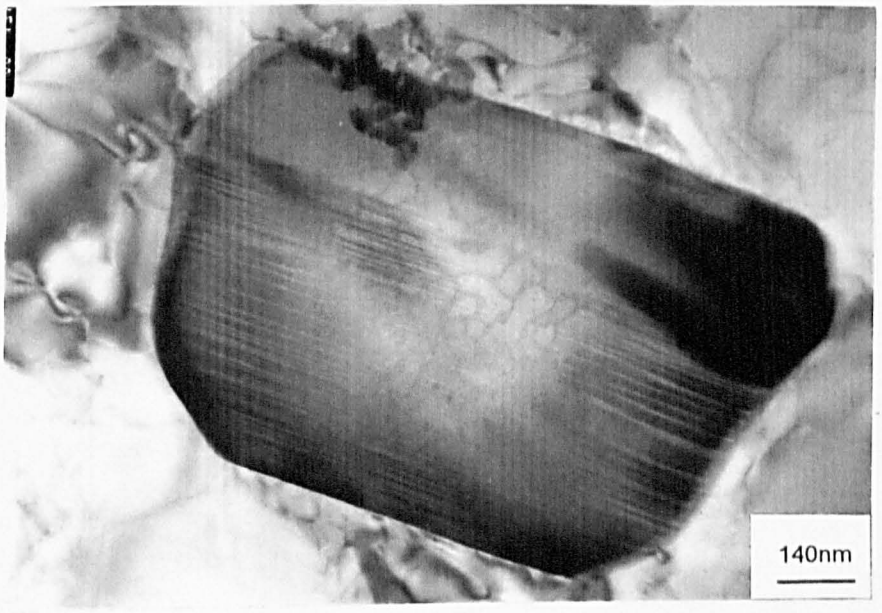

a)

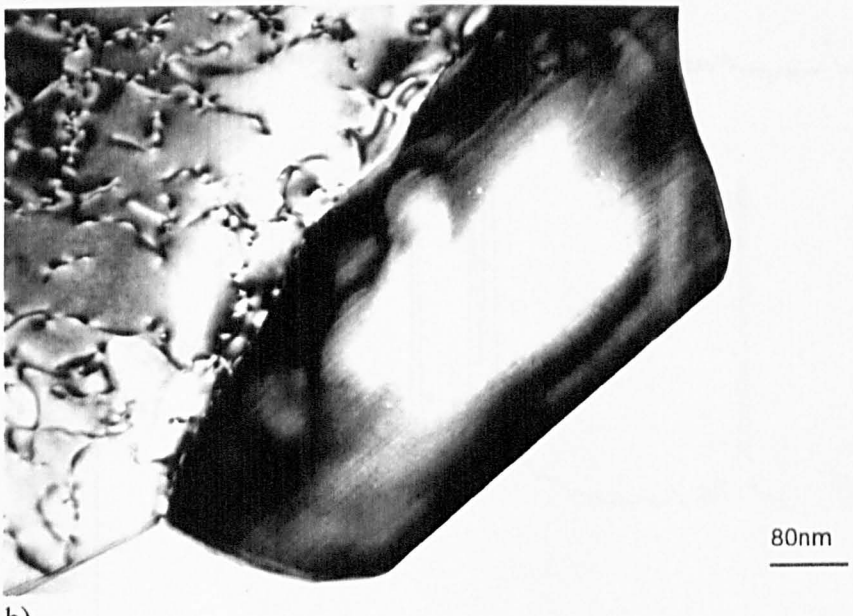

b)

Fig.4.33: a and b) Transverse section electron micrographs showing typical morphologies of $Al_{13}Fe_4$ found at α-Al cell boundaries in Al-0.25%Fe-0.1%Si-0.75%Mg which had been unidirectionally solidified at V=2.00mm/s. Both crystals shown contain (100) crystallographic faults and display no sign of (001) faulting.

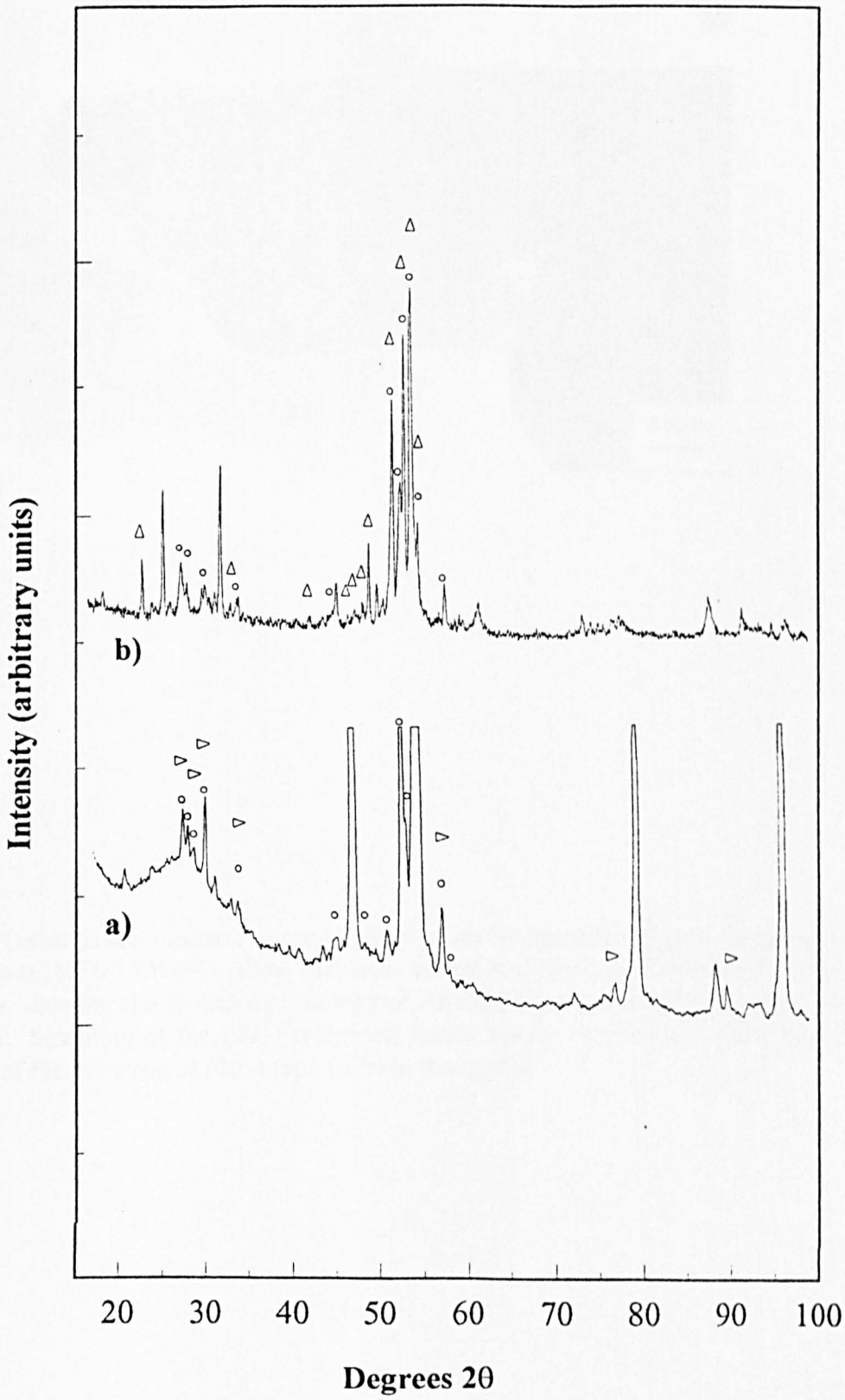

Fig.4.34: X-ray diffraction traces of second phase intermetallics extracted from Al-0.5%Fe-0.1%Si-0.75%Mg unidirectionally solidified at a) 0.05mm/s and b) 1.00mm/s respectively. The intermetallics were extracted by the HCl method in the case of a and by the butanol method in b.

Key: ○- $Al_{13}Fe_4$, Δ -Al_6Fe, ⊳ -Al_xFe.

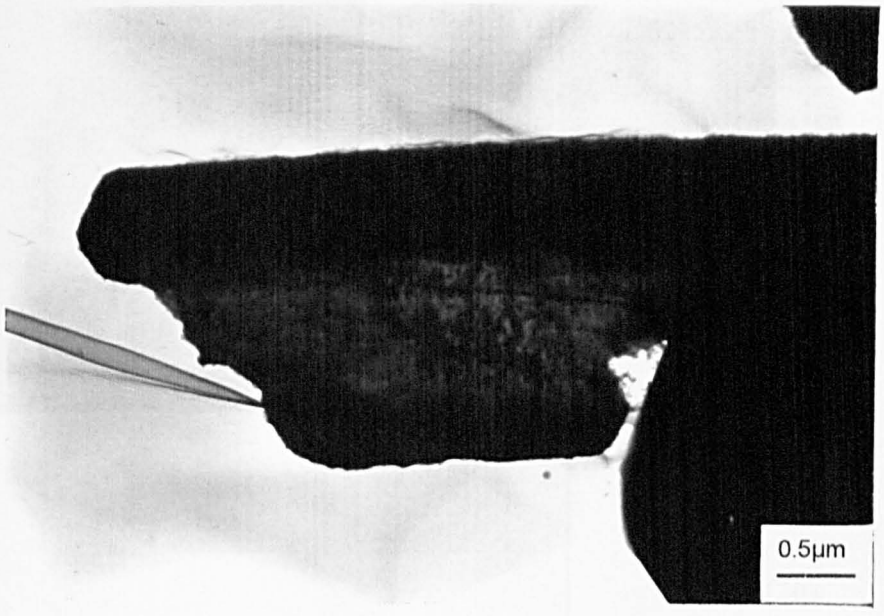

a)

Fig.4.35: Transmission electron micrograph a) of an intermetallic crystal extracted from an Al-0.5%Fe-0.1%Si-0.75%Mg alloy specimen which had been unidirectionally solidified at 0.10 mm/s, showing the typical morphology of $Al_{13}Fe_4$. b) and c), two zone axes taken from this crystal. Streaking of the (001) reciprocal lattice vector rows in the $[\bar{1}10]$ projection is indicative of the presence of (001) type faults in the crystal.

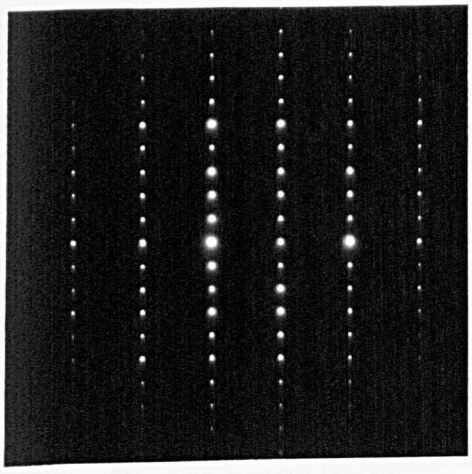

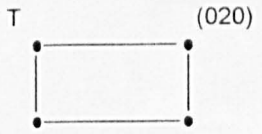

$[\bar{1}\,0\,0]Al_{13}Fe_4$

b)

27.54° (26)

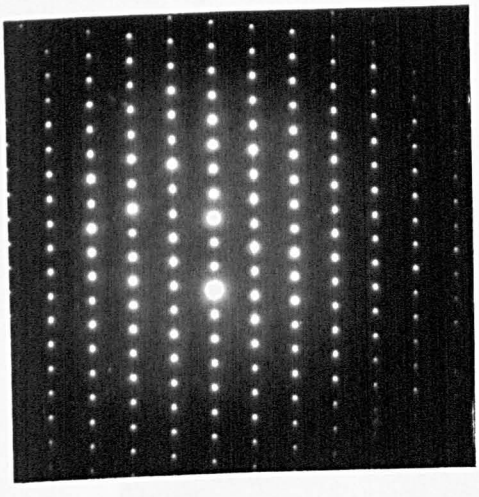

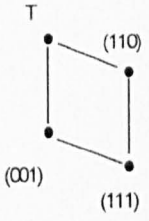

$[\bar{1}\,1\,0]Al_{13}Fe_4$

c)

Fig.4.35 continued: The number given in bold is the interzonal angle calculated based on the $Al_{13}Fe_4$ lattice parameters given in Table 2.1, whilst that in parenthesis is the experimentally determined value.

a)

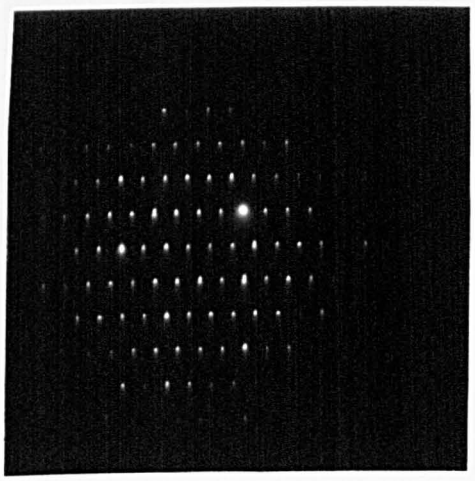

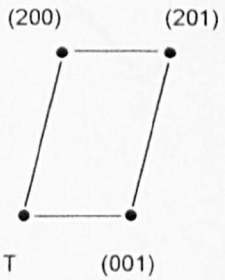

b)

Fig.4.36: Transverse sction electron micrograph a) of a group of $Al_{13}Fe_4$ crystals typical of those observed on the α-Al cell boundaries in Al-0.5%Fe-0.1%Si-0.75%Mg which had been unidirectionally solidified at 0.50 mm/s. b) $[010]_{Al_{13}Fe_4}$ SADP.

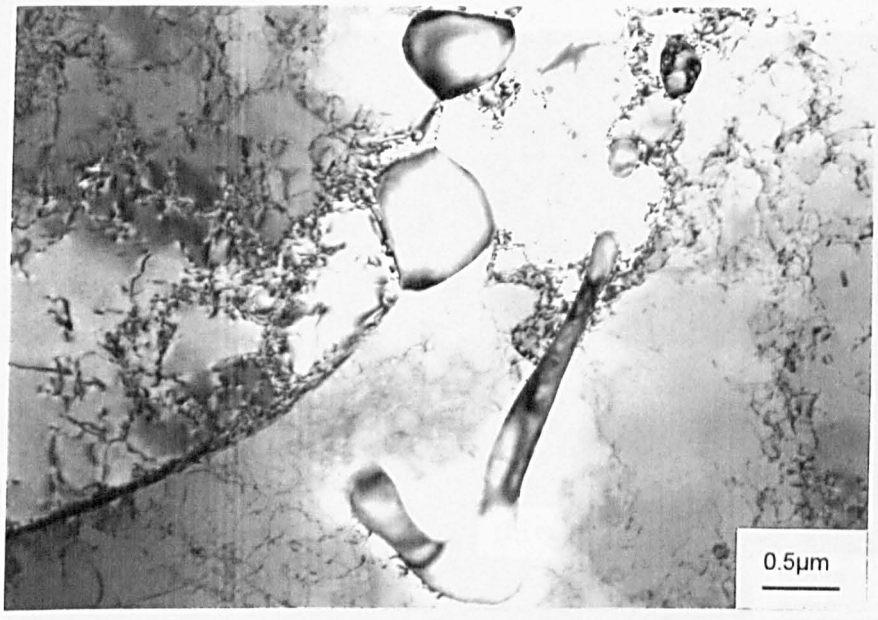

a)

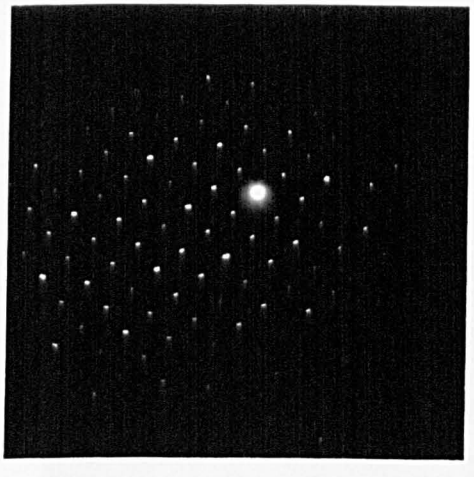

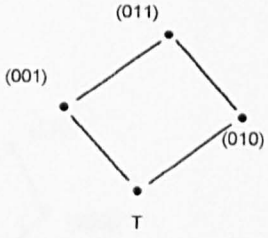

b)

Fig.4.37: Transverse section electron micrograph a) showing the typical morphology of Al_xFe crystals observed in Al-0.5%Fe-0.1%Si-0.75%Mg which had been unidirectional solidified at V= 0.5mm/s: and b) the corresponding $[100]_{Al_xFe}$ SADP.

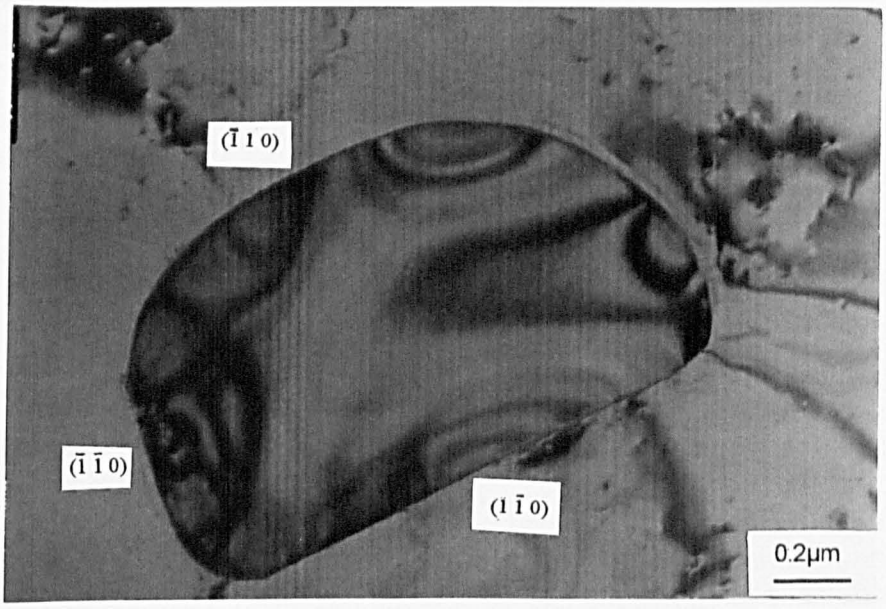

a)

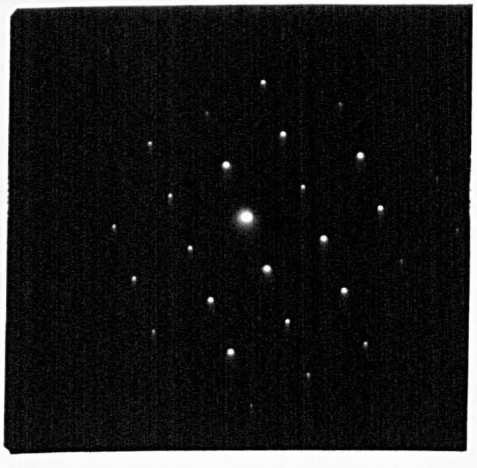

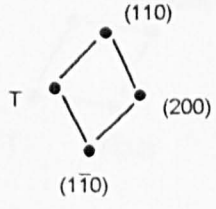

b)

Fig.4.38: Transverse section electron micrograph a) showing the typical morphology of Al_6Fe crystals observed in Al-0.5%Fe-0.1%Si-0.75%Mg which had been unidirectionally solidified at 0.5mm/s. This particular example shows evidence of faceting and the facet planes have been determined to be of the {110} type. b) The accompanying [00 $\bar{1}$] SADP.

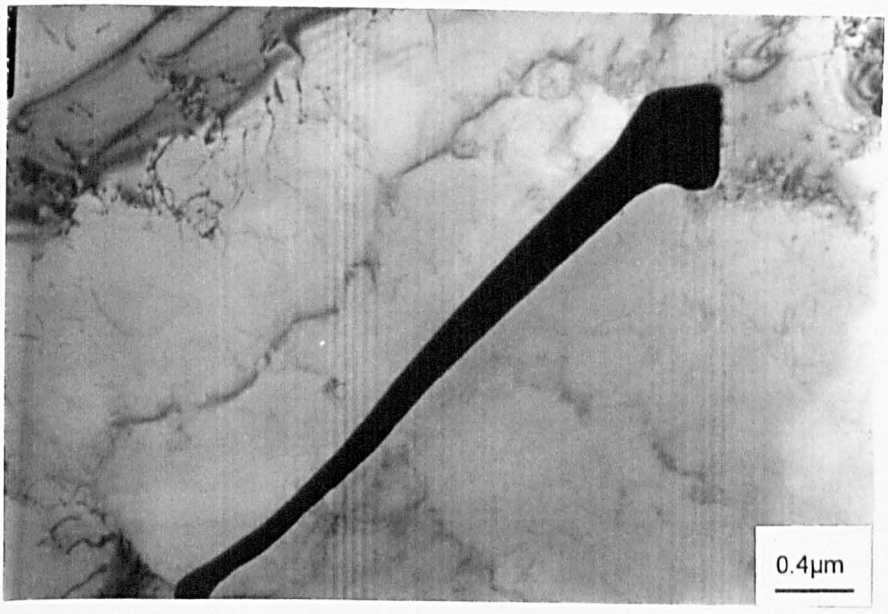

a)

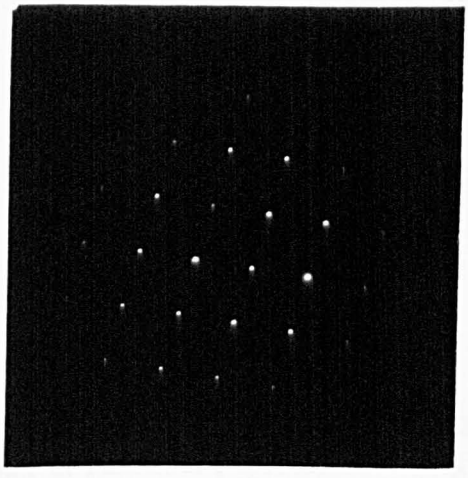

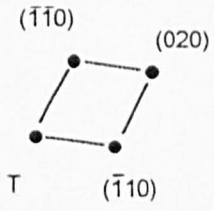

b)

Fig.4.39: a) TEM micrograph showing an example of the lath Al_6Fe morphology observed in Al-0.5%Fe-0.1%Si-0.75%Mg which had been unidirectionally solidified at 2.00mm/s. b) The accompanying [001] SADP.

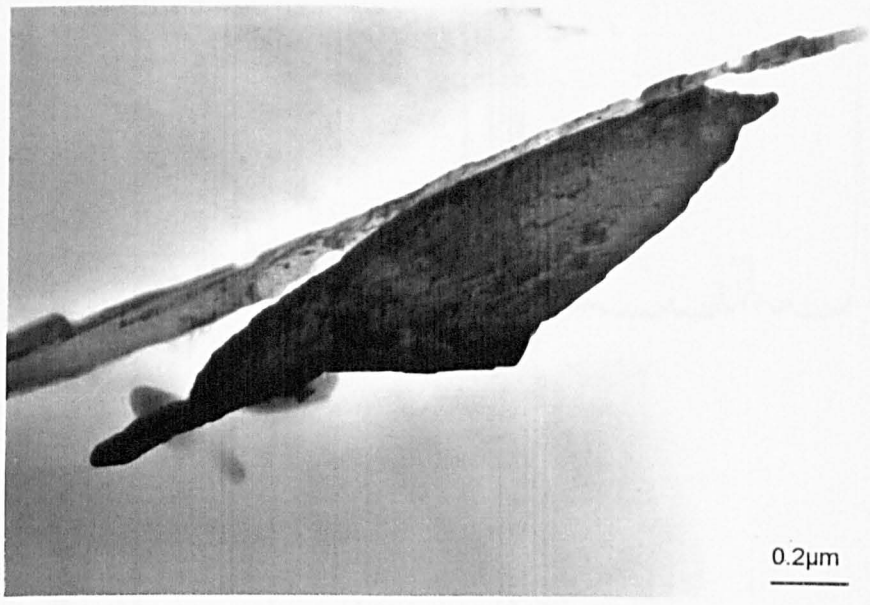

Fig.4.40: Transverse section electron micrograph of an $Al_{13}Fe_4$ crystal present as a minor constituent in Al-0.5%Fe-0.1%Si-0.75%Mg which had been unidirectionally solidified with V= 2.00mm/s.

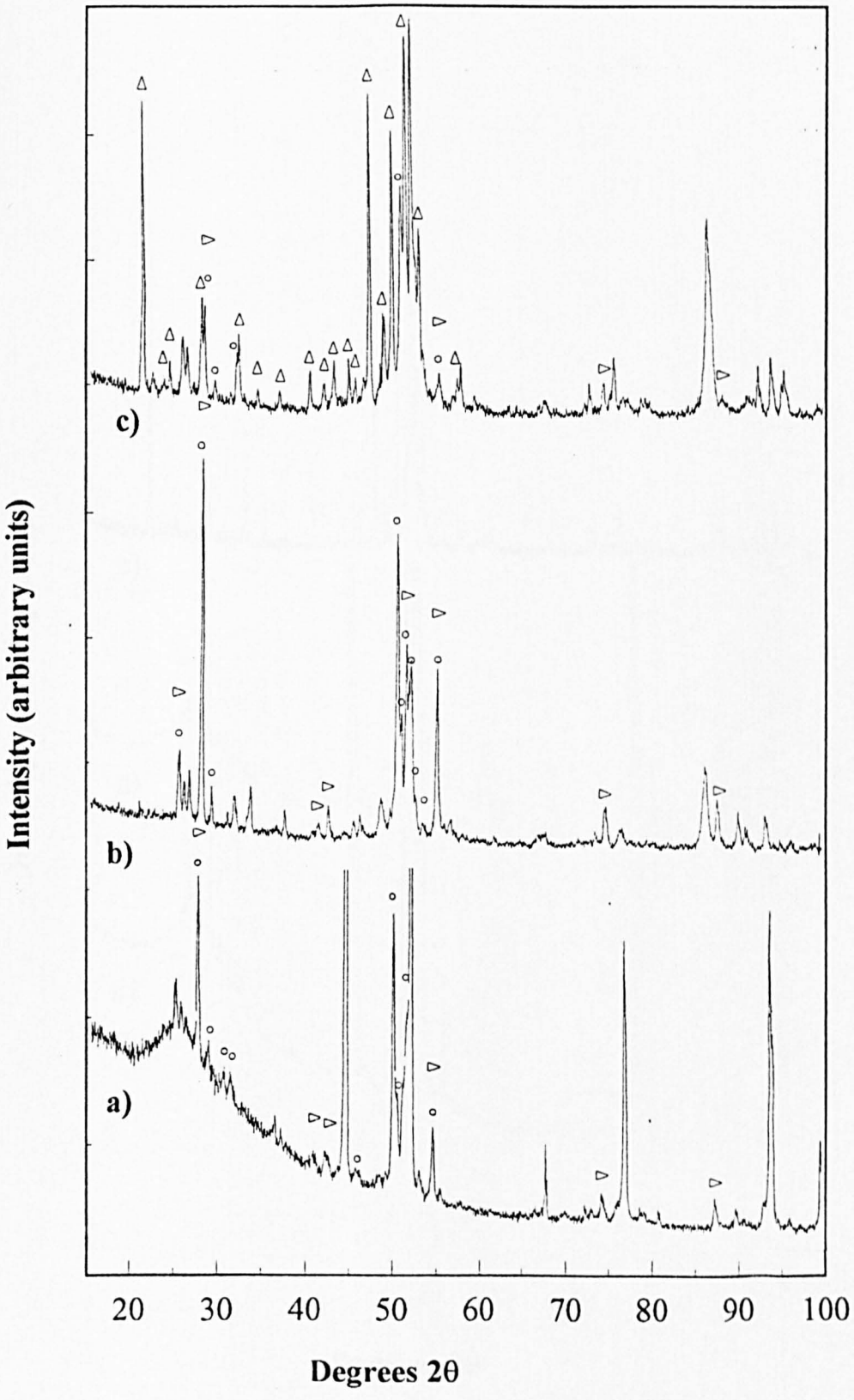

Fig.4.41: X-ray traces of second phase intermetallics extracted from Al-0.75%Fe-0.1%Si-0.75%Mg alloy specimens which had been unidirectionally solidified at a) 0.05mm/s, b) 1.00mm/s and c) 2.00mm/s respectively. Trace a was taken from intermetallics extracted by the HCl method and b and c extracted by the butanol method.

Key: ○ - $Al_{13}Fe_4$, Δ -Al_6Fe, ▷ -Al_xFe.

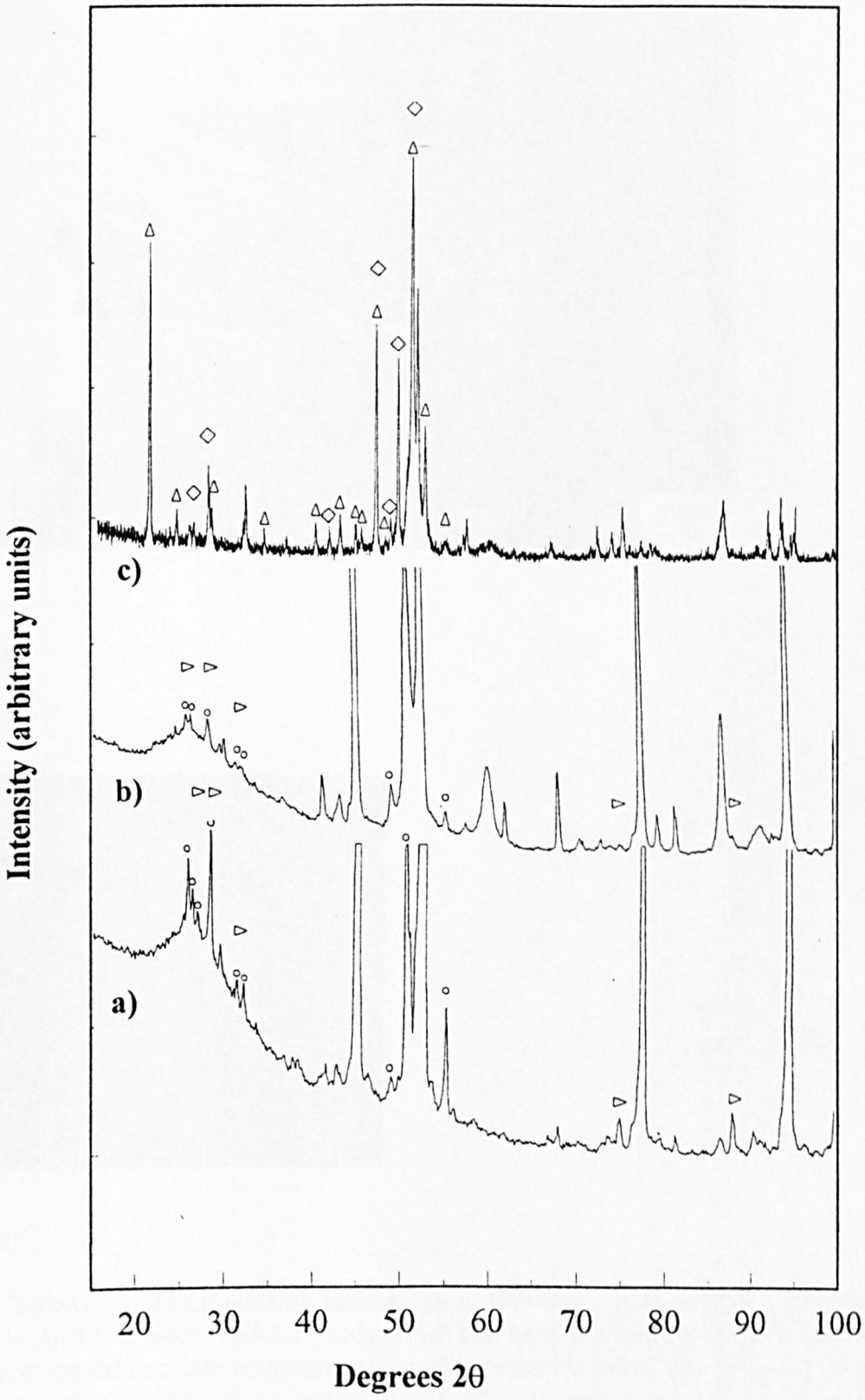

Fig.4.42: X-ray diffraction traces taken from intermetallics extracted from Al-0.5%Fe-0.05%Si-0.75%Mg alloy specimens solidified at a) 0.05mm/s, b) 0.50mm/s and c) 1.00mm/s respectively. Traces a and b were taken from intermetallics extracted by the HCl method whilst c was taken from material extracted by the butanol reflux technique.

Key: ○ - $Al_{13}Fe_4$, △ -Al_6Fe, ▷ -Al_xFe ◇ -Al_mFe.

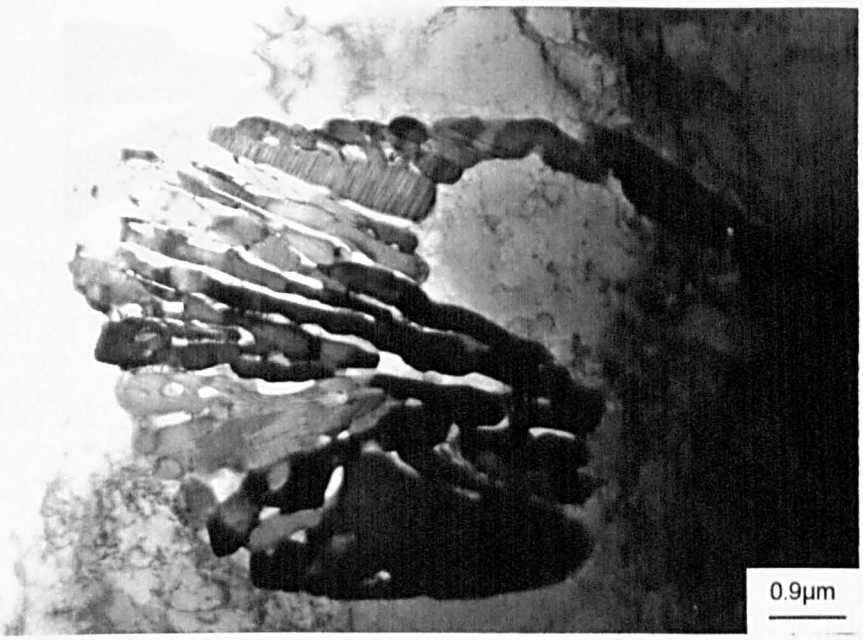

a)

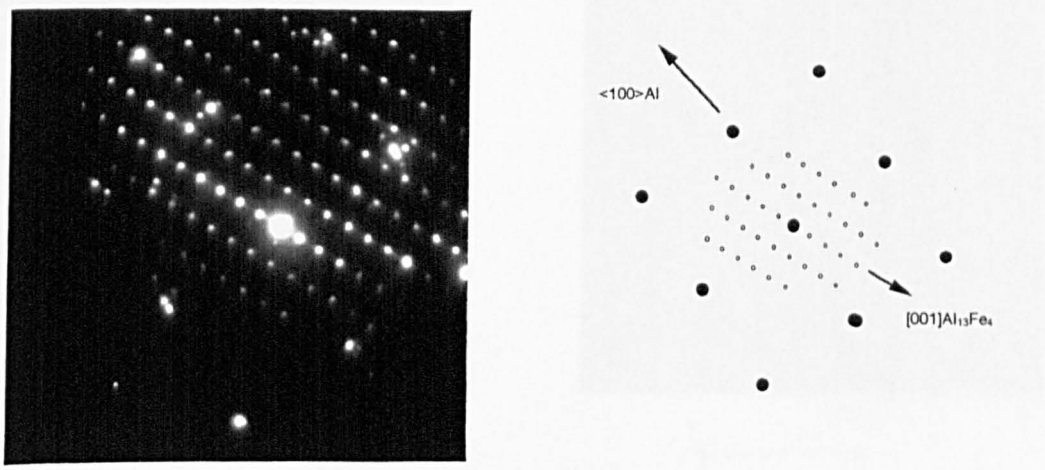

b)

Fig.4.43: Transverse section electron micrograph a) showing a typical $Al_{13}Fe_4$ crystal group observed in Al-0.5%Fe-0.05%Si-0.75%Mg which had been unidirectionally solidified at 0.10 mm/s. These crystals contain many crystallographic faults on (001) and several (100) faults are also present. The SADP, b), shows the $[010]_{Al_{13}Fe_4}$ pattern to near coincident with $\langle 100 \rangle_{\alpha\text{-Al}}$.

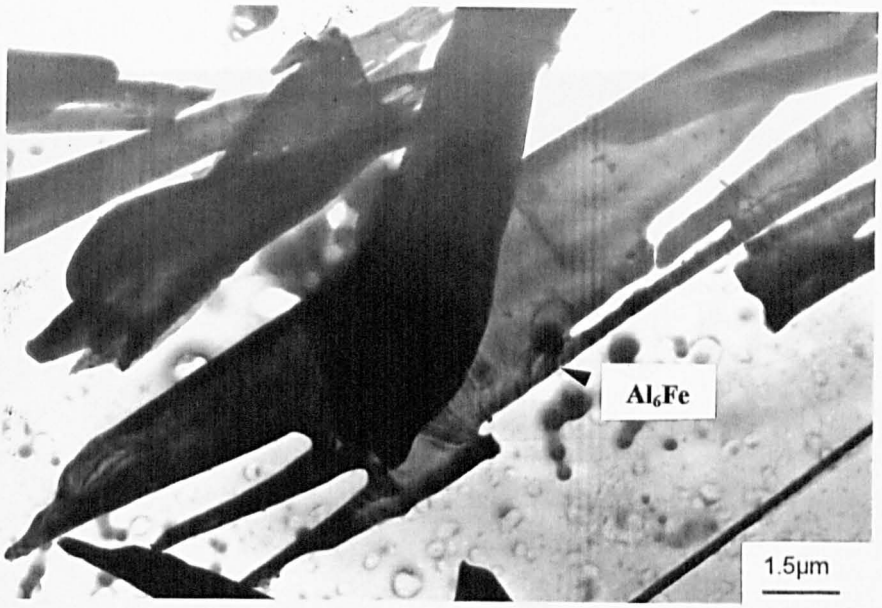

a)

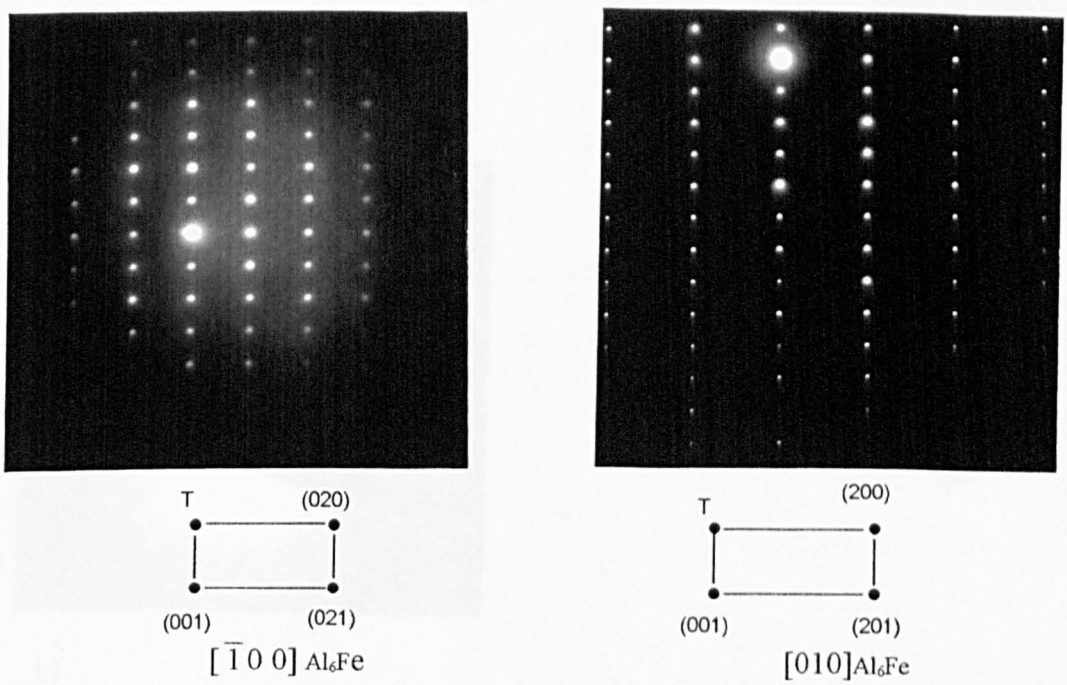

b)

Fig.4.44: Electron micrograph a) of an extracted Al_6Fe crystal (indicated) showing the lath-dendritic morphology typical of that found in Al-0.5%Fe-0.05%Si-0.75%Mg alloy specimens which had been unidirectionally solidified at 1.00mm/s: and b), accompanying SADP's taken from this particular crystal confirming the identification of the phase.

a)

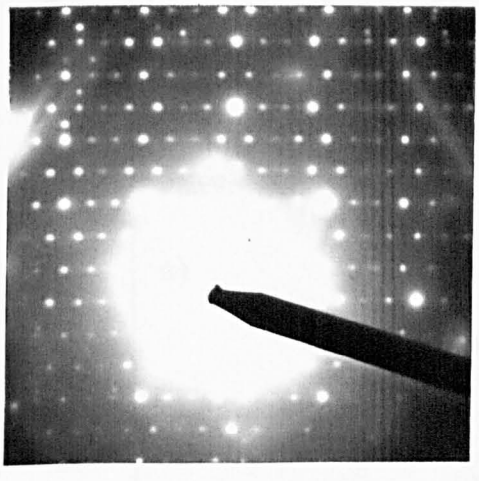

b)

Fig.4.45: Transverse section electron micrograph a) showing the typical morphology of Al_mFe found in Al-0.5%Fe-0.05%Si-0.75%Mg alloy specimens which had been unidirectionally solidified at 2.00mm/s. b) $[100]_{Al_mFe}$.

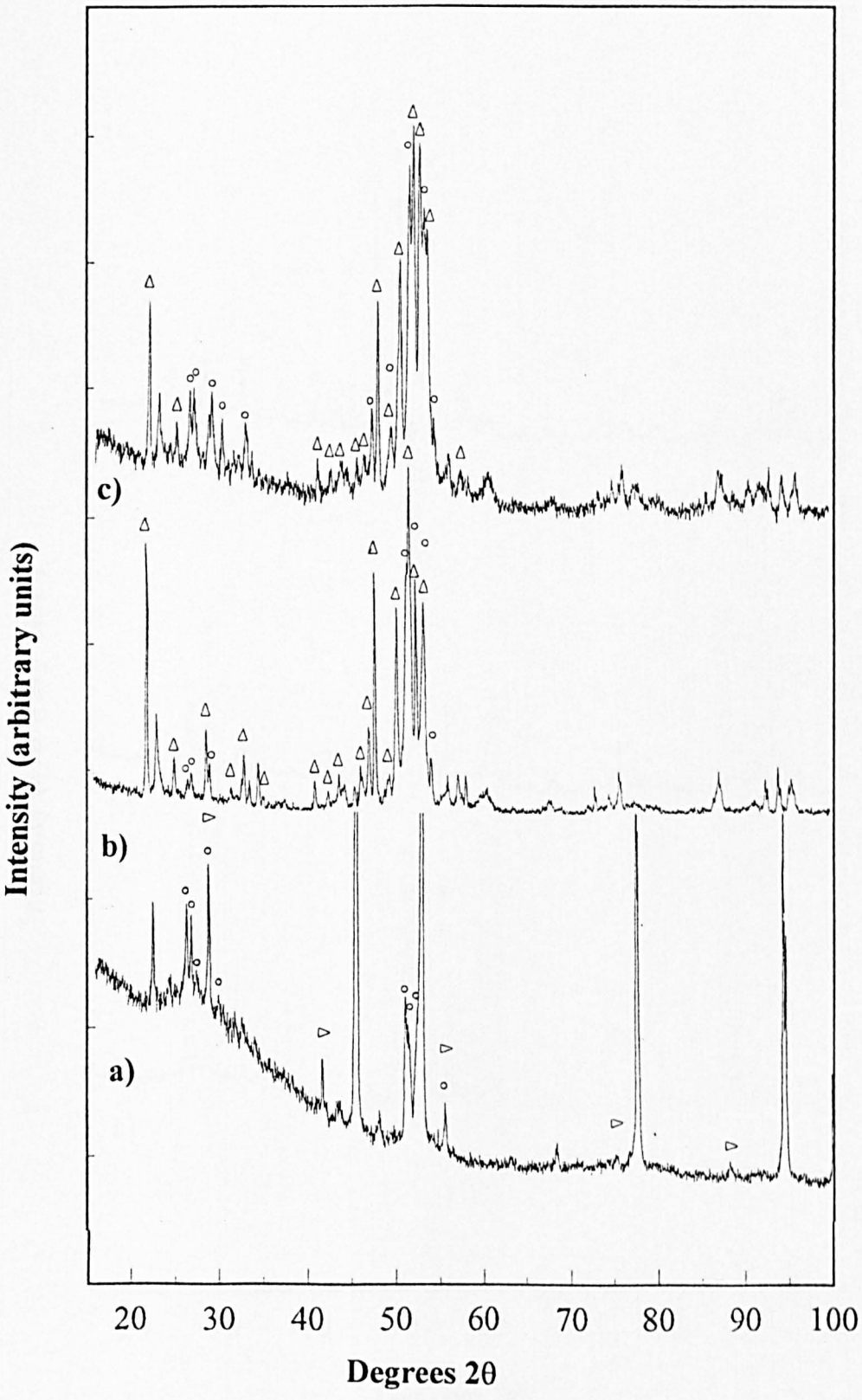

Fig.4.47: X-ray traces of second phase intermetallics extracted from Al-0.5%Fe-0.1%Si-0.75%Mg alloy specimens which had been unidirectionally solidified at a) 0.05mm/s, b) 0.50mm/s and c) 2.00mm/s respectively. The trace, a, was taken from HCl extracted material whilst b and c were taken from butanol extracted material.

Key: ○ - $Al_{13}Fe_4$, △ -Al_6Fe, ▷ -Al_xFe.

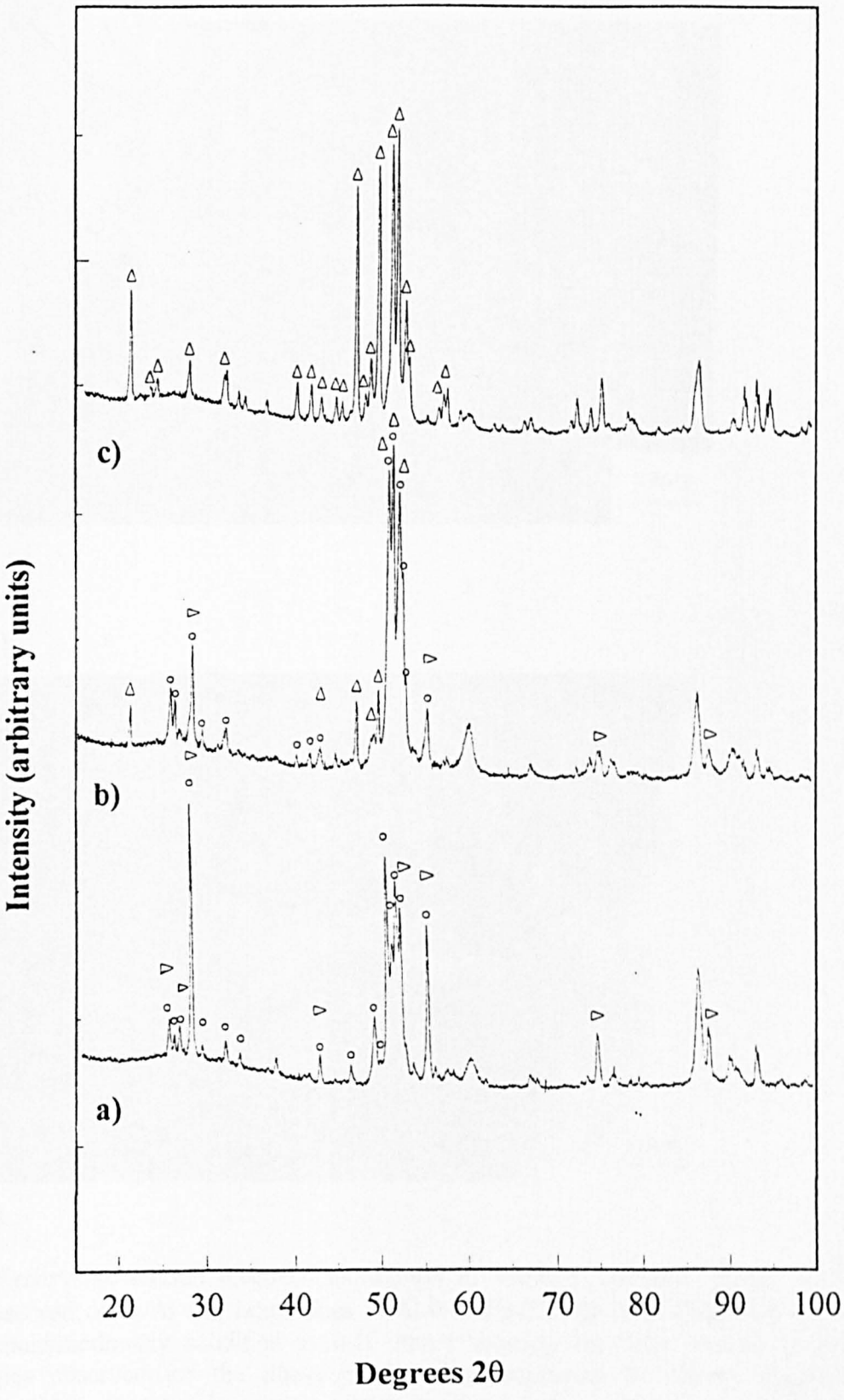

Fig.4.48: X-ray diffraction traces taken from Al-0.5%Fe-0.1%Si-0.75%Mg-0.04%Cr alloy specimens which had been unidirectionally solidified at a) 0.05mm/s, b) 0.50mm/s and c) 2.00mm/s. All traces were taken from material which had been extracted by the butanol method.

Key: ○- $Al_{13}Fe_4$, △ -Al_6Fe, ▷ -Al_xFe.

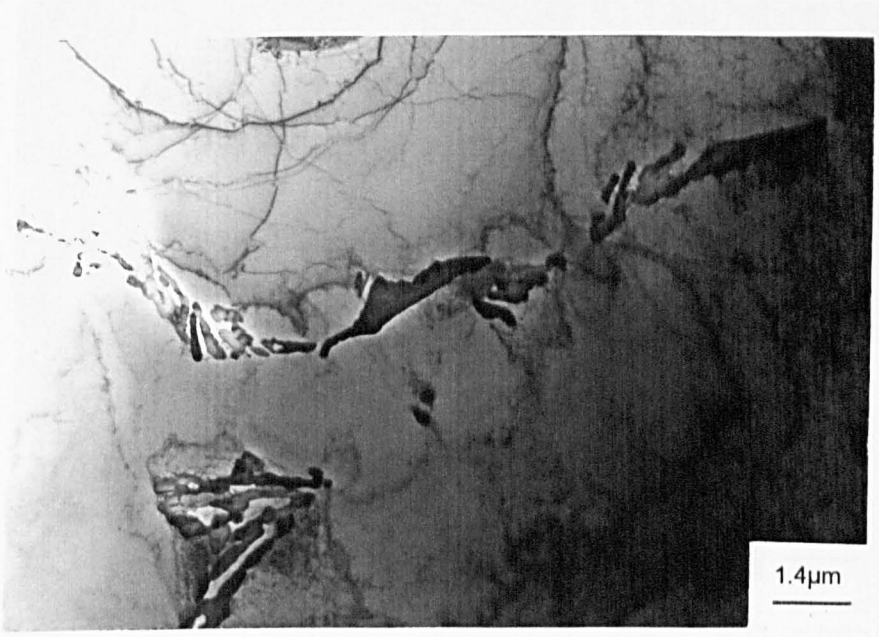

a)

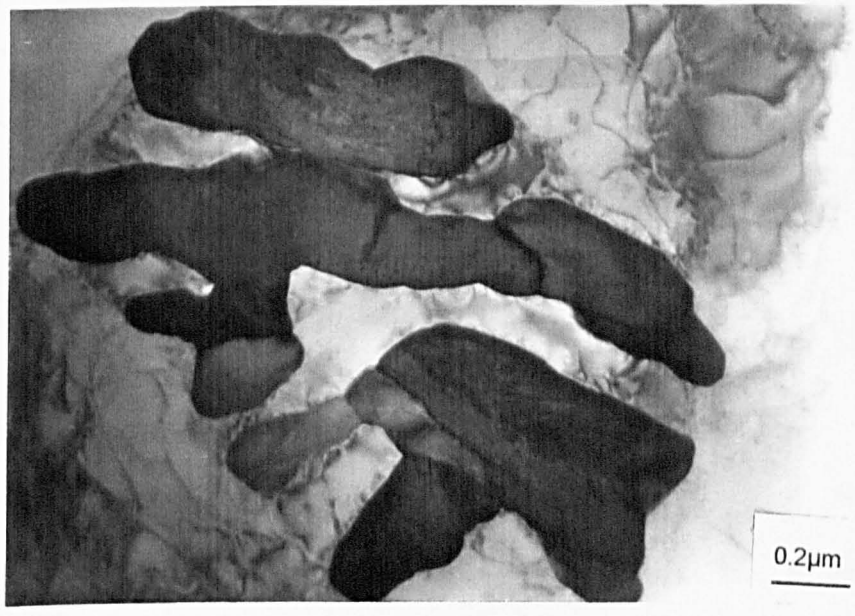

b)

Fig.4.49: Transverse section electron micrograph a) showing a typical group of $Al_{13}Fe_4$ crystals observed on α-Al cell boundaries in Al-0.5%Fe-0.1%Si-0.75%Mg-0.04%Cr which had been unidirectionally solidified at 0.10 mm/s showing the wide variety of possible morphologies observed for the phase in this alloy condition. b) Higher magnification micrograph of low aspect ratio crystals containing (001) faults and both stacking faults and twin planes on (100).

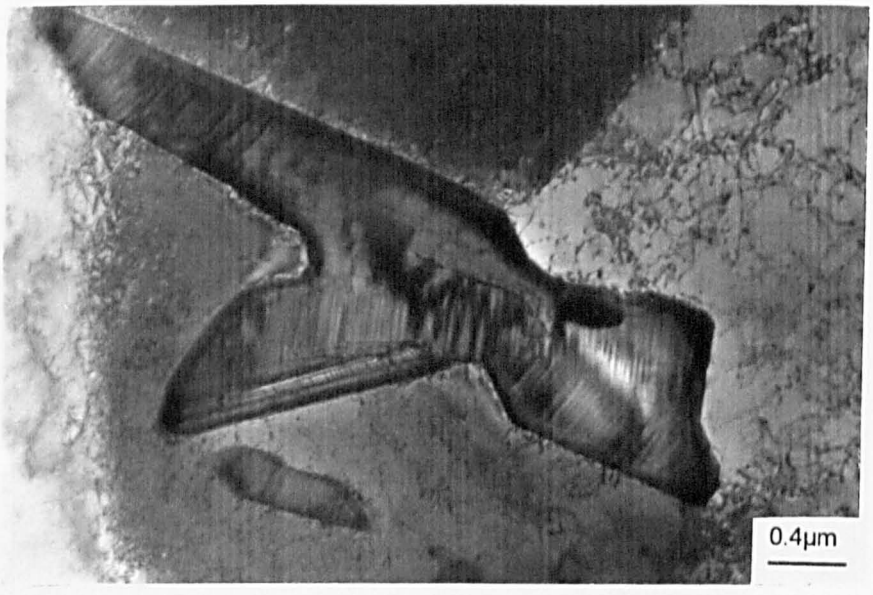

a)

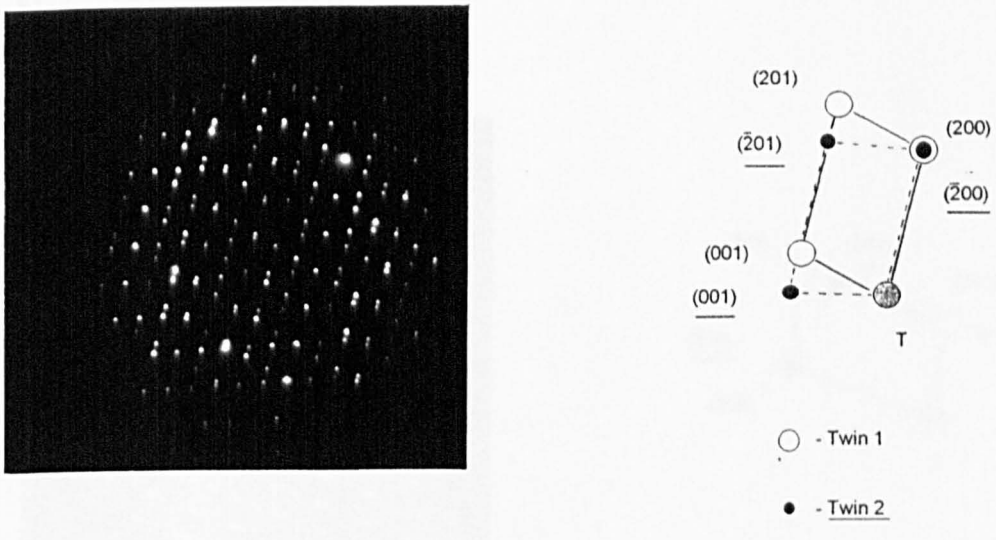

b)

Fig.4.50: Transverse section electron micrograph a) showing an $Al_{13}Fe_4$ crystal found in a specimen of Al-0.5%Fe-0.1%Si-0.75%Mg-0.04%Cr alloy which had been unidirectionally solidified at 0.10 mm/s. The crystal also contains a number of (100) twin planes which give rise to $[010]_{Al_{13}Fe_4}$ diffraction patterns of the type shown in b.

a)

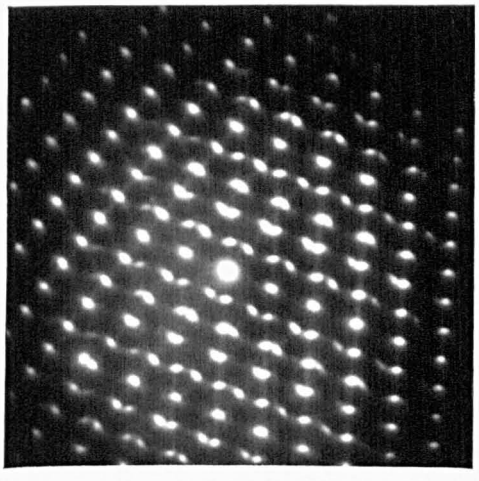

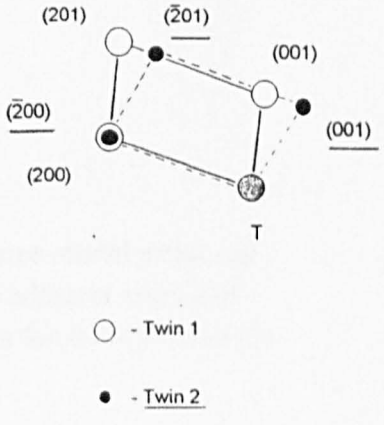

b)

Fig.4.51: Typical $Al_{13}Fe_4$ crystal found in Al-0.5%Fe-0.1%Si-0.75%Mg-0.04%Cr after unidirectional solidification at V = 0.10mm/s. The compound SADP, b, shows that the crystal contains a (100) twin plane.

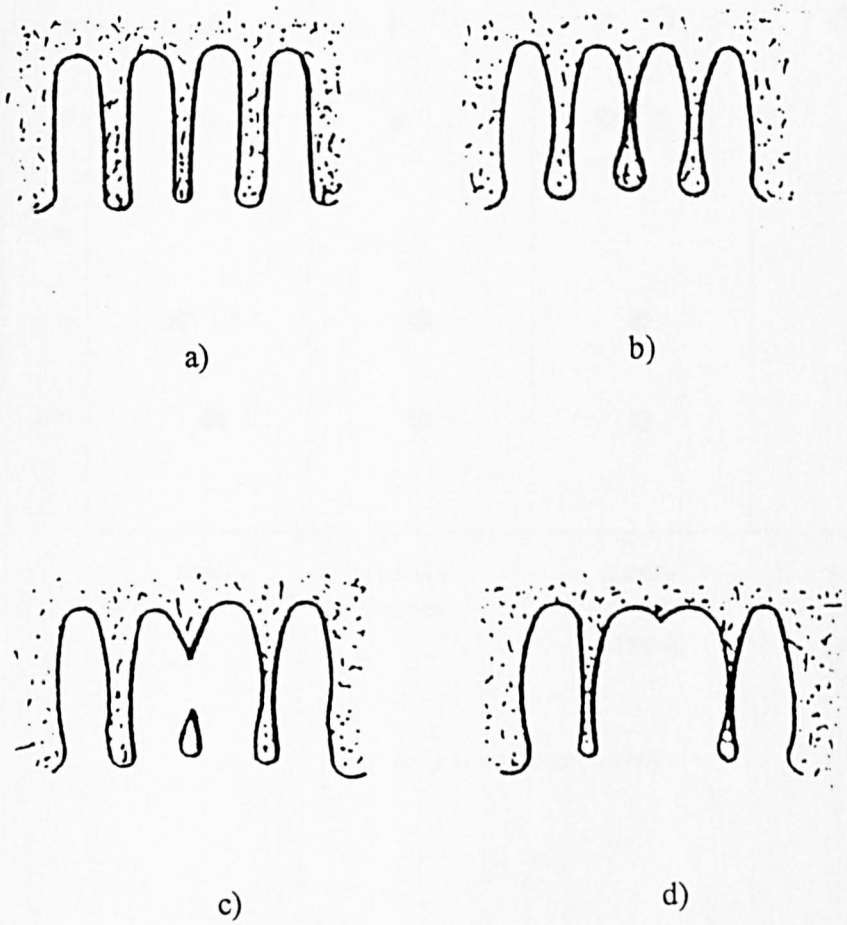

Fig.5.1: Schematic illustration of the dendrite coalescence model proposed by Genda, Yuyon and Geing [1987]. a) start, b) adjacent arms join at the mid-point, c) coalescence extending from the mid-point to the root and d) end..

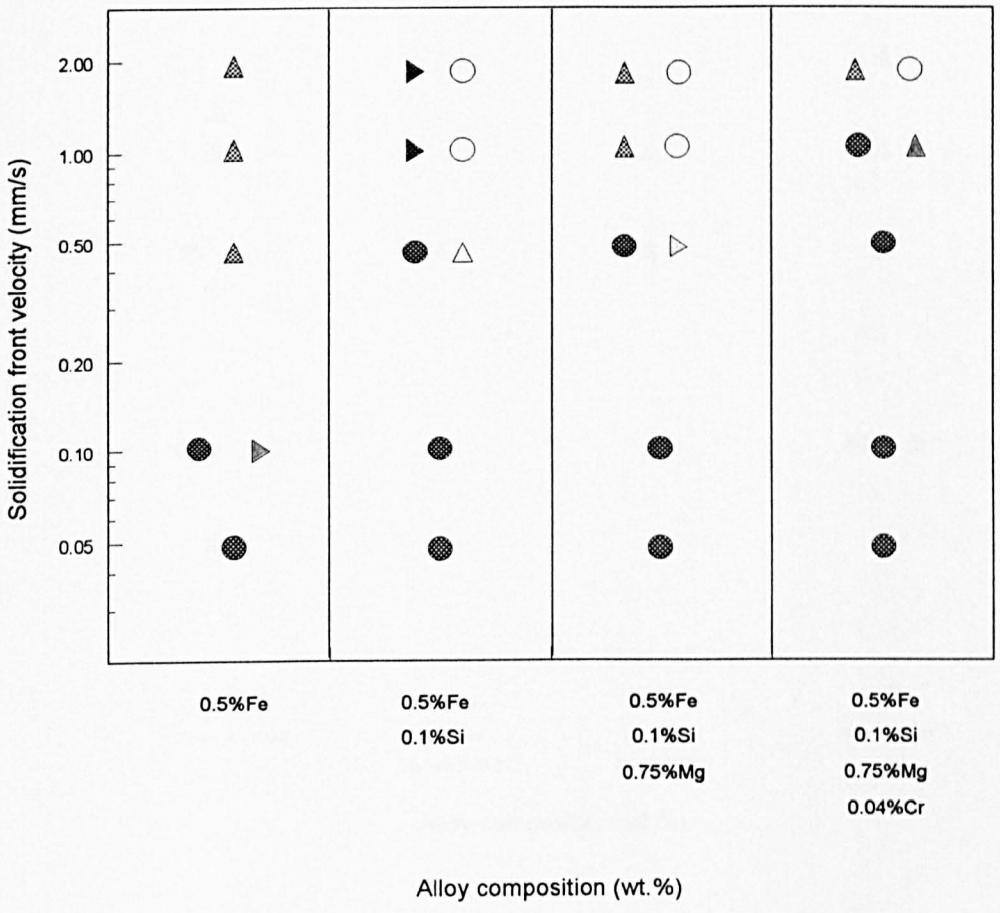

Fig.5.2: The effect of cumulative alloying additions on phase stability in Al-0.5%Fe. Phase dominance is indicated by the use of a shaded symbol. Where phases are observed to be co-dominant both are shaded.

Key:-

● ○ $Al_{13}Fe_4$ ▲ △ Al_6Fe ▶ ▷ Al_xFe ◆ ◇ Al_mFe ◀ ◁ β-AlFeSi

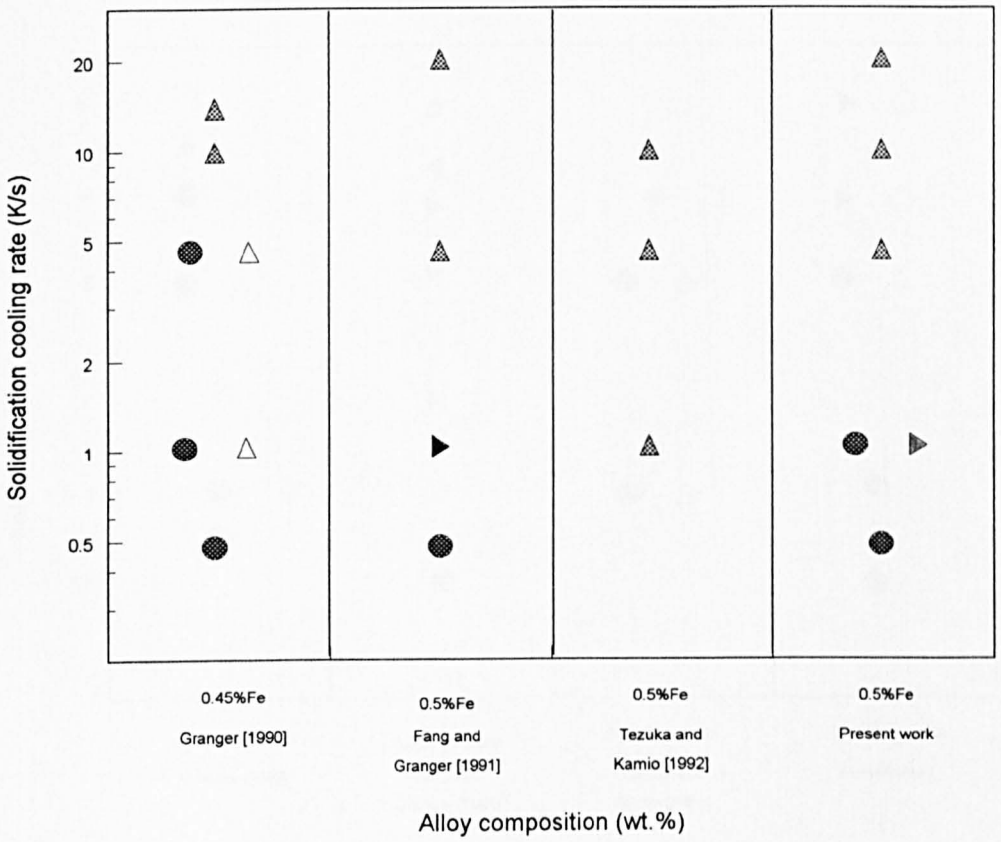

Fig.5.3: Comparison of the phase stability results for Al-0.5%Fe obtained in the present work with those taken from the available literature. Phase dominance is indicated by the use of a shaded symbol.

Key:-

● ○ $Al_{13}Fe_4$ ▲ △ Al_6Fe ▶ ▷ Al_xFe ◆ ◇ Al_mFe ◀ ◁ β-AlFeSi

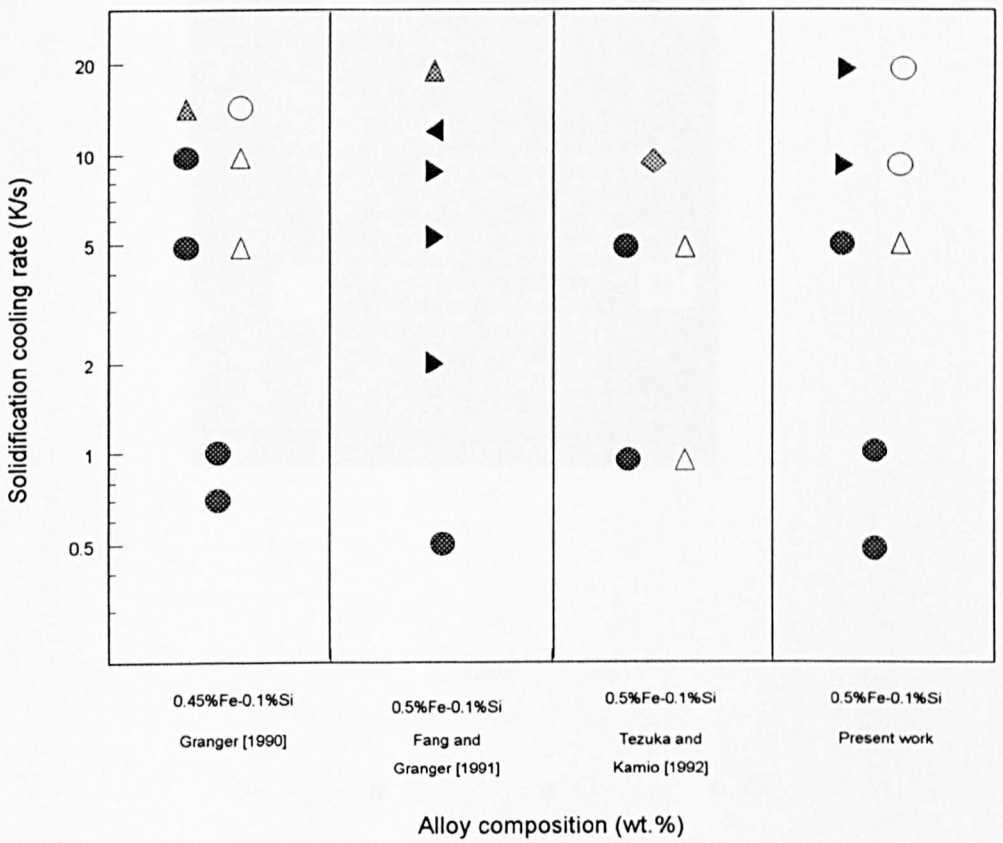

Fig.5.4: Comparison of the phase stability results for Al-0.5%Fe-0.1%Si obtained in the present work with those taken from the available literature. Phase dominance is indicated by the use of a shaded symbol.

Key:-

● ○ $Al_{13}Fe_4$ ▲ △ Al_6Fe ▶ ▷ Al_xFe ◆ ◇ Al_mFe ◀ ◁ β-AlFeSi

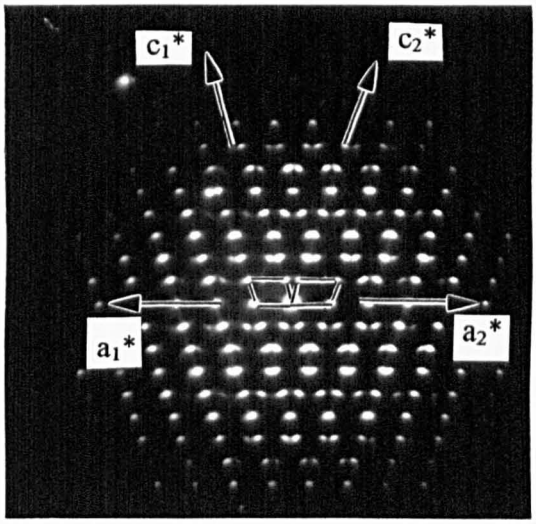

a)

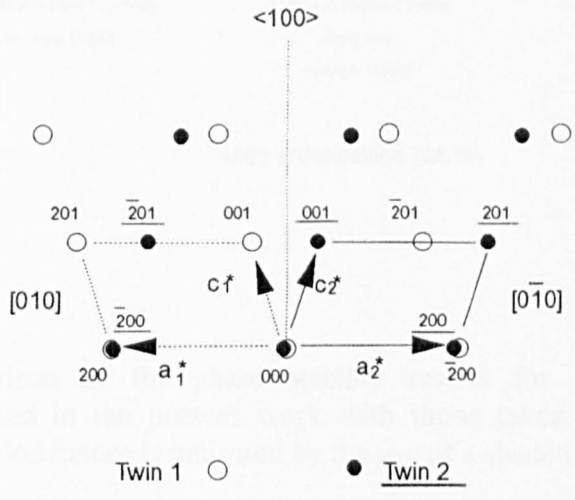

b)

Fig.5.5: A composite < 010 > SADP taken from a (100) twin in $Al_{13}Fe_4$: and b) schematic illustration of the indexing of this < 010 > pattern for comparison.

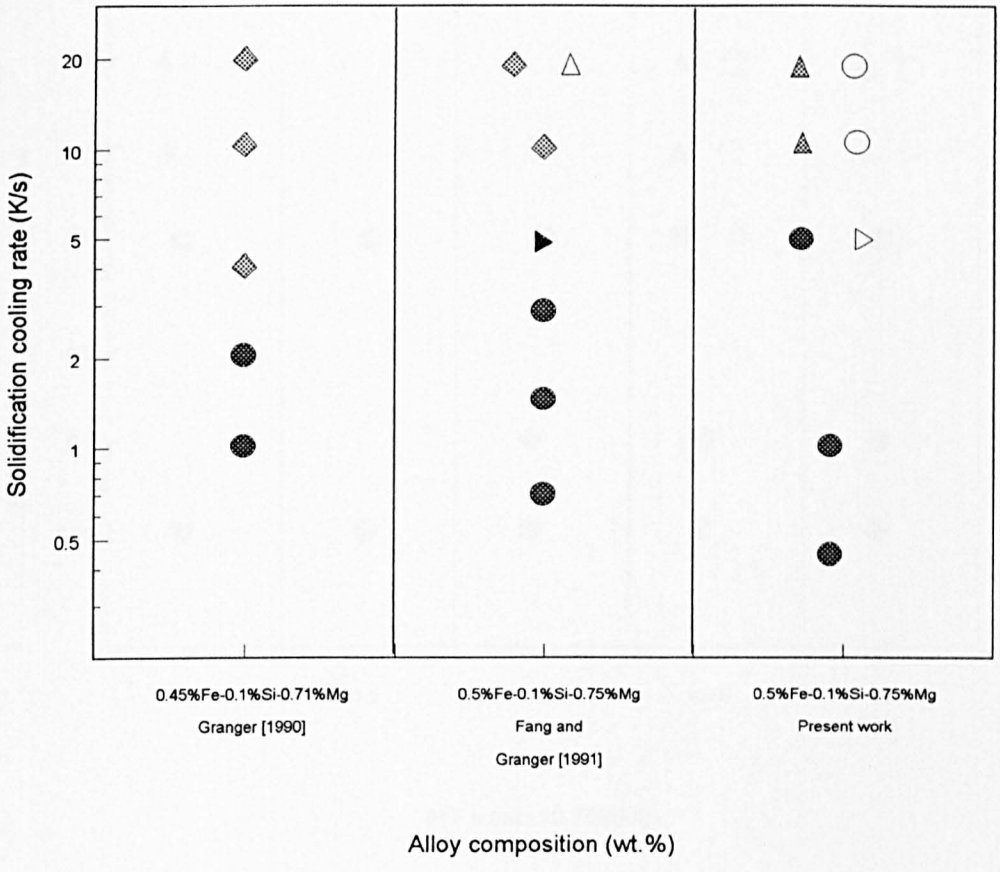

Fig.5.6: Comparison of the phase stability results for Al-0.5%Fe-0.1%Si-0.75%Mg obtained in the present work with those taken from the available literature. Phase dominance is indicated by the use of a shaded symbol.

Key:-

● ○ $Al_{13}Fe_4$ ▲ △ Al_6Fe ▶ ▷ Al_xFe ◆ ◇ Al_mFe ◀ ◁ β-AlFeSi

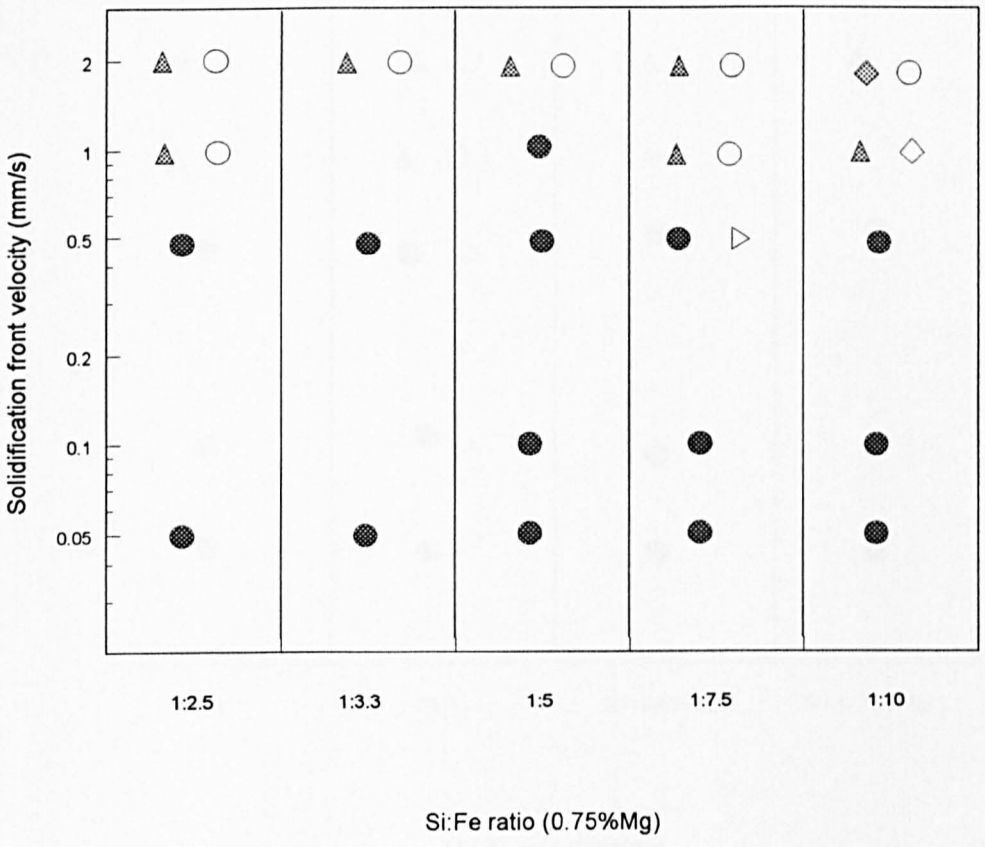

Fig.5.7: The effect of varying Si:Fe ratio on intermetallic phase stability in Al-X%Fe-Y%Si-0.75%Mg alloys. Phase dominance is indicated by the use of a shaded symbol.

Key:-

$Al_{13}Fe_4$ Al_6Fe Al_xFe Al_mFe β-AlFeSi

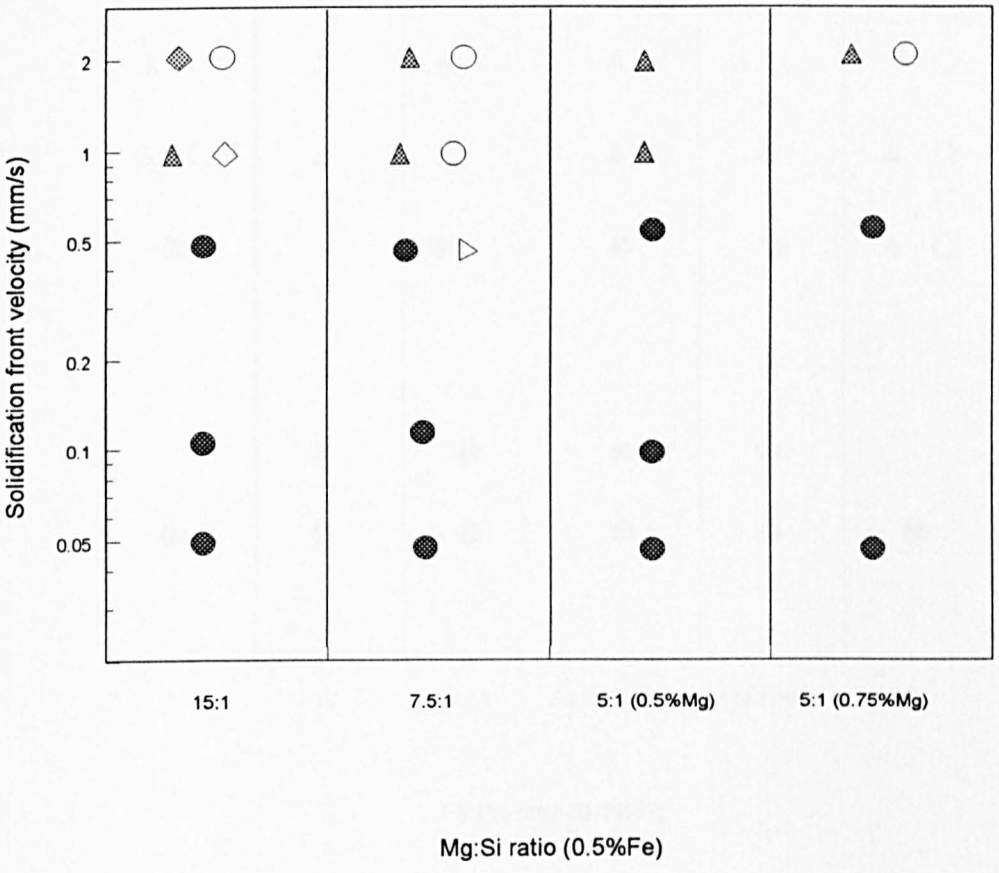

Fig.5.8: The effect of varying Mg:Si ratio on intermetallic phase stability in Al-0.5%Fe-Y%Si-Z%Mg alloys. Phase dominance is indicated by the use of a shaded symbol.

Key:-

$Al_{13}Fe_4$ Al_6Fe Al_xFe Al_mFe β-AlFeSi

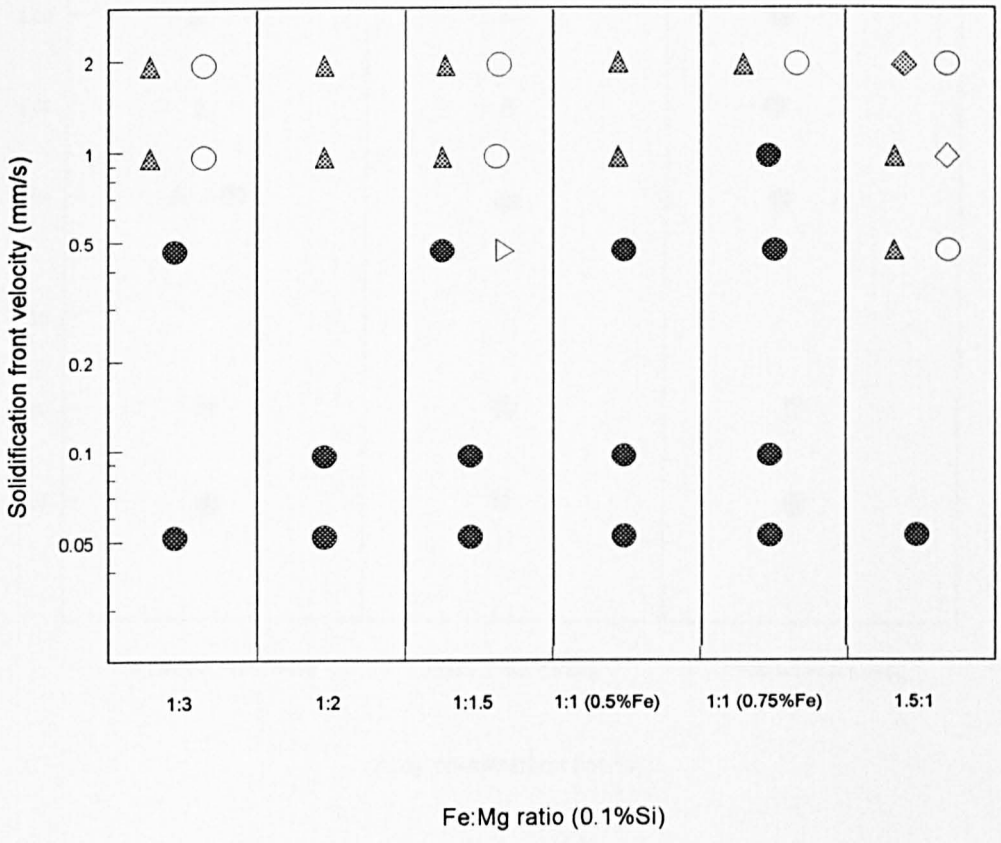

Fig.5.9: The effect of varying Fe:Mg ratio on intermetallic phase stability in Al-X%Fe-0.1%Si-Z%Mg alloys. Phase dominance is indicated by the use of a shaded symbol.

Key:-

● ○ $Al_{13}Fe_4$ ▲ △ Al_6Fe ▶ ▷ Al_xFe ◆ ◇ Al_mFe ◀ ◁ β-AlFeSi

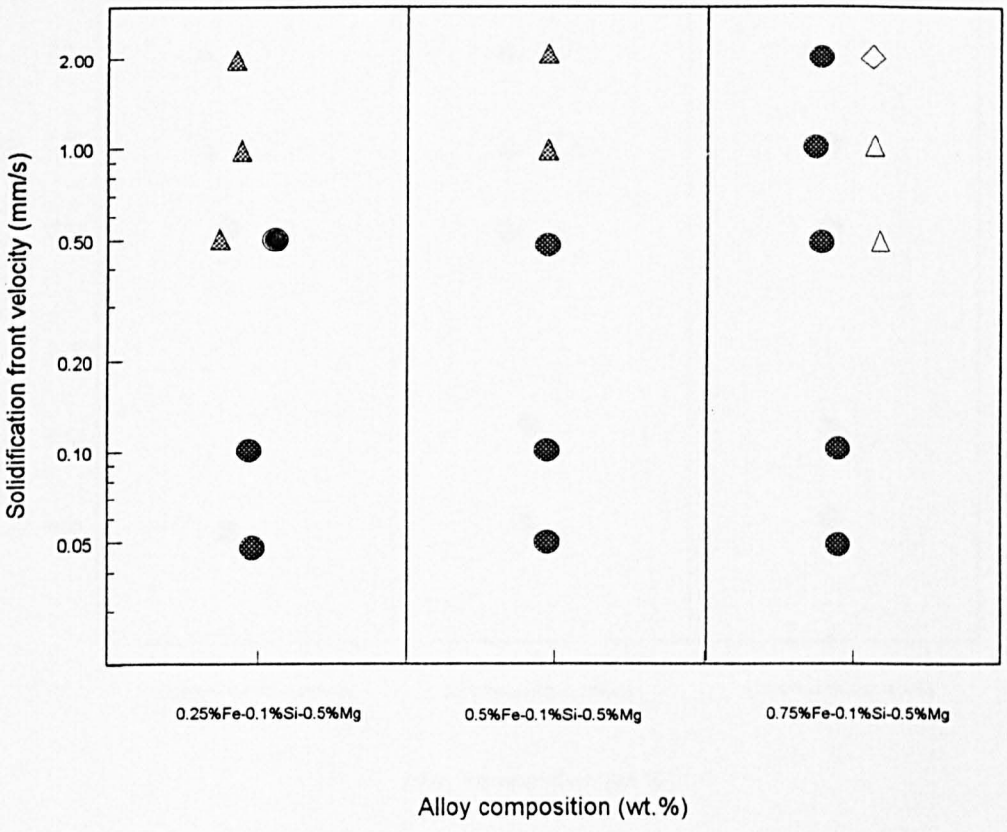

Fig.5.10: The effect on intermetallic phase stability of varying Fe content in Al-X%Fe-0.1%Si-0.5%Mg alloys. Phase dominance is indicated by use of a shaded symbol.

Key:-

● ○ $Al_{13}Fe_4$ ▲ △ Al_6Fe ▶ ▷ Al_xFe ◆ ◇ Al_mFe ◀ ◁ β-AlFeSi

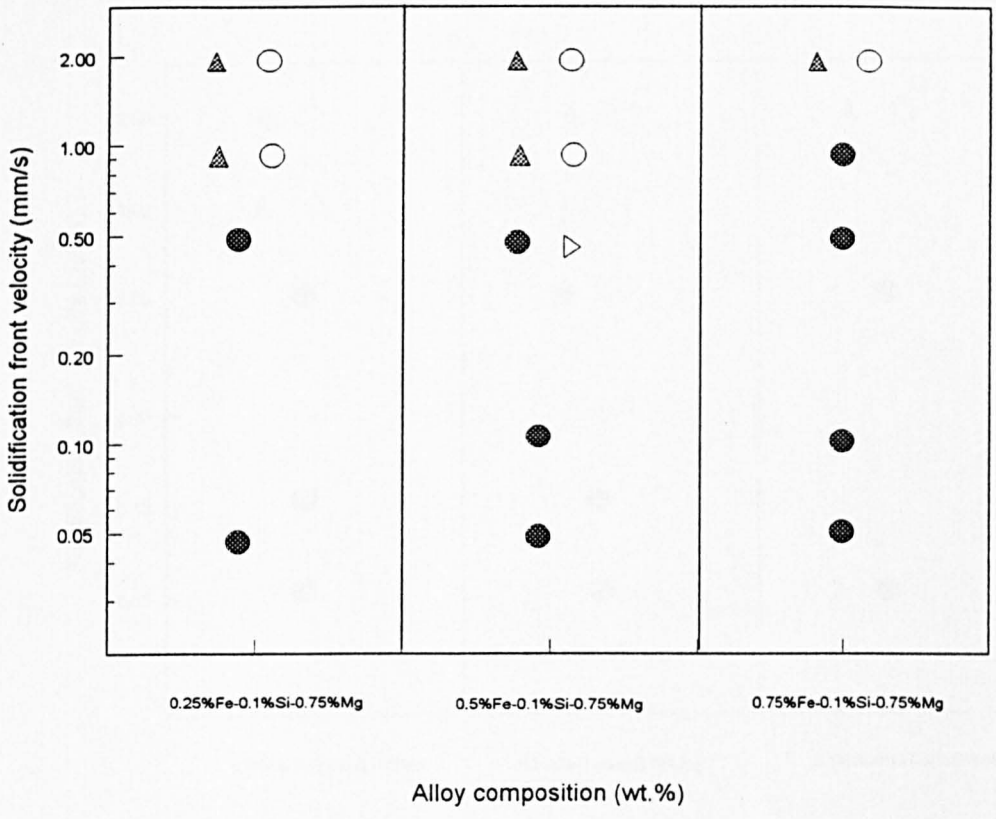

Fig.5.11: The effect on intermetallic phase stability of varying Fe content in Al-X%Fe-0.1%Si-0.75%Mg alloys. Phase dominance is indicated by use of a shaded symbol.

Key:-

● ○ $Al_{13}Fe_4$ ▲ △ Al_6Fe ▶ ▷ Al_xFe ◈ ◇ Al_mFe ◀ ◁ β-AlFeSi

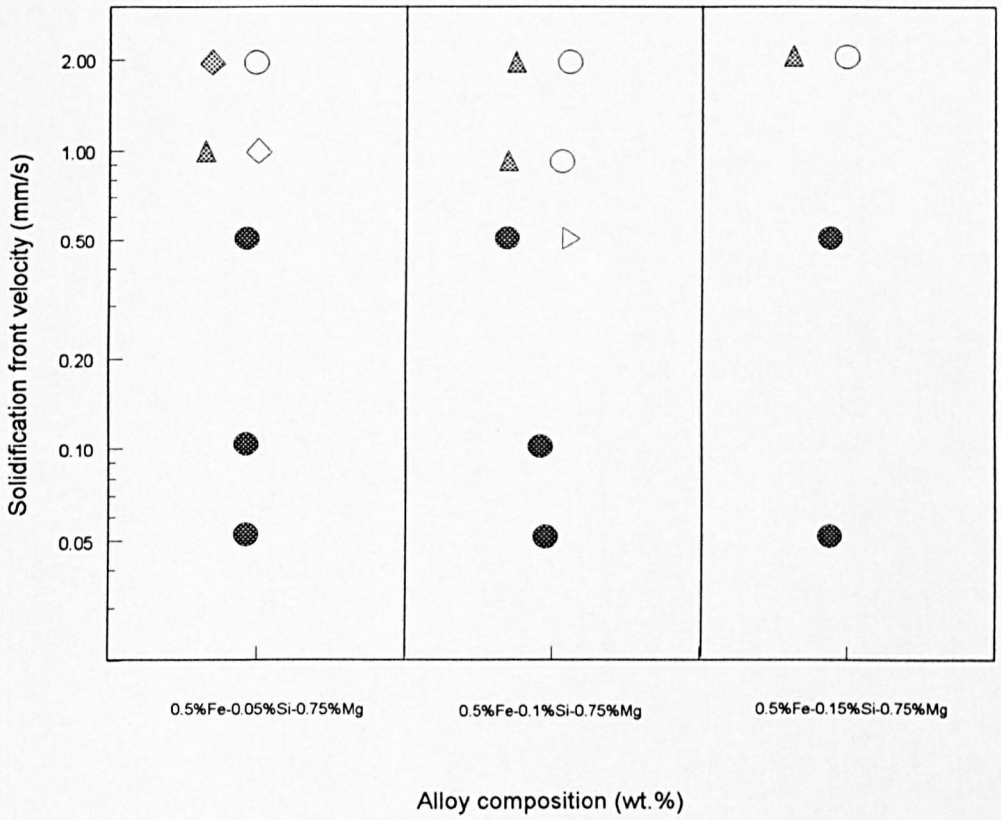

Fig.5.12: The effect on intermetallic phase stability of varying Si content in Al-0.5%Fe-Y%Si-0.75%Mg alloys. Phase dominance is indicated by use of a shaded symbol.

Key:-

● ○ $Al_{13}Fe_4$ ▲ △ Al_6Fe ▶ ▷ Al_xFe ◆ ◇ Al_mFe ◀ ◁ β-AlFeSi